Lattice Based Low Control Quantum Technology

Enrico Compagno

University College London

A dissertation submitted in partial fulfilment

of the requirements for the degree of

Doctor of Philosophy

February 2018

I, Enrico Compagno, confirm that the work presented in this thesis is my own. Where information has been derived from other sources, I confirm that this has been indicated in the work. Parts of this dissertation have been published, or submitted for publication, as follows:

- Enrico Compagno, Leonardo Banchi, Christian Gross, and Sougato Bose, *NOON states via a quantum walk of bound particles*, Phys. Rev. A **95**, 012307 (2017).

- Enrico Compagno, Leonardo Banchi and Sougato Bose, *Toolbox for linear optics in a one-dimensional lattice via minimal control*, Phys. Rev. A **92**, 022701 (2015).

- Leonardo Banchi, Enrico Compagno and Sougato Bose, *Perfect wave-packet splitting and reconstruction in a one-dimensional lattice*, Phys. Rev. A **91**, 052323 (2015).

- Leonardo Banchi, Enrico Compagno, Vladimir Korepin and Sougato Bose, *Quantum Gates Between Distant Qubits via Spin-Independent Scattering*, Quantum **1**, 36 (2017).

During the PhD work I have been also involved in a work about immersed quantum impurity systems, not covered in this thesis, that led to a publication:

- Enrico Compagno, Gabriele De Chiara, Dimitris Angelakis and Gioacchino Massimo Palma, *Tunable Polarons in Bose-Einstein Condensates*, Sci. Rep. **7**, 2355 (2017)

Abstract

The possibility to designing schemes useful for developing quantum technology devices of practical value necessitates exploiting quantum coherence effects in a scalable physical system in a feasible way. The broad aim of this thesis is to investigate the use of quantum non-equilibrium dynamics for the above, exploiting minimal control to accomplish highly coherent dynamics in a many-body system. How to harness the natural hopping dynamics of particles in a many-site lattice for controlled applications, is still an open question. Through the introduction of few impurities in the lattice potential, we devise a scheme to trigger effective tunable linear optics-like operations between arbitrary sites, that overcomes the limitations of setups based on coherent hopping dynamics, when particles are initially separated by many sites. Our scheme enables the generation of peculiar quantum interference effects as well as quantum metrology applications in a many-site lattice. We design a lattice coupling profile that enables perfect wave-packet splitting between mirror symmetric sites and leads to perfect wave-packet reconstruction, fractional revivals and perfect entanglement distribution, for arbitrary long chains. We prove that composite objects in a lattice, made of more particles initially in a lattice site, are a valuable resource for dynamically generating non-classical states between remote sites, tackling edge-localisation effects via local fields. Finally, we show how the spin independent scattering of two initially distant qubits, can be used to implement an entangling quantum gate between remote sites of a lattice. Our findings have potentially an impact on quantum information, as well as on atomic interferometry in a lattice.

Acknowledgements

First and foremost I would like to express my sincere gratitude to my supervisor Prof. Sougato Bose, for giving me the opportunity to do research at the University College of London. His support and guidance have made my Ph.D. experience full of opportunities to improve my knowledge, as his suggestions have been an occasion of personal and professional growth.

I am particularly grateful to Dr. Leonardo Banchi for the very fruitful and enjoyable cooperation, that, together with our respective skills and experiences have pushed forward the research in this thesis.

I would like to express a special appreciation to Dr. Christian Gross as his suggestions have been a determinant contribution to the work presented in this thesis.

A special thank goes to Prof. G. Massimo Palma and Prof. Gabriele de Chiara, for the help during these years and for the research on immersed impurities. I would like to thank Prof. Dimitris Angelakis and Prof. Vladimir Korepin for their contribution in the research pursued in this period. My gratitude goes also to all the people who contributed to my research and to my knowledge with interesting discussions and suggestions during these years - T. J. Apollaro, M. Genoni, P. Massignan, A. Bayat, I. Bloch, S. Balian, J. Gray, R. Antonio, V. Monenegro, G. Zucconi, A. Pontin, L. Marmugi, R. Nolli, R. Guilizzoni, M. Venturelli, A. Loreti, R. Lo Nardo, V. Capelli, M. Scala, F. Ciccarello, A. Trombettoni, G. Milburn.

I am extremely grateful to my parents and to Anna whose presence, love, support and encouragements were never missing.

Finally I would also like to thank all my colleagues at UCL and all the friends for the amazing time spent together during these years.

The results presented in this thesis were supported by the European Research Council, under the European Union's Seventh Framework Programme (FP/2007-2013) / ERC Grant Agreement No. 308253.

Contents

List of Figures

List of Tables

Acronyms

E_R Recoil Energy.

1D One-Dimensional.

2D Two-Dimensional.

2OPT Double Optimal State Transfer.

3D Three-Dimensional.

BEC Bose-Einstein Condensate.

DMD Digital Micromirror Device.

FWHM Full-Width at Half-Maximum.

OPT Optimal State Transfer.

PST Perfect State Transfer.

QFI Quantum Fisher Information.

QUTM Quasi-Uniform Tridiagonal Matrix.

RWA Rotating Wave Approximation.

SWT Schrieffer-Wolff Transformation.

XX chain XX spin $1/2$ chain model.

XXZ chain XXZ spin $1/2$ chain model.

Introduction

The development of quantum devices is hindered by the possibility to manipulate and observe a quantum system, even at the single particle level. Although a large variety of schemes have already been developed, the main obstacle towards the Third Quantum Revolution [1], associated to the control over macroscopic quantum systems and the rise of quantum technologies, is represented by the possibility to exploit a largely scalable physical system in a feasible way [2–11]. The current challenge is how to use all the advantages of the quantum coherence effects, via a physical system whose features allow the realisation of a complete quantum algorithm, with high efficiency, for practical applications. Among the possible physical systems, one of the most promising consists of cold-atoms trapped in crystal-like light structures, known as optical lattices, that allow storing atoms over large microscopic arrays [12–14]. The versatility, in terms of physical parameter regimes that can be reached, as the scalability and the high degree of insulation from the environment, make optical lattices a suitable platform for quantum technologies. On the other hand, it is known that quantum systems with a high degree of insulation from external interactions hardly offers a large amount of external control. Several milestones have been achieved in the last two decades, and the recent advances of trapping techniques for ultra-cold gases have opened up intriguing possibilities for quantum manipulation at the single atom level. Indeed, spectacular progress have been made on laser manipulation with single site level precision, making possible single atom initialisation and read-out procedures [14–20, 20–25]. Besides, programmable spatial-light modulators, which typically consist of millions of individually addressable mirrors, have been introduced in cold-atom setups to project

arbitrary light-intensity landscapes and control each micro-trap potential [26], allowing a deterministic atom preparation in the lattice [25]. The possibility to store the pattern frame and change it in real-time, provides a lattice reconfigurable geometry [27].

The internal atom degrees of freedoms can be exploited to encode a qubit state, opening up to quantum information applications with neutral atoms in a lattice [12]. The possibility to convert static qubits to flying qubits by varying the lattice depth is an important feature, as processing qubits can be moved between specific locations without the requirement of using hybrid systems to store, transfer and processing information.

Optical lattices are also a unique platform for quantum simulation applications [14, 25], in particular, of quantum magnetism models [12, 28–31], where the spin propagation and the internal states can be observed directly via a quantum-gas microscope [32–34], and of typical condensed-matter system, where the electrons can be modelled as moving particles on a periodic crystal lattice structure generated by atom cores [35–37]. As the control of spin arrays is a central resource for quantum computation, addressable optical lattices are a resource to tackle the open challenges towards the development of quantum technologies.

The amount of control available in optical lattice systems opens up new applications for exploiting quantum interference effects in a lattice. Indeed, due to the high degree of isolation from the surroundings, a nearly unitary evolution can be used to perform coherent atom manipulation over large arrays. However, despite the impressive level of control reached in experiments, nowadays it is still challenging to manipulate the natural many-body dynamics in a lattice for realising feasible quantum devices. For instance, atoms may need to be moved close together to initiate quantum gates between arbitrary pairs of qubits in the array.

While operations on the internal state of single particle has been realised with success with focussed laser techniques [15, 38], several strategies have been developed for performing operations between physically distant qubits [12]. These rely on auxiliary “marker” atoms that can be transported along the lattice [39, 40], or

via superimposed lattice merging [41], modification of the trapping potential [42], optical tweezers [4, 43–46], Rydberg atoms [47–49] and dipole-dipole interaction [50], spin dependent transport [51–55], time dependent traps [56, 57], guided transport via active potentials [58, 59] and quantum walks on a lattice [60, 61].

However, the necessity to have a high degree of control over a large collection of qubits to build up transformations of practical value (this requires both single atom control and interactions with other qubits) leads to a natural question, namely, whether a minimally controlled system can be harnessed for quantum technology tasks. Indeed, despite some efforts being made to build quantum gates in these systems, a scalable architecture to realise a complete quantum algorithm is still lacking. The broad aim of this thesis is to envision new implementations of quantum technology schemes through minimal control, driving a quantum many-body system to make it accomplish highly coherent non-equilibrium dynamics.

Specifically, one strategy to let distant qubits, belonging to different quantum registers, interact, as well as two distant qubits in the same array, is to connect them via a channel, realised by modulating the lattice geometry to obtain a 1D atom waveguide [62, 63]. In this approach, the channel takes the role of a quantum wire, where atoms naturally evolve and transfer information to distant locations, without any requirement of active control on the atom position or the necessity of auxiliary qubits. Moreover, the channel itself has an active role in the computation. Indeed, the possibility to locally design the shape of the lattice potential via single-site techniques, makes possible to tailor a configuration that performs a specific transformation during the atom dynamics. The much lower control needed, compared to other strategies, together with the high reconfigurability offered by optical lattices, constitute a compelling scheme for carrying out a sequence of quantum logic gates with high efficiency.

In this thesis, we focus our attention on 1D lattices, modelled as open chains with time independent couplings, where inputs are given at one end of and the outputs are extracted from the other side after some time. Our main goal is to tailor the coupling profile and the inter-atom interaction so that the dynamics of few particles,

initially in one/both ends of the chain, generates high efficiency transformations at the endpoints of the lattice, for applications in quantum information, quantum optics and metrology.

In Chapter 1, we introduce the main features of tight-binding lattices that model the behaviour of atoms trapped in optical lattices. Firstly, we discuss the trapping mechanism and the atom-atom interaction for ultra-cold neutral atoms and the main decoherence sources. Then, we introduce the typical tight-binding models that describe the system, showing the connection between the physical parameters and the coupling constants in the models, and highlight how spin chain models emerge from the tight-binding description. We review the main techniques for initialising and measuring the system with single-site precision and we shortly review the theory of quantum information transmission in permanently coupled chains and the main techniques to improve the transmission quality. We present a peculiar effect of lattice models, namely the formation of bound states in strongly interacting particle systems. We discuss their propagation characteristics in 1D chains. Finally, we discuss about quantum optics and metrology introducing the building blocks as well as physical quantities that are signatures of peculiar interference effects, and that are used to measure the quality of the transformations performed.

In Chapter 2, we introduce a scheme to produce tuneable linear optical transformation between far sites of lattice models based on particle scattering on a barrier. We analyse the performances of the system for interferometry applications and we show how multi-particle interference effects can be observed between the edge sites of finite lattice systems.

In Chapter 3, we discuss a strategy to tailor the chain couplings for generating 100% fidelity operations between each mirror-symmetric pair of sites of the chain. We show how the scheme can be exploited for the generation of entangled states in spin models and for the production of peculiar interference patterns.

Chapter 4 is devoted to bound states in optical lattices. We develop a model to describe the dynamics of few particles showing how localisation effects can be tackled for state transfer applications. We present a scheme for producing high

NOON states between the edge-points of the lattice exploiting the natural dynamics in the lattice and showing how the model can be used for quantum enhanced metrology applications.

In Chapter 5, we discuss a model to implement a two qubit quantum gate in a finite lattice model based on atom-atom scattering interaction.

Chapter 1

Introductory Material

In this chapter we introduce the main characteristics of tight-binding models and the methods to evaluate particle dynamics and physical quantities. Tight-binding models are realisable with cold atoms in optical lattices, which provide an excellent degree of protection from environmental effects and a high controllability of system parameters. In view of the experimental feasibility, we briefly discuss single particle preparation and read-out techniques in optical lattices, and how the system parameters can be tuned within current technology. As it is relevant to the purposes of this thesis, we explicitly show how spin chain models emerge from lattice models for strong inter-particle interaction. Since a central point is played by the ability to transfer quantum states between distant locations, we briefly analyse strategies to improve the transfer efficiency in lattice models. Then, we introduce the topic of bound states, analysing the dynamic behaviour and localisation mechanisms that limit their use for applications. In the last part of the chapter, quantum linear optics transformations and the relevant quantities useful to detect multi-particle interference effects are introduced, as well as their use for realising quantum interferometry applications.

1.1 Introduction to Tight-Binding Models

Tight-binding lattice models offer a unique platform in which particles may be either static or mobile depending on the barrier potential between sites. A direct physical realisation is through optical lattices, in which neutral ultra-cold atoms (usually al-

kali) are trapped via induced dipole interaction [64, 65] using counterpropagating laser beams [12] or projecting a light-intensity pattern via holographic masks [17], or micro-mirror devices [26, 61]. Addressable optical lattices have several appealing features for quantum applications, due to a good balance between insulation and control capabilities [13, 36]. The main characteristics are:

1. Trapped atoms can be interchanged from static to mobile, via the control of the intensity of the laser that generates the lattice [61].

2. Neutral atoms, in a detuned optical lattice, are weakly coupled with the environment and therefore they exhibit excellent coherence properties. The main source of decoherence is triggered by spontaneous emission, and can be strongly suppressed when blue detuned lasers are employed to generate the lattice [66]. Minor sources of decoherence are noise due to laser fluctuations [67], and collisions with the background gas [68].

3. The amount of control available in current experiments allows single qubit initialisation and read-out via single-atom addressing techniques and fluorescence imaging microscopy [16, 17, 19, 24, 38, 45]. The state preparation fidelity is about 98%, while single atom detection is possible with an efficiency around 99% [19, 69].

4. The parameters of the system can be tuned modulating the light intensity pattern, and the strength of the inter-atomic interaction can be controlled in a wide range via an external static magnetic field [70, 71].

In the following sections we illustrate in detail the main characteristics of optical lattices, showing how system parameters are tuned and how to initialise and measure the system in a real experiment.

1.2 Trapping of Neutral Atoms in Optical Lattices

Neutral atoms can be trapped in light crystal structures that consist of standing waves produced by the interference of laser beams. The trapping mechanism results from

the interaction of atoms with a far-detuned light [36, 64]. In this section we analyse in detail how the trapping effect naturally emerges from the atom-field interaction and how it leads to decoherence effects.

As a first step we consider a single atom, modelled as a two level system, interacting with an external laser field. The electromagnetic field consists of a highly populated mode, at the laser frequency, and of a reservoir of unpopulated modes. Specifically, as the laser beam is a coherent state [72, 73], in good approximation can be treated classically while the remaining modes need a quantum description [65, 74, 75]. An important point for cold atoms is that the centre-of-mass motion must be taken into account to describe the effect of the light field on atom trajectories. Indeed, the atom-field interaction induces spontaneous emission events which in turn, due to momentum conservation, produce a momentum variation $p_i \to p_f + \hbar k$, where p_i and p_f are respectively the initial/final atom momenta, and $\hbar k$ is the photon momentum (i.e. there is an atom recoil). The atom velocity varies of an amount $\Delta v = \hbar k_{photon}/m$, whose value is about[1] $\Delta v \simeq 1\ cm/s$. The key point is that the recoil effect is largely negligible for atoms at room temperature because the average atom velocity, $v_{atom} \simeq \sqrt{3k_B T/m}$, is $\sim 300 m/s$. Therefore, with reasonable approximation, in quantum optics effects spontaneous emission effects can be safely neglected at room temperature [65, 76]. On the contrary, in ultra-cold atoms the average velocity is of the same order of magnitude of the recoil energy, ($v_{atom} \simeq 1\ cm/s$ for a typical temperature of $T \sim 500\ nK$ [77]). Hence, spontaneous emission events induce random kicks (due to the randomness of photon emission [65]) on the atomic momentum which, as we show in the following, result in decoherence effects. A single atom interacting with a laser field is described by the Hamiltonian

$$H = H_A + H_F + H_{AF}, \tag{1.1}$$

[1] For a typical laser wavelength of $\lambda = 1064\ nm$ [15], and for an atom of ^{87}Rb (the atom mass value is in Appendix E.2).

where H_A is the two-level atom Hamiltonian

$$H_A = \frac{P^2}{2m} + \hbar\omega_0 |e\rangle\langle e|, \tag{1.2}$$

and the electromagnetic field H_F is described by

$$H_F = \sum_\mu \hbar\omega_\mu \left(\hat{a}_\mu^\dagger \hat{a}_\mu + \frac{1}{2} \right), \tag{1.3}$$

with $\mu \equiv (\mathbf{k}, \varepsilon)$ a collective index for the wave-vector $\mathbf{k}$ and the polarisation ε, and $\hat{a}_\mu$ a bosonic annihilation operator. The atom-field interaction H_{AF} is modelled as a dipolar coupling[2]

$$H_{AF} = -\mathbf{d} \cdot \hat{\mathbf{E}}(\mathbf{r}, t) \ , \tag{1.4}$$

where $\mathbf{d} = -d\varepsilon_\zeta (|e\rangle\langle g| + |g\rangle\langle e|)$ is the atomic dipole moment, ε_ζ a unit vector along the quantisation axis, and the electric field operator $\hat{\mathbf{E}}$ is evaluated[3] in the atom position $\mathbf{r}$. The expression of the quantised field is [65, 73, 75]

$$\hat{\mathbf{E}}(\mathbf{r}) \equiv \hat{\mathbf{E}}_+ + \hat{\mathbf{E}}_- = i \sum_\mu \varepsilon_\mu \mathscr{E}_\mu \hat{a}_\mu e^{i\mathbf{k}_\mu \cdot \mathbf{r}} + H.c. \ , \tag{1.5}$$

where $\mathscr{E}_\mu = \sqrt{\hbar\omega_\mu / 2\varepsilon_0 L^3}$ and L^3 is the quantisation volume. To describe the laser we consider one mode of the electromagnetic field to be macroscopically populated, while the remaining modes, initially in the vacuum state, are described by a reservoir[4]. The laser mode is described by a classical monochromatic field

$$\mathbf{E}_L(\mathbf{r}, t) = \boldsymbol{\varepsilon}(\mathbf{r}) \mathscr{E}(\mathbf{r}) \cos(\omega t + \phi(\mathbf{r})) \ , \tag{1.6}$$

[2] The main contribution to the interaction Hamiltonian arises from the potential energy of this electric dipole in the electric field of the light beam [76].

[3] The magnitude of the electron radii are of the order of the Bohr radius a_0 (see Appendix E), then their size is much smaller that the typical wavelength in the visible part of the frequency spectrum. Therefore, the spatial variation across the dimension of the atom is very small and in good approximation the field can be evaluated in the position of the atomic nucleus (this is known as *long-wavelength approximation*) [76].

[4] The typical fluctuation time of the vacuum field is $\tau_c \simeq \omega_0^{-1}$, that is much shorter than all the others characteristic times. This allows one to consider the vacuum as a reservoir and to describe its effect on the evolution as a relaxation process [75].

where ω is the laser frequency and $\boldsymbol{\varepsilon}(\mathbf{r})$ is the polarisation of the light. The atom-field interaction can be written as $H_{AF} = H_{AL} + H_{AR}$, where H_{AL} and H_{AR} are respectively the interaction terms with the laser mode and with the unoccupied modes. The coupling term with the classic field can be written directly

$$\begin{aligned} H_{AL} &= -d(\varepsilon_\zeta \cdot \varepsilon(\mathbf{r}))\mathscr{E}(\mathbf{r})\left(\cos(\omega t + \phi(\mathbf{r}))|e\rangle\langle g| + h.c\right) = \\ &= \frac{\hbar}{2}\Omega(\mathbf{r})\left(e^{i(\omega t+\phi(\mathbf{r}))} + e^{-i(\omega t+\phi(\mathbf{r}))}\right)\left(|e\rangle\langle g| + h.c\right) \ , \end{aligned} \tag{1.7}$$

where the Rabi frequency, $\Omega(\mathbf{r}) \equiv -d\left(\varepsilon_\zeta \cdot \varepsilon(\mathbf{r})\right)\mathscr{E}(\mathbf{r})/\hbar$, depends on the electric field profile and on the dipole moment [76]. The latter can be reduced in the Rotating Wave Approximation (RWA)[5] to

$$H_{AL} = \frac{\hbar}{2}\Omega(\mathbf{r})\left(e^{-i\omega t}e^{-i\phi(\mathbf{r})}|e\rangle\langle g| + h.c.\right), \tag{1.8}$$

and for the reservoir modes we have

$$H_{AR} = -id\sum_\mu (\varepsilon_\zeta \cdot \varepsilon_\mu)\mathscr{E}_\mu \hat{a}_\mu e^{i\mathbf{k}_\mu \cdot \mathbf{r}}\sigma_- + H.c. \ , \tag{1.9}$$

where $\sigma_+ \equiv |e\rangle\langle g|$ and $\sigma_- \equiv |e\rangle\langle g|$.

1.2.1 Atom Immersed in a Laser Light Field

To evaluate the effects of the light on the atomic trajectories we take into account the centre of mass motion in a quantised form, introducing the conjugate variables $\left[x_i, p_j\right] = i\hbar\delta_{ij}$, so the atom can be described via a density matrix, function of x or p, as $\rho_{ij}(x)$ or $\rho_{ij}(p)$ in the real or in the conjugate space [65]. To evaluate the change in atom momentum, we firstly consider a two level system interacting with the laser light only. In the Heisenberg picture

$$i\hbar\partial_t p = [H, p] = [H_A + H_{AL} + H_L, -i\hbar\nabla] \ , \tag{1.10}$$

[5] In the Heisenberg picture the atom-field Hamiltonian contains two rotating terms with frequency $\delta = \omega - \omega_0$, and two counterrotating terms $\omega + \omega_0$ (that correspond to two excitations processes that do not conserve the energy). The RWA consists in neglecting the counterrotating terms [76].

where H_A is the atomic Hamiltonian, H_L is the classical light field (that commutes with the momentum) and the atom-field coupling H_{AL} is in the RWA approximation. Given the identity, valid for any function $f(\hat{X})$ of position $\hat{X}$ and momentum $\hat{P}$ operators [78],

$$\left[f(\hat{X}),\hat{P}\right] = i\hbar\nabla f(\hat{X}) \,, \tag{1.11}$$

and discarding H_A and H_L that commute with p, the momentum variation of the atom is

$$\frac{dp}{dt} = -\frac{\hbar}{2}|e\rangle\langle g|\nabla\left(\Omega(x)e^{-i\omega t}e^{-i\phi(x)}\right) + H.c. \,. \tag{1.12}$$

As the right side of the (1.12) can be visualised as a force, the effect of the field on the centre of mass motion is found via

$$\mathscr{F} = \langle\frac{dp}{dt}\rangle \,, \tag{1.13}$$

where the average is carried out both on internal and external degrees of freedom. The general state of the atom is an entangled state between the internal and the centre of mass degrees of freedom, as

$$|\psi\rangle = \int dx \, \left(\psi_g(x)|g\rangle + \psi_e(x)|e\rangle\right)|x\rangle \,. \tag{1.14}$$

Because the time scale dynamics of the centre of mass is the inverse of the recoil frequency[6],

$$\tau_{cm} = 1/\omega_R \,, \tag{1.15}$$

while the internal dynamics is of the order of magnitude of the natural decay rate of the excited state [75],

$$\tau_I = \Gamma^{-1} \qquad \text{where } \Gamma = \frac{1}{4\pi\varepsilon_0}\frac{4\omega_0^3 d^2}{3\hbar c^3}, \tag{1.16}$$

[6]The recoil velocity v_r is the change in the atomic velocity when absorbing or emitting a resonant photon from the laser beam. The recoil energy is defined as the kinetic energy of an atom moving with velocity v_r, namely $\hbar\omega_R = v_r^2/2m$ [79].

if these two timescales are different from each other[7], it is possible to assume that the internal state is in a quasi-steady state and the contributions to the force due to the internal and the centre of mass state are factorised as[8] [65, 75]

$$\mathscr{F} = -\frac{\hbar}{2}\langle|e\rangle\langle g|\rangle_{internal}\ \langle\nabla\left(\Omega(x)e^{-i\phi(x)}\right)e^{-i\omega t}\rangle_{external} + H.c\ . \tag{1.17}$$

We assume that the centre of mass is sufficiently localised to approximate the spatial wavefunction to a delta function

$$|\psi(t)\rangle_{cm} = \int \psi(x,t)|x\rangle dx \qquad \text{where } \psi(x,t) = \delta(x - x_{cm})\ , \tag{1.18}$$

hence we evaluate the mean value obtaining

$$\mathscr{F} = -\frac{\hbar}{2}\nabla\left(\Omega(x)e^{-i\phi(x)} + H.c\right)|_{x=x_{cm}}\langle|e\rangle\langle g|\rangle_{internal}\ . \tag{1.19}$$

Finally, the average over the internal motion is evaluated, approximately, in a steady-state ($t \to \infty$), namely[9]

$$\langle|e\rangle\langle g|\rangle_{internal} = Tr\left(\rho|e\rangle\langle g|\right) = \rho_{ge} \simeq \rho_{ge,steady}\ , \tag{1.20}$$

so that the force on the centre of mass motion is

$$\mathscr{F}(x_{cm}) \simeq -\frac{\hbar}{2}\nabla\left(\Omega(x)e^{-i\phi(x)} + H.c\right)|_{x=x_{cm}}\ . \tag{1.21}$$

The latter describes the force that acts on the centre of mass if it was localised in its classical position x_{cm} (*ray-optics limit* of the atomic optics). Explicitly (1.21) and (1.20), together with

$$\nabla\left(\Omega(x)e^{-i\phi(x)}\right) = \Omega(x)e^{-i\phi(x)}\left(\alpha(x) - i\beta(x)\right), \tag{1.22}$$

[7] For instance for ^{87}Rb for typical transitions $\Gamma/2\pi \simeq 6\ MHz$, while $\omega_R/2\pi \simeq 4kHz$ [79].

[8] The fast internal motion can be adiabatically eliminated and reduced equations for the external variables can be derived [75].

[9] Here we do not show the explicit expression for $\rho_{ge,steady}$, which can be found in [74, 76].

where $\alpha(x) \equiv \frac{\nabla\Omega(x)}{\Omega(x)}$, $\beta \equiv \nabla\phi(x)$, lead to the expression for the mean force [65, 75]

$$\mathscr{F}(x_{cm}) = \mathscr{F}_{dissip} + \mathscr{F}_{react} \tag{1.23}$$

where

$$\mathscr{F}_{dissip} = -\frac{\hbar\Gamma}{2}\left(\frac{\Omega^2(x_{cm})/2}{\delta^2 + \frac{\Omega^2(x_{cm})}{2} + \left(\frac{\Gamma}{2}\right)^2}\right)\nabla\phi(x_{cm}) \tag{1.24}$$

$$\mathscr{F}_{react} = -\hbar\delta\left(\frac{\Omega^2(x_{cm})/2}{\delta^2 + \frac{\Omega^2(x_{cm})}{2} + \left(\frac{\Gamma}{2}\right)^2}\right)\frac{\nabla\Omega(x_{cm})}{\Omega(x_{cm})} \tag{1.25}$$

The force consists of two terms[10]: a dissipative term, (*radiation pressure*) proportional to the spontaneous emission rate Γ and to the phase gradient of the field; the other term, (*dipole force*) is proportional to the field gradient and to the detuning $\delta = \omega_L - \omega_0$ (it changes sign for positive and negative detuning). The radiation pressure term is relevant for a field with a phase gradient. For example for a monochromatic running wave $E = E_0 e^{[i(\omega t - kx)]} = E_0 e^{[i(\omega t + \phi(x))]}$, one has

$$\mathscr{F}_{dissip}(x_{cm}) = -\hbar k\frac{\Gamma}{2}\frac{\Omega^2(x_{cm})/2}{\frac{\Omega^2(x_{cm})}{2} + \delta^2 + \left(\frac{\Gamma}{2}\right)^2}, \tag{1.26}$$

and for $\Omega(x_{cm}) \gg 1$ it saturates to $-\hbar k\Gamma/2$. We are interested in the trapping effect generated by a spatially periodical potential: for a standing wave one has $\nabla\phi(x_{cm})$=0, then $\mathscr{F}_{dissip} = 0$ and

$$\mathscr{F}_{react}(x_{cm}) = -\frac{\hbar\delta}{4}\frac{\Omega^2(x_{cm})/2}{\Omega^2(x_{cm})/2 + \delta^2 + \left(\frac{\Gamma}{2}\right)^2}\frac{\nabla\Omega(x_{cm})}{\Omega(x_{cm})} = -\nabla U. \tag{1.27}$$

[10]For the purposes of this section, here we are mainly interested in the $\mathscr{F}_{react}$ component. This does not involve any absorption of energy from the field, but rather is due to a redistribution of momentum between the atom and the various plane waves composing the laser field (to have a non-zero reactive term, the laser needs to be a linear superposition of several plane waves). Indeed, photons are removed from one plane wave (absorption) and transferred to another plane wave (stimulated emission). The energy of the field does not change, because the plane waves have the same frequency, ω_L, but the momenta associated to the planes waves are not the same and the total momentum of the field, as the one of the atom, change [75].

By direct integration, we find the potential energy for a neutral atom immersed in a standing wave potential

$$U_{opt}(x_{cm}) = \frac{\hbar\delta}{2}\ln\left(1+\frac{\Omega^2(x_{cm})/2}{\delta^2+(\Gamma/2)^2}\right). \tag{1.28}$$

This means that the sign of the detuning determines if the energy minimum belongs to a region of weak or strong light field. We observe that the trapping effect does not saturate if the optical field intensity increases. For small intensity, $\Omega(x_{cm})$, we have

$$U_{opt}(x_{cm}) \simeq \frac{\hbar\delta}{2}\frac{\Omega^2(x_{cm})}{\delta^2+\left(\frac{\Gamma}{2}\right)^2}. \tag{1.29}$$

If there is no dissipation one observes that $U_{opt}(x_{cm}) \simeq \Omega^2/\delta$. This means that if the laser frequency is slightly lower than the atomic resonance (*red detuning*), $\delta < 0$, atoms are forced to regions with stronger field (i.e. the potential has minima at the intensity maxima). Conversely, a *blue detuned* laser, $\delta > 0$, forces the atoms towards zones of weak laser intensity, or equivalently the potential has minima at the intensity minima [80].

1.2.2 Damping Effect due to Spontaneous Emission

In the latter section we have shown how a standing laser wave produces a neutral atom trapping. So far, we have neglected the effect of the field unpopulated modes in the atom dynamics. In this section we explicitly consider spontaneous photon emission events that, through atom recoil, trigger decoherence effects. As spontaneous emission is an irreversible effect, the atom dynamics can be described within a Master Equation formalism [8], which includes both centre of mass and electronic degrees of freedom [65]. When the atomic motion is neglected, the system time evolution under spontaneous emission events, $\rho_{sp}(t)$, is the solution of the

system [8, 75, 76],

$$(\dot{\rho}_{ee})_{sp} = -\Gamma(\rho_{ee})_{sp}, \tag{1.30}$$

$$(\dot{\rho}_{eg})_{sp} = -\Gamma/2(\rho_{eg})_{sp}, \tag{1.31}$$

$$(\dot{\rho}_{gg})_{sp} = \Gamma(\rho_{ee})_{sp}, \tag{1.32}$$

where Eq. (1.30) and (1.32) describe the irreversible transfer of populations, while Eq. (1.31) is the evolution of the coherence. Indeed, spontaneous emission increases the population of the ground state (depleting the excited state) and meanwhile it destroys the coherence. The latter description can be extended, once the atomic motion is included, via a modification of the rate equation for the ground state, Eq. (1.32).

Indeed, due to the Galilelian invariance[11], the decay from the excited state population cannot contain terms that depend on the motion, then it is still described by Eq. (1.30) [65]. On the contrary the rate equation for the ground state depends explicitly on spontaneous emission, as atoms experience a change of momenta $\mathbf{p} \to \mathbf{p} - \hbar\mathbf{k}$, where $\mathbf{p}$ is the centre of mass momentum. The atom recoil kick, is formally described via a shift operator, that acts on momentum eigenstates as

$$e^{-ik\mathbf{n}\cdot\mathbf{r}}|\mathbf{p}\rangle = |\mathbf{p} - \hbar\mathbf{k}\rangle, \tag{1.33}$$

where $\mathbf{k} = k\mathbf{n}$, and $\mathbf{n}$ is a unit vector that indicates the photon emission direction. In the atomic reference frame, the emitted photon has energy $E = \hbar\omega_0$, hence its momentum is $k = \omega_0/c$. The rate equation for the ground state population must be proportional to $|e\rangle\langle e|\mathbf{p} - \hbar\mathbf{k}\rangle\langle\mathbf{p} - \hbar\mathbf{k}| = e^{-ik\mathbf{n}\cdot\mathbf{r}}|e\rangle\langle e|e^{ik\mathbf{n}\cdot\mathbf{r}}$. As spontaneous emission for moving atoms is not isotropic, a weight function must be carefully taken into account together with an integral along all the directions. Specifically, the emission probability within a solid angle $d^2\mathbf{n}$ is $d\Gamma_{\mathbf{n}} = \Gamma\phi(\mathbf{n})d^2\mathbf{n}$, where dA is the infinitesimal area on a sphere and $dA/r^2 = d^2\mathbf{n} = \sin(\theta)d\theta d\phi$, and the emission distribution

[11] The density operator of the system, for a system at rest and under a boost transformation must obey to the same Master Equation [65].

is [65]

$$\phi(\mathbf{n}) = \frac{3}{8\pi}\left(1 - \frac{(\mathbf{n}\cdot\mathbf{d})^2}{d^2}\right). \tag{1.34}$$

To take into account the atom recoil, the ground population rate must be proportional to $d\Gamma_{\mathbf{n}}|e,\mathbf{p}-\hbar\mathbf{k}\rangle\langle e,\mathbf{p}-\hbar\mathbf{k}| = d\Gamma_{\mathbf{n}} e^{-ik\mathbf{n}\cdot\mathbf{r}}|e\rangle\langle e|e^{ik\mathbf{n}\cdot\mathbf{r}}$, then integrating over all the possible emission directions, Eq. (1.32) takes the form

$$\dot{\rho}_{gg} = \Gamma \int d^2\mathbf{n}\ \phi(\mathbf{n}) e^{-ik\mathbf{n}\cdot\mathbf{r}} \rho_{ee} e^{ik\mathbf{n}\cdot\mathbf{r}}. \tag{1.35}$$

Eq. (1.30) and (1.31) can be rewritten via an effective Hamiltonian formalism, [74], as

$$\begin{pmatrix} -\Gamma\rho_{ee} & -\Gamma/2\rho_{eg} \\ -\Gamma\rho_{ge} & 0 \end{pmatrix} = -\frac{\Gamma}{2}\left(\rho\sigma_+\sigma_- + \sigma_+\sigma_-\rho\right) \tag{1.36}$$

where $\sigma_+ = |e\rangle\langle g|$ and $\sigma_- = |g\rangle\langle e|$, hence

$$\frac{-i}{\hbar}\left\{[H_A,\rho] + (i\hbar)\left(-\frac{\Gamma}{2}\left(\rho\sigma_+\sigma_- + \sigma_+\sigma_-\rho\right)\right)\right\} \equiv \frac{-i}{\hbar}\left(H_{\text{eff}}\rho - \rho H_{\text{eff}}^{\dagger}\right) \tag{1.37}$$

where $H_{\text{eff}} = H_A - i\hbar\frac{\Gamma}{2}\sigma_+\sigma_-$. Finally, once added by hand the term relative to the ground state, via a term $\sigma_-\rho\sigma_+ = \rho_{ee}$, the Master Equation for a two level atom, in a laser field and interacting with the vacuum modes, is

$$\frac{d}{dt}\rho = -\frac{i}{\hbar}\left(H_{\text{eff}}\rho - \rho H_{\text{eff}}^{\dagger}\right) + \Gamma\int d^2\mathbf{n}\ \phi(\mathbf{n}) e^{-ik\mathbf{n}\cdot\mathbf{r}}\sigma_-\rho\sigma_+ e^{ik\mathbf{n}\cdot\mathbf{r}}. \tag{1.38}$$

To sum up, compared with the no recoil case, Eq. (1.30), (1.31) and (1.32), the spontaneous emission produces a change in the centre of mass motion which affects the rate equation Eq. (1.32). When recoil due to spontaneous emission can be neglected (k of the emitted photons is zero) one has the usual Master equation of a damped two level atom [81, 82],

$$\frac{d}{dt}\rho = -\frac{i}{\hbar}\left(H_{\text{eff}}\rho - \rho H_{\text{eff}}^{\dagger}\right) + \Gamma\sigma_-\rho\sigma_+ \ . \tag{1.39}$$

1.2.2.1 Atom Dynamics in a Detuned Field

In the previous section we have showed that the equation of motion for a two-level atom driven by a laser light and undergoing spontaneous emission effect, is described by optical Bloch equations, Eq. (1.38). For a large detuning, $|\delta| \gg \Omega, \Gamma$, the excited state can be adiabatically eliminated to obtain a description for the external degrees of freedom only. As shown in [66], Eq. (1.38), for the density operator becomes

$$\frac{d}{dt}\rho = -i\left(H_{\rm eff}\rho - \rho H_{\rm eff}^{\dagger}\right) + \mathscr{J}\rho \ , \tag{1.40}$$

where the non-hermitian effective Hamiltonian is given by

$$H_{\rm eff} = \frac{p^2}{2m} + V_{\rm opt}(\mathbf{r}) - i\frac{\gamma(\mathbf{r})}{2}. \tag{1.41}$$

Here $V_{\rm opt}(\mathbf{r}) \equiv |\Omega(\mathbf{r})|^2/4\delta$ and $\gamma(\mathbf{r}) \equiv \Gamma|\Omega(\mathbf{r})|^2/4\delta^2$, are respectively the spatially dependent trapping potential and the effective rate of light scattering, while

$$\mathscr{J}\rho = \Gamma\int d^2\mathbf{n}\ \phi(\mathbf{n}) c_{\mathbf{n}}\rho c_{\mathbf{n}}^{\dagger}, \qquad \text{where } c_{\mathbf{n}} \equiv e^{-ik\mathbf{n}\cdot\mathbf{r}}\frac{\Omega(\mathbf{r})}{2\delta}\ , \tag{1.42}$$

is the operator that corresponds to a photon absorption followed by a scattering of a spontaneous photon in direction $\mathbf{n}$. Here $k = \omega_0/c$ is the wave number associated with the atomic transition frequency ω_0 and $\phi(\mathbf{n})$ is the distribution of directions of emitted photons, in Eq. (1.34). The detuning of the laser light, with frequency $\omega_L = ck_L$, is $\delta = \omega_L - \omega_0$, and because it is close to the atomic resonance $k \simeq k_L$. As discussed in the previous section, a spatial dependent Rabi frequency, $\Omega(\mathbf{r})$ in Eq. (1.41), determines the trapping profile.

The key point is that, from Eq. (1.41), a neutral atom in a laser field, of intensity I and detuning δ, is subjected to a trapping potential $V_{\rm opt} \propto I/\delta$ and to a damping factor $\gamma \propto I/\delta^2$. This means that the damping of the atom motion, namely the main source of decoherence effects, is strongly reduced once the light is tuned very far off the resonance, meanwhile high intensity power sources guarantee a sufficient trapping strength. Typical values are $\Gamma/\delta \sim (10^{-7} \div 10^{-6})$ [83]. We briefly mention

that minor sources of decoherence are noise due to laser fluctuations[12] [67] and collisions with the background gas[13] [68].

In this section we have showed that the dynamics of atom trapped in a laser field is described by (1.41), where the trapping field profile is given by the spatial dependent Rabi frequency $\Omega(\mathbf{r})$. For a deep periodical lattice Eq. (1.41) can be expanded in a basis of functions that are exponentially localised in each lattice site. The results of these calculations lead to a paradigmatic tight-binding model, known as the *Hubbard model*, that will be discussed in details in the following.

1.3 Tight-Binding Models for Neutral Atoms in Optical Lattices

1.3.1 BEC Hamiltonian in a Periodical Potential

The description of a system of interacting bosons in an external potential $V_0(\mathbf{r})$ can be made in terms of a field theory (*second quantisation form*), where the state of the system is represented via operators, $a_k^\dagger$, associated to the single particle states, $|\phi_k\rangle$ that create bosons as excitations on the vacuum field state. These operators satisfy the bosonic commutation rules[14], so that a N particle state,

$$|\Psi_{n_0,n_1,\ldots}\rangle = \frac{1}{\sqrt{n_0!n_1!\cdots}}\left(a_0^\dagger\right)^{n_0}\left(a_1^\dagger\right)^{n_1}\cdots|0\rangle, \tag{1.43}$$

which represents n_i bosons in the state $|\phi_i\rangle$, satisfies automatically the symmetrisation postulate [84, 85]. Because a boson, localised in position $\mathbf{r}$ can be described as

$$|\mathbf{r}\rangle = \sum_k |\phi_k\rangle|\phi_k\rangle\langle\mathbf{r}| = \sum_k \phi_k^*(\mathbf{r}) = \sum_k \phi_k^*(\mathbf{r})a_k^\dagger|0\rangle, \tag{1.44}$$

[12] As fast fluctuations takes atoms towards excited bands of the lattice.

[13] The decoherence rate depends on the cross section and on the background gas density, as showed in [68].

[14] Namely, $[a_k, a_{k'}] = \delta_{k,k'}$ and $[a_k, a_{k'}] = \left[a_k^\dagger, a_{k'}^\dagger\right] = 0$

it is convenient to introduce a field operator[15] $\Psi(\mathbf{r})^\dagger$, that creates a boson in position $\mathbf{r}$, defined as

$$\Psi(\mathbf{r}) \equiv \sum_k \phi_k^*(\mathbf{r}) a_k^\dagger. \tag{1.45}$$

The Hamiltonian for a system of interacting bosons, in second quantisation form, is given by [8, 86, 87]

$$\begin{aligned} H = &\int d\mathbf{r}\, \Psi^\dagger(\mathbf{r}) \left(-\frac{\hbar^2 \nabla^2}{2m} + V_0(\mathbf{r}) \right) \Psi(\mathbf{r}) + \\ &+ \frac{1}{2} \int\int d\mathbf{r} d\mathbf{r}'\, \Psi^\dagger(\mathbf{r}) \Psi^\dagger(\mathbf{r}') V_{\text{int}} \left(|\mathbf{r} - \mathbf{r}'| \right) \Psi(\mathbf{r}') \Psi(\mathbf{r}), \end{aligned} \tag{1.46}$$

where $V_{\text{int}}(\mathbf{r} - \mathbf{r}')$ is the two particles interaction term.

1.3.1.1 Atom-Atom Interaction

The atom-atom interaction takes a simple form for ultra-cold and diluted gases, whose average particle distance is larger than the typical length scale associated with interatomic forces [77]. Indeed, the interaction is modelled via a single parameter, the *s-wave scattering length*, a_s, with typical value $\sim 100 a_0$, where $a_0 \equiv \hbar^2/m_e e^2 \sim 0.53$ Å is the *Bohr radius*. This approximation is well justified[16] for the so called *weakly interacting Bose-Einstein Condensate (BEC)*, that satisfy the condition[17] $|a_s| \ll n^{-1/3}$, where $n = N/V$ is the density of the gas [88]. This condition makes valid two important approximations for the inter-atom interaction $V_{\text{int}}(\mathbf{r} - \mathbf{r}')$:

- Collisions of two particles are important for the scattering problem, while three-particle collisions can be safely neglected[18].

- The distance between two particles is large enough to justify asymptotic expressions for the wave-function of the relative motion.

[15] This operator satisfies canonical commutation rules, $\left[\Psi(\mathbf{r}_1), \Psi^\dagger(\mathbf{r}_2)\right] = \delta(\mathbf{r}_1 - \mathbf{r}_2)$ and , $[\Psi(\mathbf{r}_1), \Psi(\mathbf{r}_2)] = \left[\Psi^\dagger(\mathbf{r}_1), \Psi^\dagger(\mathbf{r}_2)\right] = 0$.

[16] This condition is fulfilled, for instance, for gases of alkali atoms, but not in liquid Helium [77].

[17] The typical density of a BEC of alkali atoms is in the range $n \sim \left(10^{13} \div 10^{15}\right)\ cm^{-3}$, which corresponds to an average distance between the particles of the order of 100 *nm* [77].

[18] Three body recombination processes have a rate which depends on the density n as $dn/dt = -Ln^3$, where $L \sim (10^{-29} \div 10^{-30})\ cm^6 s^{-1}$ is the rate coefficient [83], which gives a sample life-time of the order of seconds to minutes.

The interaction potential between two neutral atoms is dominated by Coulomb repulsion for short distances, while at larger distances it takes the form of a *Van der Waals interaction*[19]. For weakly interacting gases, as we are not interested in the detail of the interaction at small distances, the interaction shape can be modelled as a "hard core" potential for distances less than[20] r_c, and as a Van der Walls interaction for higher distances, namely

$$U(r) = \begin{cases} -C_6/r^6 & \text{for } r > r_c \ , \\ \infty & \text{for } r \leq r_c \ . \end{cases} \tag{1.47}$$

The neutral atom interaction has a typical length scale[21], called *Van der Waals length* of $r_0 \equiv (2m_r C_6/\hbar^2)^{1/4} \sim (50 \div 100)$ Å, where m_r is the reduced mass of the two atoms, (which is the effective interaction range) and C_6 for alkali atoms ranges from ~ 1400 for *Li* to ~ 6300 for *Cs* [77, 83]. One key point is that the associated characteristic energy $E_c \sim \hbar^2/m_r r_0^2$ is of the order of $(0.1 \div 1)\ mK$. Because, for typical BEC temperatures, the mean thermal energy $k_B T$ is much lower than E_c, the inter-atomic problem can be strongly simplified as it becomes independent from the energy. In a BEC state, the de Broglie wavelength has the same size of the average inter-atomic distance, $\lambda_T = 2\pi/k_T \sim d$, and because $d \gg r_0$ the wave-vector of all the states with a non-zero occupation probability satisfies the condition $kr_0 \ll 1$ [88]. In the elastic scattering problem, between two atoms, from a potential $U(\mathbf{r})$, the relative motion wave-function can be written, far from the interaction region, as a plane wave with relative momentum $\hbar\mathbf{k}$, plus an outgoing spherical wave, in the asymptotic form [89],

$$\psi(\mathbf{r}) \sim e^{i\mathbf{k}\cdot\mathbf{r}} + f(\theta)\frac{e^{ikr}}{r} \qquad \text{for } r \gg r_0. \tag{1.48}$$

[19] The origin of this interaction is the dipole-dipole atom-atom interaction. The $1/r^6$ dependence is the second order of approximation of this potential, while higher orders are negligible for distances greater than the Van der Waals length r_0 [77].

[20] Typical values are $r_c \sim (0.5 \div 5)$ Å

[21] It is defined as the length for which the kinetic energy of the relative motion of two atoms, with reduced mass m_r, is equal to their interaction energy [13].

In terms of eigenfunctions of the angular momentum operator (*partial wave method*)

$$\psi(\mathbf{r}) = \sum_{l=0}^{\infty} A_l P_l(\cos\theta) R_{kl}(r), \tag{1.49}$$

where A_l are constants, P_l are Legendre polynomials [90], and $R_{kl}(r)$ is the radial wavefunction, which satisfies the differential equation

$$\frac{1}{r^2}\frac{d}{dr}\left(r^2\frac{dR_{kl}(r)}{dr}\right) + \left[k^2 - \frac{l(l+1)}{r^2} - \frac{2m_r}{\hbar^2}U(r)\right] = 0. \tag{1.50}$$

The scattering amplitude can be found by using Eq. (1.48) and Eq. (1.49) [91], as

$$f(\theta) = \sum_{l=0}^{\infty} (2l+1) f_l P_l(\cos\theta), \tag{1.51}$$

where f_l are the amplitude of the partial diffusion waves. It can be proved that in the limit of low energy (namely under the condition $kr_0 \ll 1$), for potentials that vary as r^{-n}, one finds [77, 91, 92]

$$\begin{cases} f_l \sim k^{2l} & \text{if } l < (n-3)/2, \\ f_l \sim k^{n-3} & \text{if } l \geq (n-3)/2. \end{cases} \tag{1.52}$$

Therefore all the partial waves are small compared to the $l = 0$ case[22]. The latter is called *s-wave* and makes the diffusion isotropic and independent from the energy as $f(\theta) \sim -a_s$ [91]. Here a_s, the *s-wave scattering length*, can be positive or negative[23] and is connected to the potential $U(\mathbf{r})$, in the *Born approximation*[24], for $kr \ll 1$ as [91]

$$f(\theta) = -a_s = -\frac{m_r}{2\pi\hbar^2}\int d\mathbf{r}\, U(\mathbf{r}) \tag{1.53}$$

[22] Physically it means that states with $l \neq 0$ do not have enough energy to overcome the centrifugal barrier $V_l(r) = V(r) + \hbar^2 l(l+1)/2m_r r^2$ [84].

[23] We mention that, from a mean-field description, in order to have an energetically stable BEC one needs a repulsive interaction between the particles. However, Feshbach resonances can be used to make a BEC for attractive interaction (e.g. ^6Li).

[24] In this approximation the scattering amplitude is the Fourier transform of the potential.

However, it is possible to replace the real atomic potential $U(\mathbf{r})$ with an average potential $U_{\text{eff}}(\mathbf{r})$, chosen to have the same effect (i.e. it yields to the s-wave scattering length), for the low energy scattering, of the real atomic potential [88, 93], as

$$\int d\mathbf{r}\, U_{\text{eff}}(\mathbf{r}) = \frac{2\pi\hbar^2 a_s}{m_r} \equiv g. \tag{1.54}$$

The reason for which it is necessary to introduce a soft potential, $U_{\text{eff}}(\mathbf{r})$, is that the real atomic potential is highly repulsive for short distances. Therefore, a perturbation expansion cannot work in a simply way, as the Born approximation used to find the scattering amplitude would not be valid, and all perturbative terms would be necessary [92, 93]. On the contrary, the perturbation theory for the effective potential $U_{\text{eff}}(\mathbf{r})$ can be safely applied [88]. To sum up, for a weakly interacting cold

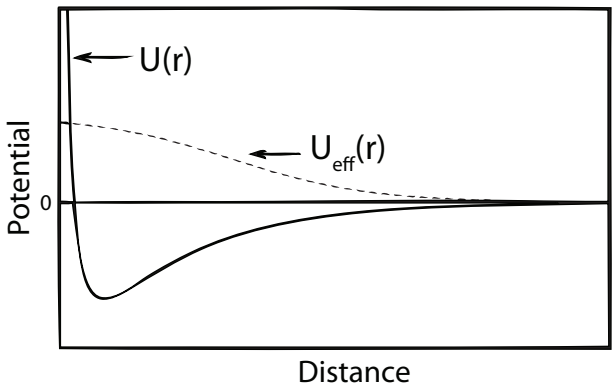

Figure 1.1: Cold atom interaction. Schematic representation of the interatomic interaction potential $U(\mathbf{r})$, as a function of the relative distance between two atoms r. The effective potential $U_{\text{eff}}(\mathbf{r})$ is built to yield the same s-wave scattering length of the real potential. Figure adapted from [88].

gas, the atom-atom interaction effects is modelled as a two-body effective contact interaction

$$V_{\text{int}}(\mathbf{r}_1 - \mathbf{r}_2) = g\delta(\mathbf{r}_1 - \mathbf{r}_2), \tag{1.55}$$

where $\mathbf{r}_1$ and $\mathbf{r}_2$ are the coordinates of the atoms involved. The effective potential is chosen to reproduce the scattering proprieties of the real atomic potential $U(\mathbf{r})$ for low energies.

The ability to tune the optical lattice potential opens up to the realisation of

tunable geometries. Specifically, it is possible to generate 1D geometries using a transverse confinement strong enough to freeze out the atom motion in two spatial dimensions [94, 95]. An important point is that the atom-atom interaction strength, for atoms confined transversally in a 1D waveguide, can be obtained directly by scaling the Three-Dimensional (3D) scattering lengths values, once known the transverse trapping frequency. Specifically the 1D s-wave scattering length a_{1D}, and the respective coupling constants g_{1D}, in Eq. (1.55), can be computed from the 3D case, a_{3D}, using

$$a_{1D} = -\frac{l_p^2}{2a_{3D}}\left(1 - C\frac{a_{3D}}{l_p}\right) , \tag{1.56}$$

$$g_{1D} = -\frac{2\hbar^2}{m a_{1D}} , \tag{1.57}$$

where $l_p \equiv \sqrt{\hbar/m\omega_T}$ is the length scale of the localisation in the transversal direction [94], ω_T is the transverse trapping frequency[25] and $C \simeq 1.4603$ [96]. Typical values, of the lattice transverse harmonic oscillator frequency, to create an array of 1D tubes are $\omega_T/2\pi \simeq (10 \div 40)\ kHz$, as shown in [36, 95].

A further condition on the transverse trapping potential, $\hbar\omega_T \gg k_B T$, ensures that there are no transverse excitations due to thermal effects. For instance, for $T = 30\ nK$ and a trapping frequency of $\omega_T \simeq 18\ kHz$ we find $\hbar\omega_T/k_B T \sim 10^2$ [94].

1.3.2 Manipulation of the Scattering Length

The atom-atom interaction can be tuned in a wide range via an external static magnetic field. The mechanism that modifies the strength and the sign of the mutual atom interaction relies on Fano-Feshbach resonances [92, 97].

In the last section we have showed that the atom-atom interaction potential, Fig. 1.1, leads to an effective interaction characterised by the s-wave scattering length. This description is modified in presence of coupling mechanisms with another collision channels [77, 92, 97]. We consider two particles, with energy

[25] We are assuming that the atom is in the ground state of a transverse 2D potential $H_T = (p_x^2 + p_y^2)/2m + m\omega_T^2(x^2+y^2)/2$, and that the kinetic energy along the longitudinal axis of the atom is less than the energy gap with the excited states $p_z^2/2m \gg \hbar\omega_T$ [96].

$E_{\text{tot}} = E(k_1) + E(k_2)$. A scattering channel is called open/close whether its energy is respectively $E \leq E_{\text{tot}}$ or $E > E_{\text{tot}}$.

Alkali atoms have a single valence electron outside a closed-shell core, and the ground state is characterised by a nuclear spin $\mathbf{I}$ and an electron spin $\mathbf{S}$, via the total angular momentum $\mathbf{F} = \mathbf{I} + \mathbf{S}$. When two atoms collides, the singlet and triplet coupling of the spins of the unpaired electrons from each atom, give rise to different atom-atom interaction potential curves, then to several scattering channels [77, 97]. A Feshbach resonance happens due to the presence of a quasi-bound level coupled to the scattering state of the colliding atoms, which has different symmetry and potential from that of the colliding atoms [97]. The elastic scattering length between two atoms can be deeply modified when the total energy in an open channel matches a low-energy bound state in a closed channel. Indeed, two particles in the open channel can scatter in a second order process, via an intermediate "virtual" state in the closed channel [77, 92]. From perturbation theory, one expects to find a contribution to the scattering length having the form

$$a_s \sim \frac{C}{E - E_{\text{res}}} \tag{1.58}$$

where C is a constant and E_{res} is the energy of the state in the closed channel. Therefore, the closer the energy of the particles in the open channel is to E_{res}, the larger is the effect on the scattering length. An external magnetic field changes the bound state energy (due to Zeeman effect), and can be tuned to let the collision energy be in resonance with the bound-state energy. The effect on the s-wave scattering length of an external magnetic field is described by [77, 97]

$$a(B) = a_s \left(1 - \frac{\Delta}{B - B_0}\right), \tag{1.59}$$

where B is magnetic field intensity, B_0 is the resonance position and Δ is the resonance width [97]. Although Feshbach resonances have been observed in several alkali atoms, they are not always easily exploitable. In the specific case of ^{87}Rb, the resonances are narrow and at high value of the field intensity, namely the broadest

resonance is at $B_0 \sim 1007\ G$ and it is $\Delta \sim 0.17\ G$ wide [98–100]. On the other hand the interaction is controllable in a wide range for other atom species, and it is also possible to achieve a non-interacting regime, for example using *Cs* atoms [71].

1.3.3 Hubbard Hamiltonian

We consider the Hamiltonian of a weakly interacting BEC, Eq. (1.46) and Eq. (1.55), in a periodical potential $V_0(\mathbf{r}) = \sum_{j=1}^{3} V_{j0}\cos^2(2\pi\ \mathbf{r}_j/\lambda)$, where λ is the laser-wavelength. The period of the potential defines the lattice spacing as $a = \lambda/2$, and the depth, $V_{j0} \propto |\Omega_0|^2/\delta$ from Eq. (1.29), is usually measured in terms of[26] Recoil Energy ($\mathbf{E_R}$). It is well known that a complete set of solution for a particle in a periodical potential is represented by Bloch functions in momentum space[27] [84]. However, in position space Bloch functions are extended, because the probability to find a particle in a Bloch state is the same for every position which is an integer multiple of the lattice spacing. Therefore, to calculate local properties of a single lattice site, it is convenient to use and alternative basis set, which elements are exponentially localised in each lattice site, known as *Wannier basis* [103, 104]. These are linear combinations of all the Bloch waves, in a given band, and are obtained via the Fourier transform of a Bloch state [80, 103, 104], which in 1D reads

$$w_m(x-x_j) \equiv \sqrt{\frac{a}{2\pi}} \int_{-\pi/a}^{+\pi/a} dk\ u_k^{(m)}(x) e^{-ikx_j}\ , \tag{1.60}$$

where, $\phi_k^{(m)}$ is a Bloch function, m is a band index and the Wannier function $w_m(x-x_j)$ is centred in site x_j, $k \in [-\pi/a, +\pi/a]$ is the quasi-momentum, and a is the lattice spacing. Conversely, Bloch functions can be obtained by the set of Wannier functions for a given band index m, as

$$u_k^{(m)} = \sqrt{\frac{a}{2\pi}} \sum_{x_j} w_m(x-x_j) e^{ix_j k}. \tag{1.61}$$

[26] The quantity $E_R \equiv \hbar^2 k^2/2m$ is a natural energy scale for the potential depth [101]. It corresponds to the energy of a particle in an infinitely deep well, with a wave-vector equal to the Brillouin zone limit value, $k = \pi/a$. Numerically is equal to the energy that an atom of mass m would acquire, once absorbed a resonant photon of momentum $\hbar k$ [77, 102]. Typical values are $\sim 10^{-30}\ J$ [79].

[27] These are defined as common eigenfunctions of the Hamiltonian and of the discrete translation operator in a lattice [84].

Wannier functions have the propriety to decay exponentially and to be orthonormal [80], namely for a 1D lattice with lattice spacing a,

$$\int_{-\infty}^{+\infty} dx\, w_m(x-x_j)w_m(x-x_k) = \delta_{x_j,x_k} \qquad \text{where } x_j, x_k \in \{0, \pm a, \pm 2a, \ldots\}. \tag{1.62}$$

We mention, as pointed out in [103, 105], that Wannier functions are not uniquely defined by Eq. (1.60), as a phase factor can be added to Bloch functions $u_k^{(m)}$, without changing the physical description of the system. However, in [103, 104], it has been shown that for each band there is only one real Wannier function, known as *maximally localised Wannier*, either symmetric or antisymmetric in $x = 0$ or $x = a/2$, that falls exponentially as $x \to \infty$. Hereafter, we use this choice for the Wannier functions. For a deep lattice, Wannier functions are well approximated by gaussian functions[28] [106]. As a standard procedure [12, 13, 37], BEC operators $\hat{\Psi}(\mathbf{r})$ can be decomposed in a complete orthonormal Wannier basis, as

$$\hat{\Psi}(\mathbf{r}) = \sum_{jm} w_m(\mathbf{r}-\mathbf{r}_j)a_j^{(m)} \simeq \sum_j w(\mathbf{r}-\mathbf{r}_j)a_j. \tag{1.63}$$

Here $a_j^{(m)}$ is the annihilation operator in the site j and band index m, and $w_m(\mathbf{r}-\mathbf{r}_j)$ is a Wannier function. In the right member of the last formula we are assuming that all the particles in the system are in the lowest state of the optical lattice, and that the energies involved in the dynamics are smaller than the excitation energy of higher bands. For a deep lattice, under a *tight-binding* approximation, the Hamiltonian (1.46) assumes the *Bose-Hubbard* form

$$H = \sum_{j=1}^{L-1} J_j \left(a_j^\dagger a_{j+1} + a_j^\dagger a_{j+1}\right) + \sum_{j=1}^{L} \frac{U_j}{2} n_j(n_j-1) - \sum_{j=1}^{L} \mu_j n_j, \tag{1.64}$$

[28] In a deep lattice the potential minima can be approximated by harmonic potential, whose ground state function is a gaussian.

where we define the parameters

$$J_j \equiv \int d\mathbf{r}\; w^*(\mathbf{r}-\mathbf{r}_j)\left(-\frac{\hbar^2\nabla^2}{2m}+V_0(\mathbf{r})\right)w(\mathbf{r}-\mathbf{r}_{j\pm1}), \tag{1.65}$$

$$U_j \equiv g\int d\mathbf{r}\; w^4(\mathbf{r}-\mathbf{r}_j)\;, \tag{1.66}$$

$$\mu_j \equiv \int d\mathbf{r}\; V_T(\mathbf{r})w^2(\mathbf{r}-\mathbf{r}_j) \simeq V_T(\mathbf{r}_j). \tag{1.67}$$

The parameter J_j is the *hopping* term between adjacent sites, U_j is the strength of the onsite interaction between particles in the same site. We assume that the external trapping potential $V_T(\mathbf{r})$ varies slowly within a site and therefore we can define a local energy offset μ_j, in site j [37]. In the derivation of the Bose-Hubbard model Eq. (1.64) we have not taken into account decoherence effects due to spontaneous emission, which has been discussed in Sec. 1.2. As for the standard Bose-Hubbard model Eq. (1.64), once expanded the field operator in a basis of Wannier functions, for a single particle in the lattice, one finds that the effective Hamiltonian is [66],

$$H_{\text{eff}} = \sum_{m,\langle j,k\rangle} J^{(m)}_{j,k} a^{(m)}_j a^{(m)\dagger}_k - \sum_{m,j}\mu^{(m)}_j n^{(m)}_j - \frac{i}{2}\sum_{m,n,j}\gamma^{(m,n)} a^{(m)\dagger}_j a^{(m)}_j, \tag{1.68}$$

where n,m are band indices and $\langle j,k\rangle$ is the sum over nearest neighbours, $w^{(m)}_j$ are Wannier functions centred in site j with band index m, and

$$J^{(m)}_{j,k} = \int d^3\mathbf{r}\; w^{(m)}_j\left(\frac{p^2}{2m}+V_0(\mathbf{r})\right)w^{(m)}_k \tag{1.69}$$

$$\mu^{(m)}_j = \int d^3\mathbf{r} w^{(m)}_j\left(\frac{p^2}{2m}+V_0(\mathbf{r})\right)w^{(m)}_j \tag{1.70}$$

$$\gamma^{(m,n)} = \int d^3\mathbf{r}\; w^{(m)}_j\gamma(\mathbf{r})w^{(n)}_k \tag{1.71}$$

Similar calculations can be performed[29] for N atoms trapped in the lattice. The key point we want to highlight here is that, as shown in details in [66], the Master

[29] We do not show explicitly the derivation, as it is out of the purposes of this thesis. Details can be found in [66]. We briefly mention that, to derive the Master Equation, in the effective Hamiltonian (1.41), discussed in Sec. 1.2, a term that takes into account of the atom-atom collision in a laser field must be added.

Equation (1.40), in the lowest band approximation reduces to

$$\frac{d}{dt}\rho = -i\left[H_{BH},\rho\right] + \sum_j \gamma\left(n_j\rho n_j - \frac{1}{2}n_j n_j\rho - \frac{1}{2}\rho n_j n_j\right), \tag{1.72}$$

where H_{BH} is the Hamiltonian (1.64) and $\gamma \equiv \Gamma|\Omega_0|^2/4\delta^2$ is the effective scattering rate, with Γ the spontaneous emission rate, δ the detuning from the atomic resonance and Ω_0 the strength of the trapping potential, discussed in Sec. 1.2.

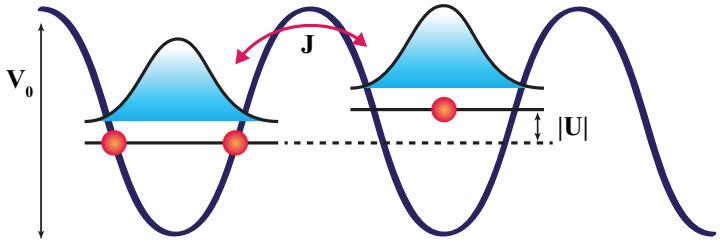

Figure 1.2: Bose-Hubbard model. Tight-binding model for cold atoms trapped in an optical lattice with depth V_0, described by Eq. (1.64). J is the hopping rate and U is the strength of the onsite interaction. An attractive interaction between the atoms $U > 0$, energetically favours a multiple occupancy of one site. Figure adapted from [101].

1.3.4 Lattice Curvature Effects

In typical experiments an additional external harmonic confinement is superimposed on the top of the lattice potential. This external potential depends both on the magnetic potential where the BEC is initially created, but also on the gaussian shape of the laser beam [107], that generates the lattice, as show in Fig. 1.3. The curvature effect of the lattice on the atom dynamics can be modelled as a spatially varying chemical potential, in Eq. (1.64), that has a harmonic profile $\mu_{\text{eff}}(x) = \mu - \frac{1}{2}m\omega_a^2(x-x_0)^2$, where x_0 is the position of the centre of the lattice, and the trapping frequency is [107, 109]

$$\omega_a = \sqrt{\omega_m^2 + \frac{8V_0}{mw_0^2}}. \tag{1.73}$$

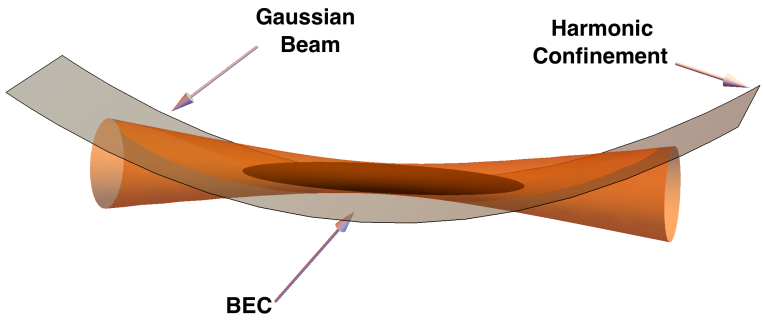

Figure 1.3: 1D BEC trapping configuration. A BEC (brown) is immersed in a trapping potential due to a combination of a magnetic potential (grey), in which the condensate is initially formed, and of an optical potential generated by a Gaussian laser beam profile (light brown). Figure adapted from [108].

Here ω_m is the magnetic trap frequency, V_0 the depth of the lattice and w the *beam waist* of the laser beam[30]. Typical values of the additional harmonic confinement are $\omega_a/2\pi \simeq (10 \div 200)\ Hz$ [36].

1.3.5 Parameters of the model

The effective Bose-Hubbard parameters (1.67) can be computed explicitly. In fact, asymptotic expressions can be found for a deep lattice ($V_0/E_R \gtrsim 6$) [37, 80] where, as discussed in Sec. 1.3.3, Wannier functions coincide with gaussian functions. Specifically, in the harmonic approximation

$$V(x) = V_0 \sin^2\left(\frac{\pi x}{a}\right) \simeq \frac{m}{2}\omega_{\text{eff}} x^2 \,, \qquad \omega_{\text{eff}} \equiv \frac{2\pi^2 V_0}{m a^2}, \tag{1.74}$$

$$W(x) = \pi^{-1/4}\sigma_0^{-1/2}\exp\left(-x^2/2\sigma_0^2\right) \,, \qquad \sigma_0 \equiv \left(\frac{\hbar^2 a^2}{2\pi^2 m V_0}\right)^{1/4}, \tag{1.75}$$

[30] A gaussian laser beam has a profile which diameter has a spatial dependence as $w(z) = w_0\sqrt{1+(z/z_R)^2}$. The beam waist w_0 is a measure of the minimum spot size, on the focus, for a gaussian beam, where the intensity decreases of a factor e^{-2} from the maximum. Typical values are $w_0 \simeq (10 \div 100)\mu m$ [107, 110].

and by direct integration of Eq. (1.67), one finds, for a homogeneous lattice $J_j = J$, $U_j = U, \mu_j = 0$ [80]

$$\begin{aligned} \frac{J}{E_R} &\simeq \frac{4}{\sqrt{\pi}} \left(\frac{V_0}{E_R}\right)^{3/4} \exp\left(-2\sqrt{V_0/E_R}\right), \\ \frac{U}{E_R} &= \sqrt{8\pi}\frac{a_s}{a} \left(\frac{V_0}{E_R}\right)^{3/4}, \\ \frac{J}{U} &= \left(\frac{\sqrt{2}}{\pi}\right) \left(\frac{a}{a_s}\right) \exp\left(-2\sqrt{V_0/E_R}\right), \end{aligned} \tag{1.76}$$

where a is the lattice spacing, a_s the s-wave scattering length and V_0 the lattice depth. The last expression shows that the tunnelling rate J can be controlled in a wide range varying the lattice depth V_0, without affecting in a significant way the on-site interaction strength. More in general, the parameters (1.67) can be computed numerically once known the Wannier functions. To determine the Wannier function numerically, we consider a single particle in a 1D optical lattice. The Schrödinger equation,

$$-\frac{\hbar^2}{2m}\partial_x^2 \psi(x) + \left(V_0 \sin^2 \frac{\pi x}{a}\right) \psi(x) = E\psi(x), \tag{1.77}$$

resembles the *Mathieu* differential equation [80],

$$\partial_z^2 \psi + (\alpha - 2q\cos(2z))\psi = 0\,, \tag{1.78}$$

with

$$\alpha = E(k)/E_R - V_0/2E_R\,, \qquad q = -V_0/4E_R\,. \tag{1.79}$$

As illustrated in details in [80], the parameter α, the Bloch functions $\psi_k(x)$ and the band structure $E(k)$, as a function of lattice depth V_0 and the crystal momentum k, can be found using *Mathieu* characteristics and *Mathieu* functions. Once known the Bloch functions $\psi_k(x)$, the lowest-band Wannier functions are found as [80]

$$w(x) = \int_{-\pi}^{+\pi} \frac{dk}{2\pi} \psi_k(x) \tag{1.80}$$

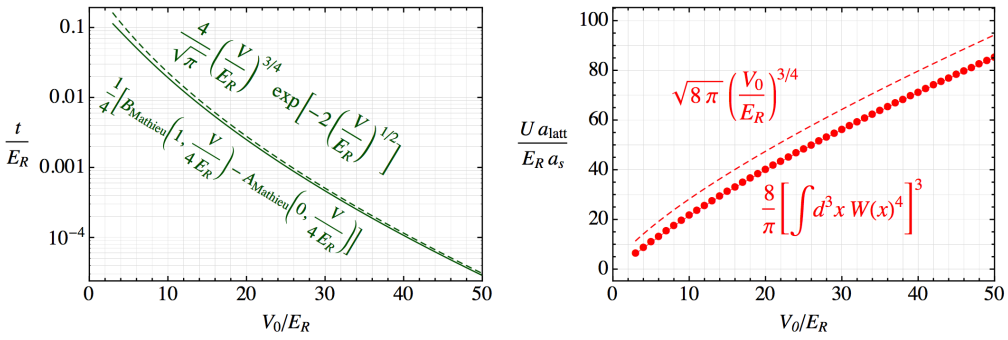

Figure 1.4: Bose-Hubbard parameters. Tunnelling rate J (left) and onsite interaction U (right) for a particles in a 3D sinusoidal lattice, as a function of the lattice depth V_0 (in recoil energy unit E_R). The lattice has a spacing a_{latt} and the s-wave scattering length is a_s. The asymptotic expressions, Eq. (1.76), are plotted with dashed lines, while the other curves are calculated from Mathieu functions and Wannier functions. Figure from [80].

The latter can be used to find the hopping tunnelling rate[31] and the onsite interaction in the Bose-Hubbard model, for a given potential shape [80]. In Fig. 1.4 we show a comparison between the asymptotic expression (1.76) and the numerical calculations, as a function of the lattice depth V_0.

1.3.5.1 Transfer Velocity in the Bose-Hubbard Model

We want to analyse more in details the propagation of particles in a lattice model. Firstly we compute the energy spectrum in the Bose-Hubbard model (1.64), with $J_j = J$, $\mu_j = 0$ in the single particle sector. We first transform the operators in momentum space via

$$a_j^\dagger = \frac{1}{\sqrt{L}} \sum_{k=1}^{L} e^{ikja} a_k^\dagger \,, \tag{1.81}$$

where $k = 2\pi n/L$ has discrete values, $n \in \{1,\ldots,L\}$, for a 1D model of length L, with periodical boundary condition and lattice spacing a. Using the orthogonality relation,

$$\frac{1}{L}\sum_j e^{i(k_n-k_m)j} = \delta_{n,m}, \tag{1.82}$$

[31] The tunnelling rate J can be easily computed by equating the bandwidth of the 1D tight-binding model to the bandwidth in terms of Mathieu functions [80].

one obtains

$$H = \sum_k \hbar\omega_k a_k^\dagger a_k, \tag{1.83}$$

where $E(k) = \hbar\omega_k = 2J/\hbar\cos(ka)$ is the excitation spectrum, with $k \in [-\pi/a, \pi/a]$. The maximum group velocity [111], is

$$v_g^{max} = \mathrm{Max}_k \frac{\partial E(k)}{\partial k} = 2Ja/\hbar, \tag{1.84}$$

and because in a single hopping, the particle has to travel for a distance a in a time τ, the hopping time is approximately $\tau \simeq \hbar/2J$. In Fig. 1.5(a) we show the hopping time, τ, for a single particle in a 1D lattice as a function of the lattice depth V_0. Typical heating time is of the order of several hundred milliseconds [32]. For the

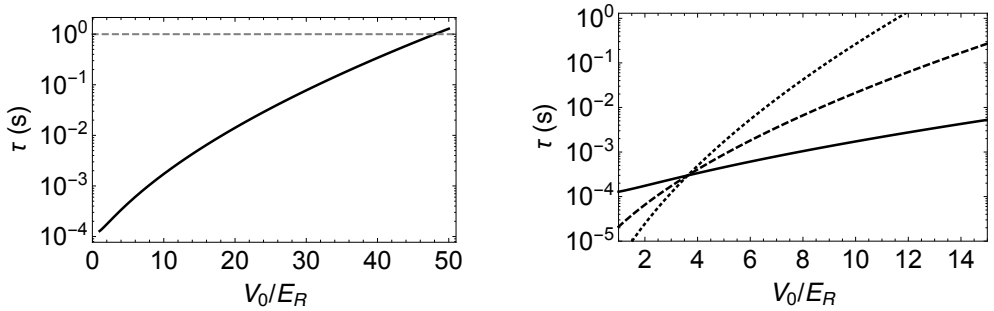

Figure 1.5: Hopping time. (a) Single particle hopping time, τ, as a function of the lattice depth V_0 (in energy recoil E_R units) using Eq. (1.76). A typical coherence time of 1 s is plotted for comparison (grey line). (b) Hopping time for a single particle, respectively with hopping rate J (black line), $J_{\text{dashed}} = J^2/U$ (dashed line), and $J_{\text{dotted}} = J^3/U^2$ (dotted line). The s-wave scattering length chosen is $a_s = 100.4a_0$, in Tab. E.3, and the lattice spacing is $a = 532$ nm.

purposes of this thesis, it is relevant to compare the hopping time of a single particle, with tunnelling rate J, with the ones of a particle in a lattice, whose effective hopping rate are respectively $J_{\text{dashed}} = J^2/U$ and $J_{\text{dotted}} = J^3/U^2$. We show the result obtained in Fig. 1.5(b).

We highlight another feature of the model (1.64). Specifically, the difference between the phase velocity, $v_{\text{p}} \equiv E(k)/k$, and the group velocity, Eq. (1.84), makes the particle dynamics dispersive [111]. This is important, as in the course of this

thesis we will discuss applications of the Bose-Hubbard model for quantum state transfer.

1.4 Single Site Addressing Techniques

The ability to design and control the transport at the single atom level plays a central role in the development of quantum technologies. This requires both high-resolution imaging and single atom manipulation techniques. In this section we introduce the state-of-the-art of single site addressing technologies for neutral atoms trapped in optical lattices.

1.4.1 Mott-Insulator Phase

The ground state proprieties of the Bose-Hubbard model (1.64) depend strongly on the ratio between the strength of hopping term J and the onsite interaction U. If the inter-particle interaction dominates over the tunnelling term $J/U = 0$, the Hamiltonian of the system becomes

$$H_{U\gg J} = \frac{U}{2}\sum_j n_j(n_j-1) - \sum_j \mu_j n_j \,, \tag{1.85}$$

and the ground state of the system, for a homogeneous system $\mu_j = \mu$, called *Mott-Insulator state*, is given by a product of local Fock states[32] [112]

$$|\psi_{\mathrm{MI}}\rangle \propto \prod_{j=1}^{L}\left(a_j^\dagger\right)^M |0\rangle = \prod_{j=1}^{L}|n_j\rangle \,, \tag{1.86}$$

where M is the total particle number in the system. A peculiar feature of this state is that the occupation number fluctuation $\sigma_j = \langle\left(n_j - \langle n_j\rangle\right)^2\rangle^{1/2}$ vanishes. Therefore, once in the Mott phase the system has a fixed number of particles per site. The external trapping potential, Sec. 1.3.4, affects the atom distribution in the lattice, which is determined by the interplay between interaction and local potential [107]. Specifically, there is a step-wise dependence of the particle number with the ratio between chemical potential and onsite interaction: $n_j(\mu)$ increases by one at integer

[32] These are defined as the eigenstates of the boson number operator $\hat{n}_j$

values of μ/U while is constant otherwise [37]. Basically, the Mott-insulator state consists of an array of Fock states, where the curvature of the lattice, Sec. 1.3.4, produces a "wedding-cake" spatial structure in the occupation number, as shown in Fig. 1.6, [107, 113]. On the other hand, when the hopping term dominates the inter-

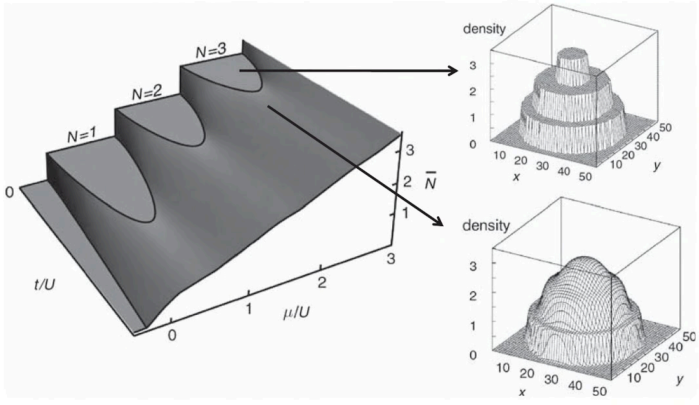

Figure 1.6: Spatial structure of a Mott-Insulator. (left) Phase diagram of a Bose-Hubbard model as a function of the chemical potential μ/U and the hopping rate t/U. Each lobe represents a Mott insulator with integer density, while for higher values of t/U the system is in the superfluid phase. (right) The density profile in a harmonic trap resembles a "wedding-cake" structure, in the Mott-insulator phase. Figure from [113].

particle interaction $U/J = 0$, the system is in the *superfluid phase*, described by the many-body M particle wavefunction

$$|\psi_{\mathrm{SF}}\rangle \propto \left(\sum_{j=1}^{L} a_j^{\dagger}\right)^{M} |0\rangle, \tag{1.87}$$

namely a simple product of zero-momentum Bloch waves. In this case an atom is delocalised over the entire lattice. In the thermodynamics limits, the superfluid state is indistinguishable from a coherent state[33] [13]. Therefore, the probability to find a specific particle occupation in a lattice site, fluctuates as a poissonian distribution [73].

[33] This is defined as an eigenstate of the annihilation operator $\hat{a}_j$ [72].

1.4.2 Single Atom Detection

The ability to perform *in situ* measurement in optical lattices, yields to the possibility to characterise the many-body physics, by providing direct access to the system parameters at the single atom level [12,114,115]. Among the varieties of techniques, as shown in Fig. 1.7, single-atom fluorescence[34] have been exploited with high efficiency, (with a fidelity almost close to 100% [16, 17, 118, 119]) to probe the system with single-site resolution [18, 19, 117].

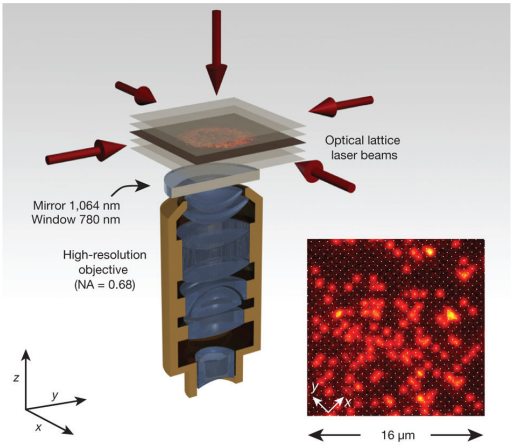

Figure 1.7: Single-site resolved imaging of a two dimensional bosonic gas. The atom number distribution is obtained via a high resolution objective which detects fluorescence photons emitted by atoms trapped in a Two-Dimensional (2D) optical lattice, while illuminated with a resonant laser beam. Atoms are pinned down in their lattice site by strongly increasing the lattice depth. Figure from [16].

The first obstacle towards single site detection in an optical lattice is that, to reach the strongly correlated regime[35] the lattice spacing, a, must be below the micron level (typically is about 500 *nm* [15, 112]). As a consequence, the distance between two sites is of the order of the optical diffraction limit of the detection method. Indeed, the resolution R of an imaging system[36] is given by the *Rayleigh criterion*, $R = 0.61\lambda_{\text{res}}/NA$, where NA is the numerical aperture [115, 117, 120] and λ_{res} is the emission wavelength (the atomic typical transition used for fluorescence

[34] Fluorescence is preferable to single-site absorption (e. g. [116]) because it achieves a larger signal/noise ratio [115, 117].

[35] Where the tunnelling strength is comparable with the on-site interaction [12].

[36] The minimum distance needed to detect two points as individuals [120].

detection is $\sim 780\ nm$ for ^{87}Rb). Therefore, single-site imaging requires the resolution to come close to this limit. To fulfil the condition $R \sim a$ values of $NA = 0.68$ and $NA = 0.8$ have been used respectively[37] in [45] and [112]. A drawback of these high values of the numerical aperture is that the depth of the focus is of the order of $\sim 1\ \mu m$. This limits the technique to 2D systems [117].

A second obstacle is that, as detectors have a finite quantum efficiency, a high detection fidelity requires to collect a certain amount of fluorescence photons (of the order of[38] ~ 1000) to produce an image of the atom position in the lattice. Therefore, the atom dynamics must be frozen to avoid thermal hopping effects, by ramping up the depth of the lattice, and atoms must be illuminated for a typical time period[39] of $\sim 1\ s$ [16, 118].

One limitation of the above detection technique is that current experiments do not detect the atom number distribution, but rather the parity of the occupation number in a site. The reason is that atom pairs are lost[40], due to light-assisted collision, as shown in Fig. 1.8, before their position can be detected [12, 117, 122]. A single site resolved image using fluorescence in a 2D Mott-Insulator with sub-micrometer resolution has been firstly shown by [16, 17]. The measurement process exploits a quasi-resonant light to induce photon emission which are revealed by a CCD detector.

The detection process can be interpreted as a projective measurement on the atom number distribution. Ideally the fluorescence imaging of the optical lattice should produce a measure of the number of atoms in each site [18]. Mathematically, this is described as a projective measurement [123], $P_{n_i} = |n_i\rangle\langle n_i|$, where n_i is the occupation number in lattice site i. Typically, all the sites are measured simultan-

[37] More in general, high-resolution microscope objectives, with $NA \simeq 0.7 \div 0.8$, are required for a single-site resolution [115].

[38] We highlight that single-atom microscopy is still an in-progress field, and recently the number of photon to be collected to produce an image has been reduced of one order of magnitude, for ^6Li [121].

[39] Because of the long imaging time, the detection fidelity can be limited by collision with the background gas. Typically, there is a 1% atom loss in one second observation time. A good compromise to get enough signal is represented by a 100 ms observation time [18, 117]. Moreover, because atoms scatter many photons, to suppress undesired hoppings, the laser field has a high power (e.g. a 100 W YAG laser to reach a lattice depth of $\sim 10^3\ E_R$) and designed to provide laser cooling during the imaging process [17, 18].

[40] The typical ejection time of a pair is $\sim 100\ \mu s$, [12].

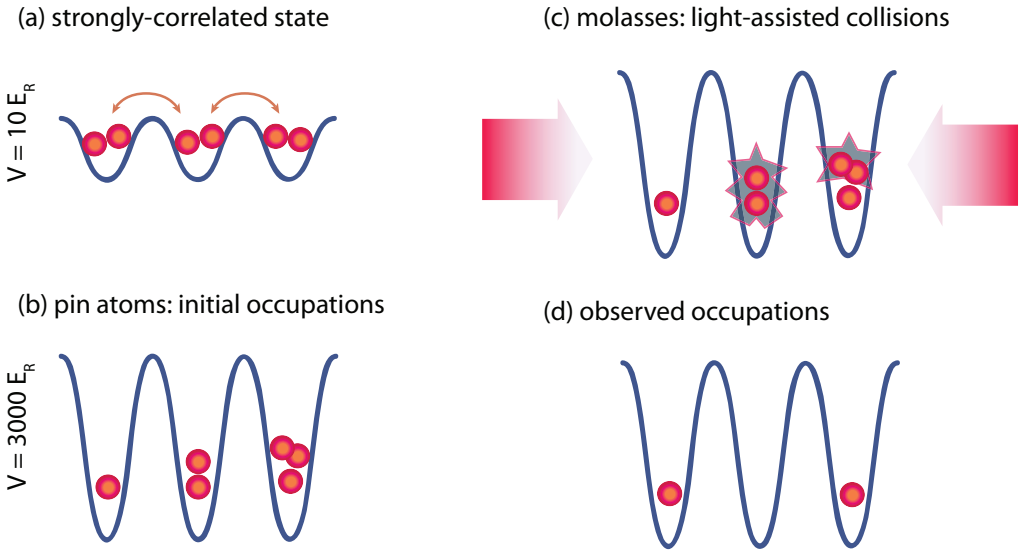

Figure 1.8: Single-site fluorescence detection. Light assisted collision limits the possibility to observe the atom distribution with single-site resolution. To image the system (a), first the dynamics is frozen (b) by increasing the lattice depth V. A resonant field let the atom emit fluorescence photons (c), but due to light-assisted collisions only the parity of the site occupation (d) can be measured. Figure adapted from [117].

eously[41], then a particular realisation of occupation numbers $|\{n_i\}\rangle = |n_1, \ldots, n_L\rangle$ is described via the projection operator

$$P_{\{n_i\}} = \bigotimes_{i=1}^{L} |n_i\rangle\langle n_i|. \tag{1.88}$$

The real fluorescence imaging of a many-body system differs from the previous description as the parity projection limits the measurement outcome, in each sites, in the subspace $\{|0\rangle, |1\rangle\}$. The measurement process is then described in terms of

[41] We mention that, alternatively to fluorescence detection, scanning electron microscopy techniques has been employed, for a local measurement of the occupation number and for a further evolution of the system after the detection [18, 109, 124].

generalised measurements[42] operators in each site [18]:

$$\begin{cases} M_{n_i} = |0\rangle\langle n_i| & \text{if } n_i \text{ is even,} \\ M_{n_i} = |1\rangle\langle n_i| & \text{if } n_i \text{ is odd.} \end{cases} \tag{1.89}$$

where $p(n_i) = \mathrm{Tr}\left(M_{n_i}^{\dagger} M_{n_i} \rho\right)$ is the detection probability, and $\rho \equiv |\psi\rangle\langle\psi|$ the density matrix of the system [123]. To circumvent parity projection effects, several techniques have been exploited in recent years, allowing one to measure the full number statistics up to four particles per site [26]. Pairs of atoms in the same site have been observed by splitting them, via a magnetic gradient, prior to the imaging procedure [22]. Alternatively, particles have been transported to another lattice, for a multi-layer read-out [61]. Finally, as shown in Fig. 1.9, to avoid pairwise atom losses during the imaging, an addressing beam generated by a Digital Micromirror Device (DMD) can be exploited to isolate one row of a Mott-Insulator and emptying all other sites [26]. Then, after the addressing beam is turned off, atoms are released into 1D tubes transverse to the cut, and perform a free vertical expansion which delocalises the atoms over ~ 100 sites, separating particles originating from the same site. The atoms are then imaged individually without being lost due to parity projection. The dynamical evolution of a single spin flip in a Heisenberg chain has been studied in [33], where a spin-sensitive imaging has been performed with single-site fluorescence and post-selection. Specifically, a positive/negative image of the flipped spin has been obtained by removing all the atoms in the other spin state. For the negative imaging, holes due to thermal effect has been discarded via a post-selection technique (i.e. taking only the images with a single hole). More recently, to simultaneously detect the spin and the density degrees of freedom, a magnetic field gradient has been exploited, for a Fermi-Hubbard chain, to separate two spin states into two different sites of a local double well [34]. This provides a direct site-resolved detection of up/down spins, holes and doublons, as shown in

[42] A set of operators $\{A_\mu\}$ that satisfy the propriety $\sum_\mu A_\mu^{\dagger} A_\mu = \mathbf{1}$. The probability of obtaining the outcome labeled by μ and the state after the measurement are respectively $p_\mu = Tr\left(A_\mu \rho A_\mu^{\dagger}\right)$ and $\rho'_\mu = \left(A_\mu \rho A_\mu^{\dagger}\right)/p_\mu$ [123, 125].

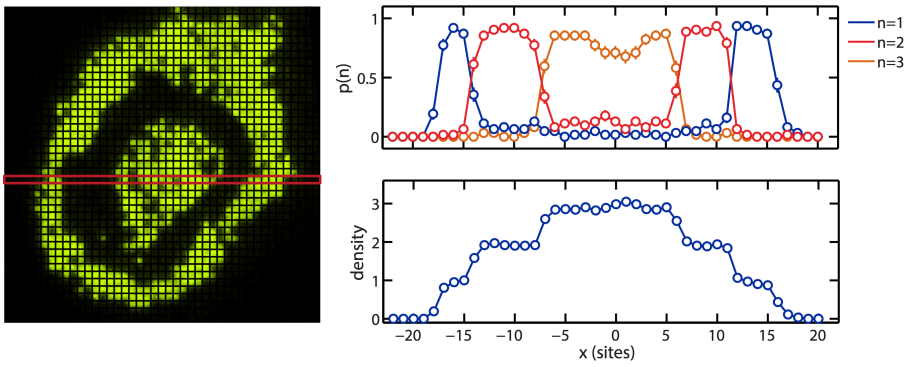

Figure 1.9: Full counting statistic in a 1D optical lattice. (left) A Mott insulator with up to $n = 3$ atoms near the centre appears as three concentric rings in the parity-projecting fluorescence imaging. A single row or atoms (red box) can be cut from the Mott insulator and all atoms are detected after a short vertical expansion. (right) Plot of the full density profile and number statistics for each site in the one-dimensional profile. Figure from [26].

Fig. 1.10.

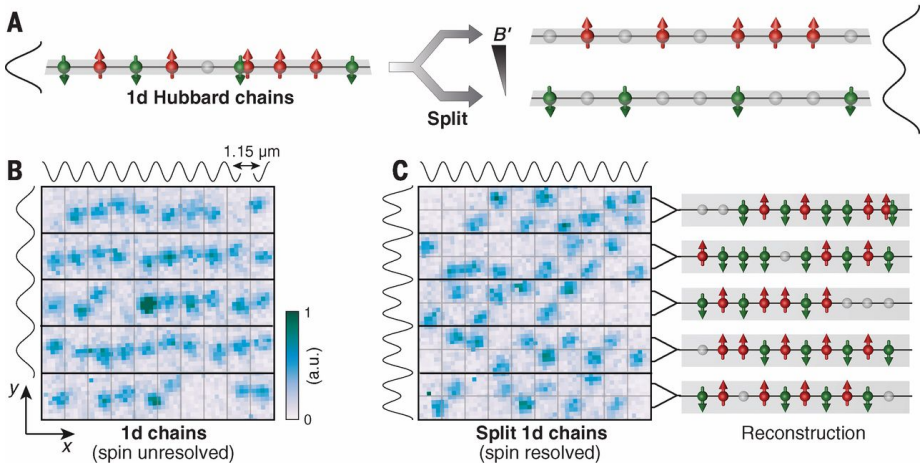

Figure 1.10: Spin and density resolved microscopy in a Fermi-Hubbard chain. Each site of the Hubbard chain (A) is split spin-dependently in a local double-well (B) via a magnetic field gradient, allowing a site-resolved detection of up/down spins, holes and doublons (C). Figure from [34].

1.4.3 Deterministic Atom Preparation in a Lattice

The quest of initialisation and of control capabilities of positions and spin states of few atoms in an optical lattice has been accomplished via single-site-resolved

addressing techniques, that exploit tightly focussed laser beams[43] [38, 45, 115].

In the following we briefly describe the main characteristics of the addressing scheme, in [15], Fig. 1.11, to prepare single atoms in specific sites of a lattice. Firstly a 2D system of ^{87}Rb is prepared in the Mott-Insulator state, with unity filling,

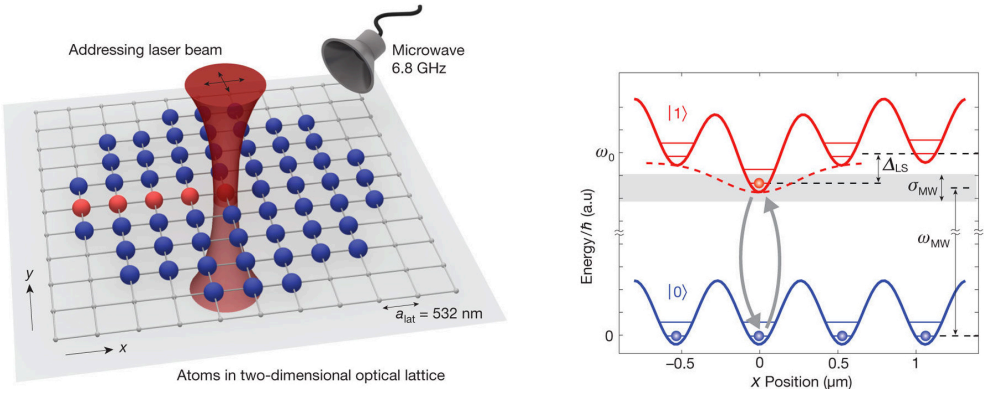

Figure 1.11: Single site addressing of a Mott-Insulator [45]. (left) A tightly focussed laser beam (red) is shined on the atom plane to address a single atom of a 2D Mott-Insulator state, prepared in the $|0\rangle$ state. (right) Energy shift induced on the addressed atom between two hyperfine levels, which brings the addressed atom in a resonance with an external microwave field ω_{MW}, inducing a spin flip from $|0\rangle$ to $|1\rangle$.

in the hyperfine state $|0\rangle = |F = 1, m_F = -1\rangle$. Then an off-resonant laser, with wavelength $\lambda = 787.55\ nm$, focussed on a target site, induces a differential energy shift from the hyperfine state $|1\rangle = |F = 2, m_F = -2\rangle$. The addressing beam has a diameter of $\sim 600\ nm$ Full-Width at Half-Maximum (FWHM), and the lattice spacing is $a_{\mathrm{lat}} = \lambda_{\mathrm{las}}/2 = 532\ nm$. As the light shift brings the target atom to be in resonance with an external microwave field (whose frequency is $\sim 6.8\ GHz$), the effect of the process is then to generate a spin flip from $|0\rangle$ to $|1\rangle$ leaving the rest of the atoms unaffected in the state $|0\rangle$.

The addressing laser is then moved to a new position, in about 5 ms, to address an atom in a different site. The procedure is repeated until all the spin in the target sites are flipped. The precision of the positioning is better than $0.1a$ [117]. Finally, a push-out laser pulse, resonant with the transition from $F = 2$ to $F' = 3$, remove

[43] Although a high-resolution objective is used to focus a laser beam, the spot size is of the order of the lattice spacing, and precise addressing has been obtained by increasing the spatial resolution via a resonance addressing technique, based on magnetic spin flips [15, 115].

all the addressed atoms in the state $|1\rangle$. The addressing scheme has been showed to have a fidelity of 95% [15]. An improvement of this technique have been made in [32] where multiple sites are addressed simultaneously with a light pattern from a DMD, instead of using a gaussian beam laser sent through the high-resolution objective [115].

The above technique is also important, as it naturally implements single qubit operations using microwave radiation, together with a tightly focussed laser [45]. Alternatively, one could use a two photons Raman transition [126]. In general Raman-based gates are faster ($\sim 37\ nm$ for a $\pi/2$ gate, with a residual rotation at the level of 10^{-3} [127]) than microwave-based gates ($\sim 30\ \mu s$ gate time in *Rb* with an error of 1.4×10^{-4} [128]). However, Raman-based gates are affected by cross-talk for the typical spacing of optical lattices [45].

1.5 Spin Chain Models with Optical Lattices

The controlled setup offered by cold atoms, is a promising route to address open problems in quantum magnetism. In fact, this can be mimicked with optical lattices, in condition which are challenging to be observed using other physical systems, due to a correspondence between Hubbard model and spin models in certain parameter regimes [12, 129, 130]. In the following section we introduce typical spin models and their connection to optical lattices.

1.5.1 Hard-Core Boson Regime

The simplest simulation of a spin model is realised in the hard-core limit, namely when $U \gg J, \mu$. In this case every site of the lattice is occupied by zero or, at most, one particle. The single spin state is encoded mapping the presence/absence of a particle in a lattice site to a spin $1/2$ model, respectively $|1\rangle \to |\uparrow\rangle$ and $|0\rangle \to |\downarrow\rangle$. The spin operators are formally obtained from the Bose-Hubbard model (1.64) via the transformation

$$a_j^\dagger \to S_j^+, \qquad a_j \to S_j^-, \tag{1.90}$$

$$n_j \to (S_j^z - \frac{1}{2}), \tag{1.91}$$

that map the system to[44] the XX spin $1/2$ chain model (XX chain)

$$H = \sum_{j=1}^{L-1} 2J_j \left(S_j^x S_{j+1}^x + S_j^y S_{j+1}^y \right) - \sum_{j=1}^{L} \mu_j S_j^z, \tag{1.92}$$

where the local chemical potential plays the role of a local magnetic field. The advantage of the above transformation is that quantum magnetism models can be simulated for relatively high temperatures (i.e. similar to the standard superfluid-Mott-Insulator transition), and in disordered chains [12]. As the tunnelling J_j in (1.92) is negative, the Bose-Hubbard mode (1.64) in the hard-core boson limit, represents a quantum simulator of a ferromagnetic XX spin model.

1.5.2 Strong Coupling Regime for Structured Bosons

The variety of spin models that can be simulated via cold-atoms can be further extended by exploiting the atoms' internal degrees of freedom. We consider a Bose-Hubbard model for particles with two internal states[45], $\sigma \in \{\uparrow, \downarrow\}$

$$\begin{aligned} H = &\sum_{j\sigma} J_\sigma \left(a_{j,\sigma}^\dagger a_{j+1,\sigma} + H.c \right) + \sum_{j\sigma} U_\sigma n_{j,\sigma}(n_{j,\sigma} - 1) + \sum_j U_{\uparrow\downarrow} n_{j\sigma} n_{j\sigma'} \\ &- \sum_{j=1}^{L} \mu_{j,\sigma} n_{j,\sigma}. \end{aligned} \tag{1.93}$$

Here the inter-particle coupling strengths are respectively $U_{\uparrow\downarrow} = U_{\downarrow\uparrow}$, $U_\uparrow \equiv U_{\uparrow\uparrow}$ and $U_\downarrow \equiv U_{\downarrow\downarrow}$ [31, 130], while $J_\uparrow$ and $J_\downarrow$ and $\mu_{j,\uparrow}$, $\mu_{j,\downarrow}$ are respectively the hopping terms and the local chemical potentials for the two species. We are interested in the strongly coupled regime, $|U_{\uparrow\downarrow}|, |U_\sigma| \gg |J_\sigma|$, for a system in the Mott-Insulator state. To clarify why the Hamiltonian (1.93) is equivalent to a spin model, we consider a two site system described in the Hilbert subspace of zero total angular momentum, namely $\mathscr{H} = \{|\updownarrow, 0\rangle, |\uparrow,\downarrow\rangle, |\downarrow,\uparrow\rangle, |0,\updownarrow\rangle\}$ with $J_\uparrow = J_\downarrow = J$. A swap operation between spins, $|\uparrow,\downarrow\rangle \to |\downarrow,\uparrow\rangle$, is generated in a spin chain language via a term $J_{\text{ex}} S_1^- S_2^+ |\uparrow,\downarrow\rangle$, where J_{ex} is the super-exchange coupling strength [131]. On the other

[44] Constant terms have been suppressed.

[45] We highlight that we are assuming that spin-exchange collision between the particles are suppressed. Spin-exchange collisions depends on the difference between the singlet and triplet scattering lengths and for ^{87}Rb are closely equal. Hence, spin-flip processes can be safely neglected [32, 77].

hand, in the Hubbard model, if $J_\sigma = 0$ the Hilbert space is separated in two energy separated subspaces, respectively $\mathscr{H}_q = \{|\updownarrow,0\rangle, |0,\updownarrow\rangle\}$ and $\mathscr{H}_p = \{|\uparrow,\downarrow\rangle, |\downarrow,\uparrow\rangle\}$, where the energy gap is $E_q - E_p = U_{\uparrow\downarrow}$. For a completely filled chain (i.e. in the Mott-Insulator state with one particle per site) a double occupancy is energetically forbidden and hopping process can occur only via second order processes. Specifically, for $|U_{\uparrow\downarrow}| \gg |J|$, the hopping term behaves as a perturbation, and an effective Hamiltonian can be obtained via a second order degenerate perturbation theory [132]. The swap operation is generated with amplitude probability

$$\langle\uparrow,\downarrow|H_{\text{eff}}|\downarrow,\uparrow\rangle \simeq \langle\uparrow,\downarrow|(H_U+T)|\downarrow,\uparrow\rangle + \sum_{|m\rangle\notin\mathscr{H}_p} \frac{\langle\uparrow,\downarrow|T|m\rangle\langle m|T|\downarrow,\uparrow\rangle}{-U_{\uparrow\downarrow}} = -\frac{2J^2}{U_{\uparrow\downarrow}} \tag{1.94}$$

where H_U contains the onsite interaction terms and T is the hopping term in Eq. (1.93). The origin of the factor $2J^2$ can be understood easily, as a swap operation is obtained following two possible paths [115]:

$$|\uparrow,\downarrow\rangle \xrightarrow{J} |\updownarrow,0\rangle \xrightarrow{J} |\downarrow,\uparrow\rangle \tag{1.95}$$

$$\xrightarrow{J} |0,\updownarrow\rangle \xrightarrow{J} |\downarrow,\uparrow\rangle \tag{1.96}$$

Therefore, a two-species Hubbard model (1.93) in the strong coupling regime is equivalent to a spin model with spin-exchange strength $J_{\text{ex}} = -2J^2/U_{\uparrow\downarrow}$ [131]. More in general, an effective low-energy Hamiltonian, for a strongly correlated many-body system, is computed through the Schrieffer-Wolff Transformation (SWT) [133, 134]. This is a canonical transformation[46] with general form

$$H_{\text{eff}} = e^{iS}He^{-iS} = H + [iS,H] + \frac{1}{2!}[iS,[iS,H]] + \ldots \equiv \sum_{m=0}^{+\infty}\frac{1}{m!}[iS,H]_m. \tag{1.97}$$

here S is a unitary operator, and we have used the Baker-Campbell-Hausdorff formula [135]. This means, the SWT is equivalent to a rotation in the Hilbert space, where S is built on the effective description of the system required. Specifically,

[46] By definition, canonical transformations preserve the hermiticity (Hamiltonians are transformed in Hamiltonians under the transformation).

once the Hamiltonian is written as

$$H = \left(\begin{array}{c|c} H_p & V \\ \hline V^\dagger & H_q \end{array}\right) \tag{1.98}$$

the unitary transformation, generated by S, is chosen so that the effective Hamiltonian has a block diagonal form

$$H_{\text{eff}} = \left(\begin{array}{c|c} H_{\text{eff},p} & 0 \\ \hline 0 & H_{\text{eff},q} \end{array}\right). \tag{1.99}$$

Generally H_{eff} and the generator of the transformation, S, are computed perturbatively. In the specific case of a strong coupled Bose-Hubbard model (1.93), the hopping term can be considered as a perturbation on the atom-atom interaction. Therefore, starting from a Mott-Insulator state, where $\langle n_{\uparrow j}\rangle + \langle n_{\downarrow j}\rangle \simeq 1$, to build S one imposes that states with more particles in the same site are not connected via first order hopping terms. Explicitly, we rewrite the Hamiltonian (1.93) as $H = H_0 + \lambda T = H_U + \lambda T$, where λ is a perturbation parameter, and we expand H_{eff} and S in power series, as shown in Appendix D. For the case of two species in a two wells system, previously considered, the explicit form of $S^{(1)}$ is found by imposing that the first order hoppings are zero $H^{(1)}_{\text{eff}} = 0$. The second order effective Hamiltonian, $H^{(2)}_{\text{eff}}$, is

$$H^{(2)}_{\text{eff},nm} = -\frac{1}{2}\sum_l T_{nl}T_{lm}\left(\frac{1}{E_n - E_l} + \frac{1}{E_m - E_l}\right), \tag{1.100}$$

where n,m indicates states in $\mathscr{H}_p$ and the sum is over states belonging to $\mathscr{H}_q$. As a concrete example for the two sites model considered before, for $\mu_{j,\sigma} = 0$, the second

order effective Hamiltonian is

$$H_{\text{eff}}^{(2)} = \begin{pmatrix} -\frac{J_\downarrow^2}{U_{\downarrow\downarrow}} & 0 & 0 & 0 \\ 0 & -\frac{J_\downarrow^2+J_\uparrow^2}{U_{\uparrow\downarrow}} & -\frac{2J_\downarrow J_\uparrow}{U_{\uparrow\downarrow}} & 0 \\ 0 & -\frac{2J_\downarrow J_\uparrow}{U_{\uparrow\downarrow}} & -\frac{J_\downarrow^2+J_\uparrow^2}{U_{\uparrow\downarrow}} & 0 \\ 0 & 0 & 0 & -\frac{J_\uparrow^2}{U_{\uparrow\uparrow}} \end{pmatrix} \tag{1.101}$$

Here the Hilbert space of the system is $\mathscr{H} = \{|\uparrow,\downarrow\rangle, |\downarrow,\uparrow\rangle, |\updownarrow,0\rangle, |0,\updownarrow\rangle\}$, and effective Hamiltonian (1.101) is written in the relevant Hilbert subspace $\mathscr{H}_p = \{|\uparrow,\downarrow\rangle, |\downarrow,\uparrow\rangle\}$. Finally, the Hamiltonian (1.101) is mapped to a spin model using the decomposition[47] in terms of Pauli matrices [123]:

$$H_{\text{eff}}^{(2)} = \sum_{i_1\ldots i_L} a_{i_1\ldots i_L} (\sigma_{i_1} \otimes \ldots \otimes \sigma_{i_L}) \tag{1.102}$$

where

$$a_{i_1\ldots i_L} = \frac{1}{2^L} \text{Tr}\left[(\sigma_{i_1} \otimes \ldots \otimes \sigma_{i_L}) H_{\text{eff}}^{(2)} \right] \tag{1.103}$$

In the general case of a L site Bose-Hubbard model (1.93), it has been proved in [31, 32, 136, 137], that the two-species Bose-Hubbard model (1.93), in the strongly interacting regime, is equivalent to the XXZ spin $1/2$ chain model (XXZ chain) model

$$\begin{aligned} H_{\text{XXZ}} &= J_\perp \sum_{j=1}^{L-1} \left(S_j^x S_{j+1}^x + S_j^y S_{j+1}^y \right) + J_z \sum_{j=1}^{L-1} S_j^z S_{j+1}^z - h \sum_{j=1}^{L} S_j^z = \\ &= -J_{\text{ex}} \sum_{j=1}^{L-1} \frac{1}{2} \left(S_j^+ S_{j+1}^- + S_j^- S_{j+1}^+ + \Delta S_j^z S_{j+1}^z \right) - h \sum_{j=1}^{L} S_j^z \end{aligned} \tag{1.104}$$

[47] Every linear operator A can be decomposed in terms of Pauli matrices as $A = \frac{1}{2}\text{Tr}[A]\mathbf{1} + \frac{1}{2}\sum_{j=1}^{3} \text{Tr}[A\sigma_j]\sigma_j$ [123].

where the parameters are

$$\begin{aligned} J_z &= 2\frac{J_\uparrow^2 + J_\downarrow^2}{U_{\uparrow\downarrow}} - \frac{4J_\uparrow^2}{U_\uparrow} - \frac{4J_\downarrow^2}{U_\downarrow} \\ J_\perp &= -4\frac{J_\uparrow J_\downarrow}{U_{\uparrow\downarrow}} \\ h &= 4\frac{J_\uparrow^2}{U_\uparrow} - 4\frac{J_\downarrow^2}{U_\downarrow} \end{aligned} \tag{1.105}$$

The above model has been experimentally realised in [32], where the parameters in Eq. (1.104) are $J_\uparrow = J_\downarrow = J$ and $U_{\uparrow\uparrow} \simeq U_{\downarrow\downarrow} \simeq U_{\uparrow\downarrow}$. Specifically, $U_{\uparrow\downarrow} = U_{\downarrow\downarrow} = 99.0\, a_0$, $U_{\uparrow\uparrow} = 100.4\ a_0$, then the anisotropy parameter is[48] $\Delta = 0.986$ and $J_{\text{ex}}/\hbar = 2\pi \times 8.6\ Hz$. The latter values is obtained from Eq. (1.104) and (1.76), setting a lattice depth of $V_0 = 11.03\ E_R$.

1.6 Quantum State Transfer

A pivotal step in developing quantum technologies is the ability to exchange quantum information between one place to another [7]. This requires the development of quantum networks to enable the transmission of a quantum state between physically separated sender/receiver parties. Quantum communication plays also an important role for quantum computation as the ability to transfer quantum states between arbitrary locations is needed to connect two quantum memory registers within the same quantum computer, or to connect two registers of two different quantum computers. Indeed, this kind of application requires both to transfer the state between two locations and to map it from/to the elements of the quantum register sending/receiving it [63]. In other words there must be an exchange between the carriers of the information and the quantum memory registers that store it. The nodes of a quantum network are typically separated from each other so quantum states may be transferred over long distance, hence photonic systems are usually exploited. On the contrary, when short distances are involved, and the mapping from mobile to static qubits is important, (i.e. for connecting two distinct quantum re-

[48] It can be shown using Eq. (1.105) that the value of Δ is independent from the lattice depth chosen.

gisters of the same quantum computer), there are more advantageous non-photonic alternatives.

One physical system that has drawn a considerable attention for short distance communication consists of a permanently coupled chain of quantum systems [62, 138]. Following a direct approach, a quantum state could be transferred from a location to another by a sequence of SWAP operations (isolating a pair of neighbouring sites with a dynamical control of the couplings). However, in a practical setup, this strategy requires an amount of external control that is too demanding in resources and prone to errors, when long distances are required. An alternative strategy that relies on the natural excitation dynamics, without the need of a dynamical control of the couplings, is to transfer the sender qubit state at large distance, via a dynamical site-to-site hopping mechanism. The most basic model consists of an open 1D XX chain, of length L, permanently connected with nearest-neighbours interaction. The chain endpoints represent the sender/receiver qubits, and the channel that transmits the information is made by bulk spins. The communication protocol consists of the following steps:

1. The system is prepared in the polarised state $|0_1,\ldots,0_L\rangle$ (e.g. all the spins point upwards).

2. The state to be transmitted $|\psi(t=t_0)\rangle = \alpha|0\rangle + \beta|1\rangle$ is encoded in the first spin of the chain, via a local rotation.

3. The spin state $|\phi(0)\rangle = |\psi\rangle \otimes |0_2,\ldots,0_L\rangle$ is transferred through the natural dynamics along the chain, via the unitary evolution $|\phi(t)\rangle = \exp(-iHt)\,|\phi(0)\rangle$.

4. The transfer time, t^*, defined as the time when the probability $P(t) = |\langle 0_1,\ldots,0_{L-1},\psi|\phi(t)\rangle|^2$ reaches the first maximum, corresponds to the time when the last qubit has to be measured.

Here we have indicated the qubit states as $|0\rangle \equiv |s=1/2, s_z=+1/2\rangle$ and $|0\rangle \equiv |s=1/2, s_z=-1/2\rangle$, and the system is described by a XX chain model, Eq. (1.92),

that we rewrite as

$$H = \sum_{j=1}^{L-1} \frac{J_j}{2} \left(S_j^- S_{j+1}^+ + S_j^+ S_{j+1}^- \right). \tag{1.106}$$

Here spin ladder operators have been introduced as $S_j^{\pm} = \left(S_j^x \pm i S_j^y \right)$, to show explicitly why the Hamiltonian Eq. (1.106) produces the transfer of a spin excitation along the chain. Indeed, the latter two terms correspond to a local spin swap (towards left or right) for a pair of spin up/down in neighbouring sites. Despite its simplicity, the main drawback to be tackled in the above transfer protocol is the dispersion effect [62, 63]. This will be discussed in the following sections.

The importance of using permanently coupled system for connecting two quantum registers is that they have a natural advantage, compared to photonic systems, to convert flying qubits that transfer the information in static qubits that store it. Bulk spins, used to convey the information along a channel, can have also an active role for quantum computation applications. Indeed, the channel couplings can be designed to transform the travelling wave-packets and eventually produce a transformation between the initial qubit in one register and a remote qubit in another one. Given the above, in a more general sense the quantum state transfer protocol, discussed in this section, can be thought as the ability of, starting from an initial state in one location $|\psi_0\rangle \equiv |\psi(t_0)\rangle$, to achieve a final state (generally in a different position than the initial one) $|\psi_f\rangle \equiv |\psi(t_f)\rangle$, after a dynamical evolution of a quantum system for a time $t = t_f - t_0$. In other words, we are interested in the ability of a quantum system to dynamically produce a specific transformation from $|\psi_0\rangle$ to $|\psi_f\rangle$, generally between far sites. In the next section we/ introduce a figure of merit to measure the quality of the process.

1.6.1 Transfer Fidelity

In the last section we have discussed how a quantum state can be transferred between two endpoints of a quantum wire, made of permanently coupled quantum systems. One important point is that physical systems usually employed to make the transmission channel are dispersive. This means that initially localised wave-packets spreads out during the dynamics due to a non-linear dispersion relation, namely

that the group velocity $v_g = \partial\omega_k/\partial k$ does not coincide[49] with the phase velocity $v_p = \omega_k/k$, where ω_k is the excitation spectrum [111]. We have shown it explicitly for the Bose-Hubbard model, in Sec. 1.3.5.1. A figure of merit to measure the efficiency of a transfer protocol for a given system is called *fidelity*, that is a measure of the probability of confusing two states in a single measurement [7]:

1. If $|\psi\rangle$ and $|\phi\rangle$ are pure states, respectively the system and the target state, the fidelity is $F(|\psi\rangle,|\phi\rangle) = |\langle\phi|\psi\rangle|^2$.

2. The fidelity between a pure and a mixed state is $F(|\psi\rangle,\rho) = \langle\psi|\rho|\psi\rangle$.

3. For two mixed states ρ and σ the fidelity is defined as $F(\sigma,\rho) = \mathrm{Tr}\,(\rho\sigma)$.

For the XX chain model, Eq. (1.106), with homogeneous couplings $J_j = J$, an expression of the transfer fidelity, averaged over all the possible pure input states, has been obtained explicitly in [62, 63]. An important key point is that, in a homogeneous coupling scheme, the quality of the communication of a state encoded in the first qubit of the chain decreases as a function of the length L of the chain. In other words, spin chains with homogeneous couplings behave as a low-quality transmission channel when long distances are involved [139]. In the following sections we show how this limitation can be overwhelmed via a suitable coupling profile design.

1.6.2 State Transfer in a Lattice Model for a Single Excitation

The faithful transmission of a quantum state from a location to another is an important feature for scalable quantum information processes, as it enables information exchange between two distant processors (or memory registers). In this regards, only perfect or nearly perfect state transfer is relevant [63]. For instance, one way to build a quantum gate between two distant location could be to first bring one qubit close to another to let them interact, via a state transfer protocol, then to take it back to the original location [45]. We consider the transfer of a single excitation from one end to the other in a 1D lattice model. Due to the conservation of the total number

[49] Physically, different Fourier transform components travel along the chain with a different velocity during the dynamics, modifying the shape of the initial wave-packet.

of excitations, the dynamics can be described in the single-particle sector, where the Hamiltonian can be recast as a hopping model

$$H = \frac{1}{2} \sum_{j,k=1}^{L} A_{jk} |j\rangle\langle k| \,, \tag{1.107}$$

where $|j\rangle \equiv |0\rangle^{\otimes j-1}|1\rangle|0\rangle^{N-j}$ and $A_{j,k}$ contains the hopping matrix elements and the local fields, accordingly to the specific model considered. For nearest-neighbour interaction in a 1D quantum wire, the latter has a tridiagonal structure

$$A = \begin{pmatrix} h_1 & J_1 & & & \\ J_1 & h_2 & J_2 & & \\ & J_2 & h_3 & & \\ & & & \ddots & J_{L-1} \\ & & & J_{L-1} & h_L \end{pmatrix} . \tag{1.108}$$

The structure of $A_{j,k}$ determines the transmission quality of the channel, and depends on the proprieties of the specific model considered. Several strategies can be employed to improve the transfer fidelity, which rely on an engineering of the matrix elements. As a rule of thumb, couplings configuration weaker in the ends and stronger in the bulk are crucial for enabling high-fidelity state transmission, regardless of specific details of the couplings [140].

1.6.3 Perfect State Transfer

An ideal transfer with a 100% fidelity, called Perfect State Transfer (PST), is not possible for homogeneous chains with more than three sites [141]. For longer chains, schemes based on pre-engineered non-homogeneous coupling profiles guarantee a high transfer quality. Although this topic is still an open research field, we mention some results that produce a PST for a single excitation in a 1D chain, based on a suitable tuning of all the couplings in the Hamiltonian (1.107) [141].

As a general point, for a PST in a 1D nearest-neighbour coupled system with open boundary conditions, one necessary requirement is the mirror-symmetry of the

couplings in the Hamiltonian (1.108) [141], namely

$$J_j^2 = J_{L-j}^2, \qquad h_j = h_{L+1-j}, \qquad \forall j \in \{1,\ldots,L\}. \tag{1.109}$$

Indeed, once set the mirror-symmetry condition[50], Eq. (1.109), the Hamiltonian (1.108) commutes with the mirror-symmetry operator [141]

$$S = \sum_{j=1}^{L} |j\rangle\langle L+1-j|. \tag{1.110}$$

The mirror-symmetry imposes some relations between the eigenvectors of the Hamiltonian [141, 142]. By taking the spectral decomposition of the Hamiltonian (1.108), with E_k and $|E_k\rangle$ respectively eigenvalues and eigenvectors, then the initial/final target states can be decomposed as

$$|1\rangle = \sum_{k=1}^{L} \alpha_k |E_k\rangle, \qquad |L\rangle = \sum_{k=1}^{L} \beta_k |E_k\rangle. \tag{1.111}$$

Since in a perfect transfer the target must be obtained via the time evolution as [143]

$$e^{-iAt_0}|1\rangle = e^{i\phi}|L\rangle\ , \tag{1.112}$$

for some phase ϕ and time t_0, then the condition

$$\forall k, \qquad e^{-iE_k t_0}\alpha_k = e^{i\phi}\beta_k, \tag{1.113}$$

must be fulfilled. Thus, $|\alpha_k|^2 = |\beta_k|^2$, and by taking the powers of A we find the condition

$$\langle 1|A^m|1\rangle = \sum_{k=1}^{L} E_k^m |\alpha_k|^2 = \langle L|A^m|L\rangle. \tag{1.114}$$

The mirror-symmetry coupling requirement, Eq. (1.109) , is obtained by taking successive powers of A: from $m=1$ one has $h_1 = h_L$; for $m=2$ one gets $h_1^2 + J_1^2 = h_3^2 + J_{L-1}^2$, which means $J_1 = J_{L-1}$, and so on for all the chain couplings. A

[50] This makes the Hamiltonian to be symmetric with respect to the skew-diagonal.

consequence is that a mirror symmetric system must be periodic if it allows perfect state transfer [143]. This means, that if exists a time t_0 and a phase ϕ for which an excitation is perfectly transferred to site 1 to L, namely

$$e^{-iAt_0}|1\rangle = e^{i\phi}|L\rangle \ , \tag{1.115}$$

then, because of symmetry of the system, by letting the system evolve for a time $2t_0$ one finds that the wave-packet is reconstructed in the first site

$$e^{-iA2t_0}|1\rangle = e^{-iAt_0}e^{i\phi}|L\rangle = e^{2i\phi}|1\rangle. \tag{1.116}$$

In other words, a perfect state transfer allows a perfect reconstruction of the wave-packet for even multiples of the transfer time t_0. A further requirement for having a perfect state transfer is that, given $A = OEO^T$ the spectral decomposition[51] of the Hamiltonian (1.108), the eigenvalue spectrum E_k satisfies the relation[52] [142]

$$e^{-iE_kt^*} = (-1)^k e^{i\alpha} \ , \tag{1.117}$$

where t^* is the transmission time and α is an unessential factor independent on k. By setting $\alpha = \pi$ one has

$$\begin{aligned} \langle n|e^{-iAt^*}|m\rangle &= -\sum_k O^*_{k,n}O_{k,m}(-1)^k = \sum_k O^*_{k,n}O_{k,m}(-1)^{k+1} \\ &= \sum_k O^*_{k,n}O_{k,L+1-m} = \delta_{n,L+1-m}. \end{aligned} \tag{1.118}$$

In the last equality we have used the propriety that mirror-symmetric tridiagonal matrices have symmetric or antisymmetric eigenvectors, Eq. (B.2), Appendix B. The latter formula means not only that the excitation is transferred from site 1 to m, but also that any excitation in site m is perfectly transferred to the mirror-symmetric site, $L-m+1$, at time t^*.

Here we present a scheme, which is an analytical solution of Eq. (1.117), to tune

[51] The matrix O has entries $O_{k,m}$ which are the l eigenvectors of A arranged in rows.
[52] It has been proved that this is a necessary and sufficient condition [142].

the hopping terms in Eq. (1.107) that guarantees PST for a single excitation [143]. By calling L the length of the chain, the choice of the coupling strengths

$$J_j^{\mathrm{PST}} = \frac{\pi J}{2L}\sqrt{j(L-j)}, \qquad h_j^{\mathrm{PST}} = 0, \tag{1.119}$$

in the Hamiltonian (1.108) realises a PST at time $t^* = L/J$.

1.6.4 Almost Perfect State Transfer

One of the shortcoming of PST schemes is that the necessity of tuning all the couplings of the chain is too demanding in resources and can be affected by noise. Indeed, random noise effects, due to environmental variables and errors in the ideal coupling tuning are detrimental for the transfer fidelity [140, 144, 145]. Moreover, the PST coupling profile in Eq. (1.119) depends on the chain length, and the coupling must be reconfigured when the transmission distances are varied, limiting the scalability of the system [139]. A more robust high quality state transfer with less resources has been achieved through the optimisation of few edge couplings, while the bulk is homogeneous (*minimal engineering schemes*).

As shown in Fig. 1.12, the simplest strategy to achieve an almost perfect transfer is to tune the first and the last chain couplings, (while the bulk is homogeneous) called Optimal State Transfer (OPT) [146, 147]. The physical mechanism that leads to an improvement of the transfer fidelity is that particle momenta are narrowed around the linear region of the excitation spectrum, allowing an almost dispersionless dynamics[53]. An added feature of the scheme [146, 147] is that it introduces an external mechanism to control particle momenta in the system. Indeed, if $\omega_k \sim v(k-k_0)$ is the linear part of the dispersion relation, where v is the group velocity, the effect of the optimal scheme is to peak, in k-space, a wave-packet initialised in one endpoint around k_0 with a width that depends on the value of the endpoint couplings [146]. Results comparable with perfect state transfer schemes, without the requirement of a fully engineered Hamiltonian, are obtained in a scheme called Double Optimal State Transfer (2OPT), Fig. 1.12, where the first two and the last

[53] This strategy is typically called *Ballistic State Transfer* [139].

two tunnelling couplings are tuned appropriately to maximise the fidelity [148]. The

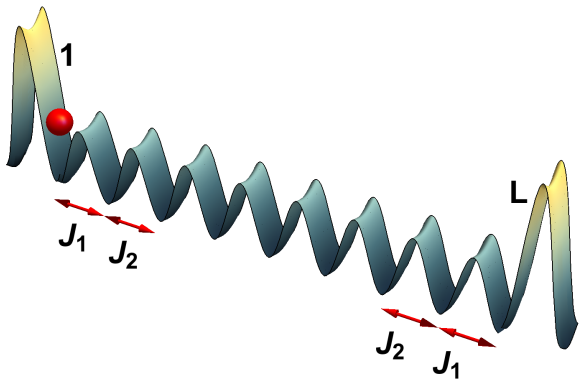

Figure 1.12: Optimal transfer schemes. A finite lattice model, with length L, where the strength of the hopping matrix elements in sites 1 and L are set to J_1 and in sites 2 and $L-1$ to J_2, while the remaining sites have have tunnelling rate J. We call J_0 the model with $J_2 = J$ and J_1 is optimised to get the maximum of the transfer fidelity, while in the $J_0 J_0$ both J_1 and J_2 are optimised.

transfer efficiency, at time t^*, for an end-to-end transfer of a single excitation in a chain of length L, is connected with the amplitude probability

$$\begin{aligned} |\langle 1|U(t^*)|L\rangle| \equiv U_{1L}(t^*) = \left| \sum_{k,k'=1}^{L} \langle 1|\varphi_k\rangle\langle\varphi_k|e^{-iAt^*}|\varphi_{k'}\rangle\langle\varphi_{k'}|L\rangle \right| = \\ = \left| \sum_{k=1}^{L} \varphi_1^{(k)*}\varphi_L^{(k)} e^{-i\omega_k t^*} \right| \equiv \left| \sum_{k=1}^{L} O_{k1}^* O_{kL} e^{-i\omega_k t^*} \right| = \left| \sum_{k=1}^{L} O_{k1}^2 e^{i\pi k} e^{-i\omega_k t^*} \right|, \end{aligned} \tag{1.120}$$

so that $|U_{1L}(t^*)| \simeq 1$ realises an almost perfect swap of the states in the boundary sites [139]. In the latter, A is a single particle mirror-symmetric Hamiltonian, Appendix B, ω_k is an eigenvalue, $|\varphi_k\rangle$ its eigenvector, and we have used the propriety (B.2). Eq. (1.120) shows that the possibility of realising an almost perfect state transfer on a 1D chain, depends both on the distribution of the momenta, O_{k1}, and on the eigenvalues ω_k. Indeed, if the distribution of modes O_{k1} is peaked in a linear region of the spectrum, $\omega_k \simeq vk$ [149], then by cutting the sum over the relevant modes, from the latter expression and Eq. (B.18) one finds that

$$|U_{1L}(t)| = \left| \sum_{k=1}^{L} \rho_k e^{ik\pi(1-t/t^*)} \right|, \qquad t^* \simeq (\pi/v)L, \tag{1.121}$$

where we called $\rho_k \equiv O_{k1}^2$. The latter means that, at time $t = t^*$, because of the normalisation $|\sum_k \rho_k| = 1$, a 100% fidelity transfer is achieved. In the next section we show how the couplings can be tuned, so that an almost perfect transfer is achieved.

1.6.4.1 Optimal State Transfer Model

One approach to optimise the state transfer fidelity is to use a uniformly coupled chain, with J as bulk strength and J_0 in the endpoints [139,146], called OPT scheme. As the single excitation Hamiltonian, Eq. (1.108), has a Quasi-Uniform Tridiagonal Matrix (QUTM) structure, then eigenvalues and eigenvectors can be computed with techniques in App. B. Specifically, for the model (1.64), with $\mu_j = 0$, the single particle Hamiltonian scaled for the bulk tunnelling strength J is

$$A^{(J_0)} = \begin{pmatrix} 0 & y & & & & & & \\ y & 0 & 1 & & & & & \\ & 1 & 0 & 1 & & & & \\ & & \ddots & \ddots & \ddots & & & \\ & & & 1 & 0 & 1 & & \\ & & & & 1 & 0 & y & \\ & & & & & y & 0 & \end{pmatrix}, \tag{1.122}$$

where and $y = J_0/J$, and the uniform block has size $L-2$. The eigenvalue problem can be solved in terms of phase shifts, as showed in Appendix B, where the explicit expression for the spectrum, $\omega_q = \cos q$, and the mode distribution $\rho(q) = O_{1q}^2$ have been found in [146, 150], namely

$$\omega_q = \cos q, \qquad \rho(q) = \frac{1}{L+1-2\phi_q'} \frac{\Delta(1+\Delta)}{\Delta^2 + \cot^2 q}. \tag{1.123}$$

The quasi-momenta q take discrete values q_n,

$$q_n = \frac{\pi n + 2\phi_{q_n}}{L+1}, \qquad n \in \{1, \ldots, L\} \tag{1.124}$$

$$\phi_q = q - \cot^{-1}\left(\frac{\cot q}{\Delta}\right) \in \left(-\frac{\pi}{2}, \frac{\pi}{2}\right), \qquad \Delta = \frac{(J_0/J)^2}{2-(J_0/J)^2}. \tag{1.125}$$

From Eq. (1.123) we observe that the mode distribution has a Lorentzian shape, centred around $q = \pm\pi/2$, whose width, Δ, decreases if the ratio J_0/J is lowered [139]. In other words, the quasi-momenta distribution is peaked around the linear region of the spectrum (i.e. $q \simeq \pi/2$), and a low value of J_0/J improves the end-to-end transfer fidelity for a single particle in a finite chain. However, when the end couplings are too weak, $J_0/J \ll 1$, the two edge sites are effectively decoupled from the rest of the chain making the transfer a resonant transmission mediated by one mode[54]. This in turn can be modelled via perturbation theory as an effective Hamiltonian and results in a non ballistic dynamics with a very long transmission time. In other words, a ballistic transfer needs more modes involved in the spectrum and a narrow quasi-momenta distribution around the linearity region [139]. Moreover, the dispersion relation is modified by low values of J_0/J, which influences the linear region where the ballistic transfer occur [139, 146]. The almost perfect transfer is then realised for an optimal choice of the edge coupling parameters, that can be found by maximising the amplitude probability, Eq. (1.120), as a function of J_0. Therefore, an almost perfect transfer happens physically due to a trade-off between the width of the mode distribution and the linearity zone of the spectrum, as showed in Eq. (1.121). From Eq. (1.125) it can be found that the group velocity around the linear region is [146],

$$\begin{aligned} \partial_n \omega_{q_n} = \sin q_n \; \partial_n q_n = \frac{\pi \sin q_n}{L+1-2\phi'_{q_n}} = \\ = \frac{\pi}{t^*}\left[1+\left(2\frac{1-\Delta^2}{t^*\Delta^3}-\frac{1}{2}\right)\cos^2 q_n + \mathscr{O}(\cos^4 q_n)\right], \end{aligned} \tag{1.126}$$

where $t^* = L+1+2(1-\Delta)/\Delta$ is the transfer time. A key point is that transfer time t^*, which has been evaluated in [146], is comparable with the one of a uniform chain, with corrections of the order of Δ, Eq. (1.125). For a finite chain, the edge coupling values that maximises the transfer fidelity are found numerically. In Tab. 1.1 we show the results for the optimal ratio J_0/J and for the transfer amplitude, which is always above the 84% even for very long chains. From Eq. (1.123), it is clear

[54] The decoupling effect between edge and bulk sites has been exploited for state transfer applications between edge topological states [151, 152], and using a strong near-to-the edge field [153].

that the spacing between the modes decreases and the number of modes increases for longer chain. Therefore, when $L \to \infty$, the sum over the modes in Eq. (1.120) can be replaced by an integral and using the Jacobi-Anger expansion, Eq. (B.35), asymptotic expressions can be found. Specifically, the optimal ballistic transfer is maximised with a choice of $J_0/J \propto L^{-1/6}$, for $L \gg 1$ [146], as reported in Tab. 1.1.

1.6.4.2 Double Optimal State Transfer Scheme

In the previous section we have showed that the end-to-end state transfer fidelity is improved with a lattice coupling design. As the fully engineering produces a unitary fidelity and a minimal engineering allows reaching an almost perfect transfer, it is natural to expect that when more and more couplings are tuned, leaving a uniform bulk, the efficiency must improve. The natural question is how many sites are needed to be engineered for achieving a certain threshold of fidelity with the minimal amount of resources. The optimisation of both the first two and the last two tunnelling couplings, as showed in [148] in a XX chain model, it is sufficient to generate a pretty good state transfer (this is called 2OPT model), as illustrated in Fig. 1.12. In the model (1.64), with $\mu_j = 0$, the single particle Hamiltonian, Eq. (1.108), has a QUTM form, as

$$A^{(J_0 J_0)} = \begin{pmatrix} 0 & x & & & & & & & \\ x & 0 & y & & & & & & \\ & y & 0 & 1 & & & & & \\ & & 1 & 0 & 1 & & & & \\ & & & \ddots & \ddots & \ddots & & & \\ & & & & 1 & 0 & 1 & & \\ & & & & & 1 & 0 & y & \\ & & & & & & y & 0 & x \\ & & & & & & & x & 0 \end{pmatrix}, \tag{1.127}$$

where $x = J_1/J$ and $y = J_2/J$, and using techniques in Appendix B, it can be proved that, with an appropriate tuning of the coupling parameters J_1 and J_2, an almost unitary transfer fidelity can be achieved [148]. The transfer time in the 2OPT scheme

has been evaluated in [148], and for large chains it scales as $t^* \simeq L+1+3.239L^{1/3}$. The optimal values of the coupling parameters, J_1/J and J_2/J, for the 2OPT scheme is reported in Tab. 1.1.

	2OPT			OPT	
L	$(J_1/J)^{\rm opt}$	$(J_2/J)^{\rm opt}$	$u^{\rm opt}$	$(J_0/J)^{\rm opt}$	$u^{\rm opt}$
51	0.4322	0.7338	0.99514	0.5542	0.9493
101	0.3584	0.6742	0.99395	0.4931	0.9324
251	0.276	0.5982	0.9929	0.4216	0.9127
501	0.2247	0.5439	0.99239	0.3742	0.9003
1001	0.1818	0.4923	0.99235	0.3322	0.8899
2501	0.1367	0.4300	0.99179	0.284	0.8791
5001	0.1097	0.3869	0.99167	0.2523	0.8726
10001	0.0878	0.3474	0.99159	0.2242	0.8674
25001	0.0652	0.3004	0.99153	0.192	0.8621
50001	0.05209	0.26925	0.99151	0.1708	0.859
100001	0.0415	0.24072	0.99149	0.1519	0.8565
$L \to \infty$	$1.954\, L^{-1/3}$	$1.662\, L^{-1/6}$	0.98715	$1.030\, L^{-1/6}$	0.8469

Table 1.1: Almost perfect state transfer. Comparison between the OPT and the 2OPT engineering schemes. L is the chain length, J_0 and J_1, J_2 indicated respectively the coupling strength for the OPT and for the 2OPT scheme, and $u^{\rm opt} \equiv |U_{1L}(t^*)|$. The last row indicates the asymptotic behaviour for large L. Data from [148].

1.7 Bound States in Lattice Models

The study of few excitations in lattice models provides unexpected phenomena that could be exploited for applications. Strongly interacting quantum systems in a periodical potential have peculiar features if they are sufficiently decoupled from the environment, namely the possibility to create composite objects, stable against the dissociation, when the interaction terms are larger than the hopping rate, in optical lattices and in the XXZ chain model.

In a Bose-Hubbard model, bound states are created when more than one particle are initially located in the same site and the atom-atom interaction is much larger than the hopping rate [154]. Bound states have their counterpart in an XXZ chain, for strong anisotropy parameter Δ in Eq. (1.104): starting from a fully polarised chain, a bound-magnon state consists of several spins flipped in adjacent sites [32].

The underlying physical reason for which the excitations are held together is that

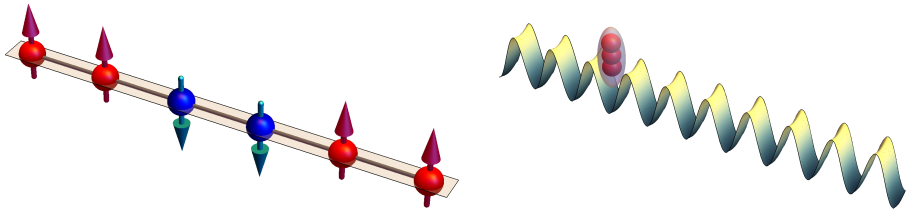

(a) (b)

Figure 1.13: Bound states in a lattice model. (a) Two adjacent spin down in a fully polarised chain in an XXZ chain with strong anisotropy. (b) Three particles in the same site in Bose-Hubbard model with strong onsite interaction.

an energy gap, between bound the free states, prevents the dissociation during the dynamics of the system [155–159].

For a Bose-Hubbard chain with two excitations, the energy spectrum has been evaluated[55] in [159]. There are two class of solutions: the first is the scattering solution (states with two particles in different sites belong to this band) which has energy

$$E^{(2)}_{K,k} = -4J\cos(Ka/2)\cos(ka). \tag{1.128}$$

Here K and k are respectively the centre of mass and the relative quasi-momenta, $K,k \in [-\pi/a, \pi/a]$ and a the lattice spacing. The minimum and the maximum energy, for fixed centre of mass quasi-momentum K, are respectively for relative quasi-momentum $k = 0$ and $k = \pi/a$. The bandwidth is $-4J \leq E^{(2)}_{K,k} \leq 4J$. The second class of solution corresponds to two particles bounded together in a dimer, whose spectrum is

$$E^{(2)}_{K,k} = \pm\sqrt{U^2 + 4\left(2J\cos(Ka/2)\right)^2}\,, \tag{1.129}$$

where the sign plus is for repulsive interaction, $U > 0$, and the minus for the attractive case, $U < 0$. A peculiar characteristic is that, even if the particle-particle interaction is repulsive, the particles constitute a dimer, due to an energy gap with the scattering state band[56]. This effect has been confirmed experimentally in [154].

[55] The time independent Shrödinger equation can be solved via the two-body centre of mass and relative coordinates description [159, 160].

[56] This effect depends on the absence of a dissipative environment in the system.

In Fig. 1.14 we show the complete energy spectrum for a two particle state in a Bose-Hubbard model with periodical boundary conditions, for $U/J = 5$ [159]. The band of states with two particles per site (bound pair) and the band of particles in different sites (scattering continuum) are clearly showed, as their energy separation for strong enough onsite interaction. Similar calculations have been performed for the spectrum of a three particles bound state [158].

1.7.1 Effective hopping of a Bound State in the Bose-Hubbard Model

An effective model for the dynamics of few bound particles can be derived from a perturbative expansion [132]. We firstly consider two particles, initially located in the left well of a two sites Bose-Hubbard model. Because of the energy gap, a simultaneous hopping of two particles to the right site required a hopping term of the form $(a_R^\dagger)^2(a_L)^2$, where L and R are respectively the left/right well. However, the Bose-Hubbard model (1.46) allows only hopping processes of single particles. Therefore, a simultaneous hopping of two particles is a second order process, namely $|2_L, 0_R\rangle \to |1_L, 1_R\rangle \to |0_L, 2_R\rangle$, where the occupation of the state $|1_L, 1_R\rangle$ is a virtual process, as it is forbidden by the energy gap. Bound state dynamics is described by an effective Hamiltonian where the effective hopping are computed via a second order degenerate perturbation theory[57] as [132]

$$J_{\text{eff}} = \frac{\langle 2_L, 0_R|H_J|1_L, 1_R\rangle\langle 1_L, 1_R|H_J|0_L, 2_R\rangle}{U} = \frac{J^2}{2U}, \tag{1.130}$$

where U is the onsite interaction strength and H_J is the hopping term in the Bose-Hubbard model (1.46). In other words, the bound state dynamics of two particles in a double-well system is equivalent to a single particle effective Hamiltonian, where the hopping terms depend both on the bare hopping rate J and on the onsite interaction strength U. Clearly, in the strongly interacting regime $U \gg J$, then $J_{\text{eff}} < J$ and consequently the propagation velocity of a bound state is slower than the cor-

[57] First order hopping are suppressed due to the energy gap, and we are neglecting constant terms that come out from the chemical potential term.

respondent single particle case, as showed in Fig. 1.5(b). Few efforts have been

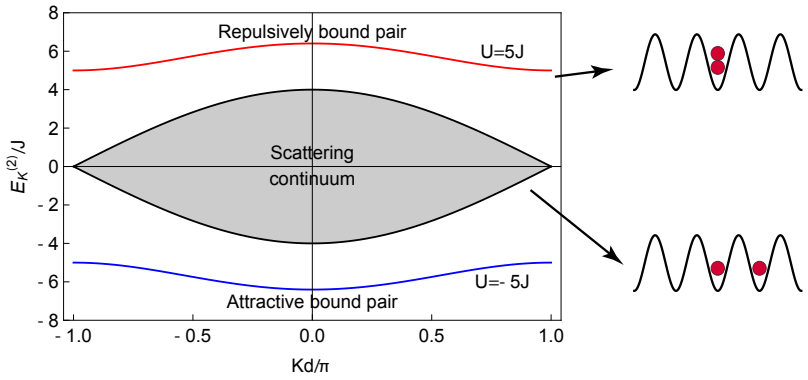

Figure 1.14: Bound state stability. Energy spectrum for a two particle state in a Bose-Hubbard mode with fixed centre of mass quasi-momentum, as a function of the relative momentum k. The red and the blue lines are the energy bands for a state with two particles in the same site, while the grey region belongs to states of two particles in different sites. Figure adapted from [159].

made in literature to go beyond the two particle description. We mention that the energy spectrum for a three particle bound state has been computed in [158], while the effective dynamics has been evaluated in [134], using a SWT transformation[58].

1.7.2 Edge-Localisation Effects

The possibility to use bound states in a lattice model is hindered by the possibility to engender and control the tunnelling dynamics. When few excitations are involved in a strongly interacting open lattice, well insulated from the environment, edge-locking effects appear close to the boundaries of the system. The edge-locking phenomenon must be tackled because it inhibits the tunnelling dynamics of bound states in a lattice and consequently limit their use for technological applications [161–163].

1.7.3 Edge-Localisation for the XXZ Chain Model

The edge-localisation effect in a XXZ chain model has been analysed in [161, 162]. In Fig. 1.15 we show some spin configurations that show edge-localisation effects. Specifically, when the anisotropy parameter Δ of the model (1.104) is much stronger than the hopping strength, robust edge states are built by initialising a spin flip in

[58] Although the SWT, as shown in Appendix D, can be used to compute the effective dynamics for more then two particles, it generally involves cumbersome calculations.

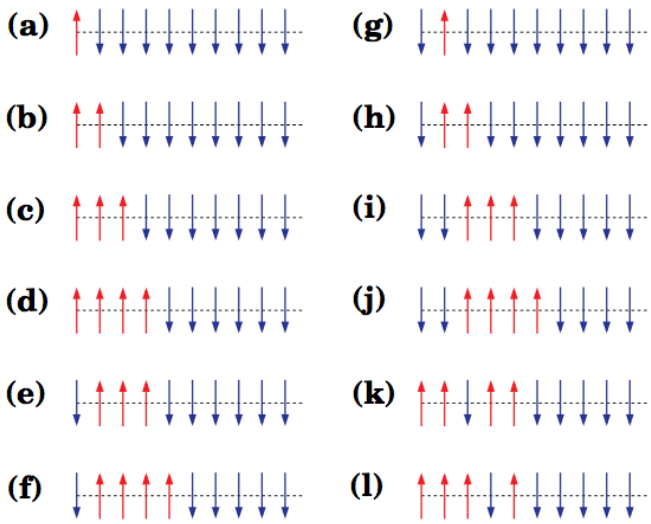

Figure 1.15: Edge-localised configuration in an XXZ open chain. The spin configuration (a-f) show localisation effects while (g-l) are not edge-localised. Figure from [162].

one edge of a fully polarised open chain. A second class of edge-localised states are block of flipped spins whose the leftmost spin is in the bulk of the chain. We represent with $|\Psi_{N_\uparrow,(k)}\rangle$ a spin configuration, where a block has $N_\uparrow$ adjacent spin flips while k is the site of the leftmost spin. It has been found in [162] that a spin block is a stable edge-locked state when $N_\uparrow \geq (2k-1)$. In Fig. 1.16 we show the excitation spectrum for three flipped spin inan open and a closed XXZ chain [162]. It is clear that the edge-localisation effect is due to the energy separation between the bands in the spectrum. For example, we consider two specific block configurations, respectively $|L_{N_\uparrow},(1)\rangle$ and $|R_{N_\uparrow},(1)\rangle$, where L and R indicates that k is the position of the leftmost/rightmost spin in the block from the left/right end of the chain. Because these two states have a single favourable aligned bond, they have higher energy than the other possible configurations in the chain and therefore they are edge-localised.

1.7.4 Edge-Localisation in the Bose-Hubbard Model

In the case of the Bose-Hubbard model, as shown in Fig.1.17, edge-localisation effects exists at the boundary sites for any number of particles greater than two. In other words, when three o more particles are initially located in the first or in the last

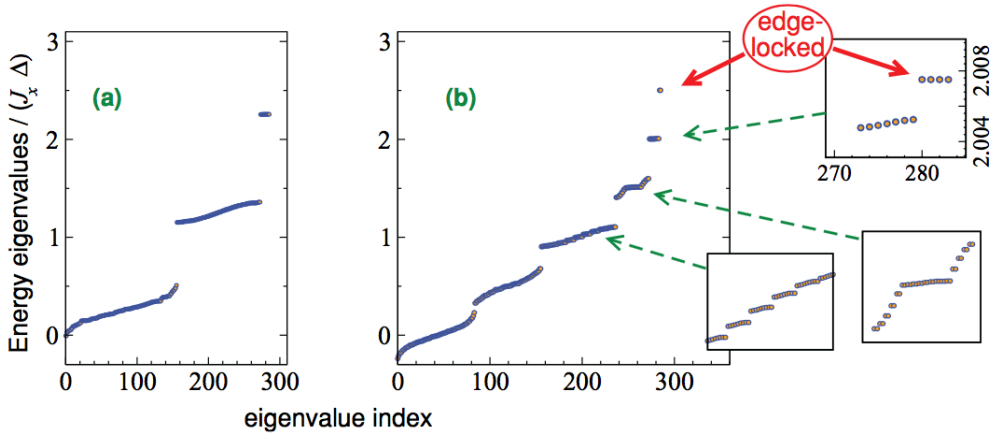

Figure 1.16: Localisation for an open XXZ spin chain. Energy spectrum for three excitation $N_\uparrow = 3$ for a periodical chain (a) and for an open chain (b). Here the chain length is $L = 13$ and the anisotropy parameter strength is $\Delta/J = 10$. Figure from [162].

site of the chain, the hopping dynamics is suppressed[59] [163]. The physical reason for the localisation effect can be found by analysing the excitation spectrum for a finite chain. As it appears clearly in Fig. 1.17 (b), the localisation effect is due to a pair of eigenvalues which are gap separated (blue arrow in the inset) from the energy band of three particles per site (red arrow). On the other side, for the case of a finite Bose-Hubbard with two particles, inset of Fig. 1.17 (a), the bound states show no energy gap and localisation effects do not occur[60]. Edge-localisation effects, due to an energy gap, characterise every state with $N \geq 3$ particles, initially located in one end of an open Hubbard model[61] [163].

1.8 Quantum Linear Optics

Quantum optics deals with phenomena that can be only explained by treating light as a stream of photons rather than an electromagnetic wave [76, 164]. Linear optical networks are indispensable tools for both fundamental investigations of quantum in-

[59] More precisely, as edge states are decoupled from the bulk sites, the transfer happens due to a direct resonant transition between resonant states, in a time scale hundreds to thousands of J^{-1} units [151, 163].

[60] Although a two particle bound state in a finite model is not localised, we will show later on in this Thesis that the delocalisation time from one edge point is affected by an effective edge field. We call this phenomenon *quasi-localisation effect*.

[61] We mention that with four or more bosons there are further configurations that are edge-localised (e.g. two bosons in the first site and two in the second) [163].

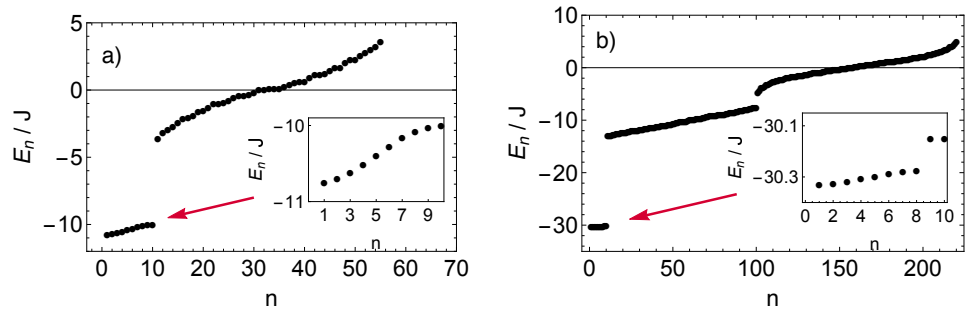

Figure 1.17: Edge-localisation for an open Bose-Hubbard chain. Energy spectrum for a ten-site Bose-Hubbard chain for (a) two particles and (b) three particles with $|U/J| = 5$. The red arrows shows the states respectively with (a) two bosons (b) three bosons in the same site. The blue arrow highlights the edge-localised states which are located in the edge points. Figure adapted form [163].

terference effects and for practical applications, as quantum computation and metrology [165,166]. The main elements that constitute these networks are beam splitters, mirrors and phase shifters. In this section we introduce the essential components of a linear optical device and we discuss methods to detect multi-particle interference effects.

1.8.1 Quantum Mechanical Formulation of the Beam Splitter Theory

A beam splitter is a device that generates a linear coupling of two incoming modes [8, 76], accordingly to the input-output relations

$$\begin{pmatrix} \hat{a}_3 \\ \hat{a}_4 \end{pmatrix} = \begin{pmatrix} \mathscr{R} & \mathscr{T} \\ \mathscr{T} & \mathscr{R} \end{pmatrix} \begin{pmatrix} \hat{a}_1 \\ \hat{a}_2 \end{pmatrix} = \begin{pmatrix} \cos\theta/2 & i\sin\theta/2 \\ i\sin\theta/2 & \cos\theta/2 \end{pmatrix} \begin{pmatrix} \hat{a}_1 \\ \hat{a}_2 \end{pmatrix} \tag{1.131}$$

where (1,2) and (3,4) label respectively the input/output arms. Here $\mathscr{R}$ and $\mathscr{T}$ are respectively reflection and transmission coefficients and θ is a parameter that control the weight of the superposition, known as *mixing angle*. Generally, beam splitters are used in conditions where they receive particles one by one. However, when more particles impinge on a beam splitter the output results from interference effects which depend on the particle statistics, accordingly to their commutation rules.

When a beam splitter receives groups of particles as input, described by Fock

states of bosons, the general expression for the probability to find m_1 and m_2 bosons in the detectors given N_α, N_β particles in the input arms, for a 50/50 beam splitter, has been evaluated in [167]. Specifically, given the initial state

$$|N_\alpha, N_\beta\rangle = \frac{1}{\sqrt{N_\alpha! N_\beta!}} \left(a_\alpha^\dagger\right)^{N_\alpha} \left(a_\beta^\dagger\right)^{N_\beta} |0\rangle, \tag{1.132}$$

the amplitude probability to find respectively m_1 and m_2 particles in the detectors 1 and 2 given N_α and N_β particles in the input arms is

$$C_{m_1,m_2}(N_\alpha, N_\beta) = \frac{1}{\sqrt{m_1! m_2! N_\alpha! N_\beta!}} \langle 0| a_1^{m_1} a_2^{m_2} \left(a_\alpha^\dagger\right)^{N_\alpha} \left(a_\beta^\dagger\right)^{N_\beta} |0\rangle, \tag{1.133}$$

and the probability is

$$P_{m_1,m_2}(N_\alpha, N_\beta) = \frac{m_1! m_2! N_\alpha! N_\beta!}{2^{N_\alpha+N_\beta}} \sum_{p=0}^{m_1} \frac{(-1)^p}{p!(m_1-p)!(N_\alpha-p)!(p+m_2-N_\alpha)!}\,. \tag{1.134}$$

When two bosons are incident on a balanced beam splitter ($\theta = \pi/2$) in Eq. (1.131), interference effects makes the probability amplitude of getting one photon in each mode equal to zero. Indeed, let us start from a configuration in which one particle is initialised in each input arm of the beam splitter, namely $|\psi(0)\rangle = |1,1\rangle$. the beam splitter transformation produces a different state, accordingly to particle statistics:

$$|\psi\rangle_b = \frac{1}{\sqrt{2}} \left(|2,0\rangle + |0,2\rangle\right), \qquad |\psi\rangle_f = |1,1\rangle, \tag{1.135}$$

where the subscripts b/f indicate respectively bosons and fermions. The absence of the term $|1,1\rangle$ for bosons, is a clear signature of a quantum effect, known as *Hong-Ou-Mandel effect* [168]. This is interesting because it allows generating a non-classical output state (namely a two particles NOON state [8]), using linear optics transformations. On the other hand, fermions, due to anti-commutation canonical rules, are characterised by anti-bunching effects, namely the absence of two particles in the same output arm. Bunching and anti-bunching effects can be experimentally detected via the two particle correlator, $\Gamma_{jk} = \langle \hat{a}_j^\dagger \hat{a}_k^\dagger \hat{a}_k \hat{a}_j \rangle$, between one

particle in the output arm j and the other in k [22, 60, 73, 169], or equivalently by analysing the correlation function $C_{jk} \equiv P_{jk} - P_j P_k$, where $P_j \equiv \sum_k P_{jk}$ takes into account of the distinguishable motion of atoms in the lattice [32]. Indeed, a positive value of the function C_{jj} means that the two particles has a higher joint probability to go both in the output arm j than the single particle probabilities (due to interference effects), while a zero value means that the two particle dynamics are completely uncorrelated. The two particle correlation functions $C_{jk}(t)$ can be defined on a lattice, (where it measures the correlation between a particle in site j and the other in k) and is completely identified via the amplitude probabilities $A_{jk}(t)$, by simulating the dynamics of two walkers in a lattice [33, 169–171]. Alternatively bunching and anti-bunching effects can be measured by analysing the quantity

$$\Delta n_3^2 = \langle n_3^2 \rangle - \langle n_3 \rangle^2, \tag{1.136}$$

where we have indicated with the index 3 one of the two of output arms of the beam splitter. Indeed, for the bosonic state in Eq. (1.135), this quantity reads

$$\langle n_3^2 \rangle = 2, \qquad \langle n_3 \rangle^2 = 1. \tag{1.137}$$

Therefore, for bosons/fermions one finds respectively $\Delta n_3^2 = 1$ and $\Delta n_3^2 = 0$. Finally, a phase shifter transformation is described by the operator

$$U_\phi \equiv \exp\left(i\phi \hat{N}\right), \tag{1.138}$$

where $\hat{N} \equiv a^\dagger a$ is the number operator [8].

1.9 Interferometry and Quantum Metrology

1.9.1 Mach-Zehnder Interferometer

A Mach-Zehnder interferometer, shown in Fig. 1.18(a), is a configuration of two balanced beam splitters and two mirrors. The incoming beam is split from the first beam splitter into two paths, which are then recombined in a second beam splitter.

Finally the two output modes are measured using a pair of detectors. The output results from the interference effects between the two paths (red and blue), which can be controlled via a phase shifter operation in one of the two arms. Specifically, when the scheme is used as a probe, the phase factor is the unknown quantity to be detected, which can be inferred by measuring the output modes of the system. The Mach-Zehnder transformation is then the combination of two balanced beam

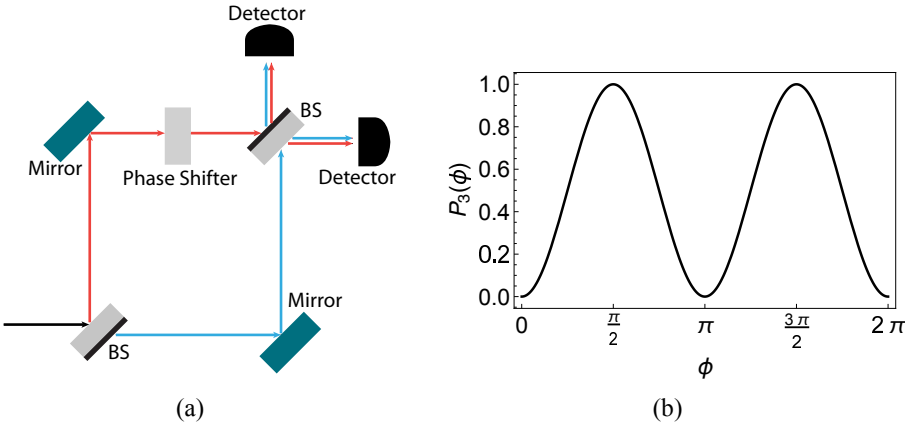

Figure 1.18: Scheme of a Mach-Zehnder interferometer. (a) Configuration of two balanced beam splitters (BS) and two mirrors. The incident beam (black) is split by a balanced beam splitter (BS) in two paths (red and blue) which are recombined, via two mirrors, in a second 50/50 beam splitter. A phase factor ϕ is introduced in the red path to modulate the interference effects. Finally two detectors measure the output modes of the system. (b) Probability to find a particle in the output mode 3 as a function of the phase factor ϕ introduced. The input state is a single particle in a Fock state (black line).

splitters and a phase shifter operation[62]. By calling respectively a_1, a_2 and a_3, a_4 the input/output annihilation operators, for a configuration of a single incoming particle in a Fock state, $|\psi_0\rangle = a_1^\dagger|0\rangle$, we have

$$\begin{aligned}\begin{pmatrix} a_1 \\ a_2 \end{pmatrix} &= \frac{1}{2}\begin{pmatrix} 1 & i \\ i & 1 \end{pmatrix}\begin{pmatrix} e^{i\phi} & 0 \\ 0 & 1 \end{pmatrix}\begin{pmatrix} 1 & i \\ i & 1 \end{pmatrix}\begin{pmatrix} a_3 \\ a_4 \end{pmatrix} = \\ &= \begin{pmatrix} \sin\phi/2 & \cos\phi/2 \\ \cos\phi/2 & -\sin\phi/2 \end{pmatrix}\begin{pmatrix} a_3 \\ a_4 \end{pmatrix}.\end{aligned} \tag{1.139}$$

[62] Mirrors introduce only an irrelevant global $e^{i\pi/2}$ phase factor.

Therefore, the Mach-Zehnder transformation produces the state

$$|\psi_f\rangle = \sin\phi/2|1,0\rangle + \cos\phi/2|0,1\rangle. \tag{1.140}$$

The output probabilities for a particle to emerge from one of the output arms, as a function of the phase factor, ϕ, are

$$P_3(\phi) = \sin^2\phi/2, \qquad P_4(\phi) = \cos^2\phi/2. \tag{1.141}$$

This results in an interference pattern as a function of ϕ, as shown in Fig. 1.18(b). From the measurement of the population of the outputs, the phase factor ϕ can be inferred. For N independent particles[63] the number of particles at the two output is given by a binomial distribution. Therefore, the joint probability that m and $N-m$ particles are detected in outputs 3 and 4 is [172]

$$P(m,N-m) = \binom{N}{m} P_3^m P_4^{N-m} = \binom{N}{m} \cos^{2m}\phi/2 \sin^{2(n-m)}\phi/2. \tag{1.142}$$

The mean number of particles detected at port 3 is $\langle n_3\rangle = N\cos^2\phi/2$ and the uncertainty in the measurement of ϕ can be found from the variance

$$(\Delta n_3)^2 = (\Delta n_3)^2 = N\sin^2\phi/2\cos^2\phi/2. \tag{1.143}$$

From the error-propagation [173], the uncertainty in the phase measurement ϕ is given by

$$(\Delta\phi)^2 = \frac{(\Delta n_3)^2}{(\partial_\phi\langle n_3\rangle)^2} = \frac{1}{N}. \tag{1.144}$$

The key point is that the phase estimation precision, using a Fock state $|N0\rangle_{12}$ as input state in the interferometer, scales with the number of independent measurement as,

$$\Delta\phi = 1/\sqrt{N}, \tag{1.145}$$

[63] We consider the particle-particle interaction to be zero, then a stream of N particles can be treated independently [172].

which is the so-called *shot-noise limit* [173].

1.9.2 Quantum Enhanced Metrology

It is interesting to compare the interference fringes generated from a Fock state with the ones obtained using a NOON state[64] as input. We suppose that a NOON state between the modes 1 and 2 is produced by a "magic beam splitter" [174], in the first stage of a Mach-Zehnder setup, Fig. 1.18, namely[65]

$$|\psi\rangle = \frac{1}{\sqrt{2}}\left(|N0\rangle_{12} + |0N\rangle_{12}\right). \tag{1.146}$$

Then a phase factor operation in one of the two modes, generates the state

$$|\psi_0\rangle = \frac{1}{\sqrt{2}}\left(e^{iN\phi}|N0\rangle_{1,2} + |0N\rangle_{1,2}\right). \tag{1.147}$$

because, from Eq. (1.138), the phase shifter operator produces a phase factor ϕN for a Fock state with N particles. The state after the second beam splitter is

$$|\psi_f\rangle = \frac{1}{\sqrt{2^{N-1}}}\sum_{m=0}^{N}\binom{N}{M}^{1/2}\cos\left[\frac{1}{2}\left(N\phi + \pi(m - n/2)\right)\right]|m, N-m\rangle\ , \tag{1.148}$$

which gives the phase estimation precision to follow [172]

$$P(\phi|m, N-m) \propto |\langle m, N-m|\psi\rangle|^2 \propto 1 + (-1)^m \cos\left[N(\phi - \pi/2)\right]\ . \tag{1.149}$$

In this case the interference fringes produced by the Mach-Zehnder transformation oscillate N times faster than the single particle case [172,177]. This results in a larger slope of the probabilities as a function of ϕ that, in turn, enables the estimation of the phase ϕ from the measurements with higher sensitivity [177]. This argument can be made more precise by introducing a quantity that gives an lower limit for the phase estimation precision, given an initial state of the system.

[64] This is also known as all-or-nothing states, namely in which all the particles are found after a measurement in one mode or in the other.

[65] This state cannot be produced just by linear optical transformations, but it requires non-linear components in the system [172, 174–176].

1.9.3 Estimation Theory - Quantum Fisher Information

It the last section we have discussed how the estimation precision for the parameter ϕ can be enhanced using more particles as input of the interferometer. However, as it not always possible to increase the number of resources to improve the precision, an optimal strategy could be to optimise the initial state and the phase read-out method. Once entangled states are introduced in the system as initial states (e.g. NOON), the read-out precision overcomes the classical one. However, given an initial state in the interferometer input, it is not clear a priori what is the best measurement and estimation strategy that yield to the optimal estimation precision [173]. The precision capabilities of a given state, that is independent from the read-out procedure, is characterised by a parameter called *Fisher information* F_Q. This is a measurement of the precision once the read-out method is optimised, (namely the theoretical best precision achievable) which allows one to choose what are the optimal states for interferometry applications.

In a typical scenario, an N-point data set $\mathbf{x} = \{x_1, \ldots, x_N\}$ of measurement outcomes is known. These are realisations of N identically distributed random variables X^N, accordingly to a common probability density function $p_\phi(X)$, that depends on an unknown parameter, ϕ, one wishes to determine. In other words, ϕ is a parameter which is not directly accessible in a measurement, and must be evaluated via an estimator, $\tilde{\phi}(\mathbf{x})$, built on a given data set of outcomes, that represents the function which outputs the most accurate value of the parameter ϕ, based on a given data set. In Estimation Theory, one approach is to consider ϕ as a deterministic value[66], (in principle its value could be stated to any precision) which is unknown [173]. The goal is to find the estimator $\tilde{\phi}(\mathbf{x})$ that minimises the variance with respect to the true value ϕ, thus that optimises the precision. To formalise the estimation problem: given $p_\phi(\mathbf{x}$ a family of probability density functions, parametrised by ϕ, the performance of an estimator $\tilde{\phi}(\mathbf{x})$ is given by the mean square error,

$$\Delta^2\tilde{\phi}(\mathbf{x}) = \langle\left(\tilde{\phi}(\mathbf{x}) - \phi\right)^2\rangle = \int d^N\mathbf{x}\; p_\phi(\mathbf{x})\left(\tilde{\phi}(\mathbf{x}) - \phi\right)^2. \tag{1.150}$$

[66] This is called *Fisher Information* approach [173].

A propriety of an unbiased estimator is that the average coincides with the true value,

$$\langle \tilde{\phi}(\mathbf{x}) \rangle = \int d^N\mathbf{x}\; p_\phi(\mathbf{x})\tilde{\phi}(\mathbf{x}) = \phi. \tag{1.151}$$

The goal of estimation theory is to look for the optimal estimator that minimises the error, Eq. (1.150). It has been proved that [173], for any unbiased estimator there is a threshold in the precision estimation, known as *Cramer-Rao bound*,

$$\Delta^2\tilde{\phi}(\mathbf{x}) \geq \frac{1}{MF\left[p_\phi\right]}, \tag{1.152}$$

where M is the number of measurements and $F\left[p_\phi\right]$ is the *Fisher Information*. From the latter is evident that higher values of the Fisher information gives a better estimation precision. An explicit formula for the classical Fisher Information is given in [173], namely

$$F[p_\phi] = \int dx\; p(x|\phi)\left(\frac{\partial \ln p(x|\phi)}{\partial\phi}\right)^2 = \int dx\; \frac{1}{p(x|\phi)}\left(\frac{\partial p(x|\phi)}{\partial\phi}\right)^2. \tag{1.153}$$

The Fisher information is non-negative and also additive for uncorrelated events, so that in particular for N uncorrelated measurements $F\left[p_\phi^N\right] = NF\left[p_\phi\right]$. An estimator that saturates the threshold (1.152) is called *efficient*, and it is also the optimal one. In a quantum scenario the parameter ϕ is encoded in a quantum state ρ_ϕ, and subjected to a quantum measurement[67] $M_\mathbf{x}$. The measurement result, $\mathbf{x}$, is then recorded with probability $p_\phi(\mathbf{x}) = \mathrm{Tr}\left(\rho_\phi M_\mathbf{x}\right)$. The quantum Cramer-Rao bound is a function of the Quantum Fisher Information (QFI), [173, 178],

$$\Delta^2\tilde{\phi}_N \geq \frac{1}{NF_Q[\rho_\phi]}, \qquad \text{where} \quad F_Q[\rho_\phi] = \mathrm{Tr}\left(\rho_\phi L[\rho_\phi]^2\right), \tag{1.154}$$

[67] This can be the standard projective measurement or a generalised measurement [123], as a positive operator valued measure (POVM) with the constraint $M_\mathbf{x} \geq 0$ and $\int M_\mathbf{x} = \mathbf{1}$, as the single particle read-out, in Eq. (1.89).

and $L[\rho_\phi]$ is the symmetric logarithmic derivative, defined by

$$\partial_\phi \rho_\phi = \frac{1}{2}\left(\rho_\phi L[\rho_\phi] + L[\rho_\phi]\rho_\phi\right). \tag{1.155}$$

Therefore, the QFI is determined only by the dependence of the state ρ_ϕ on the estimated parameter, namely the QFI quantifies the maximal precision with which a parameter can be estimated using a given quantum state ρ_ϕ. Explicitly, in the eigenbasis $\rho_\phi = \sum_j \lambda_j(\phi)|e_j(\phi)\rangle\langle e_j(\phi)|$, it is

$$L[\rho_\phi] = \sum_{i,j} \frac{2\langle e_i(\phi)|\partial_\phi \rho_\phi|e_j(\phi)\rangle}{\lambda_i(\phi)+\lambda_j(\phi)} |e_i(\phi)\rangle\langle e_j(\phi)|, \tag{1.156}$$

where the sum is over all the term with non-zero denominator. As in the classical case, the QFI is additive for product states, and it particular $F_Q[\rho_\phi^{\otimes N}] = NF_Q[\rho_\phi]$. For pure states $\rho_\phi = |\psi(\phi)\rangle\langle\psi(\phi)|$ the QFI simplifies to [178]

$$F_Q = 4\left[\langle\psi'(\phi)|\psi'(\phi)\rangle - |\langle\psi'(\phi)|\psi(\phi)\rangle|^2\right], \tag{1.157}$$

where $|\psi'(\phi)\rangle = \partial|\psi(\phi)\rangle/\partial\phi$. As an example we consider the NOON state, Eq. (1.147), for which we find

$$\langle\psi'(\phi)|\psi'(\phi)\rangle = \frac{1}{2}(N^2+1), \qquad \langle\psi'(\phi)|\psi(\phi)\rangle = \frac{1}{2}(-iN+1), \tag{1.158}$$

and finally $F_Q = N^2$. Therefore, NOON states saturate the Cramer-Rao bound as $\Delta\phi_{\min} = 1/N$. Compared to Eq. (1.145), it is clear that the phase estimation precision can be highly enhanced using entangled states as input in the interferometer. We compute explicitly the QFI in a Bose-Hubbard model (1.64), using Eq. (1.157) and the lower precision bound from $\Delta\phi_{\min} = 1/\sqrt{F_Q}$. We consider a system in the state $|\psi(0)\rangle$ and we add a phase factor in the last site, as $|\psi(\phi)\rangle = \exp(-i\hat{n}_L\phi)|\psi(0)\rangle$. From Eq. (1.157) we find

$$F_Q = 4\left(\Delta_L^2\right) = 4\left(\langle\psi(0)|n_L^2|\psi(0)\rangle - \langle\psi(0)|n_L|\psi(0)\rangle^2\right). \tag{1.159}$$

For the purposes of this thesis, it is relevant to consider as initial state, in a L site chain, a NOON state as $|\psi(0)\rangle = \frac{1}{\sqrt{2}}\left(|N\rangle|0\rangle^{\otimes L-1} + |0\rangle^{\otimes L-1}|N\rangle\right)$. From Eq. (1.159) we find that $\Delta\phi_{\text{min}} = 1/N$.

Chapter 2

Toolbox for linear optics in a 1D lattice via minimal control

2.1 Introduction

Tight-binding lattices offer a unique platform in which particles may be either static or mobile depending on the potential barrier between the sites [14].

In the last decade, advances in trapping techniques for ultra-cold gases, together with the introduction of spatial-light modulators [16–18,23–26,33,34,44,45,45,117, 129, 179] have opened up intriguing possibilities for quantum manipulation at the single atom level, opening up the control of interference effects and consequently new applications for quantum technology [27,32,57,180]. Although the impressive level of control achieved in experiments, what is still challenging is how to harness the natural many-body system dynamics in a many-site lattice for realising useful operations. Indeed, despite the unprecedented abilities to initialise and measure the position of individual atoms, dispersion effects limit the observability of interference phenomena [22, 60, 170]. Large lattices are indeed required for many applications, where the complexity dramatically increases for a number of sites much larger than the particle number in the system [165, 166, 181–183]. While single particle operations have been realised with microwave field and focussed lasers or with a two-photons Raman transition [15], many schemes have been proposed to implement quantum operations between two atoms, which rely on active transport of the

particles or on active reshaping of the lattice. For instance, quantum gates have been implemented with Rydberg atoms [47,48] and in double well systems [29,42], using a combination of suitably designed pulses and natural interactions, and with spin-dependent optical lattices [53, 54] using controlled collisions. Controlled interactions, via Feshbach pulses in optical lattices, have been proposed to perform operations between actively movable and static register atoms [39,45].

The recent atomic realisation of a controlled beam splitter in a double well potential [46] highlights the importance of atomic linear optics. Recently, it has also been shown that the wavefunction of a one-dimensional excitation can be split into a transmitted and reflected components by introducing localised impurities [184,185] or via suitably designed time dependent control fields [58]. One compelling question is whether a many-site lattice can be used for performing arbitrary linear-optics operations. At a first glance, the realisation of arbitrary operations seems improbable, as atoms in a multi-site lattice typically perform a "quantum walk" which is dispersive. As the particles quickly spread out between multiple modes, the observability even of basic linear-optics effects is reduced. In fact, such phenomena have not been observed unless particles are initially in nearest neighbours sites, or in the same site [22, 32, 46, 60, 170, 171]. On the other hand it is fruitless to hope that a high level of control can be easily acquired for large systems, making extremely difficult to build a device of practical value. Thereby an important question is whether minimally controlled systems [146,148] can be harnessed for quantum applications.

In this chapter we firstly show how arbitrary remote linear-optical operations can be implemented in a finite lattice, exploiting the natural dynamics of trapped neutral atoms. Secondly, we show how to the efficiency of our scheme can be improved by introducing a minimal engineering of the chain couplings.

Unlike other studies that simulate specific linear optical effects [46, 186], our aim is to convert 1D tight-binding lattices in quantum wires, for scalable and arbitrary linear-optical transformations between static atoms initially located in distant sites. Applications of our scheme range from quantum sensing [187], to linear-optical quantum computation [165] and quantum information [188], for instance as

an atomic boson-sampling device [166, 181]. Our scheme exploits the natural atom dynamics in a time-independent configuration, and therefore makes more straightforward its experimental realisation within the current technology.

2.2 Remote Linear Optics via a Quantum Walk in a 1D Lattice

We have mentioned, in Sec. 1.8, that beam-splitters, mirrors and phase shifters are the building blocks of linear optics networks. As a first step, we focus our attention on how a high efficiency tunable atom beam-splitter can be developed in a finite lattice model. Firstly we analyse the natural dynamical behaviour of few atoms in a lattice, for a small and large chain. The simplest model arises for a two wells system described by a Bose-Hubbard model, as, in the single particle subspace, Eq. (1.64) reduces to a linear coupling between two sites [189], namely

$$H_1 = -\frac{J}{2}\left(a_L a_R^\dagger + a_L^\dagger a_R\right). \tag{2.1}$$

A beam splitter transformation is easily generated by the natural dynamics of a single particle, due to the analogy of the Hamiltonian (2.1) with an ideal beam-splitter Hamiltonian, $H_{\rm BS} = \lambda\left(a_1 a_2^\dagger + a_1^\dagger a_2\right)$ [8]. Specifically, once the time-evolution operator is computed analytically[1]

$$U_2(t,0) = \exp\left(-iH_2 t\right) = \begin{pmatrix} \cos(Jt/2) & i\sin(Jt/2) \\ i\sin(Jt/2) & \cos(Jt/2) \end{pmatrix}, \tag{2.2}$$

for a single particle in the state $|\psi_0\rangle = a_1^\dagger|0\rangle$, an ideal $50/50$ beam splitter transformation, Eq. (1.131), is obtained at time $t^{II}_{\rm split} = \pi/2J$ [189]. For two non-interacting bosons, in the initial state $|\psi(0)\rangle = a_1^\dagger a_2^\dagger|0\rangle$, at time $t^{II}_{\rm split}$, the state of the system,

$$|\psi(t^{II}_{\rm split})\rangle = \frac{1}{\sqrt{2}}\left(|20\rangle + |02\rangle\right), \tag{2.3}$$

[1] Hereafter we set $\hbar \equiv 1$.

is a signature of the Hong-Ou-Mandel effect, Eq. (1.135). This has been observed experimentally for a system of two merged optical tweezers [46]. It is tempting to extend the model to a multi-site lattice, to generate a beam-splitting operation between remote sites. However, in the case of three sites, for the initial state $|\psi_0\rangle = a_1^\dagger a_3^\dagger |0\rangle$ it can been shown (e.g. [189]), that the state of the system at time $t_{\text{split}}^{III} = \pi/\sqrt{2}J$ is

$$|\psi(t_{\text{split}}^{III})\rangle = -\frac{1}{\sqrt{8}}|200\rangle - \frac{1}{\sqrt{2}}|020\rangle - \frac{1}{\sqrt{8}}|002\rangle + \frac{1}{2}|101\rangle. \tag{2.4}$$

This means that an ideal Hong-Ou-Mandel effect, $|\psi_{\text{HOM}}\rangle \propto (|200\rangle + |002\rangle)$, cannot be generated with high efficiency just using the natural particle dynamics in a lattice for a chain longer than two wells. In other words, a multi-site lattice requires a new approach for implementing linear-optics transformations between remote sites.

2.2.1 Linear-Optics via Barrier Scattering

We firstly consider an odd length chain, (where $L = 2N+1$) described by a homogeneous Bose-Hubbard model (1.64), with $J_j = J$. We also add a local potential, in site $N+1$, which gives rise to an impurity in the chemical potential,

$$\mu_j = \mu + J\beta\,\delta_{j,N+1}, \qquad j \in \{1,\dots,L\} \tag{2.5}$$

as shown in Fig. 2.1a. Once the particle number is fixed, the constant term μ only produces an irrelevant global phase, while the potential barrier, β, favours the splitting of an incoming single particle wave-function into a transmitted and a reflected component. Our aim is to analyse whether the barrier, with a suitable choice of β, can be exploited to resemble an ideal beam-splitter transformation (1.131) in a multi-site finite lattice model.

The advantages of our strategy are twofold: firstly, the introduction of a local field in the chain can be produced by a focussed laser, making the system within the experimental reaches with optical lattices (e.g. with a DMD device [32] or a focussed laser beam [15]); secondly, in the single particle subspace the Hamiltonian of the system has a QUTM structure, Appendix B, which makes possible to find

analytical expression for the splitting field. Moreover, we expect that the local impurity, Eq. (2.5), has a negligible effect on the transfer time, thus the splitting time for a single particle initially in one end of the lattice (the time in which the wavepacket reaches the lattice edges), has to be of the same order of magnitude of the natural transfer time of the chain ($t^* \simeq L/J$ for a homogeneous chain, as showed in Sec. 1.3.5.1).

To understand the transformation generated by the barrier, we set the initial position of the particle on site 1, and we define transmission and reflection coefficients (respectively T and R) as

$$T(t) = \langle 0|a_L e^{-itH} a_1^\dagger|0\rangle \tag{2.6}$$

$$R(t) = \langle 0|a_1 e^{-itH} a_1^\dagger|0\rangle, \tag{2.7}$$

which represent the amplitude probability that a single particle, initially in site 1, reaches site L for the transmitted component, and is reflected back in site 1 for the reflected component. Because of the symmetry of the system, the same coefficients describe the case of a particle initially in site L of the chain. These initial locations are chosen to force the particles to travel in a single direction, namely towards the optical impurity and ultimately towards the other end[2].

Via techniques for computing eigenvalues and eigenvectors of a QUTM matrix, Appendix B, we find analytical expressions for $T(t)$ and $R(t)$. Details of the calculations are reported in Appendix C. For the relevant values of β the coefficients $T(t)$ and/or $R(t)$ display their first maximum at the same time, t^*, which does not depend on β. Therefore, t^* coincides with the transmission time of the $\beta = 0$ case, with some finite-size corrections [149]. The important point is that an effective tunable beam splitter operator, $S(t^*)$, whose input/output ports are respectively site 1 and L,

[2]This is the natural initial configuration in an optical lattice as single particles are initialised in the Mott-Insulator state, where the hopping dynamics is frozen [15].

at time $t = 0$ and at time $t = t^*$, can be defined as

$$S(t^*) = \begin{pmatrix} R(t^*) & T(t^*) \\ T(t^*) & R(t^*) \end{pmatrix} \simeq D \begin{pmatrix} \frac{\beta}{i+\beta} & \frac{-i}{i+\beta} \\ \frac{-i}{i+\beta} & \frac{\beta}{i+\beta} \end{pmatrix} + \mathscr{O}(L^{-1}) \tag{2.8}$$

where the second equality holds for $L \gg 1$. In other words, the effective beam splitting operation in Eq. (2.8), is the product of a unitary matrix $\tilde{S} = S(t^*)/D$, and of a damping factor D. The latter is due to the non-linear dispersion relation of the model: as we consider a homogeneous chain, the wave function is not perfectly reconstructed at t^* (i.e. there is a non-zero probability to find the particle far from the endpoints). However, the factor $|D|$ can be made arbitrary close to 1 with a further engineering of the couplings that avoids wave-packet dispersion. This will be addressed in detail in the following sections.

Eq. (2.8) quantifies the ratio between the transmitted/reflected component. It is clear that for $\beta \to 0$ and for $\beta \to \infty$ respectively only the transmitted/reflected components are present. The key point is that $\beta \sim 1$ realises the condition for a balanced beam-splitter, namely where the reflected/transmitted components have the same amplitudes. For the Bose-Hubbard model (1.64), this means that a balanced beam splitter is obtained when the local impurity β have the same strength of the tunnelling rate J. As the condition $\beta = 1$ is valid for $L \gg 1$, in a finite chain, with size L, one expects to find finite-size corrections. In Fig.2.1b we show the reflection $R(t)$ and the transmission $T(t)$ coefficients as a function of the time, in the $50/50$ splitting regime, for a single particle initially in $|\psi_0\rangle = a_1^\dagger|0\rangle$. Deviations from the ideal value of $\beta^{50/50}$ has been obtained numerically[3], by imposing the condition, $|R(t^*)| = |T(t^*)|$, in a $L = 51$ homogeneous chain $J_j = J$. Starting from the initial state $\psi(0) = a_1^\dagger|0\rangle$ in Fig. 2.2a we analyse how the value of β for having a 50/50 splitting in a homogeneous chain (red points), differs from the analytical prediction $\beta = 1$, which holds for $L \gg 1$, (grey dashed line), as a function of the chain length

[3]The function $f(\beta) \equiv |R(t^*)| - |T(t^*)|$ varies monotonically with the value of β, and the balanced beam splitting condition can be found by solving numerically $f(\beta) = 0$. Once a value of β is set, using exact-diagonalisation techniques, Appendix A.1, we preliminary find t^*. However, we do not find any relevant changing to the transfer time as a function of β.

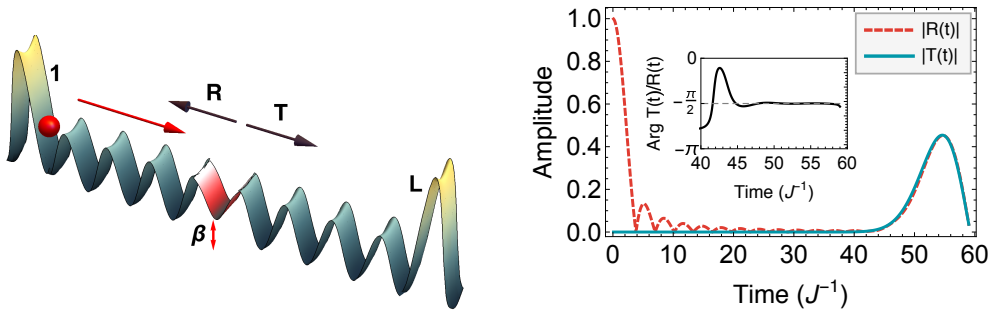

(a) (b)

Figure 2.1: Remote beam splitter in a quantum walk via single impurity scattering. (a) Scheme of the model: in a multi-site open lattice a single particle is initially in site 1. Through scattering across an optical impurity β, the wave-packet (red arrow) is split in a reflected R and transmitted component T. (b) Reflection and transmission coefficients for a single particle. Amplitudes $R(t)$ and $T(t)$ and relative phase (inset) as a function of time t, in units of the hopping rate J , for a uniform chain with size $L = 51$ and $\beta = \beta^{50/50} \simeq 0.95$ in the initial state $|\psi_0\rangle = a_1^\dagger|0\rangle$. The transfer time is $t^* \simeq 55J^{-1}$.

L.

We also evaluate the effect of the damping factor D, Fig. 2.2b, for a homogeneous chain (red points), via the output probability $P^{50/50} = |T(t^*)|^2$ as a function of the chain length L. As it appears clear, particle dispersion limits the observability of beam splitter effects for long chains. In the following section we analyse how an extra minimal engineering of the couplings can improve the efficiency of our scheme.

2.2.2 Efficiency improvement via engineered coupling schemes

In Sec. 1.6 we have discussed how the effect of the dispersion can be drastically reduced, for state transfer applications, tuning appropriately the tunnelling couplings of the lattice. However, a key point is that although a full coupling engineering brings the fidelity up to 100%, Sec. 1.6.3, it is in general too demanding in resources in comparison with the level of fidelity required for the implementation of most quantum technology tasks [140]. In fact, for many practical purposes, an almost perfect transfer via a minimal coupling engineering, Sec. 1.6.4, provides a high enough transfer efficiency without the need of a fine tuning of too many parameters.

In the previous sections we have shown that the splitting scheme, Eq. (2.8),

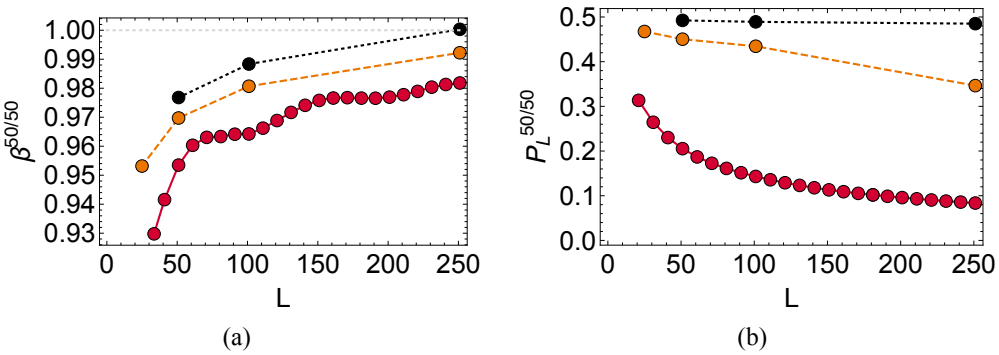

Figure 2.2: Single impurity beam splitter for an odd chain. (a) Optimal value of the impurity strength, $\beta^{50/50}$, which generates a balanced beam splitter operation, as function of the chain length L for (red line) homogeneous couplings, (orange dashed) using the J_0 coupling scheme, and (black dotted) for the J_0J_0 coupling scheme. (b) Output probability $P^{50/50} = |T(t^*)|^2$ as a function of the chain length L for $|\psi(0) = a_1^\dagger|0\rangle\rangle$, when $\beta = \beta^{50/50}$.

is affected by a damping factor D, related to the dispersion proprieties of the chain. Motivated by the pursuit of minimal control strategies, in this section we consider how to minimal engineering schemes can improve our model. Specifically, we take into consideration strategies based respectively on the control of the first and the last tunnelling couplings, Sec. 1.6.4.1, and on the control of the first two and last two couplings, Sec. 1.6.4.2. As these engineering schemes require at most to tune few edge couplings, we expect that no relevant modification should appear for the optimal splitting field strength $\beta^{50/50}$ find for a homogeneous chain[4]. In Fig. 2.2 we study as a function of the chain length L both the value of β that fulfils the $50/50$ condition and the output efficiency $P^{50/50} = |T(t^*)|^2$, whose deviation from the ideal case ($P^{50/50} = 1/2$) is due to damping factor D. We observe that, for fixed L, the impurity strength β for optimal coupling schemes (orange and black points) is much closer to the asymptotic value $\beta^{50/50} = 1$, compared to the uniform case. Moreover, from the analysis of $P^{50/50}$, we observe that the optimal coupling schemes, in particularly the 2OPT scheme (black points), Sec. 1.6.4.2, offer a remarkable improvement compared to the homogeneous case, enabling one to obtain

[4]It is clear that the same situation cannot be valid whether all the chain is engineered. Indeed, for a 100% fidelity, one expects to need an optimised field profile close to the splitting region. This specific case will be treated in details in the following chapter.

an almost ideal beam splitting device. This is of fundamental importance for technological applications.

2.2.3 Even Chain

In the previous section we have analysed chains with an odd number of sites. For an even chain length the splitting strategy is still valid, where the impurity has to be introduced in the tunnelling coupling profile (i.e. for a homogeneous chain with an impurity in the middle hopping parameter, $J_j = J\eta\delta_{j,N}$). Indeed, as for the odd length case, the Hamiltonian in the single-particle sector is still a QUTM matrix, and the reflection and the transmission coefficients (2.7) depend on the impurity strength, $\eta = J'/J$, as shown explicitly in Appendix C. In this case the effective transformation achieved between the edge sites, $S(t^*)$, has the form

$$S(t^*) = \begin{pmatrix} R(t^*) & T(t^*) \\ T(t^*) & R(t^*) \end{pmatrix} \simeq D \begin{pmatrix} \frac{1-\eta^2}{1+\eta^2} & \frac{-2i\eta}{1+\eta^2} \\ \frac{-2i\eta}{1+\eta^2} & \frac{1-\eta^2}{1+\eta^2} \end{pmatrix} + \mathscr{O}(L^{-1}). \tag{2.9}$$

The balanced beam splitter condition is then fulfilled for $\eta = \eta^{50/50} = \sqrt{2}-1$. Deviations from this value, due to finite-size effects have been investigated in Fig. 2.3a, where the optimal value $\eta^{50/50}$ has been found through a numerical minimisation of the difference between the reflection and the transmission coefficients. The efficiency of the scheme, as a function of the chain length L, is shown in Fig. 2.3b, for a homogeneous chain (red points), and in an engineered chains respectively with the OPT scheme, Sec. 1.6.4.1, (orange points) and with the 2OPT scheme, Sec. 1.6.4.2 (black points). Qualitatively, the results obtained are comparable with those found for an odd length chain.

2.3 Interferometry via Quantum Walk on a 1D Lattice

The possibility to generate a high fidelity beam splitter operation between remote site opens up to interferometry applications. In fact, a Mach-Zehnder configuration, Sec. 1.9.1, can be implemented in a finite 1D lattice using boundary reflections

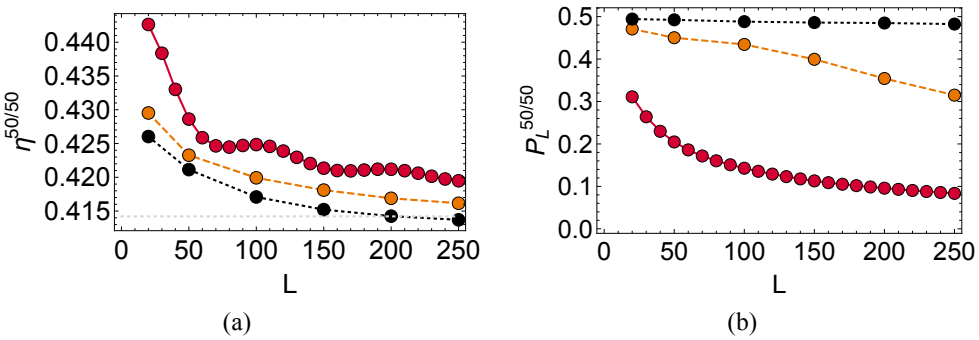

Figure 2.3: Single impurity beam splitter for an even chain. (a) Optimal value of η for the balanced beam splitting effect as function of the chain length for (red line) uniform coupling scheme, (orange dashed) optimal couplings, and (black dotted) double optimal couplings. The grey constant line represents the asymptotic value for $L \gg 1$, namely $\eta = \sqrt{2}-1$. (b) Output probability $P_L^{50/50} = |T(t^*)|^2$ as a function of the chain length L for $|\psi(t{=}0\rangle = a^\dagger|0\rangle$, when $\eta = \eta^{50/50}$.

to implement mirrors, while a phase factor, Eq. (1.138), can be introduced in the system freezing the hopping dynamics and tilting the lattice, so that the system acquires a phase due to the chemical potential. Alternatively, in view of experimental applications, to avoid introducing time-dependent procedures in our setup, it is more compelling to devise a scheme which minimises the dynamical control required on the chain. Specifically, we show that the combined action of a beam splitter and a controllable phase shifter can be achieved by applying a homogeneous optical potential, with non-zero values in the right half of the chain: in this case the profile of the chemical potential is

$$\begin{cases} \mu_j = J\gamma_R & \text{if } j > N+1, \\ \mu_j = J\beta^{50/50} & \text{if } j = N, \\ \mu_j = 0 & \text{otherwise}, \end{cases} \tag{2.10}$$

where $L = 2N+1$ is the chain length. Indeed, when $\gamma_R \neq 0$ a particle that travels in the right half of the chain acquires a phase factor $\phi \propto \gamma_R$. For the relevant values of the splitting field, we find that a balanced beam splitter operation is still obtained, even for $\gamma_R \neq 0$, with a choice of $\beta_{\gamma_R}^{50/50} \simeq \beta_{\gamma_R=0}^{50/50} \simeq 1$. As in the $\gamma_R = 0$ case, the scattering matrix can be approximately factorised as $S_\phi(t^*) \simeq D\tilde{S}_\phi(t^*)$, where D is

a damping factor and $\tilde{S}_\phi(t^*)$ is a unitary matrix, hence for $\beta = \beta_{\gamma_R}^{50/50}$ we find that the effective transformation between the lattice edge-sites is

$$\tilde{S}_\phi(t^*) \simeq \frac{1}{\sqrt{2}} \begin{pmatrix} 1 & -ie^{i\phi} \\ -ie^{i\phi} & e^{2i\phi} \end{pmatrix}, \tag{2.11}$$

where

$$\phi = \gamma_R t^*/\pi. \tag{2.12}$$

In other words the system made of a splitting field with an additional constant field in one half of the chain is equivalent to a beam splitter operation plus two phase shifter operations. Therefore, a Mach-Zehnder configuration is resembled by letting a particle, initially in $|\psi(0)\rangle = a_1^\dagger|0\rangle$, to travel twice along the chain, so that it meets two beam-splitter operations (namely the particle is let evolve for a time $t \simeq 2t^*$). We show that, by properly tuning the phase $\phi \propto \gamma_R$, one can vary the probability outcomes on the two output ports, as in a Mach-Zehnder interferometer, Eq. (1.139). Specifically, depending on the value of ϕ chosen, a particle travelling from site 1 reaches site 1 or L after a time $2t^*$. This is shown in Fig. 2.4, where we plot the local mean particle number, $\langle n_j(t)\rangle$, as a function of the position in the lattice j and the time t, (in unit of J) for the initial state $|\psi(0)\rangle = a_1^\dagger|0\rangle$. By tuning γ_R we obtain three different output results accordingly to the phase factor ϕ, Eq. (2.12), introduced in the system[5].

2.4 Long Distance Multi-Particle Interference Effects

The possibility of generating an effective beam splitter operation in a multi-site lattice, shown in the previous sections, opens up to observe multi-particle interference effects in long chains. Specifically, peculiar quantum statistical effects can be generated using two walkers, initially in opposite chain sites 1 and L to mimic the two input arms of a beam splitter, Eq. (1.131). For the Hamiltonian (1.64) with the

[5]The γ_R field is much weaker that $\beta^{50/50}$, then we find there are no relevant modification to the balanced splitting condition $\beta^{50/50} \simeq 1$.

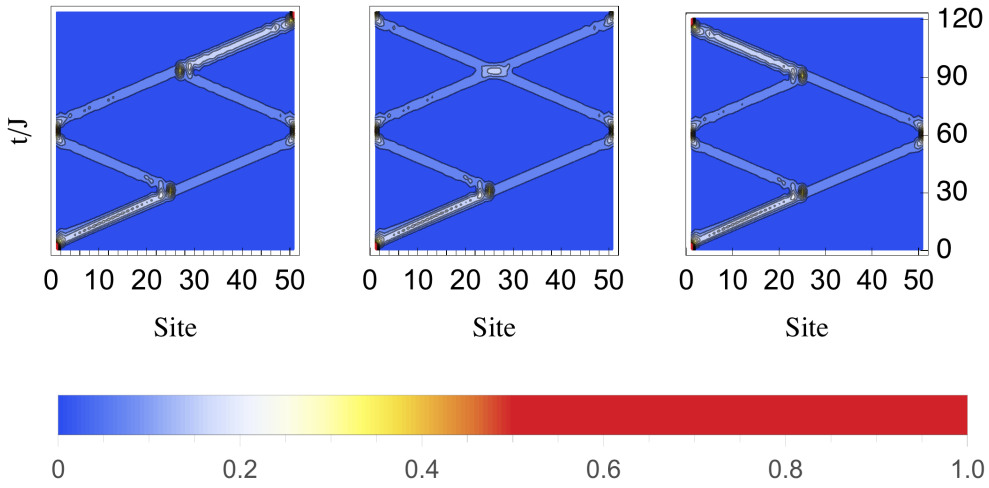

Figure 2.4: Effective Mach-Zehnder interferometer where $\beta = \beta^{50/50}$ and γ_R is tuned such that $\phi = 0$ (left),$\phi = \pi/4$ (centre), and $\phi = \pi/2$ (right). We plot $n_j(t)$ vs position j and time t/J, in a chain with $L = 51$. The first two and the last two couplings are engineered according to the 2OPT scheme, to reduce the wave-packet dispersion. An effective beam splitter operates twice in the middle of the chain, while an effective phase shifter appears due to a constant field applied on the right half of the chain.

splitting impurity, β, in Eq. (2.5), we expect to observe bunching effects for two non-interacting particles, $U = 0$, and anti-bunching effects in the hard-core boson limit $U \to \infty$. The optimal value of the impurity strength, β, that generates a $50/50$ splitting of an incoming wave-packet, from Eq. (2.8), is a propriety that holds for each particle in the lattice independently. Therefore, once set the impurity strength to optimal value $\beta^{50/50}$, we expect to be able to observe peculiar interference effects by letting two particles, in the initial state $|\psi(0)\rangle = a_1^\dagger a_L^\dagger |0\rangle$, to evolve in the lattice for a time $t^* \simeq L/J$.

It is important to underline that when $M > 1$ particles are initialised in the lattice, to determine the dynamics of the system, the Hamiltonian (1.64) must be projected in the Hilbert subspace of states with total number of particles M. In this case the Hamiltonian, which is still a sparse matrix, does not have a tridiagonal structure. This means that analytical methods, that we have exploited in the single particle case, Appendix C, cannot be used to design the Hamiltonian of interacting particles, for finite values of the interaction parameter, U, in Eq. (1.64). Indeed, it is

worth mention that coupling engineering schemes that optimise the transfer fidelity, Sec. 1.6, are designed in the single particle sector.

The effect of a finite atom-atom interaction, $U \neq 0$, affects the state transfer fidelity and consequently limits the efficiency of our scheme. Therefore, in order to evaluate the quality of the multi-particle interference generated, we numerically analyse the dynamics of a system of two walkers. A generic state of two particles in the lattice is described by [170, 171],

$$|\psi(t)\rangle = \sum_{jk} A_{jk}^{b/f}(t) a_j^\dagger a_k^\dagger |0\rangle, \tag{2.13}$$

where b/f indicate are the amplitude probability to find one particle in site j and the other one in site k, respectively for bosons $A_{jk}^b(t) = A_{jk}(t)/\sqrt{1+\delta_{jk}}$, and fermions $A_{jk}^f(t) = A_{jk}(t)$. The evolution of the amplitudes $A_{jk}(t)$ follow the Shrödinger equation as

$$i\partial_t A_{jk}(t) = \sum_{mn} K_{jk,mn} A_{mn}(t), \tag{2.14}$$

where $A_{jk}(0) = \delta_{j1}\delta_{kL}$ and $K_{jk,mn}$ is obtained from Eq. (1.64), via the algebra of commutation relations. We set $A_{jk} = 0$ for $j > k$ ($j \geq k$) for bosons (fermions). Details of the calculations[6] are shown in Appendix A.3.

To analyse quantitatively the interference effect produced, as discussed in Sec. 1.8, we compute the correlation function $C_{jk}(t) = P_{jk}(t) - P_j(t)P_k(t)$, where $P_j(t) = \sum_k P_{jk}(t)$ takes into account the distinguishable motion of the atoms in the lattice. This quantity is experimentally accessible in optical lattice implementations, using single-site addressing techniques[7] [22,32]. From the explicit expression of the effective beam splitter transformation, Eq. (2.8), one obtains the maximum bunching/antibunching effect with bosons/fermions, at time $t^* \simeq L/J$, when the impurity strength is tuned to produce a balanced splitting. As shown in Fig. 2.2 and 2.3, this value is influenced by finite-size effects. The value of $\beta = \beta^{50/50}$ is then found

[6] Here we highlight that, in the real space, the dynamics of two fermions is completely indistinguishable from the one of two hard-core bosons, as proved in Appendix A.3.

[7] The two particle joint probability, $P_{jk}(t)$, can be detected, avoiding the effect of the light-assisted collision, as discussed in Sec. 1.4.2. For instance, in [22], a pair of atoms in the same site are separated, with a magnetic gradient, prior to the detection.

numerically, in the single particle sector, prior to the study of the two particle correlation function. In Fig. 2.5 we plot the correlation function $C_{jk}(t')$ for two particles initially in $|\psi(0)\rangle = a_1^\dagger a_L^\dagger |0\rangle$ in a homogeneous chain with $L = 21$ at[8] time $t' = 18J^{-1}$ in a balanced beam splitter configuration, (here we find $\beta^{\rm opt} = 0.94$). As it appears

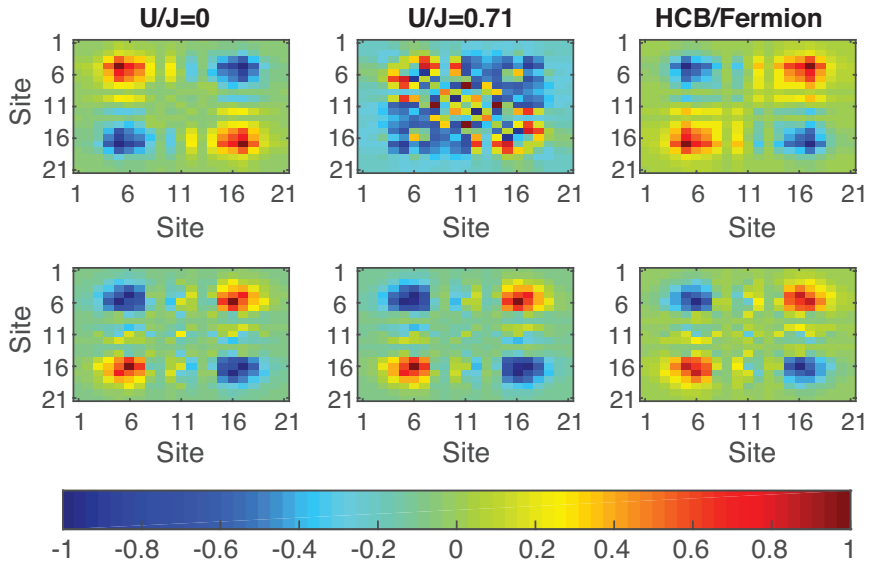

Figure 2.5: Bunching/Anti-bunching for two walkers in a lattice. (Top) Two-particle correlation function $C_{jk}(t') = P_{jk}(t') - P_j(t')P_k(t')$, at time $t' \simeq 18J^{-1}$, in a homogeneous chain with $L = 21$ with a local impurity in the central site with strength $\beta \simeq 0.94$. The plots are for (left) bosons, (right) fermions/hard-core bosons and for the intermediate regime (centre) $U/J = 0.71$. (Bottom) $C_{jk}(t')$ in absence of impurity, $\beta = 0$.

clear in Fig. 2.5(top row), bosons bunch while fermions and hard-core bosons anti-bunch. Although the effect is damped, as the chain is homogeneous, due to the dispersive transmission, (i.e. $|D| \neq 1$ in Eq. (2.9)) we clearly observe an increase of the probability to have two particles in the same side of the chain, for bosons, while fermions show a maximum of $C_{jk}(t')$ for particles in opposite sides.

An important point to address is whether bunching/antibunching effects can be generated, without the splitting impurity, $\beta = 0$, using a finite value of the onsite interaction U/J. We mention that bunching and antibunching effects have been observed in an optical lattice, for two particles initially in neighbouring sites [22]. On the other hand we find that when the particles are initially in distant sites no bunching

[8] Here we choose $t' < t^* \sim L/J$, to avoid boundary effects.

effect appears even when the on-site interaction U/J is different from zero. This is shown in Fig. 2.5(bottom row), where the correlation function $C_{jk}(t')$ between two particles initially in sites 1 and L is plotted for $\beta = 0$. A similar conclusion has been given in [60], where the dynamics of two particles initially separated by an empty site is analysed[9]. These results justify the importance of introducing an optical impurity to produce interference phenomena such as the Hong-Ou-Mandel effect when distant sites are involved.

In Fig. 2.5 the optimal bunching/antibunching effects are obtained for non-interacting walkers and in the strongly interacting regime. A finite value of the onsite interaction U reduces the probability of a double occupancy of two bosons in the same site. It is clear that a transition from boson to fermion behaviour is expected when U goes from 0 to ∞. Our results show that $P_{jk}(t^*)$ is almost indistinguishable from the fermion case when $U/J \gtrsim 10$. First of all we show that the value of β to obtain a balanced beam splitter is independent from the value of U chosen. For fixed U, t^* and $\beta^{50/50}$ are found numerically by maximising $P_{LL}(t,\beta)$ around $t \sim L/J$ and $\beta \sim 1$. As shown in Fig. 2.6 (inset), the observed optimal β for different U is approximately equal to the value $\beta^{50/50}$ obtained when $U = 0$. In fact, in the inset of Fig. 2.6 we plot the two-particle joint probability $P_{LL}(t^*)$ as a function of the impurity strength β, and it can be seen clearly that the β which maximises P_{LL} is almost independent on U.

To highlight the transition from bosons to hard-core bosons in Fig. 2.6 we plot the two-particle probability $P_{LL}(t^*, \beta^{opt})$ as a function of U, in a homogeneous chain, whose length is $L = 51$, normalised with respect to the $U = 0$ case. For $U \lesssim 0.1J$ the bunching effect is almost unaffected, while for $U \gtrsim 3J$ a power-law decay occurs and there is a rapid change of behaviour near $U \simeq J$. The threshold value U^c separating the two regions is obtained by fitting the data in the power-law region (red line) and taking the intersection value with a unit constant line (grey line). For $L = 51$ in particular we estimate $U^c \simeq 0.71J$. Although this could be a numerical

[9] An insightful explanation can be found analysing a two boson-boson scattering in a lattice. Explicit formulas are provided in Chap. 5, Eq. (5.5), where we show that the result of the collision produces an additional phase factor, but it does not generate a bunching effect.

coincidence, the value found for U^c is surprisingly similar to the critical value of the Mott-insulator transition at the boundaries of a 1D chain (coordination number $z = 1$) [190], raising interesting questions on the possibility to detect the Mott phase transition via specific features of the chain's non-equilibrium evolution. In view of

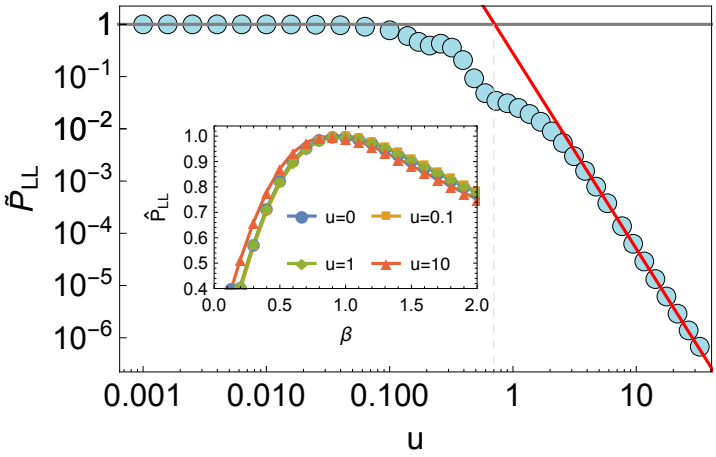

Figure 2.6: Transition from bunching to anti-bunching. Two-particle probability $\tilde{P}_{LL} = P_{LL}/P_{LL}^{U=0}$, in a uniform chain, to have two bosons in the last site as a function of $u = U/J$ for $\beta = \beta^{opt\cdot}$ and $t = t^*$, normalised with respect to the $U = 0$ case for $L = 51$. (Inset) $\hat{P}_{LL} = P_{LL}/\max_\beta P_{LL}$ as a function of β for fixed values of u ($L = 51$).

other possible applications we explore more in detail the weak interacting regime, analysing how the bunching effect is affected by the interaction. In this respect it is worth mentioning that the weakly interacting regime $U/J < 1$ has been realised in [22], but also that a non-interacting regime has been experimentally achieved with *Cs* atoms in a one-dimensional lattice, exploiting Feshbach resonances [71]. We evaluate the relative variation of the two-particle correlator $|\Delta P_{LL}|/P_{LL}(0)$, where $\Delta P_{LL} \equiv |P_{LL}(u) - P_{LL}(0)|$, as a function of the on-site interaction $u = U/J$ for a uniform chain with different chain lengths L. As it is shown in Fig. 2.7 the relative variation is lower than 5% in the range $0.06 < u < 0.1$, and the threshold depends on the chain length. We argue that this effect is due to the larger spatial extent of the two travelling wave-packets that, accordingly, interact for more time in longer chains.

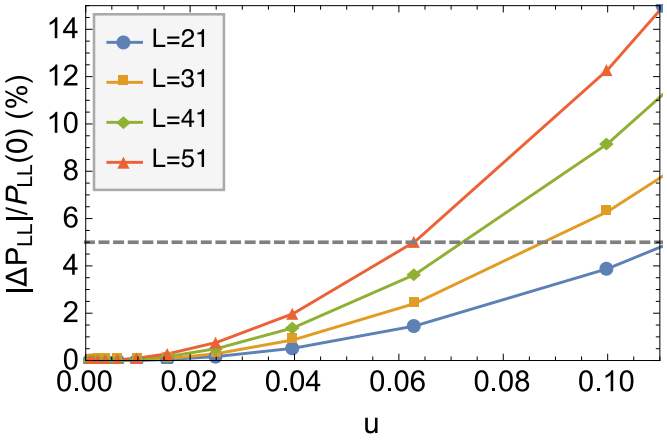

Figure 2.7: Weakly interacting regime analysis. Relative variation of the two-particle correlation $|\Delta P_{LL}|/P_{LL}(0)$ as a function of the on-site interaction $u = U/J$ in the weakly interacting regime $u < 1$ for a uniform chain with length L. The grey dashed line represents a deviation of 5% with respect to the free-bosons case.

2.5 Robustness to Decoherence Effects

Among the main features of optical lattice systems it is particularly relevant for quantum technological applications their degree of insulation from environmental effects. Optical lattices are made of neutral atoms, trapped by a detuned laser light, in a vacuum chamber. Therefore, due to the weak coupling with the environment, they are quite robust against decoherence processes, as discussed in Sec. 1.2.2. However, because we are interested in long chains, it is important to evaluate whether there are significant deviations to the optimal parameters in our scheme. The relevant quantities are the splitting fidelity $P_1(t^*)$ and the optimal field value $\beta^{50/50}$. In this section we take into account the effect of the dominant source of decoherence in optical lattices, namely decoherence induced by spontaneous emission effects. The dynamics of the system in the lowest band is described by a Master equation Eq. (1.72). To simulate the dynamics under spontaneous emission events we numerically solve Eq. (1.72), exploiting a vectorisation procedure, as shown in Appendix A, which converts the latter equation in the system

$$\mathrm{vec}(\dot{\rho}) = \mathscr{L}_v \mathrm{vec}(\rho) \tag{2.15}$$

where the operator $\mathscr{L}_v$ is defined as

$$\mathscr{L}_v = -i\left\{(\mathbf{1}_L \otimes H) - \left(H^t \otimes \mathbf{1}_L\right)\right\} - \Gamma \sum_j \left\{\left(n_j^t \otimes n_j\right) + \right. \tag{2.16}$$
$$\left. - \frac{1}{2}\left(\mathbf{1}_L \otimes n_j^2\right) - \frac{1}{2}\left((n_j^2)^t \otimes \mathbf{1}_L\right)\right\},$$

with Γ is the effective scattering rate, with the initial state $\rho(0) = |\psi(0)\rangle\langle\psi(0)|$ and $|\psi(0)\rangle = a_1^\dagger|0\rangle$. By minimising the difference between the reflection and the transmission coefficient we find the optimal value for having a balanced beam splitting operation $\beta^{50/50}$ and the fidelity of the operation $P^{50/50}$ as a function of the effective scattering rate Γ. The results, for a homogeneous chain, are shown in Fig. 2.8, for several chain length L. It appears clear that in the range $\Gamma/J \in \left[10^{-4} \div 10^{-2}\right]$,

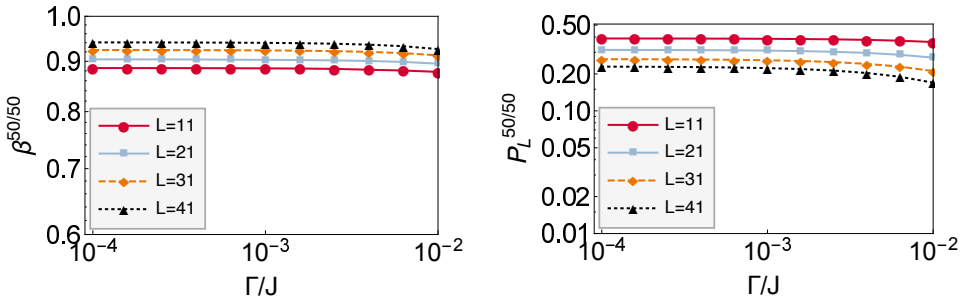

Figure 2.8: Decoherence effect in the splitting process. The system is initially in $\rho(0) = |\psi(0)\rangle\langle\psi(0)|$, where $|\psi(0)\rangle = a_1^\dagger|0\rangle$, and the decoherence strength Γ is plotted in units of J. Several chain length L are considered. (a) Variation of the impurity strength $\beta^{50/50}$ for producing a balanced beam splitting operation. (b) Splitting fidelity $P^{50/50}$ as a function of the decoherence strength.

which is typical in current experiments [191], no significative deviations are found compared to the unitary dynamics results.

2.5.1 Imperfections

In this section we discuss how possible imperfections could affect our theoretical results. As discussed in Sec. 1.3.4, we model the lattice curvature as an effective chemical potential,

$$\mu_j^{\text{eff}} = \mu - J\omega^2 j^2/2\,. \tag{2.17}$$

We consider deviations of the balanced splitting strength β, for a single particle in $|\psi(0)\rangle = a_1^\dagger|0\rangle$, by analysing[10] the probability to be in first/last lattice site, respectively $P_1(t^*) = |\langle 1|\psi(t^*)\rangle|^2$ and $P_L(t^*) = |\langle L|\psi(t^*)\rangle|^2$. In Fig. 2.9(a) we show the

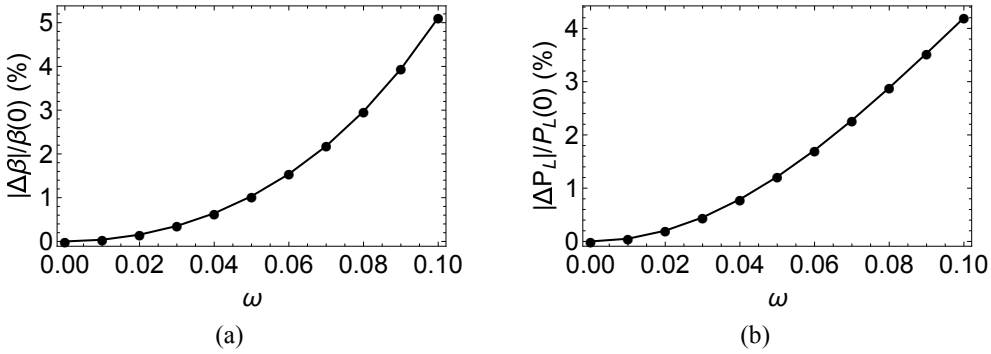

Figure 2.9: Lattice curvature effect. Relative variation of the optimal $|\Delta\beta|/\beta(0)$ and of the efficiency $|\Delta P_L|/P_L(0)$ as a function of the lattice curvature ω in Eq. (2.17). The lattice length is $L = 11$.

relative deviation of the splitting field strength as a function of the curvature, where $\Delta\beta \equiv |\beta(\omega) - \beta(0)|$. In Fig. 2.9(b) we show how the efficiency of the scheme $\Delta P_L \equiv |P_L(\omega) - P_L(0)|$ is affected by the lattice curvature. For realistic values in Sec. 1.3.4, with lattice curvature of $\omega_a/2\pi \simeq 10\ Hz$, lattice depth of $V_0 = 3E_R$ and lattice spacing $a = 532\ nm$, we find $\omega = \sqrt{m\omega_a^2 a^2/J} \simeq 0.03$. The parameters' deviation, compared to the ideal case is only of few percent, for a chain of $L = 11$ and a curvature of $\omega < 0.1$, Eq. (2.17). We consider a non-perfectly localised optical impurity, modelling it as a gaussian profile $\beta_j = \beta^{50/50}\exp[-(N+1-j)^2/\sigma^2]$. We analyse the deviation $\varepsilon = [|R(t^*)| - |T(t^*)|]/|R(t^*)| \simeq 0$. With a suitably optimised $\beta^{50/50}$, we observe small deviations ($\varepsilon \lesssim 5\%$) when[11] FWHM $\lesssim 8a$ in a chain with $L = 51$ sites.

2.6 Conclusions

In this chapter we have analysed a low control strategy to simulate arbitrary linear optics-like transformations between remote sites in a finite lattice setup. Compared to existing strategies [46, 58, 192], our scheme does not require an active trans-

[10] The optimal value of β is found from the zero of the function $f(\beta) = P_L(t^*) - P_1(t^*)$.
[11] For a gaussian function FWHM $= 2\sqrt{2\log 2}\sigma \simeq 2.35\sigma$.

port, or an active reshaping of the lattice with external potentials, as it exploits the natural atom hopping dynamics in a lattice. Specifically, we have shown that tunable optics-like operations between arbitrary remote sites are obtained by mixing quantum walks with suitably inserted local impurities in the lattice potential. In relation to recent experiments showing the Hong-Ou-Mandel effect in adjacent wells [46], or for particles initially located in neighbouring sites [22, 60, 170], our protocol opens up to scalable generalisations to many-site lattices.

We have considered several applications, namely how to build a balanced remote beam splitter, a Mach-Zehnder transformation and how to generate multi-particle interference effects (e.g. the Hong-Ou-Mandel effect), rather robust against the on-site atom interaction, showing the existence of a sudden dynamical transition from bosonic to a fermionised regime as a function of the inter-particle interaction. In relation to recent studies that simulate specific linear optical effects and that show basic linear-optics effects for particles initially in nearest neighbours sites, or in the same site, our protocol opens up to scalable applications in a many-site lattice.

In view of the recent experimental achievements in terms of initialisation and measurement with single site precision [18,25,34,45,117], our scheme has a natural realisation with ultra-cold atoms in optical lattices. Compared to purely photonic setups, this alternative arena for linear optics has the advantages of Fock state (e.g. single atom) preparation, naturally a very large number of modes (sites), and potentially a higher detection efficiency of single atoms in comparison to single photons.

We have analysed how the efficiency of our scheme can be enhanced via minimal engineering strategies, namely by tuning few edge tunnelling couplings, showing that an almost ideal transformation can be achieved even for long chains. Our proposal exploits the natural atom dynamics in a time-independent configuration, and therefore makes more straightforward its experimental realisation within the current technology. Our scheme as natural applications for interferometry and for the realisation of reconfigurable linear optics atomic networks. This in turn may pave the way for the study of interference effects in a many-boson optical lattice, such as the boson sampling.

In the next chapter we explore the possibility to design the lattice profile so that a perfect wave-packet splitting is generated, showing how to exploit it for applications.

Chapter 3

Perfect wave-packet splitting and reconstruction in a 1D lattice

3.1 Introduction

The quest for a quantum computer is boosting the development and engineering of new sophisticated quantum devices that allow us to observe the space-time evolution of its constituents. Indeed, in recent years several experimental groups successfully measured the quantum dynamical evolution of particles and/or quasiparticle hopping in a lattice [22, 32, 33, 69, 193]. In the previous chapter we have analysed the possibility to generate tunable linear optics transformations between remote sites of a finite lattice model, exploiting the quantum dynamical evolution of particles or quasiparticles, together with a local impurity in the chain couplings. We have also shown that the efficiency of the scheme is highly enhanced via a suitable tuning of few edge tunnelling couplings.

In Sec. 1.6.3 we have discussed how the lattice interactions can be designed so that a quantum state, initially in one end of the chain, is perfectly transferred to the opposite end. A lattice of localised particles represents an alternative paradigm for quantum communication where information carriers are not physically moving particles but rather collective excitations whose space extent is reconstructed at a different position after a certain time [63, 138]. In this respect spin chains, as discussed in Sec. 1.5.2 and 1.6, represent one of the most viable solutions and there are

various protocols to exploit their dynamics for transferring states and entanglement between remote sites [63, 138].

A natural question is whether it is possible to realise a perfect splitting operation (with 100% efficiency), by engineering a coupling profile in a lattice (or in a spin chain). This is important as perfect linear optics operations may have a strong impact for applications. First of all, maximally entangled states could be generated between remote locations. Furthermore, a sequence of several splitting operations produces splitting and revivals of an initial wave-packet, namely the shape of an initial state is periodically perfectly split and reconstructed. Aside from its fundamental implication, revivals could occur in a position different from the initial one, making the scheme attractive for ideal quantum transmission in a quantum network [63, 194, 195]. This is important as the possibility of combining local quantum processing with quantum transmission between the nodes of the network can be exploited for linking distant quantum registers[1]. Finally, it is known that quantum interference can give rise to particular structures and patterns in the space-time evolution $|\psi(x,t)|^2$, known as "quantum carpets" [196], quantum revivals [197], or quantum Talbot effect [198, 199], quantum walks [200–202], and quantum self-imaging [203]. In this chapter we focus on a strategy aiming at obtaining a perfect fractional revival in a 1D finite chain. Once generalised the idea of the fractional revival to a many-particle setting, multi-particle interference effects, such as perfect bunching or anti-bunching could be generated. On the other hand, in spin systems, we analyse how the perfect fractional revival can be used to dynamically generate long-distance entanglement. We show that our scheme can also be used in a multiple excitation scenario to dynamically generate a maximal set of Bell pairs in a spin-chain setup, and to provide a more general version of previous proposals [204, 205]. Finally, we analyse the robustness of our scheme under deviations from the couplings' ideal values.

[1]For instance an atom can be brought from a remote location to a site next to another, to realise a quantum gate and then moved back to the initial position, without requiring an active atomic transport, e.g. [45, 58].

3.2 Perfect Splitting with a Full Coupling Engineering

To design a profile of the couplings to generate a perfect splitting in a lattice model, we start considering a single excitation in a one dimensional lattice model, described by the Hamiltonian

$$H = \sum_{n=1}^{L-1} J_n \left(|n\rangle\langle n+1| + H.c \right) - \sum_{n=1}^{L} B_n |n\rangle\langle n| \ , \tag{3.1}$$

where J_n are the hopping elements and B_n are the local fields and $|n\rangle$ represents the state for a particle in the n site. As derived in Sec. 1.6.3, a perfect transfer of an excitation initially localised in site 1, to site L, requires some mathematical conditions on the chain coupling constants. Specifically, the Hamiltonian (3.1) must have mirror symmetric couplings,

$$J_{L-n} = J_n \ , \qquad B_{L+1-n} = B_n \ , \tag{3.2}$$

for any $1 \leq j \leq L$, where L is the length of the chain. To generate a perfect splitting, we impose a condition on the spectrum, namely that it exists a time t^*, where the eigenvalues of the Hamiltonian (3.1) satisfy

$$e^{-iE_k t^*} = \cos\theta + i(-1)^k \sin\theta, \tag{3.3}$$

for some angle θ. This is a sufficient condition for perfect splitting as

$$\begin{aligned} \langle n|e^{-iHt^*}|m\rangle &= \sum_{k,k'} \langle n|E_k\rangle\langle E_k|e^{-iHt^*}|E'_k\rangle\langle E'_k|m\rangle = \sum_k \langle n|E_k\rangle e^{-iE_k t^*}\langle E_k|m\rangle = \\ &= \sum_k \cos\theta O^*_{k,n} O_{k,m} + i\sin\theta O^*_{k,n} O_{k,m}(-1)^k = \cos\theta\,\delta_{n,m} + i\delta_{n,L+1-m}, \end{aligned} \tag{3.4}$$

which means that a wave-packet initially localised in site n is perfectly split between two mirror symmetric sites of the chain. For instance a single excitation in site n is

transformed at time t^* in

$$|n\rangle \to \cos\theta|n\rangle + i\sin\theta|L-m+1\rangle. \tag{3.5}$$

The key result, Eq. (3.3), shows that with a choice of the mixing angle $\theta = \pi/4$ it is possible to obtain a perfect balanced splitting of an initially localised wave-packet, between two mirror symmetric sites of the chain. A lattice profile that satisfies the splitting condition, Eq. (3.3), can be found via an inverse eigenvalue technique, namely finding the coupling values that generates a specific eigenvalue spectrum of the Hamiltonian (3.1). In other words, we call $E(\lambda)$ the ordered spectrum of the Hamiltonian (3.1) correspondent to a specific choice of the couplings $\lambda \equiv (J_1,\ldots,J_{L-1},B_1,\ldots,B_L)$ and the target spectrum, given in Eq. (3.3) is called $\tilde{E}$. The inverse eigenvalue method consists in finding the zeroes of the function $f(\lambda) = E(\lambda) - \tilde{E}$. Among the numerical methods the most used rely on the application of the Newton method. This algorithm starts with an initial guess $\lambda^{(0)}$ and updates it according to the rule [206, 207]

$$\mathscr{J}(\lambda_n)[\lambda^{(n+1)} - \lambda^{(n)}] = f(\lambda^{(n)}) \,, \tag{3.6}$$

where the matrix $\mathscr{J}$, with elements

$$\mathscr{J}_{mk}(\lambda^{(n)}) = \frac{\partial f_m(\lambda^{(n)})}{\partial \lambda_k^{(n)}} = \langle m|O(\lambda^{(n)})^T \frac{\partial H_p(\lambda^{(n)})}{\partial \lambda_k^{(n)}} O(\lambda^{(n)})|k\rangle \,, \tag{3.7}$$

is the Jacobian matrix and $H(\lambda)$=$O(\lambda)E(\lambda)O(\lambda)^T$ is the eigenvalue decomposition of $H(\lambda)$. The linear system (3.6) has a unique solution provided that $\mathscr{J}$ is an invertible matrix. This in turn implies that the number of parameters have to match the number of eigenvalues, namely the dimension of the matrix.

The mirror symmetric Hamiltonian Eq. (3.1) has L independent parameters (L being the number of sites). Indeed, because of the mirror symmetry, when $L = 2N$ (N being an integer) there are N independent values of J_n and N independent values of B_n. On the other hand, when $L = 2N+1$, there are N independent values of J_n and

$N+1$ independent values of B_n. We apply the inverse eigenvalue technique to find a coupling pattern which allows a perfect balanced splitting, imposing the condition (3.3) with $\theta=\pi/4$, so that the target eigenvalues are

$$\frac{L\tilde{E}}{J} = \left(\ldots, -\frac{\pi}{4}, \frac{\pi}{4}, -\frac{\pi}{4}+2\pi, \frac{\pi}{4}+2\pi, -\frac{\pi}{4}+4\pi, \ldots\right)^T , \tag{3.8}$$

where, without loss of generality, we have set $t^* = L/J$. Because $f(\lambda)$ has in general many local minima, it is possible that the Newton algorithm fails to converge to the right solution. However, it is well known that to avoid this issue the initial parameters $\lambda^{(0)}$ must be set not too far[2] from the solution $\tilde{\lambda}$ for which $E(\tilde{\lambda}) = \tilde{E}$ [206]. Motivated by the solution found in the chapter 2, where the splitting is implemented via a local perturbation in the middle of the chain, we expect that the profile of the couplings that generates a perfect wave-packet splitting, is given by a local perturbation of a fully engineered chain which guarantees a PST condition. For this reason we choose the profile in Eq. (1.119) as an initial guess $\lambda^{(0)}$ for initialising the inverse eigenvalue problem.

We find that the algorithm quickly converges to an optimal set of parameters J_n^{split} and B_n^{split}, respectively the tunnelling elements and the local fields. Surprisingly, we find that for even L the algorithm always converges to a solution where $B_n^{\text{split}} = 0$, while for odd L the local fields B_n^{split} are different from zeros, in particular near the centre of the chain. To check that the coupling profile result is not dependent from our guess, we have also considered an initial condition, $\lambda^{(0)}$, of randomly distributed parameters. In this case we find that the algorithm takes more time to converge, but it generates the same solution for the optimal coupling profile.

As a concrete example of our procedure, we show the Hamiltonian that generate a perfect balanced splitting for a chain of length $L = 5, 6$. These are respectively (in

[2] As only a finite number of iterations are possible, it is important that the successive approximations of the solution be close to the final result. How close depends on the computing resource available and on the accuracy required [207]. Moreover, for a function with local minima the algorithm could converge to an incorrect result if the initial guess is not close enough to the solution.

unit of J):

$$H_{L=5} = \begin{pmatrix} -0.08378 & 0.6195 & 0 & 0 & 0 \\ 0.6195 & -0.2932 & 0.6664 & 0 & 0 \\ 0 & 0.6664 & 0.7540 & 0.6664 & 0 \\ 0 & 0 & 0.6664 & -0.2932 & 0.6195 \\ 0 & 0 & 0 & 0.6195 & -0.08378 \end{pmatrix}$$

$$H_{L=6} = \begin{pmatrix} 0 & 0.5999 & 0 & 0 & 0 & 0 \\ 0.5999 & 0 & 0.8279 & 0 & 0 & 0 \\ 0 & 0.8279 & 0 & 0.3927 & 0 & 0 \\ 0 & 0 & 0.3927 & 0 & 0.8279 & 0 \\ 0 & 0 & 0 & 0.8279 & 0 & 0.5999 \\ 0 & 0 & 0 & 0 & 0.5999 & 0 \end{pmatrix}.$$

The coupling profile J_n^{split} and B_n^{split} which generates a perfect splitting in a chain with $L = 49$ and $L = 50$ is plotted respectively in Fig. 3.1(a) and 3.1(b) for a chain with $L = 49$ and $L = 50$. To highlight the differences, in Fig. 3.1, we also plot a PST profile, Eq. (1.119), called J_n^{PST}. It is clear from the picture that the splitting profile in an odd chain requires a non-local field tuning close to the centre on the chain, and a couple profile of the tunnelling elements which differs from the perfect state transfer profile, Eq. (1.119), in few sites in the middle of the chain. For the case of an even chain, the splitting profile does not to require a local field, but consists of a tunnelling profile engineering which differs from the PST scheme close to the centre of the chain.

3.3 Applications

3.3.1 Perfect Bunching and Anti-bunching and Quantum Carpets

In the previous section we have shown how a coupling profile can be engineered, in a finite lattice model, to produce a perfect splitting of a localised wave-packet

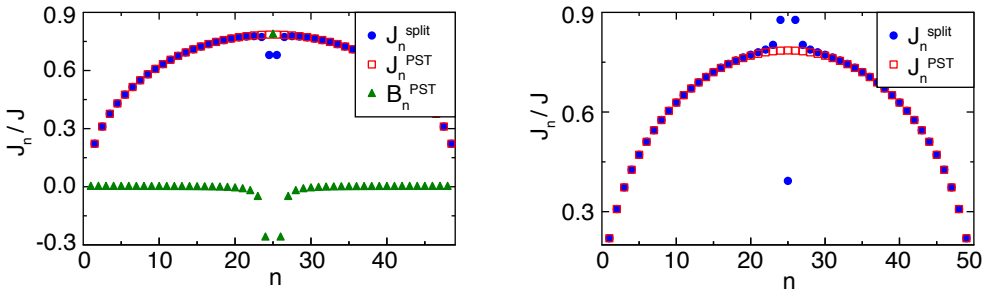

Figure 3.1: Perfect wave-packet splitting coupling profile. Values of the coupling parameters J_n^{split} and B_n^{split}, found from the inverse eigenvalue technique, which generates a perfect splitting between mirror symmetric sites, for an (a) odd chain with $L = 49$ and (b) for an even chain with $L = 50$. The perfect state transfer couplings, from Eq. (1.119), J_n^{PST} are also plotted for comparison.

between mirror-symmetric site of a finite lattice. In this section we show how, in a multi-particle setup, our scheme opens up to the generation of perfect interference effect. We consider a Bose-Hubbard model with site-dependent parameters,

$$H = -\sum_{n=1}^{L} J_n \left(a_n^{\dagger} a_{n+1} + H.c. \right) + \sum_{n=1}^{L} U_n n_n (n_n - 1) - \sum_{n=1}^{L} B_n n_n, \tag{3.9}$$

where J_n and B_n are set respectively to J_n^{split} and B_n^{split}, found in the previous section. The onsite interaction parameter $U_n = U$ (hereafter in units of J) can be tuned globally via Feshbach resonances[3]. We consider two atoms initially located in site n and m of a 1D lattice, described by the Hamiltonian (3.9). If the onsite interaction is set to zero, the configuration of the couplings, $J_n^{\text{split}}, B_n^{\text{split}}$, produces a perfect delocalisation of the two wave-packets in the mirror-symmetric sites of the chain, namely

$$|n\rangle \to |n\rangle + i|L-n+1\rangle, \tag{3.10}$$

$$|m\rangle \to |m\rangle + i|L-m+1\rangle, \tag{3.11}$$

[3]For our purposes it is important to underline that the onsite interaction can be controlled in a wide range. We also mention that a non-interacting regime $U = 0$ has been achieved using Cs atoms [71].

at the transfer time $t^* = L/J$. Therefore, in order to maximise the interference effects between the two carriers, we set n and m to be two mirror-symmetric sites of the lattice. Starting from the state $|\psi(0)\rangle = a_n^\dagger a_m^\dagger |0\rangle$ the system reaches, at time t^*, the state

$$|\psi_b\rangle = \frac{1}{\sqrt{2}} \left(|2\rangle_n |0\rangle_m + |0\rangle_n |2\rangle_m \right). \tag{3.12}$$

The absence of any term of the form $|1\rangle_n |1\rangle_m$ is a signature of the Hong-Ou-Mandel effect. Therefore, the perfect reconstruction of wave-packets at the transfer time leads to perfect bunching between arbitrary mirror-symmetric sites of an optical lattice. On the other hand, perfect anti-bunching, $|\psi(t^*)\rangle = |1\rangle_m |1\rangle_n$, can be observed in the strongly interacting regime, namely $U = \infty$, where the two particles behave as hard-core bosons.

Consecutive applications of our scheme produce alternatively a perfect splitting, at time $t = (2n+1)t^*$, followed then a reconstruction of the wave-packet at time $t = (2n)t^*$, being n an integer. This propriety can also be exploited to produce periodic space-time quantum interference patterns in a lattice, known as "Quantum Carpets". This effect is shown in Fig. 3.2, where we represent the time evolution of a system of two free bosons, in the initial state $|\psi(0)\rangle = a_{10}^\dagger a_{31}^\dagger |0\rangle$, in a chain with length $L = 40$. In Fig. 3.2 it can be clearly observed that the wave-packets, composing the initial state, are split into two copies, reconstructed into different positions after a time t, and then they go back to the initial position after a time $2t^*$, producing a periodical interference pattern. On the other hand, quantum interference effects, dependent on the particle statistics, happen during intermediate times, for the overlap of the wave-packets of the two walkers. We study the quantum carpets generated by the space-time evolution of the mean occupation number $\langle n_n(t) \rangle$ and of the square occupation mean $\langle n_n(t)^2 \rangle$ for a system of four particles in a $L = 14$ chain, in the initial state $|\psi(0)\rangle = a_2^\dagger a_6^\dagger a_9^\dagger a_{13}^\dagger |0\rangle$. We show the results obtained in Fig. 3.3, for (top) $\langle n_n(t) \rangle$ and (bottom) $\langle n_n^2(t) \rangle$. The left column represents free bosons, while the right one is for hard-core bosons/fermions walkers. As discussed in Sec. 1.8.1, clear bunching/anti-bunching effects are visible at t^* respectively for boson/hard-core bosons particles. Moreover, partial bunching effects for bosons are

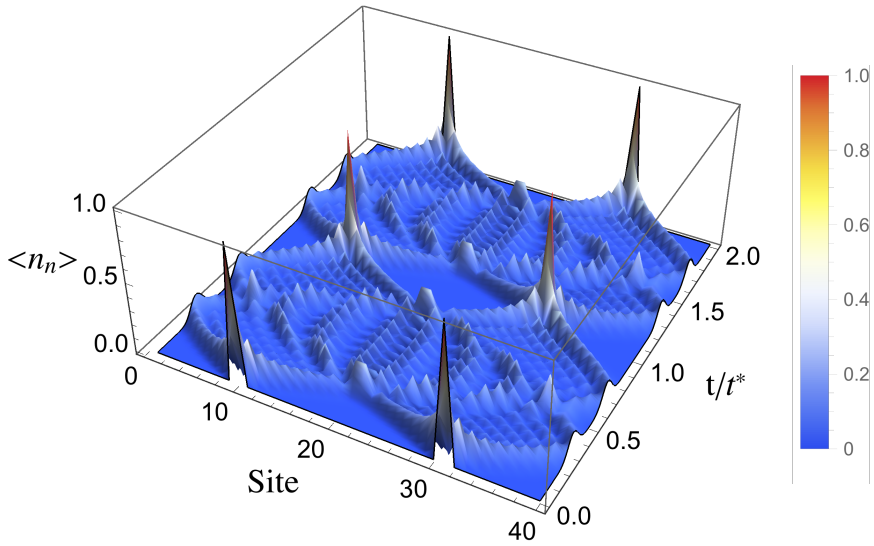

Figure 3.2: Quantum carpet generation. Evolution of the mean number of particles $\langle n_n(t)\rangle$ in a 1D chain with $L = 40$. The coupling constants are set to J_n^{split} and B_n^{split} to produce a perfect splitting of the incoming wave-packet. The two particles are initially located in mirror-symmetric sites, namely $|\psi(0)\rangle = a_{10}^{\dagger} a_{31}^{\dagger}|0\rangle$. Here we are considering the free boson regime $U_n = 0$.

visible before that splitting time $t < t^*$. To better highlight this effects, we plot in Fig. 3.4, the mean occupation number and the mean-square occupation number of site 2 as a function of time t.

We also take into consideration the role of the onsite interaction, which affects the perfect reconstruction of a two-particle wave packet. As expected, it turns out that from the space-time dynamics of $\langle n_n(t)\rangle$ it is not possible to discriminate free evolution ($U = 0$) from the hard-core limit ($U = \infty$), while particle statistics give rise to different dynamics for $\langle n_n^2(t)\rangle$. On the other hand, for intermediate values of the onsite interaction, in the middle column of Fig. 3.3, the Hamiltonian cannot be mapped into a free model (either bosonic or fermionic), so scattering effects prevent the perfect reconstruction of the wave packet. Indeed, for $U = 1$ we find $\langle n_n^2(t = 2t^*)\rangle < \langle n_n^2(t = 0)\rangle$ and $\langle n_n^2(t = 2t^*)\rangle < \langle n_n^2(t = 0)\rangle$. A partial fractional revival effect for $t = t^*/2$ and $t = t^*/4$ can be observed for bosons in Fig. 3.3. This is more clearly shown in Fig. 3.5 where we show the results for $\langle n_j(t = t^*/4)\rangle$ and $\langle n_j^2(t = t^*/4)\rangle$.

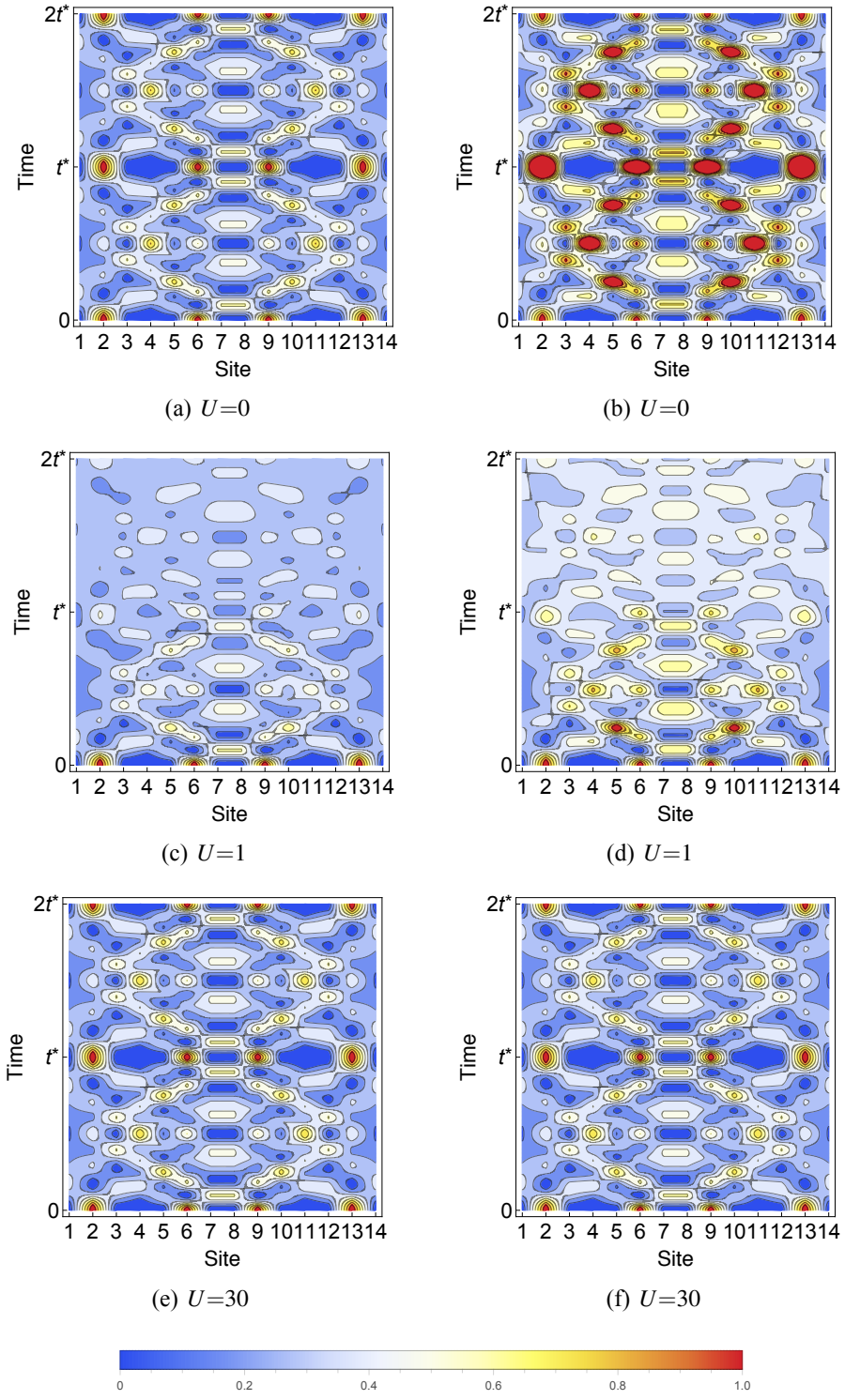

(a) U=0 (b) U=0

(c) U=1 (d) U=1

(e) U=30 (f) U=30

Figure 3.3: Quantum carpet due to four particle interference. Staring from the initial state $|\psi(0)\rangle = a_2^\dagger a_6^\dagger a_9^\dagger a_{13}^\dagger |0\rangle$ we consider the space-time evolution of $\langle n_n(t)\rangle$ (a), (c) and (e) and the space-time evolution of $\langle n_n^2(t)\rangle$ (b), (d) and (f). The chain length is $L = 14$ and several values of the onsite interaction $U_n = U$ (expressed in J units) are considered: $U = 0$ (a) and (b), $U = 1$ (c) and (d), and $U = 30$ (e) and (f). Here t^* is the fractional revival time, while $2t^*$ is the full revival time. The difference between the first and second row is due to bunching and anti-bunching effects. Note the transition from bosonic ($U = 0$) to fermionic and hard-core boson ($U = \infty$) behaviour as a function of U.

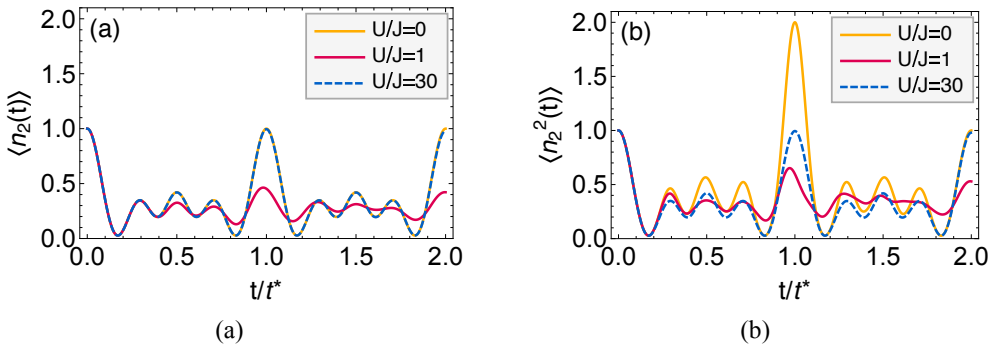

Figure 3.4: Perfect bunching/anti-bunching effects. Plot of the (a) mean occupation number and of the (b) mean-square occupation number of site 2 as a function of time t for several values of the onsite interaction. Here $L = 14$ and the initial state is $|\psi(0)\rangle = a_2^\dagger a_6^\dagger a_9^\dagger a_{13}^\dagger |0\rangle$. Note the transition from bosonic ($U = 0$) to fermionic and hard-core boson ($U = \infty$) behaviour as a function of U.

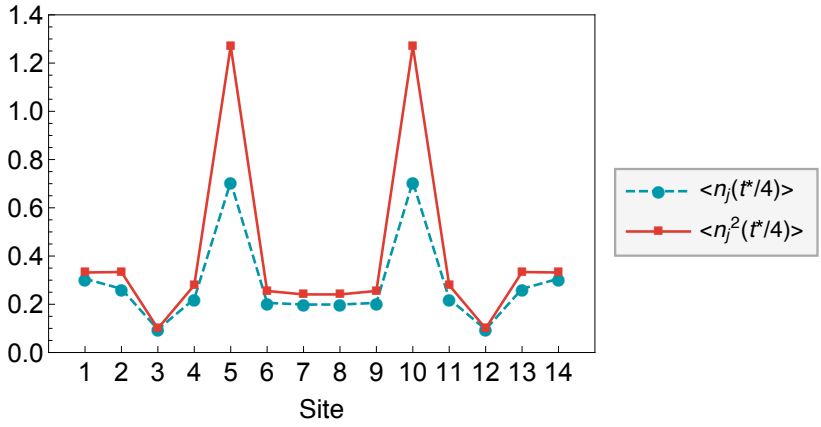

Figure 3.5: Partial bunching effect. Plot of the mean occupation number and of the mean-square occupation number for each site at $t = t^*/4$ for $U/J = 0$. Here $L = 14$ and the initial state is $|\psi(0)\rangle = a_2^\dagger a_6^\dagger a_9^\dagger a_{13}^\dagger |0\rangle$.

3.3.2 Perfect Entanglement Generation in a XX Spin Chain

An interesting application of the perfect splitting scheme is the entanglement generation in spin chain models. We consider an XX chain model, with tunable couplings in an external magnetic field,

$$H_{XX} = -\sum_{n=1}^{L-1} \left(J_n S_n^+ S_{n+1}^- + H.c\right) - \sum_{n=1}^{L} \frac{B_n}{2} S_n^z \,, \tag{3.13}$$

where $S_n^{\pm} = (S_n^x \pm i S_n^y)$ are spin ladder operators. As shown in Sec. 1.5.1 this setup could be realised experimentally by means of ultra-cold bosons in 1D optical lattice, as in the hard-core limit this system is mapped into an effective spin $1/2$ model. The Hamiltonian (3.13) can be transformed in a fermion lattice model via the Jordan-Wigner transformation, Appendix D.2, namely the Hamiltonian (3.13) is mapped into

$$H = \sum_{nm} \langle n|H_{XX}|m\rangle c_n^{\dagger} c_m, \tag{3.14}$$

where the operators c_n satisfy the canonical anti-commutation rules of fermions. In the Heisenberg picture [139] we have

$$c_n(t) = \sum_m \langle m|e^{-iHt}|m\rangle c_m. \tag{3.15}$$

Because a many-body spin state can be obtained by applying the annihilation operation c_n to the fully polarised state $|\Omega\rangle = |\uparrow_1, \ldots, \uparrow_L\rangle$, the time evolution of a spin state can be found using the Eq. (3.15). We now show how one can create entanglement between two remote mirror symmetric sites by exploiting the perfect wave-packet splitting scheme. We consider a single spin flip state in position n, whose state is $c_n|\Omega\rangle$. Using Eq. (3.15), when the Hamiltonian is tailored to generate the perfect splitting transformation, Eq. (3.5), at the transfer time t^* one obtains

$$c_n|\Omega\rangle \xrightarrow{t^*} \frac{1}{\sqrt{2}} \left(c_n|\Omega\rangle + i c_{L-n+1}|\Omega\rangle\right). \tag{3.16}$$

Using the inverse Jordan-Wigner transformation, Appendix D.2, for going back to the spin picture, the state generated, at time t^*, is the entangled state

$$\frac{1}{\sqrt{2}}\left(|\uparrow_\alpha\downarrow_\beta\rangle + i|\downarrow_\alpha\uparrow_\beta\rangle\right) , \tag{3.17}$$

where $\alpha = n$ and $\beta = L-n+1$ are two mirror symmetric sites of the chain. Once the above argument is generalised to a many spin flips setting, the perfect splitting scheme allows generating the maximal amount of entangled pairs, starting from a separable state. Indeed, if the system is initially in one of the two states

$$|\psi_{DM}\rangle = |\uparrow \ldots \uparrow\downarrow \ldots \downarrow\rangle, \tag{3.18}$$

$$|\psi_{AFM}\rangle = |\uparrow\downarrow\uparrow \ldots \uparrow\downarrow\rangle, \tag{3.19}$$

namely, the domain-wall state $|\psi_{DM}\rangle$ or the antiferromagnetic state $|\psi_{AFM}\rangle$, the time evolution at time t^*, under the perfect splitting Hamiltonian, results in the state

$$\left(c_1 + e^{i\alpha_1}c_L\right)\left(c_2 + e^{i\alpha_2}c_{L-1}\right)\ldots|\Omega\rangle \tag{3.20}$$

where α_i depend on the initial state. By carefully dealing with the Jordan-Wigner phase entering into the definition of the operators, c_n, one can easily find, via the inverse transformation in Appendix D.2, that the resulting state corresponds to a state in which every pair of qubits sitting in positions n and $L-n+1$ in maximally entangled, namely $|\psi_{n,L-n+1}(t^*)\rangle = \frac{1}{\sqrt{2}}\left(|\uparrow\downarrow\rangle + e^{i\alpha'_n}|\downarrow\uparrow\rangle\right)$, where α'_n can differs from α_n by a π factor. The perfect splitting dynamics thus represents an alternative to other methods existing in the literature to generate nested Bell pairs [204, 205]. Compared to previous proposals, our scheme it is more general as it allows one to tune the number of generated Bell pairs by simply choosing the number of flipped spins in the initial state.

3.4 Effect of the imperfection in the Optimal Splitting Profile

From experimental perspective, when a real physical system is considered, random perturbations to the coupling constants, due to engineering failures, imperfections or defects in the fabrication processes, produce deviations from the ideal profile which generates perfect operations [140].

The effect of the coupling randomness, even for non-interacting systems, is to produce a localisation of the eigenstates of the system and consequently to inhibit the state transfer [208]. We also mention that it has been shown [209, 210] that the interaction of bosonic atoms with static fermionic impurities, randomly distributed in the lattice, may yield a Bose-Hubbard model where the parameters J_n and B_n are subject to noise.

Given the above, we investigate what degree of imperfections is tolerable in our scheme or, in other terms, what is the precision required in tuning the coupling strengths according to the desired pattern. In this section we evaluate the influence of random errors added in the optimal coupling profile, for several chain lengths L. We

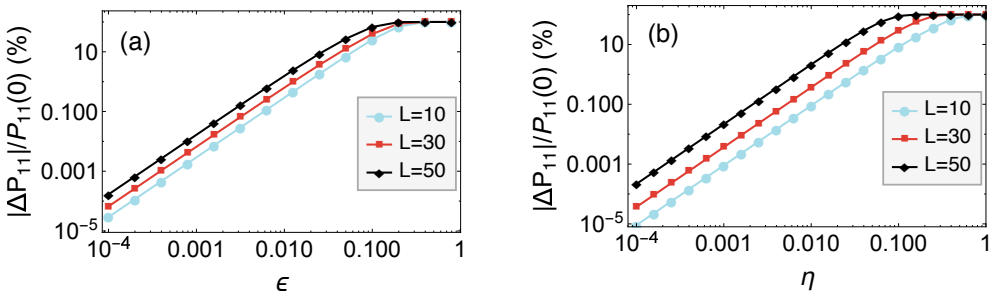

Figure 3.6: Effect of the imperfections. Relative variation of the bunching probability $P_1 1(t = t^*)$ in the noninteracting regime $U_n = 0$, in the presence of (a) random hopping noise and (b) random diagonal noise, respectively, with coupling strength ε and η. Several chain lengths L are considered.

firstly include an off-diagonal disorder term (hopping disorder) in the Hamiltonian (1.64) as $J_n{=}J(J_n^{split}{+}x_n)$, where $x_n{\in}[-\varepsilon,\varepsilon]$ is a uniform random distribution and ε is the perturbation strength [144]. In Fig. 3.6 the relative variation $|\Delta P_{11}|/P_{11}(\varepsilon{=}0)$

is shown as function of the degree of disorder ε. Here $P_{11}=|\langle\psi_b|\psi(t^*)\rangle|^2$, where $|\psi_b\rangle$ is defined in (3.12), and $\Delta P\equiv|P_{11}(\varepsilon)-P_{11}(\varepsilon=0)|$ represents the deviation of the bunching probability respect to the ideal case.

We also consider the effect of diagonal noise $B_j=B+Jx_n$ with $x_n\in[-\eta,\eta]$ in an even site chain. The effect of signal noise is shown in figure Fig. 3.6 as function of the noise coupling strength ε. As clear from Fig. 3.6 a power law behaviour, under a certain threshold value of ε and η, characterises both the deviations due to hopping disorder and due to the diagonal disorder. Clearly, a high degree of disorder produces state localisation, which completely destroys the effect.

3.5 Conclusions

In this chapter we have analysed the wave-function dynamics of hopping particles and/or quasiparticles in a quantum chain. We have studied how the coupling profile can be engineered so that it enables a perfect wave-packet splitting and reconstruction of a single localised wave-packet with 100% efficiency (inhibiting the dispersion effect) between far sites of a 1D lattice model.

We have devised the exact conditions that the Hamiltonian spectrum has to satisfy to allow for the perfect splitting and reconstruction and, via an inverse eigenvalue technique, we have found the coupling pattern that satisfies the perfect splitting condition. We have shown how our findings can be applied to harness the hopping dynamics of quasiparticles for the generation of fractional revivals and reconstruction of initially localised wave-packets. We have shown how peculiar quantum interference patterns that result in regular structure in the space-time evolution of the many-particle wavefunction, known as quantum carpets [196–198]. Besides shedding light into quantum interference phenomena in one dimension, our results are particularly useful for applications. Indeed, we have shown how our scheme can be exploited for entanglement distribution in a XX chain and to generate scalable perfect bunching/anti-bunching effects in a 1D lattice model. Compared to existing schemes [204, 205] our model opens up the dynamical generation of Bell pairs by simply choosing the number of flipped spins in the initial state.

In the next chapter we consider how a wave-packet splitting strategy, together with a strong interacting system of bosons can lead to the generation of non-classical states in 1D optical lattices.

Chapter 4

NOON state generation via dynamics of bound particles

4.1 Introduction

In Chap. 2, Sec. 2.3, we have shown how a 1D finite optical lattice, together with the ability of designing the lattice potential and single-site techniques, can be exploited for quantum interferometry applications. One peculiarity of atoms, trapped in optical lattices, is that they do interact. At first glance the interaction seems to be an unwanted characteristic, as it limits the possibility to generate useful interference effects. In fact, state transfer schemes, Sec. 1.6, are challenging to be designed for interacting particles and, as show in Sec. 2.4, bunching and anti-bunching effects are reduced for interacting walkers.

Nevertheless, atom interaction is a non-linear term and could be exploited to generate non-classical states (e.g. NOON states) and to enhance the phase precision estimation in metrology application, Sec. 1.9.2, overcoming the classical shot-noise limit. So far, in existing photonic realisations NOON states have been generated, for instance, by mixing quantum and classical light on a beam splitter. Nonetheless, up to now, the largest NOON state generated has $N = 5$ (with a limited 42% fringe visibility and a theoretical threshold of 94.3%) [211–213]. The lack of strong non-linearities is a major disadvantage in photonic systems and several schemes (e.g.based on measurement [175,176,214]) have been proposed for overcoming this

limitation. On the other hand, in atomic systems, the natural atom-atom interaction could open up the possibility to go beyond the traditional regime studied in quantum optics, paving the way towards quantum enhanced interferometry in a lattice. However, as far as distant sites are concerned, it is still an open question whether it is possible to generate non-classical states, between far sites, in a finite 1D lattice model, exploiting the natural atom dynamics. In a lattice setup, this type of scheme is important because it avoids the necessity of measurement based schemes [175,214] (which are still challenging in current optical lattice experiments with few particles), time-dependent external potentials [215], engineered-bath-based schemes [216], or ring lattices [217,218].

In Sec. 1.7 we have shown that strong interaction in lattice models creates stable composite objects when more walkers are initially in the same site. This is due to a gap in the energy spectrum that prevents the dissociation during the dynamics. At first glance it seems reasonable to believe that the dynamics of a bound state, made of co-propagating bosons, should somehow resemble the propagation of a single particle. Then, a coherent split a state of M bosons between distant sites could eventually produce a NOON state. The simplest configuration of the chain profile that could produce such transformation is illustrated in Fig. 4.1. Indeed if the initial

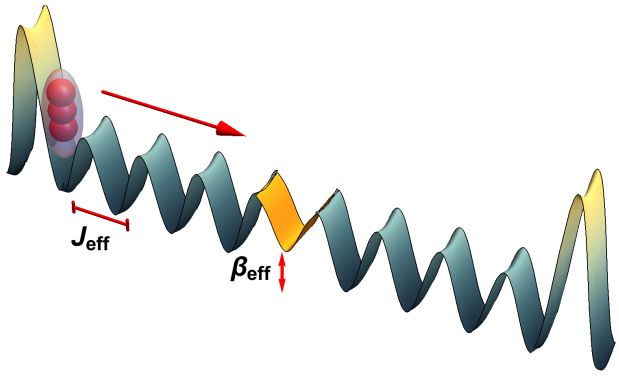

Figure 4.1: Scheme of the model. A bound state made of three particles is initially in the first site of a finite lattice. The red arrow represents the natural propagation direction, once the lattice depth is lowered at $t = 0$. J_{eff} is effective hopping rate and β_{eff} is an impurity added in the chemical potential which splits the incoming wave-packet in a reflected/transmitted component.

bound state, $|\psi(0)\rangle \propto \left(a_1^M\right)^\dagger |0\rangle$, was equivalent to an effective single particle state,

then it would be dynamically transformed at the transfer time t^*, under a balanced split operation, in

$$a_1^M|0\rangle \xrightarrow{t^*} \left(a_1^M + i\, a_L^M\right)|0\rangle = |M0\rangle_{1L} + i|0M\rangle_{1L}, \tag{4.1}$$

where L is the chain length. This would be equivalent to a "magic beam splitter" transformation, as described in [174]. However, single particle and a bound state are not completely equivalent. In fact, as shown in Sec. 1.7.4, an effective energy gap between edge and bulk sites creates edge-locking effects that suppresses bound-state propagation along the lattice, for $M \geq 3$ particles [162, 163]. Therefore, is still an open problem how to tune the lattice potential to realise transformations between far sites when strongly interacting particles are involved. In this chapter we will discuss how high fidelity NOON states can be generated between remote sites, by exploiting the natural dynamics of bound states.

4.2 Effective Hopping in the Bose-Hubbard Model

The Bose-Hubbard model Eq. (1.64), for a large ratio J/U, enables the creation of "bound" states composed of several particles in the same site, as discussed in Sec. 1.7. The physical reason is that states with M particles in a site belong to an energy band well separated from all the other states. This naturally suggests describing the dynamics via an effective Hamiltonian, H_M^{eff}, in the Hilbert subspace of bound states, namely

$$\mathscr{H}_M = \{|\{M\}, j\rangle = (a_j^\dagger)^M|0\rangle/\sqrt{M!} : j{=}1,\ldots,L\}, \tag{4.2}$$

where $\{|\{M\}, j\rangle$ indicates a state with M particles in site j. In other words, because the bound state dynamics, in good approximation remains confined inside $\mathscr{H}_M$, an M-particle state can be effectively remapped to a single particle model, with effective parameters. This description has clear advantages, as the effective Hamiltonian is a tridiagonal matrix, as in Eq. (1.108) , which can be used to engineer the coupling constants J_j and μ_j of the Bose-Hubbard model (1.64), such as the effective Hamiltonian pattern is designed for applications (i.e.state transmission of bound states and

state splitting). Details of calculations of the effective description[1] are shown in Appendix D.3. The result we find is that the effective Hamiltonian description, H_M^{eff}, using the basis $|\{M\}, j\rangle$, j=1,...,L in $\mathscr{H}_M$, is

$$H_M^{\text{eff}} = \begin{pmatrix} B_1^{\text{eff}} & J_1^{\text{eff}} & & & \\ J_1^{\text{eff}} & B_2^{\text{eff}} & J_2^{\text{eff}} & & \\ & \ddots & \ddots & \ddots & \\ & & J_{L-2}^{\text{eff}} & B_{L^-1}^{\text{eff}} & J_{L-1}^{\text{eff}} \\ & & & J_{L-1}^{\text{eff}} & B_L^{\text{eff}} \end{pmatrix}. \tag{4.3}$$

An important point is that the hopping of an M-particles bound state involves $M-1$ "virtual" transitions through states outside $\mathscr{H}_M$, so that the effective hopping scales as $J_j^{\text{eff}} \propto J_j^M/U_j^{M-1}$, where J_j^{eff} decreases with M for large U. Because $|U/J| > 1$, and the tunnelling time is of the order of $1/J_{\text{eff}}$, Sec. 1.3.5.1, the evolution of a bound state is slower[2] than a single particle dynamics in a lattice [3] (with hopping rate J).

4.3 Edge effects for Bound States in a Finite Lattice Model

To highlight the differences between the dynamics of a bound state and a single particle, we consider a homogeneous Bose-Hubbard model, Eq. (1.64), with $J_j = J$, $U_j = U$, $\mu_j = \mu$, whose effective Hamiltonian is

$$H_M^{\text{eff}} = \left(\frac{J}{U}\right)^{M-1} \begin{pmatrix} B_1^{\text{eff}} & J_1^{\text{eff}} & & & \\ J^{\text{eff}} & B_2^{\text{eff}} & J^{\text{eff}} & & \\ & \ddots & \ddots & \ddots & \\ & & J^{\text{eff}} & B_{L^-1}^{\text{eff}} & J^{\text{eff}} \\ & & & J^{\text{eff}} & B_L^{\text{eff}} \end{pmatrix}, \tag{4.4}$$

[1] Here we highlight that, while to other techniques (e.g. in Appendix D) are difficult to be exploited for $M > 2$, our method it is easily generalisable to higher M.

[2] We have already shown it, in Sec. 1.7.1, for the case $M = 2$ in a two well system.

[3] Environmental effects could be relevant when bound states and long chains are involved.

where $J^{\text{eff}} = \mathcal{O}(J)$, $B_1^{\text{eff}} = B_L^{\text{eff}} = \mathcal{O}[J(U/J)^{M-2}]$, while B_j^{eff} for $j \neq 1, L$ is much smaller than B_1^{eff} (boundary elements may be of order $\mathcal{O}(J)$ or less, while in the bulk they are even smaller). The large effective boundary field gives rise to a phenomenon called *edge-locking*, which has been discussed in Sec. 1.7.2 and 1.7.4, and is connected to an energy gap between edge and bulk sites states, Fig. 1.17(right). Although a two particle spectrum does not have this kind of energy gap, Fig. 1.17(left), in the following we show the existence of a *quasi-locking* effect, that corresponds to an increase of the delocalisation time from the initial site during the dynamics, compared to the single particle case. From a different prospective, edge-locking effects can be analysed through the theory of QUTM, Appendix B, once applied to the effective Hamiltonian, Eq. (4.4).

We consider an initial wave-packet localised in site 1, which evolves through a tridiagonal matrix Hamiltonian, Eq. (4.4), to $|\psi(t)\rangle = \sum_j (e^{-itH_M^{\text{eff}}})_{j1} |\{M\}, j\rangle$. Calling $H_M^{\text{eff}} = O^\dagger E O$ the spectral decomposition, then $|\psi(t)\rangle = \sum_{kj} e^{-itE_k} O_{k1}^* O_{kj} |\{M\}, j\rangle$, and we find that $O_{kL} = O_{k1}(-1)^k \approx O_{k1} e^{iLk}$ and $E_k \propto \cos(k)$ where k is the quasi-momentum, $k = k_j + \mathcal{O}(L^{-1})$ where $k_j = \pi j/(L+1)$ and $j = 1, \ldots, L$. Therefore, the quantum walk of the bounded particle displays the wave-packet evolution $\langle \{M\}, L|\psi(t)\rangle = \sum_k e^{-i(tE_k - Lk)} |O_{k1}|^2$, where $|O_{k1}|^2$ is the probability to excite the quasi-momentum state k by initialising the system in the site 1.

To simplify the theoretical analysis we assume that $B_j^{\text{eff}} \equiv B_{\text{bulk}}^{\text{eff}}$ is constant for $j \neq 1, L$ so, without loss of generality, we can set[4] $B_{\text{bulk}}^{\text{eff}} = 0$. Within this description it is now clear that edge-locking appears when $B_1^{\text{eff}} \gg E_k$, since no quasi-momentum state can be excited by initialising the system in a state where the bounded particle is in the first site (namely $|O_{1k}|^2 \approx 0$ for all the quasi-momentum states). Indeed, in this regime this initialisation excites out-of-band modes which are localised near the edges and do not propagate [146, 150]. As it is clear from Eq. (4.4), since $B_1^{\text{eff}} = B_L^{\text{eff}} = \mathcal{O}[J(U/J)^{M-2}]$, the edge-locking condition $B_1^{\text{eff}} \gg E_k$ happens when $M \geq 3$, as discussed in Sec. 1.7.4.

However, we find that there is another form of quasi-locking for $M = 2$, not de-

[4] Indeed, the Hamiltonian (4.4) and $H_M^{\text{eff}} - B_{\text{bulk}}^{\text{eff}} \mathbf{1}$ give rise to the same evolution aside from an irrelevant global phase.

scribed in [163]. Indeed, for $M = 2$ we find that B_1^{eff} is of the same order of the energy band E_k of the quasi-momentum states and, as a consequence, the quasi-momentum states with energy $B_1^{\text{eff}} \approx E_k$ are the ones involved in the dynamics. Since $E_k \propto \cos(k)$ when $B_1^{\text{eff}} \approx 0$ the relevant excitations consist mostly of quasi-momentum states with almost-linear dispersion relation ($E_k \approx k$ around $k = \pi/2$ where $E_{\pi/2} \simeq 0$). These states propagate without dispersion in the chain and therefore give rise to a high transmission quality. On the other hand, if $B_1^{\text{eff}} \neq 0$ other states with non-linear dispersion relation are involved, which drastically lower the transmission quality. In other words the difference in effective energies B_j^{eff} between bulk and edge sites favours non-linear excitations which, in turn, leads to a dispersive dynamics. As a result we find that the state $|\psi(0)\rangle = (a_1^\dagger)^2/\sqrt{2}|0\rangle$ has a long delocalisation time from the initial site during the relevant time $t^* \sim LU/J^2$, namely the delocalisation time from one end of the chain is slower than the transfer time t^*. This can be clearly observed in Fig. 4.2(a), where the probability $P_{11}(t)$ is still non-zero at the transfer time $t^* \sim L/J_{\text{eff}}$, when the wave-packet has reached the other end. As edge-locking

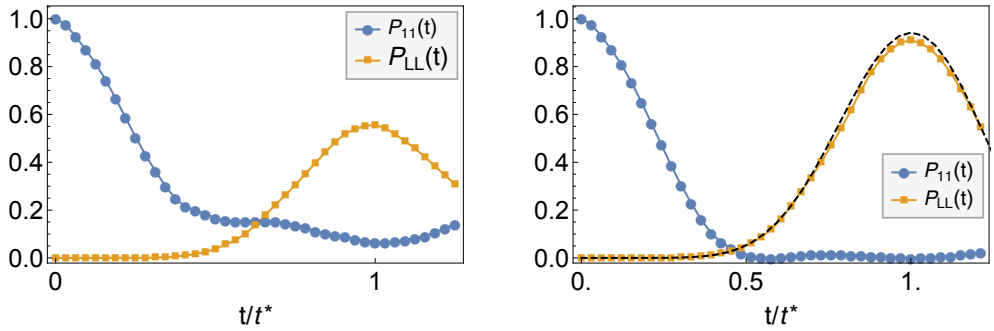

Figure 4.2: Edge-delocalisation for a two particle bound state. Plot of the probability $P_{11}(t)$ to have the bound state in the first site or in the last $P_{LL}(t)$ at time t (scaled for the transfer time $t^* \sim L/J_{\text{eff}}$), for a homogeneous chain with $L = 5$ and $U/J = 5$ in the initial state $|\psi(0)\rangle \propto \left(a_1^\dagger\right)^2/\sqrt{2}|0\rangle$. A local field $\mu_j = \beta'(\delta_{j,1} + \delta_{j,L})$ has been added with strength (a) $\beta' = 0$ and (b) $\beta' = J^2/4U$. To compare the results with the single-particle case we plot (dashed black line) the probability $P_L(t) = |\langle 0|a_L|\psi(t)\rangle|^2$ for a single particle initially in $a_1^\dagger|0\rangle$ (here $t^* \sim L/J$).

is detrimental for quantum transfer applications, in the following section, we show that how to eliminate it adding a local edge potential. Indeed, a suitable local chem-

ical potential could make the effective field, B_j^{eff} in Eq. (4.4), to be constant over all the sites, making the effective chain homogeneous.

4.4 Bound States Dynamical Behaviour in a Finite Lattice Model

In this section we analyse the dynamical behaviour of a bound state made of M particles in a finite lattice, starting from the homogeneous chain case $J_j = J$, $U_j = U$, $\mu_j = \mu$, to find the conditions to eliminate edge effects.

Besides, we show how to tailor the effective Hamiltonian (4.3) to dynamically trigger transformations using bound states, showing also how minimal engineering coupling profiles, discussed in Sec. 1.6.4, can be applied to maximise the transfer fidelity. Then we quantify how decoherence influences bound states transfer in a 1D lattice. As a second application, we design the coupling profile to trigger a bound state splitting, which in turn produces high fidelity NOON states between distant sites.

Finally, we analyse the efficiency of our scheme in a Mach-Zehnder configuration for quantum enhanced metrology. Although our theoretical analysis is fully general and readily extensible for larger values of M, we focus our attention on the case $M = 2,3$, which are more feasible given the current experimental capabilities.

4.5 Two Particle Bound States

For a two particle bound state, $M = 2$, in a homogeneous chain we find that the effective Hamiltonian, Eq. (4.4), has coupling constants

$$J_j^{\text{eff}} = \frac{J^2}{2U}\,, \tag{4.5}$$

$$B_j^{\text{eff}} = \begin{cases} \frac{J^2}{2U} + U\,, & \text{for} \quad j = 1, L\,, \\ \frac{J^2}{U} + U\,, & \text{for} \quad j \neq 1, L\,. \end{cases} \tag{4.6}$$

Starting from the initial state $|\psi(0)\rangle = \left(a_1^\dagger\right)^2/\sqrt{2}|0\rangle$, we compute the joint probability $P_{ij}(t) = \frac{1}{1+\delta_{ij}}|\langle 0|a_i a_j|\psi(t)\rangle|^2$, via numerical techniques in Appendix A. As

previously mentioned, the effective field B_j^{eff} difference between bulk and edge sites effect gives rise to quasi-locking effects. Indeed, we find in Fig. 4.2(a) that there is a non-zero probability $P_{11}(t)$ to have the particle in site 1 even at the transfer time $t^* \sim L/J_{\text{eff}}$, where the wave-packet has reached site L.

To compensate the quasi-localisation effect we add an edge local chemical potential, $\mu_j = -\beta' \left(\delta_{j,1} + \delta_{j,L}\right)$, where $\beta' = J^2/4U$. Its effect is clearly visible in Fig. 4.2(b) where, once the β' field is added, the delocalisation time from the first time, $P_{11}(t^*)$, and consequently the transfer fidelity $P_{LL}(t^*)$, are strongly increased.

We compare the results obtained for the transfer of a bound state with the propagation of a single particle in the lattice, initially in $a_1^\dagger|0\rangle$, by plotting, Fig. 4.2(b) (black dashed line) the probability $P_L(t) = |\langle 0|a_L|\psi(t)|^2$ (single particle data are scaled for their transfer time $t^* \sim L/J$). The difference between the single particle and the bound particle results, depends on the finite value of the interaction chosen ($U/J = 5$ in Fig. 4.2). Indeed, the effective model (4.4) is valid when the subspace of bound states is energetically well separated from the other states of the system, namely for $U/J \gg 1$ and the agreement improves increasing U/J. Therefore, single particle data provides a threshold to the maximum fidelity achievable with bound states.

We analyse deviations from the theoretical value of β', for a system in $|\psi(0)\rangle \propto (a_1^\dagger)^2|0\rangle$, computing numerically the value of β' that maximises the probability, $P_{LL}(t^*)$, to find the bound state in site L, at time $t^* \sim L/J_{\text{eff}}$. We find a complete agreement of the numerical data with the theoretical prediction,

$$\beta' = J^2/4U, \tag{4.7}$$

independently[5], as long as $U/J \gtrsim 5$.

4.5.1 Optimal State Transfer of a Two Particle Bound state

The effective single particle description, Eq. (4.3), can be tailored to engineering the coupling profile and improve the transfer fidelity of bound states. Firstly we

[5]This is not surprising, as quasi-localisation is a boundary effect, and the optimal value of β' cannot depend on the chain length.

design the effective profile to implement an almost-perfect transfer strategy, Sec. 1.6.4.1, then we find the coupling values that produce the desired transformation in the model (1.64).

We compute the effective Hamiltonian (4.3) for a Bose-Hubbard model, whose edge couplings are set to $J_1 = J_{L-1} = J_0$, while the rest of the chain is homogeneous ($J_j = J$ for $j \neq \{1, L\}$), finding

$$J_j^{\text{eff}} = \begin{cases} \frac{J_0^2}{2U} & \text{for} \quad j = 1, L-1 \ , \\ \frac{J^2}{2U} & \text{for} \quad j \neq 1, L-1 \ , \end{cases} \tag{4.8}$$

$$B_j^{\text{eff}} = \begin{cases} \frac{J_0^2}{2U} + U & \text{for} \quad j = 1, L, \\ \frac{J_0^2}{2U} + \frac{J^2}{2U} + U & \text{for} \quad j = 2, L-1, \\ \frac{J^2}{U} + U & \text{for} \quad j = 3, \ldots, L-2. \end{cases} \tag{4.9}$$

To achieve a ballistic regime, as discussed in Sec. 1.6.4, the values of J_j^{eff} are optimised using the value of J_0 that maximises the transfer fidelity for a single particle state, Sec. 1.6.4.1.

To compensate the effective local field B_j^{eff} inhomogeneities it is clear, from Eq. (4.9), that we need to add local chemical potentials in both the first/last two chain sites, to remove the local energy difference[6] in B_j^{eff}. The two pair of local fields that maximise the transfer fidelity are respectively $\mu_j = -\beta_1(\delta_{j,1} + \delta_{j,L})$ and $\mu_j = -\beta_2(\delta_{j,2} + \delta_{j,L-1})$, with strengths $\beta_1 = \left(J_0^2 - 2J^2\right)/2U$ and $\beta_2 = \left(J_0^2 - J^2\right)/2U$.

In Fig. 4.3(a), we show the results obtained for the transfer fidelity $P_{LL}(t^*)$ as a function of U/J for the optimised chain. We observe a significant improvement of transfer fidelity, compared to the homogeneous chain case. We compare the results obtained with a single particle dynamics in a chain optimised with the scheme OPT (dashed lines) in Fig. 4.3(a), for several chain lengths L. As expected, strong inter-particle interaction U makes bound states similar to single particle states. To better highlight that minimal engineered schemes have already a significant impact to reduce the dispersion in the system, in Fig. 4.3(b) we plot the

[6] From the technical point of view, this choice makes all the diagonal terms homogeneous in the effective model (4.3).

probability $P_{jj}(t) = |\langle 0|a_j^2|\psi(t)\rangle|^2/2$ to have a two particle bound state in site j as a function of the time t/t^*, for a minimal engineered chain with $L = 21$ and $U/J = 8$. Although in this section we have analysed a minimal coupling scheme, our findings

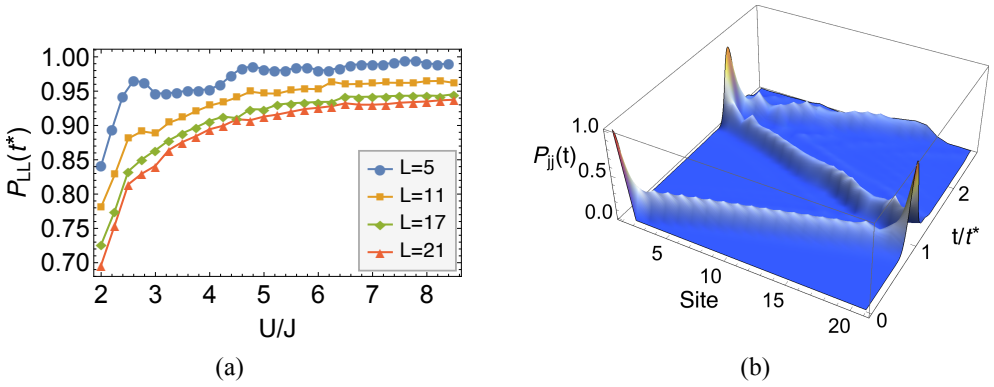

Figure 4.3: Optimal transfer of a two-particle bound state. (a) Transfer fidelity $P_{LL}(t^*)$ for the initial state $|\psi(0)\rangle \propto (a_1^\dagger)^2|0\rangle$ as a function of the onsite interaction U/J when the optimal transfer scheme $J_1 = J_L = J_0$ and $J_j = J$ for $j \neq (1,L)$ is included in the model 1.64. Two local impurities $\mu_j = -\beta_1(\delta_{j,1} + \delta_{j,L})$ and $\mu_j = -\beta_2(\delta_{j,2} + \delta_{j,L-1})$ where $\beta_1 = \left(J_0^2 - 2J^2\right)/2U$ and $\beta_2 = \left(J_0^2 - J^2\right)/2U$ have been added to eliminate the edge-locking effect. The J_0 value is chosen by numerically maximising the transfer fidelity in a single particle manifold, as discussed in Sec. 1.6.4. To compare the difference between a single particle and a bound state, we plot (with a dashed line) the single-particle transfer fidelity $P_L(t^*) = |\langle 0|a_L|\psi(t^*)\rangle|^2$ obtained for a system initially in $a_1^\dagger|0\rangle$. (b) Probability $P_{jj}(t)$ to have a two particle bound state in site j at time t/t^* for an engineered chain with the J_0 scheme with $L = 21$ and $U/J = 8$.

can be straightforwardly extended for PST applications with bound states, for instance tailoring the effective Hamiltonian tunnelling couplings via Eq. (1.119), and adding local potentials to make the effective model homogeneous. In the same way a perfect splitting can be achieved using the results in Chap. 3.

4.5.2 Decoherence Analysis

In this section we analyse the robustness of our scheme under environmental effects, namely dephasing due to spontaneous emission, which represents the main source of decoherence in optical lattices. The typical hopping time for a bound state as a function of the depth of the lattice potential has been discussed in Sec. 1.3.5.1, in Fig. 1.5(b). As shown in Eq. (1.72), the dynamics of the system in the lowest band is typically modelled as a Master equation in Lindblad form, where Γ is the effective

scattering rate, and $H_{\rm BS}$ is the Bose-Hubbard Hamiltonian (1.64) that can be solved numerically, as discussed in Sec. 2.5.

Compared with the no-decoherence case, we do not find any relevant modification to the delocalising field β', in Eq. 4.7, for $\Gamma/J_{\rm eff} < 0.1$, where $J_{\rm eff} = J^2/2U$. In Fig. 4.4(a) we show the results obtained for the transfer fidelity $P_{LL}(t^*)$ as a function of the damping rate $\Gamma/J_{\rm eff}$ in Eq. (1.72) for $U/J = 3$. To better evaluate the difference with the zero decoherence case, in Fig. 4.4(a) we plot the relative variation $|\Delta P_{LL}(t^*)|/P_{LL}(0) = |P_{LL}(\Gamma) - P_{LL}(\Gamma = 0)|/P_{LL}(\Gamma = 0)$ as a function of the damping parameter $\Gamma/J_{\rm eff}$. We observe deviations of less than the 5% for $\Gamma/J_{\rm eff} \simeq 10^{-2} \div 10^{-3}$ for chain lengths between $L \in \{5,\ldots,21\}$, which are typical values for blue detuned optical lattices [66, 191]. For comparison we plot, Fig. 4.4(b), the results obtained for relative variation of the transfer fidelity $|\Delta P_L|/P_L(\Gamma = 0)$, with $\Delta P_L \equiv P_L(\Gamma = -P_L(\Gamma = 0)$ for a single particle initially in $a_1^\dagger|0\rangle$.

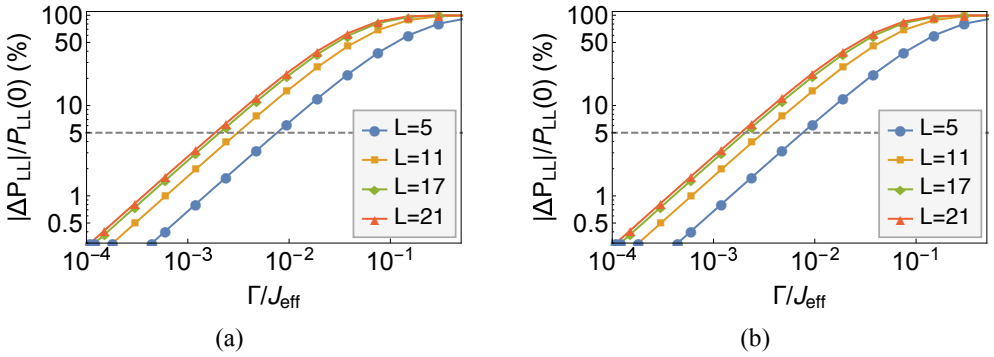

Figure 4.4: Decoherence effects for a two particle bound state. (a) relative variation $\Delta P_{LL}/P_{LL}(t^*,\Gamma = 0)$ of the transfer fidelity $P_{LL}(t^*)$ with respect to the case in absence of decoherence, for a uniform chain with $U/J = 3$ and length L. Here $\Delta P_{LL} = |P_{LL}(t^*,\Gamma) - P_{LL}(t^*,\Gamma = 0)|$ and the dashed grey line is a threshold of a relative variation of the 5%. Several chain length L are considered. (b) Relative variation $\Delta P_L/P_L(t^*,\Gamma = 0)$ for a single particle state initially in $a_1^\dagger|0\rangle$.

4.5.3 NOON State Generation with Bound States

In the previous sections we have shown that the effective dynamics of bound states, Eq. (4.3), can be used to tailor the Bose-Hubbard model (1.64) for state transfer applications. Although bound states and single particle dynamics have some simil-

arities, the advantages of using bound states, have not been exploited in full yet. In this section we prove that by tailoring the effective dynamics, Eq. (4.3), to produce a splitting effect, a bound state generates a NOON state between the edge sites of the chain.

The important point is that, if two non-interacting particles are initially in one input arm of a beam splitter, the output state contains a non-zero probability to measure one particle in each output arm, as shown in Sec. 1.8. On the other hand, for two strongly bound particles, the splitting process should produces a two-particle NOON state, as output. Indeed, when the bound particle impinges a balanced splitting field, as it effectively behaves like a single particle, the output state, measured at the endpoints, should be $|\psi(t^*)\rangle_{1L} = \frac{1}{\sqrt{2}}(|2,0\rangle + i|0,2\rangle)$. With the same strategy higher NOON states can be obtained for bound states with more particles.

We first analyse the case of $M = 2$. The simplest scheme to produce a wave-packet splitting, Chap. 2, consists in introducing a local barrier in the middle of a homogeneous chain. To remove edge quasi-locking effects we preliminary set the value $\beta' = J^2/4U$ for the edge fields $\mu_j = -\beta'(\delta_{j,1} + \delta_{j,L})$. Then we add a local field $\mu_j = -\beta\,\delta_{j,L/2+1}$ to trigger a wave-packet splitting. As shown in Chap. 2 for a single particle, a balanced splitting is obtained for a splitting field strength of the same order of the hopping term. Therefore, we expect that for a bound state, the field strength required must be of the order of the effective hopping rate $\beta \simeq J_{\rm eff} = J^2/2U$.

For two non-interacting particles, $U/J = 0$, the splitting field produces a non-zero probability, $P_{1L}(t^*)$, to have one particle in each end, as discussed in Sec. 1.8. On the other hand if the particles are still bounded, after the splitting process, this term is completely suppressed (as it is equivalent to the splitting of an effective single particle state). This is shown in Fig. 4.5 where, for a $L = 5$ chain and $U/J = 5$, the term $P_{1L}(t^*)$ is completely suppressed, for a bound particle.

As in Chap. 2, we expect to find finite length correction to the theoretical value $\beta \simeq J_{\rm eff} = J^2/2U$ which produces a 50/50 splitting. These are found numerically by finding the value of β that make zero the difference $P_{11}(t^*) - P_{LL}(t^*)$. As shown in the inset in Fig. 4.6, for a $L = 5$ homogeneous chain, $\beta^{50/50}$ scales with the

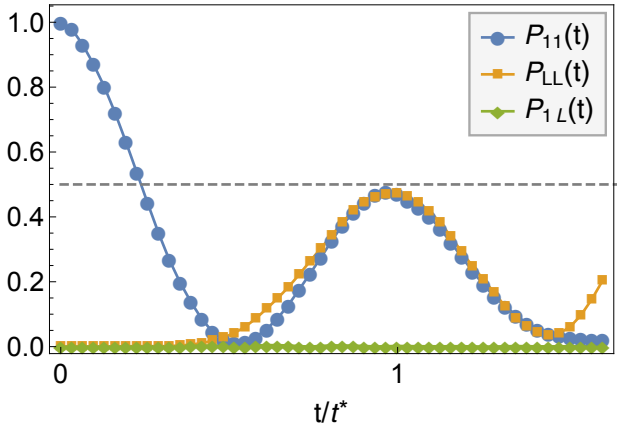

Figure 4.5: Two particle NOON state. Plot of the probabilities $P_{ij}(t)$ to have one particle in site i and the other in j, as a function of the time, in unit of the transfer time t^*, for two particles initially in $|\psi(0)\rangle \propto \left(a_1^\dagger\right)|0\rangle$. Here we consider a uniform chain with an impurity $\mu_j = -\beta\delta_{j,L/2+1}$ where $\beta = 0.789(J^2/2U)$ in a a chain with $U/J = 5$ and length $L = 5$. The absence of the $P_{1L}(t^*)$ term is an evidence that the output state at $t = t^* \simeq UL/J^2$ is the NOON state with two particles. The grey dashed line represents the results for an ideal lossless NOON state generation.

onsite interaction as $1/U$. The finite length factors, found from a fit over the data for several chain lengths, are shown in Fig. 4.6, where we show that for long chains L the $\beta^{50/50}$ values are closer to $J_{\rm eff} = J^2/2U$ in agreement with the effective Hamiltonian analysis.

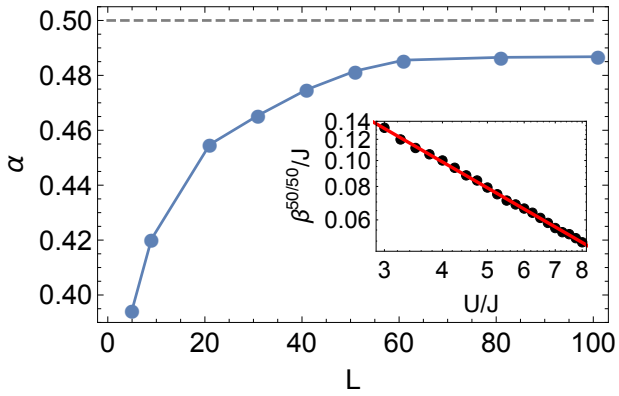

Figure 4.6: Finite-size effects in the two particle NOON state generation. Analysis of the scaling factor α where $\beta^{50/50} = \alpha J^2/U$, as a function of the chain length L for generating a two particle NOON state. The grey line represents the theoretical results from the effective Hamiltonian theory, which holds for $L \gg 1$. (Inset) Analysis of the optimal value of β of the local field $\mu_j = -\beta\delta_{j,L/2+1}$ which produces the NOON state with two particles as a function of U/J for $L = 5$. The red line is the fit $\beta = \beta^{50/50} = 0.395J^2/U$.

4.5.4 Even Chains

As discussed in Chap. 2, the splitting model is not limited to odd length chains but can be also applied to even chains. We find that this requires tuning both the middle tunnelling coupling strength $J_{L/2}$, and additionaly two pairs of local fields, respectively $\mu_j = -\beta_1(\delta_{j,1} + \delta_{j,L})$ and $\mu_j = -\beta_2(\delta_{j,2} + \delta_{j,L-1})$ in the Hamiltonian (1.64). Using the results of Chap. 2, for the splitting of a single particle we find, from the effective Hamiltonian model, that the optimal coupling strengths to generate a two particle NOON state between the endpoints of a uniform chain are respectively $J_{L/2} = J(\sqrt{2}-1)^{1/2}$, $\beta_1 = J/4U$ and $\beta_2 = J(2-\sqrt{2})/4U$.

4.6 Three Particles Bound State

The analysis of the dynamics of a two particle bound state of the previous section can be straightforwardly extended to the case of $M = 3$. This is important because the more particles are involved, the higher is the NOON state produced. As for the two particle case, the stability of a three particle bound state have been proved in [158] from energy consideration. When three particles are initially located in the same site, one would expect that the results of the splitting process, for strong enough onsite interaction, is to produce a NOON state with $N = 3$. For a homogeneous chain we find that the effective hopping, Eq. (4.3), is $J_{\text{eff}} = 3J^3/16U^2$, and that the edge-locking effect is eliminated through two local fields $\mu_j = -\beta'\left(\delta_{j,1} + \delta_{j,L}\right)$, where $\beta' = J^2/8U$. As for the two particle case, we investigate finite length corrections to β' for several chain length L for the initial state $|\psi(0)\rangle \propto \left(a_1^\dagger\right)^3 |0\rangle$ as a function of the onsite interaction U. We find that with high accuracy the estimated field $\beta' = J^2/8U$ is independent on L.

From the analysis of the probability $P_{LLL}(t^*)$ to have three particles in the site L at the transfer time $t^* \sim L/J_{\text{eff}}$, in a homogeneous chain, as a function of the onsite interaction, we find that values above $U/J \gtrsim 4$ guarantee an almost constant value of transfer fidelity for chain lengths $L \in \{5, \ldots, 21\}$ (this represents a threshold for the effective single particle behaviour).

In Fig. 4.7 we analyse the effect of decoherence due to spontaneous emission,

Eq. (1.72), for several chain lengths L as a function of the decoherence rate $\Gamma/J_{\rm eff}$ where $J_{\rm eff} = 3J^3/16U^2$. We observe relative variation of less than the 5% with respect to the decoherence free case, for $\Gamma/J_{\rm eff} \lesssim 1.3\times10^{-4}$ up to $L=7$ sites. The

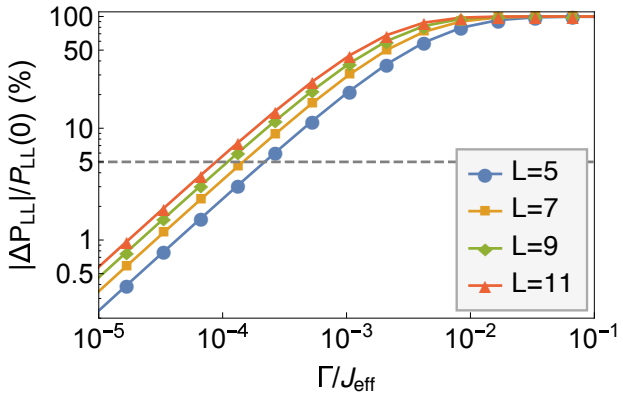

Figure 4.7: Decoherence effects for a three particle bound state. Relative variation $\Delta P_{LL}/P_{LL}(t^*,\Gamma=0)$, with respect to decoherence free case, for a uniform chain with $U/J=2$. Here $\Delta P_{LL} = |P_{LL}(t^*,\Gamma) - P_{LL}(t^*,\Gamma=0)|$ and the dashed grey line is a threshold of a relative variation of the 5%. Several chain length L are considered.

state transmission fidelity of a three bound particle state can be optimised by engineering the end tunnelling couplings of the chain, as shown explicitly in Appendix D.4. In this case to bypass the edge-localisation effects we also need to add a local chemical potential tuning in the first two and last two sites of the chain, as for the two particles case.

4.6.1 NOON States Generation with a $M=3$ Bound State

We consider three non-interacting particles, initially located in site 1, $|\psi(0)\rangle \propto (a_1^\dagger)^3|0\rangle$. As shown in Sec. 1.8, by defining $P_{jkl}(t) = \frac{|\langle 0|a_i a_j a_k|\psi(t)\rangle|^2}{1+\delta_{ij}+\delta_{jk}+\delta_{ik}+2\delta_{ij}\delta_{jk}}$, the probability to have the three particles in sites i,j,k, an ideal beam splitter transformation (for non-interacting particles) generates an output state with probabilities: $P_{111} = P_{LLL} = 1/8$, $P_{1LL} = P_{11L} = 3/8$. For three strongly interacting particles, the bound state effectively behaves as a single particle, thus the terms P_{1LL}, P_{11L} should be suppressed. Therefore, the output should result in the three particle NOON state $|\psi(t^*)\rangle_{1L} = \frac{1}{\sqrt{2}}(|3,0\rangle + i|0,3\rangle)$, where $|3\rangle = (a^\dagger)^3|0\rangle/\sqrt{6}$. The evidence of the NOON generation is shown in Fig. 4.8, where we plot, as a function of time (in

$t^* \simeq L/J_{\text{eff}}$ units) the probability to have a three particle bound state respectively, in the first site $P_{111}(t)$, in the last $P_{LLL}(t)$ and one particle in the first site and two in the last $P_{1LL}(t)$, for a homogeneous chain with $U/J = 5$ and $L = 5$. Here we set the strength of the edge fields to $\beta' = J^2/8U$, to remove edge-localisation effects, and we find numerically that the splitting field for a balanced operation is $\beta = \beta^{50/50} = 0.099J^3/U^2$. The absence of the term $P_{1LL}(t^*) = P_{11L}(t^*)$ is a clear signature that a NOON state with $N = 3$ is generated between the edges of the chain.

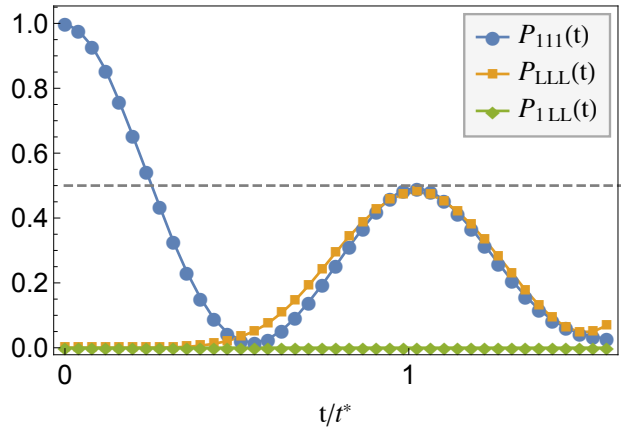

Figure 4.8: Three particle NOON state. Joint probabilities $P_{ijk}(t)$ as a function of the time, in unit of the transfer time t^*, for three particles initially in $|\psi(0)\rangle \propto \left(a_1^\dagger\right)|0\rangle$ for a uniform chain with an impurity $\beta = 0.099J^3/U^2$ and $\beta' = J^2/8U$ in the middle of the chain with $U/J = 5$ and length $L = 5$. The absence of the $P_{1LL}(t)$ term is an evidence that the output state at $t = t^*$ is the NOON state with two particles. The grey dashed line represents the results for an ideal lossless NOON state generation. We found also that $P_{1LL}(t) = P_{11L}(t)$.

From the effective Hamiltonian description we find that to generate a balanced splitting of a bound three particle wave-packet, we need to add a local field $\mu_j = -\beta^{50/50}\delta_{j,L/2+1}$ whose strength, when $L \gg 1$, is $\beta^{50/50} = J^3/8U^2$ (as explained in appendix *B*). However, finite size corrections change the value of $\beta^{50/50}$, and by performing a numerical fit over the data for a uniform chain with $L = 5$ (whose results are shown in the inset of Fig. 4.9), we find that $\beta^{50/50}$ scales with the onsite interaction as $\beta^{50/50} = \alpha J^3/U^2$ where $\alpha \simeq 0.099$. Deviations from the theoretical value of $\beta^{50/50} = J^3/8U^2$, which are shown in Fig. 4.9, have been found by analysing the results obtained for several chain lengths L. Here the dashed grey line represents the theoretical value of the coefficient α of the splitting field for $L \gg 1$.

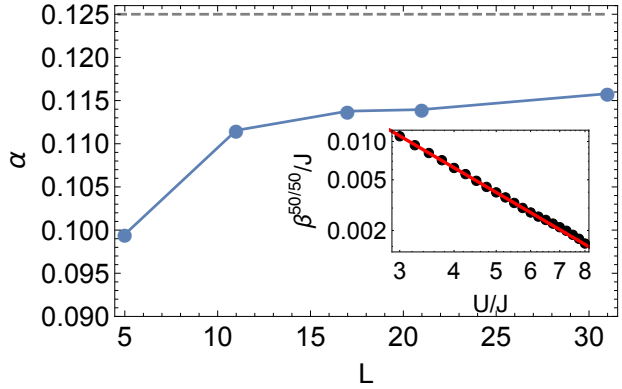

Figure 4.9: Finite-size effects in the three particle NOON state generation. Analysis of the scaling factor α as a function of the chain length L for a three particle bound state, where $\beta^{50/50} = \alpha J^3/U^2$. The dashed grey line represents the theoretical value from the effective Hamiltonian description. (Inset) Analysis of the optimal value of β to produce the NOON state with three particles as a function of U/J in a uniform chain with length $L = 5$. The red line is the fit $\beta^{50/50} = \alpha J^3/U^2$ where $\alpha = 0.099$.

4.7 NOON States for Interferometry Applications

In this section we show how bound states provide an advantage, compared to single particle configurations, for quantum metrology applications. In Sec. 2.3 we have shown how to implement a Mach-Zehnder configuration in a 1D finite lattice model. Specifically, a local impurity in the optical potential implements a beam splitting operation, while mirrors are naturally provided by boundary reflections. By starting from the initial state $|\psi(0)\rangle \propto \left(a_1^\dagger\right)^N |0\rangle$, we generate a NOON state in site $1, L$, as discussed in the previous sections, using the splitting field in the middle of the chain. The next step is to add a phase factor between the two NOON components. This is achieved by freezing the dynamics of the system at the transfer time t^*. Indeed, a controllable phase factor can be added using a local field in the last site of the chain. Finally, once lowered the lattice potential, a second beam splitter operation is performed by the splitting field which produces interference fringes at the endpoints of the chain at time[7] $2t^*$.

For an ideal lossless transformation, the state produced at the two boundary

[7] We have already discussed, in Chap. 2, that the splitting field does not introduce relevant modification of the transfer time.

sites of the chain, at the transfer time t^*, would be

$$|\psi(t^*)\rangle_{1L} = \frac{1}{\sqrt{2}}\left(|N0\rangle + i|0N\rangle\right) . \tag{4.10}$$

Once we apply the phase transformation $\Phi = \mathrm{diag}(1, e^{i\phi})$ (namely a phase shift on site L), a second ideal beam splitting transformation would produce the output state at time $2t^*$,

$$|\psi(2t^*)\rangle_{1L} = \frac{1}{2}\left[\left(1 - e^{iN\phi}\right)|N0\rangle + i\left(1 + e^{iN\phi}\right)|0N\rangle\right] , \tag{4.11}$$

where the phase accumulated is $N\phi$ with N being the number of particle in the NOON state. Therefore, the presence of a NOON state is revealed by measuring the interference fringes[8] (i.e. the probability to have N particle in the first site as a function of ϕ).

We evaluate numerically the interference fringes for a two particle bound state in a uniform chain with length $L = 5$ and $U/J = 5$. A controllable phase factor is introduced after freezing the dynamics of the system, namely by increasing the lattice depth at time $t^* \simeq LU/J^2$, by applying a local field in the last site. Indeed, the Hamiltonian (1.64) is then quenched at t^* to

$$H' = \sum_{j=1}^{L} U n_j(n_j - 1) - \beta_L n_L , \tag{4.12}$$

and once the system evolves for a time t', the phase difference generated between site L and 1 is $\phi = \beta_L t'$. Then for $t > t'$ the lattice potential is lowered again and the dynamics is described again by the Hamiltonian (1.64). We finally let the system evolve for a time t^* and evaluate the probability P_{11} to have the bound particle in the first site at the transfer time[9].

[8] Although previous experimental results measured just the parity of single sites (which would exclude a direct observation of the $N = 2$ case discussed so far), this detection issue in optical lattice has been recently circumvented up to four particles in the same site, as discussed in Sec. 1.4.2.

[9] Alternatively, in Chap. 2 we have discussed a time independent mechanism to introduce a controllable phase factor, via a step-like potential on the right-half of the effective chain, which corresponds to a piecewise constant potential in the Bose-Hubbard model (1.64).

In Fig. 4.10 we show the results for P_{11} as a function of the phase factor ϕ. By comparing our data with the results of an ideal lossless transformation, from Eq. (4.11), (shown as a line in Fig. 4.10) we observe the interference fringes are in the same positions as in the ideal transformation. Because we have considered

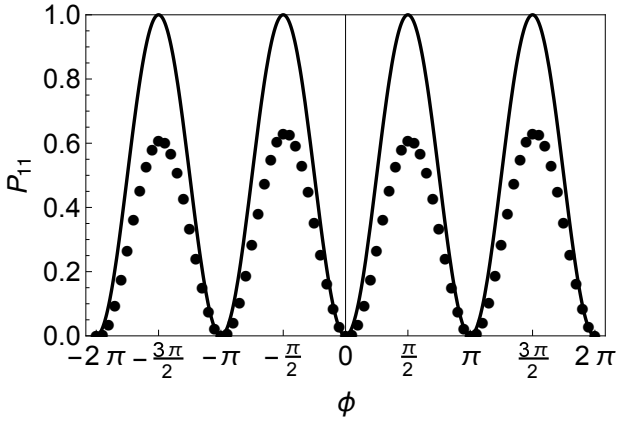

Figure 4.10: NOON state detection with bound particles. Interference fringes in a Mach-Zehnder scheme for a two particle bound state for a chain with $L = 5$ and $U/J = 5$. We plot the probability $P_{11}(t^*)$ to have the bound state particle in the first site after a time evolution of $t^* \simeq LU/J^2$, when a phase factor ϕ is introduced in the system. The line data represent the result for an ideal lossless Mach-Zehnder transformation.

a homogeneous chain, the effect of the dispersion reduces the height of the peaks compared to the ideal case. However, the efficiency of our scheme can be pushed up to 100%, by first engineering the effective Hamiltonian (4.3), using the techniques developed in Chap. 3 for producing a perfect splitting, or via an almost perfect splitting, developed in Chap. 2. Our scheme can be easily extended to bound states with a higher number of particles.

Although parity projection effects has been recently circumvented, up to four particles per site, as discussed in Sec. 1.4.2, we show that the interference fringes generated by the NOON state can be detected, limited the case of $M = 2$, by quenching the inter-particle interaction ($U/J = 0$, i.e. via Feshbach resonances) just after the phase factor is added in the system. In the lossless case the final state of the two boundary sites is

$$|\psi(t'')\rangle_{1L} \propto \left[(1 - ie^{iN\phi})|20\rangle + (ie^{iN\phi} - 1)|02\rangle + 2i(1 + e^{iN\phi})|11\rangle\right] .$$

Here t'' is the transfer time of free particles in the lattice $t'' \simeq L/J$. The probability to find one particle in each end at t'' is

$$P_{1L}(t'') = \frac{2\,(\sin N\phi - 1)}{\sin N\phi - 3}\ . \tag{4.13}$$

From the latter we see with a choice of $\phi = -5\pi/4$ the output state results in $|\psi(t'')\rangle_{1L} = |11\rangle$, which can be measured using single particle fluorescence techniques. The latter detection scheme has two main advantages: first of all it circumvents the parity projection measurement issue, because the fringe measurement requires only single atom detection. In second place the decoherence influence is reduced, because after the phase factor is added, the particles are non-interacting, which means that this scheme is faster compared to the bound state case. In Fig. 4.11 we show the results obtained for the probability to observe one particle in each end, in a chain with $L = 5$ and $U/J = 5$, at time t'', compared to the lossless case in Eq. (4.13).

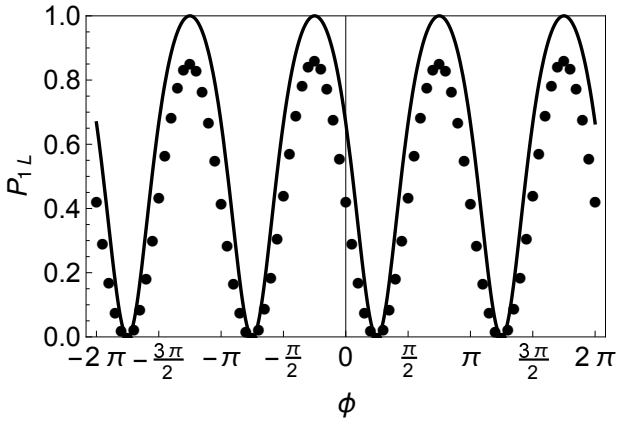

Figure 4.11: Two particle NOON Detection after Quenching Dynamics. Interference fringes after a quench to $U/J = 0$. The chain has length $L = 5$ and we set $U/J = 5$ for generating the two particles NOON state in the edges at time $t^* \simeq LU/J^2$. Once the NOON state is generated the dynamics is frozen by increasing the lattice depth, then a controllable phase factor ϕ is added by tilting the lattice. Once the inter-particle interaction is quenched to $U/J = 0$ we let the system evolve, and we measure the probability $P_{1L}(t'')$ where $t'' \simeq L/J$ is the transfer time of the free chain.

4.8 Quantum Enhanced Metrology with Bound States

As shown in Fig. 4.10, the interference fringes using a two particle NOON state have half the spacing compared to a single-particle case in Fig. 1.18. This is important because a larger slope of the probabilities as a function of ϕ that, in turn, enables the estimation of the phase ϕ from the measurements with higher sensitivity, as discussed in Sec. 1.9.2.

To make this point quantitative, a threshold on the phase precision estimation can be made by computing the Quantum Fisher Information F_Q, which provides a lower bound on the variance of an estimator $\hat{\phi}$ of the phase ϕ via the Cramér-Rao bound $\left(\Delta\hat{\phi}\right)^2 \geq 1/(\nu F_Q)$, where ν is the number of independent measurements. Indeed, the variance of the phase estimation precision for and ideal NOON states scales as $1/M$, as shown in Sec. 1.9.2. Here we evaluate numerically F_Q when our scheme for producing NOON state is employed.

We generate a NOON state by letting the initial state $|\psi_{t=0}\rangle \propto \left(a_1^\dagger\right)^M |0\rangle$ to evolve for $t \simeq LU^{M-1}/J^M$. We add a relative phase factor between the edge sites, as described in the previous section, by using a local field in the last site of the chain. After these steps we get then the state $|\psi(\phi)\rangle = \exp\left(-in_L\phi\right)|\psi_t\rangle$ which, in the ideal case, would be a ϕ-dependent NOON state $(|M0\rangle_{1L} + ie^{-i\phi M}|0M\rangle_{1L})/\sqrt{2}$ on sites $1, L$. In Sec. 1.9.2 we find that the Quantum Fisher Information can be computed using the formula

$$F_Q = 4\Delta n_L^2 = 4\left(\langle n_L^2\rangle - \langle n_L\rangle^2\right), \tag{4.14}$$

which in the ideal case results in $F_Q = M^2$. We now show that even the imperfect NOON states obtained with uniform chains are sufficient to achieve a quantum enhanced sensitivity. We consider a uniform chain with length $L = 5$ and a bound state with $M = 2, 3$. In Fig. 4.12 we plot the best achievable phase uncertainty $\Delta\phi = 1/\sqrt{F_Q}$, in a single measurement $\nu = 1$, as a function of the onsite interaction U/J for a two and a three bound state. The grey and the red lines represent respectively the "classical" limit $\Delta\phi_{\rm cl} = 1/\sqrt{M}$ (obtained e.g. using coherent states where

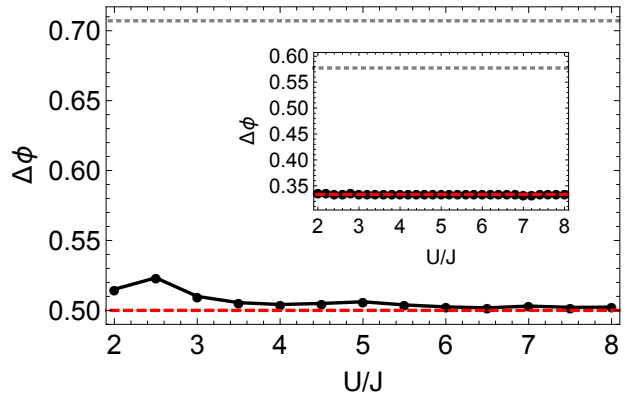

Figure 4.12: Phase estimation precision for bound states. Phase estimation precision $\Delta\phi = 1/\sqrt{F_Q}$, where F_Q is the Quantum Fisher Information for the estimator n_L in a uniform chain with $L = 5$ respectively for a two particle bound state and for a three particle bound state (inset), as a function of the onsite interaction U/J. The red dashed/grey dotted lines represent the ideal quantum/classical lower bound, respectively $\Delta\phi_{\text{quant}} = 1/M$ and $\Delta\phi_{\text{cl}} = 1/\sqrt{M}$.

M is the average number of particles) and the ideal quantum limit $\Delta\phi_{\text{quant}} = 1/M$.

The results obtained for F_Q for a homogeneous chain can be improved by a full engineering of the coupling profile. Indeed, as discussed previously, by engineering the effective coupling profile (4.3), with a perfect splitting strategy, Chap. 3, the NOON state created has unit fidelity and it fulfils the scaling $1/M$ for the value of F_Q.

4.9 Conclusions

In this chapter we have analysed the possibility to transfer bound particle states between the endpoints of a finite lattice and their use for small cat state (NOON state) generation, using a minimal control setup. We have derived an effective single-particle theory to describe the dynamics of bound states in a Bose-Hubbard model showing how edge-localisation effects, that correspond to effective edge fields, influence the dynamics when the system is initially located in one lattice end. We have found the existence of a quasi-localisation effect for a two particle bound-state and we have shown that it increases of the delocalisation time from one end, compared to the single particle case.

Via suitable static local impurities, located close to the lattice edges, we have

inhibited localisation effects. This in turn has allowed us to realise transformations between far sites when strongly interacting particles are involved. Specifically, we have showed how minimal engineering schemes, developed in a single-particle framework, can be implemented for bound states to enhance the state transfer efficiency. Then, we have found how to split the propagating bound state wavefunction, with a local barrier, which in turn has been exploited to produce small cat states (NOON states) with high fidelity, in a minimal control setup.

The obtained NOON states in a Mach-Zehnder configuration has shown to provide an improvement of the phase estimation between the output arms opening up to quantum enhanced interferometry applications. Our method can be straightforwardly extended to fully engineered chains to realise 100% fidelity operations between distant sites, such as the perfect state transfer of bound-particle states or the perfect NOON state generation in an arbitrary long chain.

Compared with classical setups [177], and also to other schemes for atom interferometry [187, 219] the generation of NOON is important to enhance the estimation precision of the phase difference between the output arms of an interferometer [173, 175, 177, 220], making it highly attractive for technological applications. For example super-resolution for NOON states with $N = 2, 3$ has been recently shown experimentally for microscopy purposes [212].

In the previous chapters we have analysed how the lattice profile can be modelled in low control setups to realise useful transformations between remote sites of a quantum wire. In the next chapter we exploit directly the role of the interaction to analyse the possibility to generate a quantum gate between remote qubits, via scattering interaction.

Chapter 5

Quantum Gates via Scattering Interaction

5.1 Introduction

In the previous chapters we have analysed applications of quantum walk of single and multiple excitations, in a weakly and strongly interacting regime, in a 1D lattice model. The possibility to control the motion of neutral atoms in reconfigurable geometries opens up a natural question, namely whether atoms, as "flying qubits" in a lattice, can be used for quantum computation applications. In this scenario, as sketched in Fig. 5.1, a 1D lattice waveguide, where atoms can naturally move, acts as an "on-demand" bus for connecting well separated quantum registers or distant qubits of the same register.

Quantum logic between flying qubits usually exploits the atom indistinguishability of non-interacting particles, hence the name "linear optics" quantum computation [165, 214]. An effort towards the realisation of the linear optics paradigm with atoms has been explored in Chap. 2, where for such an approach to be viable one has to engineer circumstances so that the effect of the inter-particle interactions can be neglected. On the other hand, it is known that information processing applications (e.g. two qubit quantum gates) in photonic systems can be realised introducing large cross-Kerr non-linearities through atomic media [214]. However, because the strength of these terms is usually weak, an open question is whether the atom nat-

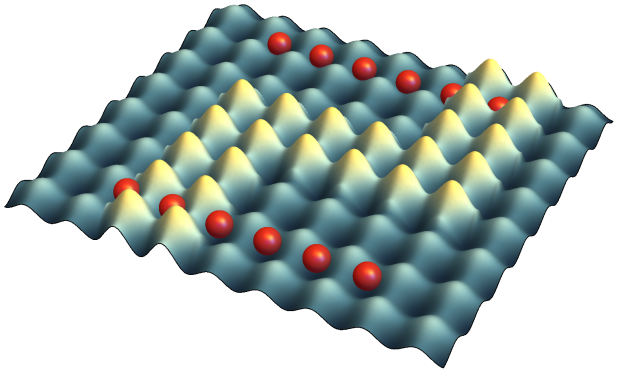

Figure 5.1: Quantum gates between flying qubits. Two atom registers, made of neutral atoms (red) trapped in an optical potential are connected with an "on demand" quantum channel, made of an atom waveguide (yellow), realised via optical potential control. Once the trapping potential is lowered, the addressed atoms propagate through the guide, realising a interaction between two qubits of different quantum registers.

ural interaction could provide an advantage for quantum computation compared to photonic setups. Indeed, strong non-linearities, from the atom-atom interaction, are easily achievable in optical lattices.

Another advantage of using atoms, compared to photonic system, is that qubits can be interchanged from static (e.g. for building a quantum register) to dynamics, (e.g. for quantum gates and state transfer) by controlling the lattice potential depth.

In this chapter we consider a system of two particles in a 1D lattice, and we exploit their internal degree of freedom (i.e. two hyperfine levels of the atoms) to encode two states of a qubit. Single qubit operations are easily implemented via microwave radiation, together with a tightly focussed laser, or using a two photons Raman transition [15,45]. We consider an intermediate interaction regime, (i.e. with finite value of the onsite interaction U in the Hamiltonian (1.64)) with the aim of realising a quantum gate between two flying particles in the lattice. A two qubits entangling gate is indeed important, as it enables universal quantum computation when combined with arbitrary single qubit rotations [221].

While quantum gates exploiting the mutual interactions of two material flying qubits have not been considered yet in full detail, the corresponding situation for static qubits has been widely studied (e.g., [29, 47, 48, 53, 54]). However, these methods typically require a precise control of the interaction time of the qubits or

between them and a mediating bus (e.g., [222–224]. Still static qubits offer the natural candidate for information storage.

While it is known that both spin-dependent [225, 226] and spin-independent [227,228] scattering can entangle, it is highly non-trivial to obtain a useful quantum gate. One example is provided in [229], where a two-qubits quantum gate is implemented via a scattering process between a flying and a static qubit (as a magnetic impurity) and a potential barrier in a 1D waveguide. However, generally the reflection and transmission amplitudes in scattering processes depend on the internal states of the particles involved, making difficult to ensure a unitary operation, for instance a quantum gate that acts exclusively on the limited logical space (e.g. internal/spin) that encodes the qubits. A scattering based approach for creating entanglement in a lattice setup has been consider in [230], although it requires periodic boundary conditions and careful initialisation and control of particles' momenta. On the contrary in this chapter we show how an entangling gate can be implemented, in a low control process, through the scattering of flying qubits in a finite lattice, that does not require any external control for controlling the particle momenta. This makes our setup attractive for applications as the qubits can be interchanged from static to mobile, thus making possible both storage and computation with the same physical setup [63].

5.2 Entangling Gate via Spin Independent Elastic scattering of Two Particles

As a first step, to build a model for a quantum gate between two distant register atoms, we consider a spin independent contact interaction between two particles, with initial momenta $\mathbf{p}_1 \equiv (p_1, 0, 0)$ and $\mathbf{p}_2 \equiv (p_2, 0, 0)$, in a 1D waveguide. Such a one-dimensional system may be experimentally realised by confining the atoms to a highly elongated harmonic trap of transverse frequency $\omega_\perp$ and axial frequency $\omega_z = \lambda \omega_\perp$, with $\lambda \ll 1$ [77]. In a 1D waveguide, the system can be described by a

Lieb-Liniger model, with Hamiltonian [77, 94],

$$H = -\sum_{j=1}^{2} \frac{\partial^2}{\partial x_j^2} + 2c\delta(x_1 - x_2), \tag{5.1}$$

where x_1 and x_2 are the position of the two particles and c is the strength of the collisional delta interaction. For two incoming particle with momenta p_1 and p_2, the energy is $E = p_1^2 + p_2^2$, and the Hamiltonian (5.1) preserves the total momenta and the energy during the scattering process [77], namely the outgoing particles also have the same values p_1 and p_2. We consider the elastic scattering of two particles, with initial momenta p_1 and p_2 in a 1D system. The result of the collision can be described through a scattering matrix formalism, as a transformation between initial states to reaction products [84, 231]. The matrix elements of S are related to the transition probability from free particle in-states to free particle out-states. In other words, calling $U(t,t_0) = \exp(-iH(t-t_0))$ the time-evolution operator and $|\psi_a(-\infty)\rangle = |\phi_a\rangle$ and $|\psi_a(+\infty)\rangle = S|\phi_a\rangle$ the initial/final state of the system, with $|\phi_a\rangle$ an eigenfunction of H, the S-scattering matrix is defined as

$$S = \lim_{t\to+\infty} \lim_{t_0\to-\infty} U(t,t_0), \tag{5.2}$$

whose matrix elements are explicitly connected to the transition probability from a state $|\phi_a\rangle$ to $|\phi_b\rangle$ as $P_{a\to b} = |\langle\phi_b|S|\phi_a\rangle|^2$. A generic two particle state, in a domain $0 \le x_1 \le x_2 \le L$, that can be written as

$$|\psi\rangle = \sum_{0\le x_1\le x_2\le L} \psi(x_1,x_2)|x_1,x_2\rangle\ , \tag{5.3}$$

where x_1 and x_2 are the positions of the two particles and p_1 and p_2 their momenta. The wavefunction for two spinless particles in the model (5.1) must satisfy the free-particle Shrödinger equation except when they occupy the same position [77]. This

means that one ansatz for the wavefunction of the system is

$$\begin{aligned}\psi(x_1,x_2) &= e^{ip_1x_1}e^{ip_2x_2} + S(p_1,p_2)e^{ip_2x_1}e^{ip_1x_2} = \\ &= e^{i\left(p_1x_1+p_2x_2-i\frac{\phi_{12}}{2}\right)} + e^{i\left(p_2x_1+p_1x_2+i\frac{\phi_{12}}{2}\right)}, \qquad \text{for } x_1 \leq x_2,\end{aligned} \tag{5.4}$$

where $S(p_1,p_2) \equiv e^{i\phi_{12}}$ is a phase factor acquired[1] by the wavefunction when the two particles scatter through each other [234, 235]. For incident particles with momenta $p_2 > p_1$, the scattering matrix, has been computed in [236], whose expression is

$$S(p_1,p_2) = \frac{p_2 - p_1 - ic}{p_2 - p_1 + ic}. \tag{5.5}$$

We consider the case in which two particles, with some internal degrees of freedom to encode a qubit state, collide. We assume that the collision can be modelled as a spin independent contact interaction for point-like particles, as in Eq. (5.1), and we label the relevant internal states as $|\uparrow\rangle$, $|\downarrow\rangle$. For the case of two bosons (e.g. a spin-1 particle), in a symmetrical state of the internal degrees of freedom, the external degrees of freedom have also to be symmetric, and the S scattering matrix is the same as for spinless bosons, Eq. (5.5). On the other hand, because the two particles are bosons, an antisymmetric spin state means that the spatial wave function of the two particles is also antisymmetric, so that the amplitude of the total wavefunction for $x_1 = x_2$ is zero (the chance of a contact interaction is zero, then the two particles do no scatter from each other). These observations lead to the S-scattering matrix,

$$S^B(p_1,p_2) = \frac{(p_2 - p_1) - ic\Pi_{12}}{p_2 - p_1 + ic}, \qquad \text{for } p_2 > p_1, \tag{5.6}$$

where Π_{12} is the SWAP (permutation) operator acting on the spin degree of freedom. More precisely, calling $|v\rangle_1$ and $|u\rangle_2$ two arbitrary spin state of particles 1 and 2,

$$\Pi_{12}|v\rangle_1|u\rangle_2 = |u\rangle_1|v\rangle_2, \tag{5.7}$$

[1] Indeed, for instance, for $p_1 > p_2$, because $x_1 \leq x_2$ the second term means that the two particles have acquired a phase factor due to the collision. In the S-matrix formalism one can interpret the two total wavefunction as the superposition of an "incoming wave" and an "outcoming wave", while the S-matrix is defined as their ratio [232, 233].

so that Π_{12} is a 4×4 matrix that can be rewritten in terms of projectors in the symmetric/antisymmetric subspaces, $\Pi_{\pm}$, as

$$\Pi_{\pm} = \frac{1}{2}\left(\mathbf{1} \pm \Pi_{12}\right) \ . \tag{5.8}$$

If the spin state is symmetric the spatial wavefunction is also symmetric so a phase factor given by Eq. (5.5) is acquired during the collision. Conversely for an antisymmetric spatial wavefunction the particles has zero probability to be in the same site so no phase factor is acquired during the collision. Therefore, the scattering matrix for bosons with an internal degree of freedom is

$$S^B(p_1,p_2) = \Pi_- + S(p_1,p_2)\Pi_+ \ , \tag{5.9}$$

which, by direct substitutions leads to Eq. (5.6). In the fermion case (e.g.for a spin $1/2$ particle), the S-scattering matrix has been computed by C. N. Yang [237]. Using the decomposition in terms of projection operators,

$$S^F = S(p_1,p_2)\Pi_- + \Pi_+ \ , \tag{5.10}$$

the scattering matrix for fermions with an internal degree of freedom is

$$S^F(p_1,p_2) = \frac{(p_2-p_1)+ic\Pi_{12}}{p_2-p_1+ic}, \qquad \text{for } p_2 > p_1. \tag{5.11}$$

We consider a frame in which two qubits are moving towards each other, so that we label the qubit that moves towards right as A and B the one with momentum towards left. Hereafter we represent the state of the system in the typical second quantisation form for flying qubits [238], as for instance $|\uparrow\rangle_A \equiv a^{\dagger}_{p_A,\uparrow}|0\rangle$. Given the possible input state of the two flying qubits system, the output results from the scattering matrix

Eq. (5.6) and Eq. (5.11), as

$$\begin{aligned}
S^{B/F}|\uparrow\rangle_A|\uparrow\rangle_B &= e^{i\phi_{B/F}}|\uparrow\rangle_A|\uparrow\rangle_B,\\
S^{B/F}|\downarrow\rangle_A|\downarrow\rangle_B &= e^{i\phi_{B/F}}|\downarrow\rangle_A|\downarrow\rangle_B,\\
S^{B/F}|\uparrow\rangle_A|\downarrow\rangle_B &= \frac{p_{A+B}|\uparrow\rangle_A|\downarrow\rangle_B \mp ic|\downarrow\rangle_A|\uparrow\rangle_B}{p_{A+B}+ic},\\
S^{B/F}|\downarrow\rangle_A|\uparrow\rangle_B &= \frac{p_{A+B}|\downarrow\rangle_A|\uparrow\rangle_B \mp ic|\uparrow\rangle_A|\downarrow\rangle_B}{p_{A+B}+ic},
\end{aligned} \tag{5.12}$$

where $p_{A+B} = p_A + p_B$. The phase factors accumulated are $e^{i\phi_B} = \frac{p_{A+B}-ic}{p_{A+B}+ic}$ and $e^{i\phi_F}=1$, where B/F indicate the two bosons/fermions case. It is clear from Eq. (5.12) that, unless either p_{A+B} or c are equal to zero, the result of the collision process is an entangled state, for the initial state $|\uparrow\rangle_A|\downarrow\rangle_B$ or $|\downarrow\rangle_A|\uparrow\rangle_B$. Specifically, the optimal condition

$$p_{A+B} \approx c, \tag{5.13}$$

generates the maximum entanglement possible from the collision, as the right hand sides of the last two lines of Eq. (5.12) correspond to the maximally entangled states $\frac{e^{-i\frac{\pi}{4}}}{\sqrt{2}}(|\uparrow\rangle_A|\downarrow\rangle_B \mp i|\downarrow\rangle_A|\uparrow\rangle_B)$ and $\frac{e^{-i\frac{\pi}{4}}}{\sqrt{2}}(|\downarrow\rangle_A|\uparrow\rangle_B \mp i|\uparrow\rangle_A|\downarrow\rangle_B)$ respectively, as sketched in Fig. 5.2(a). The above gate could aid universal quantum computation through scattering with both bosonic and fermionic qubits. The quantum gate, Eq. (5.12), exploits a low control process, as the only requirement is local rotations of the qubit state, to initialise the internal state of the colliding atoms.

5.3 Quantum Gate for Distant Stationary qubits in a Lattice

In the previous section we have discussed a mechanism to implement a quantum gate between two flying qubits in a 1D waveguide, exploiting a spin independent collisional interaction. In this section we consider the implementation of the model in an optical lattice for two particles with an internal spin degree of freedom. A discrete variant of the Hamiltonian (5.1) is represented by the Hubbard model [232,

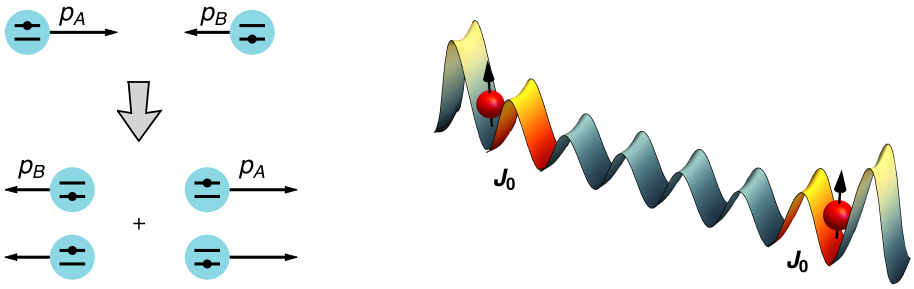

Figure 5.2: Quantum gate between flying atomic qubits. (a) Two identical particles in a 1D waveguide, labelled as A,B accordingly to their momenta direction p_A, p_B, produce an entangled state after the collision. An internal state encodes the qubit state. (b) Implementation of the scheme in a finite lattice. Two particles, with an internal spin degree of freedom, are initially located in the edge sites of a finite lattice. The chain couplings, in Eq. (1.64), are set to $J_j = J_0$ in sites $1, L$, and $J_j = J$ in the bulk sites.

236], as

$$H = \sum_{j,\alpha} \frac{J_j}{2} \left(a^\dagger_{j,\alpha} a_{j+1,\alpha} + H.c. \right) + \sum_{j,\alpha,\beta} \frac{U_j^{\alpha\beta}}{2} n_{j,\alpha} n_{j,\beta}, \tag{5.14}$$

where $\alpha, \beta \in \{\uparrow, \downarrow\}$ label the two relevant internal state (e.g. two hyperfine states). In a chain of length L, the free-space evolution in Eq. (5.1) is replaced by particle hopping. For a homogeneous chain $J_j = J$, $U_j^{\alpha\beta} = U^{\alpha\beta}$, particle collisions lead to the scattering matrix given by Eq. (5.6), with the substitutions [232, 239, 240],

$$p_j \to \sin p_j, \qquad c \to U^{\alpha\beta}/J. \tag{5.15}$$

Therefore, the condition to get the maximum entanglement, Eq. (5.13), is realised for $\sin p_1 - \sin p_2 \sim 2U$, where $U \equiv U^{\uparrow\downarrow}/2J$.

As a concrete realisation we consider two ^{87}Rb atoms loaded in a 1D optical lattice of length L, where two particles are initialised in the edge-points via single-site addressing techniques, as discussed in Sec. 1.4.2. To encode the spin degree of freedom, as relevant internal states we consider two distinguishable hyperfine states, namely[2] $|\uparrow\rangle \equiv |F = 1, m_F = -1\rangle$ and $|\downarrow\rangle \equiv |F = 2, m_F = 1\rangle$. As discussed,

[2] Spin-exchange collisions are highly suppressed for these states, due to the little difference, less than 5%, between the triplet and the singlet scattering lengths [77].

in Sec. 1.3.5, the collisional interaction parameters $U^{\alpha\beta}$ depends on the strengths $g_{3D}^{\alpha\beta}$, accordingly to Eq. (1.76). The coupling strength $g_{3D}^{\alpha\beta}$ are connected, via Eq. (1.54), to the s-wave scattering lengths. Numerical values are reported in Tab. E.3. Typically, as discussed in Sec. 1.3.2, the s-wave scattering length values can be tuned via Feshbach resonances. However, as discussed in Sec. 1.3.2, this is usually difficult in the specific case of ^{87}Rb. Therefore, to control the interaction parameters $U^{\alpha\beta}$, we control the depth of the lattice potential, as shown in Eq. (1.76). To reach a one-dimensional regime we set the harmonic lattice transverse trapping frequency to $\omega_\perp/2\pi\simeq 18$ kHz. The 1D pseudo-potential coupling constants, $g_{1D}^{\alpha\beta}$, are obtained from the 3D measured values, Tab. E.3, via Eq. (1.57). We find $g_{1D}^{\uparrow\uparrow} = 1.14\times10^{-37}$ Jm, $g_{1D}^{\uparrow\downarrow} = 1.12\times10^{-37}$ Jm and $g_{1D}^{\downarrow\downarrow} = 1.09\times10^{-37}$ Jm.

In the previous section we have shown that in a 1D waveguide, an entangling gate is obtained, via Eq. (5.12), by initialising the two particle momenta and tuning the interaction collisional parameter, via Eq. (5.13). Then for flying qubits we have considered a fixed c, and we have tuned p_j to obtain the desired gate. On the other hand, in an optical lattice setting we initialise two particles in the edge sites with zero initial velocity. Therefore, because of the dispersive dynamics in the scattering region the quasi-momenta have a distribution, whose width depends on the number of lattice sites L. In other words, in a lattice, although $U_{\alpha\beta}$ can be controlled precisely, a control of the quasi-momentum requires the creation of a wave-packet namely control and initialisation of many-sites. This kind of control can be avoided, by initially placing two particles in the boundaries of the lattice, as sketched in Fig. 5.2(b), (particle A on the left and particle B on the right) and locally tuning the coupling J_0 between the boundaries and the rest of the chain (all the other couplings are uniform J_j=J), as discussed in Sec. 1.6.4.1. Indeed, an optimal choice of J_0/J has a two-fold effect: firstly it generates two wave-packets whose momentum distribution is Lorentzian, narrowed respectively around p_A=$-p_B\simeq\pm\pi/2$, whose width depends on J_0; secondly it generates a ballistic quasi-dispersionless evolution, allowing an almost perfect reconstruction of the wave-packets after the transmission, (occurring at time $t^* \sim L/J$) in the opposite end.

In the scheme, Fig. 5.2(b), two particles are initially located in opposite edge sites, then they interact close to the centre of lattice. Finally, they reach the end-points again where, because of the OPT coupling scheme, Sec. 1.6.4.1, they are almost localised, allowing a single site read-out procedure. As we previously mention in this section, because p_{A+B} is fixed, the maximum amount of entanglement is generated from the transformation, Eq. (5.12) and Eq. (5.15), for

$$U^{\uparrow\downarrow}/2J = |\sin p_{A+B}| = 1. \tag{5.16}$$

We find, from Eq. (1.76), that for ^{87}Rb the optimal condition is satisfied for a lattice depth of $V_0/E_R \simeq 2.18$, which corresponds to $J/\hbar \simeq 242\ Hz$. This is shown in Fig. 5.3, where the ratio $U^{\alpha\beta}/J$, evaluated from asymptotic expressions, Eq. (1.76), is plotted as a function of the lattice depth V_0, for the one dimensional coupling strength $g_{1D}^{\alpha\beta}$.

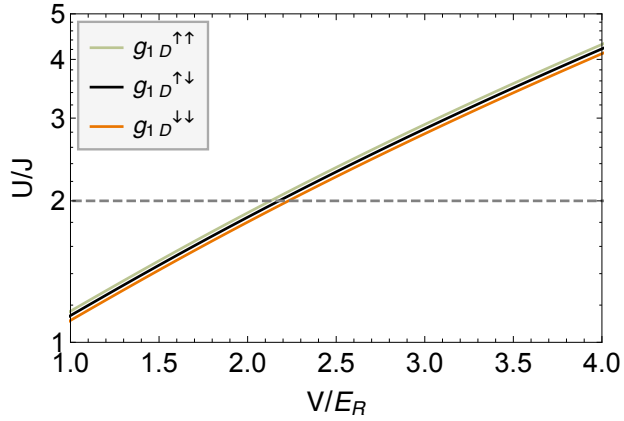

Figure 5.3: Optimal condition for the gate. Plot of the ratio $U^{\alpha\beta}/J$ as a function of the lattice depth V_0 (in recoil energy units), using the one dimensional coupling strength $g_{1D}^{\alpha\beta}$, where $\alpha,\beta \in \{\uparrow,\downarrow\}$ for a transverse confinement of $\omega_T/2\pi = 18\ kHz$. The grey dashed line is the value, in Eq. (5.16), that optimises the quantum gate Eq. (5.12).

5.4 Efficiency of the Scheme

The efficiency of the scheme developed in the previous section is affected by the transmission quality in the lattice and by the quasi-momenta distribution width, close to the interaction region. The optimal coupling scheme in our setup guarantees that

the transmission quality is above 85% even for long chain, as shown in Tab. 1.1. On the other hand, once the interaction parameter $U^{\alpha\beta}$ is set to the optimal value, Eq. (5.16), because the momentum profile has a finite width around $p_{A+B} \simeq \pi/2$, the transformation, Eq. (5.12), yields to slightly different gates for different momentum components. In this section we quantify the efficiency of our scheme numerically finding the join probability amplitude, $A_{jk}^{\alpha\beta}(t^*)$, to have the particle A in site j and internal state α, and a particle B in site k and internal state β. The gate time is indicated with t^* and L is the chain length. The output of our system depends on the internal state of the initial condition, namely $A_{1L}^{\alpha\beta}(0) = 1$. As we are considering two boson/fermion particles with two distinguishable internal state, we simulate the dynamics through methods developed in Appendix A.3.

As a preliminary step, we consider a single particle, in $|\psi(0)\rangle = a_1^\dagger|0\rangle$, in a chain described by a Bose-Hubbard model (1.64), with J and J_0 respectively the bulk/endpoint tunnelling strength, as discussed in Sec. 1.6.4.1. We numerically find the values of J_0/J and t that maximises the probability $P_L \equiv |\langle L|\psi(t)\rangle|^2$ close to $t \sim L$. We call these values J_0^{opt}, the optimal coupling parameter, and t^* the gate time. As we are considering a finite chain, we expect finite-size corrections on the optimal interaction value compared to the ideal condition, Eq. (5.16). Therefore, to find the condition that maximise the efficiency of the transformation Eq. (5.12), we consider two distinguishable particles in the initial state $A_{1L}^{\uparrow\downarrow}(0) = 1$ and we numerically compute $A_{1L}^{\uparrow\downarrow}(t^*)$ and $A_{L1}^{\uparrow\downarrow}(t^*)$, finding that

$$A_{1L}^{\uparrow\downarrow}/A_{L1}^{\uparrow\downarrow}(t^*) = -iU^{\uparrow\downarrow}/U^{\text{opt}}\,, \tag{5.17}$$

where U^{opt} is the value of $U^{\uparrow\downarrow}/2J$ that optimises the transformation Eq. (5.12) for distinguishable particles, as shown in Fig. 5.4. Indeed, in Fig. 5.4(a) we find that $|A_{1L}^{\uparrow\downarrow}/A_{L1}^{\uparrow\downarrow}|(t^*)$ has a linear dependence from $U \equiv U^{\uparrow\downarrow}$. We find the optimal value U^{opt} from a linear fit over the data. The value found is used in Fig. 5.4(b), where we show that for a chain of $L = 21$, the optimal choice of $U^{\uparrow\downarrow}/J = 2U^{\text{opt}} = 2 \times 0.95$ realises the condition $P_{1L}^{\uparrow\downarrow}(t^*) = P_{L1}^{\uparrow\downarrow}(t^*)$, where we have defined the probabilities $P_{jk}^{\uparrow\downarrow}(t^*) \equiv |\langle jk|\psi(t^*)\rangle|^2$. The phase difference is shown in the inset of Fig. 5.4(b),

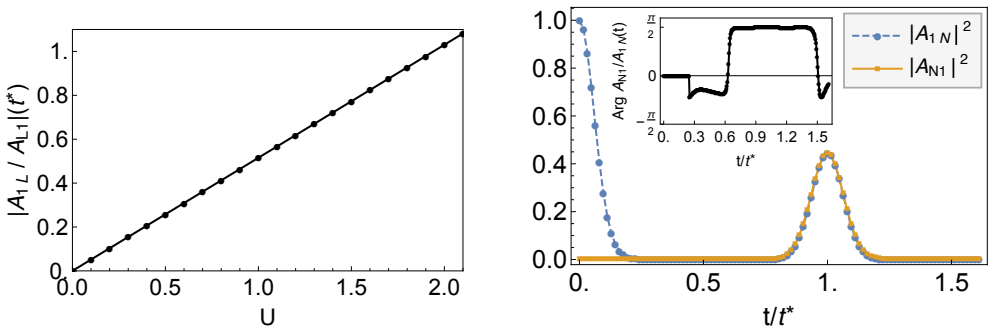

(a) (b)

Figure 5.4: Quantum gate via scattering collision. (a) Plot of the ratio $|A^{\uparrow\downarrow}_{1L}/A^{\uparrow\downarrow}_{L1}|(t)$ as a function of the interaction $U \equiv U^{\uparrow\downarrow}$. The value of $U^{\rm opt}$ is found from a linear fit over the data. (b) Plot of the probability $|A^{\uparrow\downarrow}_{1L}(t)|^2$ (dashed blue) and $|A^{\uparrow\downarrow}_{L1}(t)|^2$ (orange line), as a function of t (in units of the gate time $t^* \simeq 26.08/J$ in a $L = 21$ chain. The mutual interaction is set to the optimal value $U^{\uparrow\downarrow} = 2U^{\rm opt} = 2 \times 0.95$. (inset) Phase difference between the amplitude probability $A^{\uparrow\downarrow}_{L1}(t)$ and $A^{\uparrow\downarrow}_{1L}(t)$ as a function of the time t/t^*.

where we observe that the phase factor at the gate time $t^* \simeq 26.08/J$ is $\pi/2$. The results are then compatible with the gate Eq. (5.12), where the $U^{\rm opt}$ is close to the ideal value in Eq. (5.16).

To better characterise the system, we evaluate how the optimal parameter $U^{\rm opt}$ depends on the chain length L, showing that the agreement with the ideal value (grey dashed line) improves for longer chains, as shown in the inset of Fig. 5.5(a). We evaluate the amount of entanglement generated in the transformation via the Concurrence [241–243]. Specifically, it can be shown that Concurrence between the first and the last sites of the chain is $C_{1L}(t^*) = 2|A^{\uparrow\downarrow}_{1L}A^{\uparrow\downarrow *}_{L1}|(t^*)$ [244–246]. By exploiting techniques in Appendix B and C, from an asymptotic analysis, since the wave-packets are peaked around $p_j \simeq \pm\pi/2$, we find that

$$C^{\uparrow\downarrow}_{1L} = f^4_{1L}\frac{2U/U^{\rm opt}}{(U/U^{\rm opt})^2+1}, \tag{5.18}$$

where f_{1L} is the transmission probability from site 1 to site N at the transmission time and $1-U_{\rm opt} \propto \Delta^2$, where Δ is the width of the wave-packet. For optimal values, Sec. 1.6.4.1 and [146], of $J_0 \approx 1.03L^{-1/6}$ one finds $\Delta \simeq 0.53L^{-1/3}$ and accordingly $U_{\rm opt} \approx 1-0.41N^{-2/3}$, as shown in the inset of Fig. 5.5(a) (red line). In Fig. 5.5(b) we

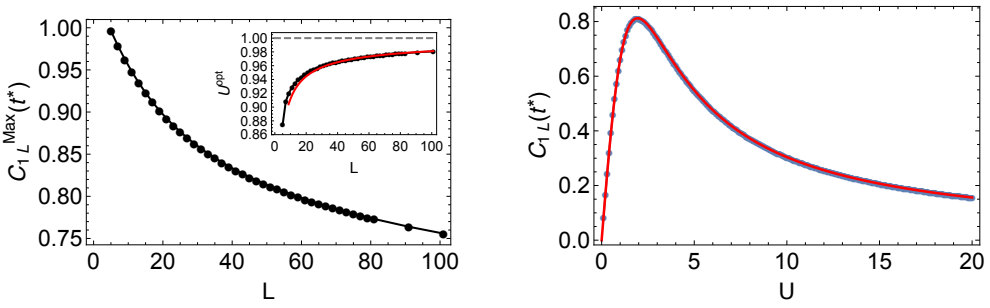

(a) (b)

Figure 5.5: Scattering of two distinguishable particles. (a) Scaling of the maximum of Concurrence $C_{1L}^{\uparrow\downarrow}(t^*)$ as a function of the chain length L. The maximum is found from the fit, Eq. (5.18), over the data in Fig. 5.5(b). (inset) Optimal inter-particle interaction strength U^{opt} as a function of the chain length L. Numerical values are found via a linear fit over the data of the ratio $|A_{1L}^{\uparrow\downarrow}/A_{L1}^{\uparrow\downarrow}|(t^*)$ as a function of the interaction $U^{\uparrow\downarrow}/J$ in Fig. 5.4(a). (b) Concurrence $C_{1L}^{\uparrow\downarrow}$ as a function of $U \equiv U^{\uparrow\downarrow}/J$ for a chain of $L = 51$. The maximum of concurrence $f_{1L}^4 = 0.81$ appears for $U^{\text{opt}} = 0.97$.

show the concurrence $C_{1L}^{\uparrow\downarrow}$ as a function of $U \equiv U^{\uparrow\downarrow}$, where the red line represents a fit over the data, accordingly to Eq. (5.18), for a chain with $L = 51$. On the other hand, the maximum value of the concurrence depends only on the transfer quality f_{1L} which is non-zero even in the thermodynamic limit, as shown in Sec.1.6.4.1, which results in the maximal concurrence $C_{1\infty}^{\max} = f_{1\infty}^4 \simeq 0.51$. Explicit results for a finite chain are shown in Fig. 5.5(a), where we show how the maximum of concurrence, found from a fit over the data in 5.5(b), scales with the length of the chain L.

5.5 Conclusions

In view of the recent unprecedented capabilities of observing atomic quantum walks in lattice experiments [22, 32, 33, 69, 129], in this chapter we have shown how the natural interaction between atoms can be harnessed for quantum logic. Specifically, we have analysed a low control method to exploit the spin independent scattering of two qubits, initially in remote sites of a lattice, to implement an entangling quantum gate. Compared to existing studies [45, 53, 54, 57, 230] our strategy represents a low control technology as it requires only single-site rotations (to initialise the gate) and the lattice depth control (or the onsite-interaction), while atom momenta control

is naturally provided via a tuning of the end hopping couplings. Our scheme is compelling for applications as the lattice depth control makes possible to interchange static to flying qubits, avoiding the necessity to seek some mechanism to couple static to mobile particles. Indeed it is highly desirable to apply entangling gates between distant qubits without bringing those physically together [63], to allow one both to store and to process information with the same physical setup.

Chapter 6

General Conclusions and Future Prospects

The ability to generate trapping potentials for ultra-cold gases has revolutionised the research field of many-body physics. With the introduction of optical lattices, both boson and fermion atomic species can be trapped and controlled in ranges of parameters not easily accessible with other physical systems. Together with single-atom-resolved detection techniques, optical lattices embody one of the most advanced platforms for quantum simulations of discrete models on a lattice, providing a valuable tool for investigating a plethora of phenomena in condensed matter physics, ranging from quantum magnetism to particle-phonon interaction, in ranges of parameters which go beyond standard models in these fields.

In this thesis we have introduced novel results aimed at exploring the possibility of using lattice models for the development of new quantum devices. To pursue this goal, we exploit their features to realise a 1D model of a quantum wire, focussing our attention on their ability to convey information between distant locations without the necessity of active control strategies. Besides, we have explored 1D channels as a tool to dynamically trigger highly coherent transformations, exploiting the natural particle dynamics in a lattice through a minimal control of the lattice potential and of the inter-particle interactions.

To accomplish our objectives, the main strategy followed in this thesis is based on the introduction of few suitably tuned impurities in the lattice potential, and on

the exploitation of the mutual interaction between atoms.

We have proposed a strategy, that does not rely on active atomic transport with external potentials. In this way we can simulate arbitrary linear optics networks with minimal control on static (potentially remote) bosons in a many-site lattice. Specifically, we have shown that fundamental operations between arbitrary remote sites are obtained by mixing quantum walks with suitably tuned local impurities. Several applications have been considered: in particular, the achievement of a balanced remote beam splitter, a Mach-Zehnder interferometer, and the two-mode Hong-Ou-Mandel effect, rather robust against atom-atom mutual interactions. We have also shown the existence of a sudden dynamical transition from bosonic to fermionic behaviour triggered by the on-site interaction. Our scheme has a natural importance for metrology applications, and may pave the way for the study of interference effects in a many-boson optical lattice, such as boson sampling.

As a further step, we have also devised conditions for which the dynamics produces a perfect splitting and reconstruction. The lattice potential profile has been designed to completely neutralise dispersion effects, so that a localised wave-packet evolves coherently along the chain and at a particular point is perfectly split into transmitted and reflected components that propagate in opposite directions without dispersion. Besides shedding light on quantum interference phenomena in 1D, our results are particularly useful for applications. In this respect, in atomic lattices we have generated perfect interference effects, (i.e. bunching and anti-bunching) and peculiar quantum interference patterns that result in regular structure in the space-time evolution of the many-particle wave-function, known as quantum carpets. Finally, in a spin-chain setting, we have made use of the particle splitting scheme to generate maximally entangled states between distant parts. We expect that the perfect wave-packet splitting could become a general tool for a variety of applications in controlled quantum interference and quantum information processing, for instance for fractional revivals in spin models [247, 248].

We have explored the possibility to transfer states of bound particles between the endpoints of finite lattices, and to employ them for the generation of small cat

states (i.e. NOON states), in a minimal control setup. Indeed, with the introduction of local impurities we have realised a "magic" beam splitter [174] that allows producing atomic NOON states with strongly interacting bosons, going beyond the traditional regime of linear optics. We derive an effective single-particle theory for describing the dynamics of a bound-particle state in a Bose–Hubbard model, finding the existence of a quasi-localisation effect for a two particle bound state. By introducing static local impurities we have inhibited edge-localisation effects, enabling the bound-state dynamics in finite lattices. A major goal has been accomplished by evaluating quantitatively how the phase detection sensitivity improves in a lattice Mach-Zehnder setup, using the NOON states generated as inputs.

Finally, we have shown how the spin independent scattering of two initially distant qubits in a 1D lattice can be used to implement an entangling quantum gate. A feature of the scheme is that particle quasi-momenta control is naturally provided by few local edge impurities in the lattice potential. The only control required is on the mutual atom interaction, via lattice depth control or Feshbach resonances.

Our findings have an impact for quantum information processing as well as for metrology applications with atoms in a lattice. The result of our research could open up a variety of applications. In the following, we indicate several points that, in our opinion, are worth further investigation.

Bound States Applications in Lattice Models and Domain-Walls in Spin Chains In Chap. 4 we have shown some applications of bound states in a finite lattice model for quantum enhanced metrology applications. Strongly interacting particles have also been recently used for a direct resonant transfer between topological edge states in a staggered chain for a single doublon system [151, 152]. The main drawback of the above schemes is that the transfer time scales exponentially with the number of particles in the system, limiting the scalability for long chains. One solution could come from a global shaking of the lattice. Indeed, in [249] it has been showed that, in a two wells system, a time-periodically modulation of the tunnelling barrier can increase the tunnelling period. One idea that could be developed is to develop an effective theory for describing the dynamics of bound state under a global period-

ical shaking of the tunnelling couplings, (i. e. of the lattice depth), to improve the scalability of bound state systems. This eventually opens up to applications with many-particles bound states, as high NOON states generation, high efficiency state transfer. Moreover, as the mutual crossing of two bound state is forbidden by energy considerations, a lattice shaking could be introduced for building up quantum gates via scattering interaction. A similar strategy could lead, in spin chin systems, for applications with magnetic domain-walls.

Tuneable Quantum Magnetism Simulators with Optical Lattices . In Sec. 1.5.2 we have shown that quantum magnetism models can be simulated in optical lattices using a two specie Mott-Insulator state. The mapping between spin and lattice parameters has been found in [31] and experimentally realised in [32], where a quasi-Heisenberg model has been realised. However, the effectively anisotropy parameter Δ, in the effective XXZ chain model, is hard to be tuned as it is independent from the lattice depth and due to the difficulty to exploit Feshbach resonances in ^{87}Rb.

Because of connection between Bose-Hubbard parameters and effective spin parameter [31], a lattice shaking could be introduced to induce an effective parameters renormalisation, within the Floquet formalism [250], that leads to an effective spin exchange modulation. This would have a huge impact on the field of simulation of quantum magnetism with optical lattices [115].

KLM Quantum Computer and Boson Sampling. The building blocks of quantum linear optics developed in this thesis work, could be arranged in a structured network to realise a complete sequence of quantum gates. This is important for quantum information applications, as an efficient quantum computer can be realised within the linear optical paradigm, together with single-site measurement capabilities [165, 192]. In this case atoms have a huge advantage, with respect to photonic implementations, as that atom detectors and sources are far more efficient than single photon ones [251]. However, there are two main obstacles towards a concrete realisations of a linear optics quantum computer with atoms in a lattice.

The first one is the mutual atom-atom interaction, as the KLM paradigm [165], is based on non-interacting particles and non-linear effects, obtained via measure-

ment of one the beam splitter output in the network. However, through a control of the atom-atom interaction, the non-interacting regime has been already achieved, for instance, for Cs atoms [71]. Although single-site detection is available for Rb [16, 17] and Yb [23, 24], we are not aware of any realisation, at the present moment, of a quantum-microscope with Cs atoms. Nonetheless, it is reasonable to believe that this will probably be available in the near future. The second obstacle is the current single-atom detection technique. Indeed, with current fluorescence detection all the atoms position are revealed simultaneously and atoms are lost after the detection, due to heating effects. A solution could be provided by non-demolition techniques (i.e. Faraday rotation), which are already developed for ultra-cold gases [252, 253], once they reach the single-site precision. This seems a reasonable goal for the near future, as in a very recent work, a non-demolitive atom imaging technique has been showed with single site resolution [179].

Another possible application of our scheme is for the simulation of boson sampling devices [166, 181], as scaling up boson sampling to a large number of photons still represents a nontrivial experimental challenge [182, 183]. Indeed, a random beam-splitter network could be mimicked introducing several impurities in the chain. Moreover, as the atom-interaction is a tuneable parameter from free bosons to a fermionised regime, our setup could opens up the study the role of a finite interaction in the complexity of the boson sampling problem.

Quantum Gates with Scattering Collisions. An alternative possibility for realising quantum gate in a lattice is the direct exploitation of the atom interaction. In Chap. 5 we have indeed shown how a Quantum Gate can be obtained from the collision of more atoms. Our findings could be extended to more complex structures, as star-graph configurations, to realise complex operations and multi-particle entanglement from the simultaneous collision of more atoms.

Metrology Application in a Lattice Model In Chap. 2 and 4 we have shown that few particle initially in a finite lattice model, are a valuable resource for interferometry, in a Mach-Zehnder configuration. However, the capabilities of this setup to sense spatial inhomogeneous external field, as its sensitivity should be analysed

in full with realistic fields. Furthermore, the setup could be extended to ring configurations to resemble a Sagnac configuration for potential application in quantum enhanced gyroscopy.

Appendix A

Numerical Techniques for Quantum Dynamics

In this section we show briefly the methods used to evaluate numerically the dynamics of few excitation in the model described by the Hamiltonian (1.64). A convenient finite basis to describe a 1D lattice of length L and total number of particles M is given by the Fock states [254]

$$|n_1,\ldots,n_L\rangle = \frac{1}{\sqrt{n_1!\ldots n_L!}}\left(a_1^\dagger\right)^{n_1}\ldots\left(a_L^\dagger\right)^{n_L}|0\rangle, \tag{A.1}$$

where n_j are the number of particles in site j and $\sum_{j=1}^{L} n_j = M$ is the total excitations number. Once known the basic structure[1] and the dimension of the Hilbert space with fixed particle numbers, every state can be naturally stored in a computer as a 1D array [255]. For M bosons and L sites the size of the Hilbert space is

$$\dim\mathscr{H}_{(L,M)}^{\text{boson}} = \frac{(L+M-1)!}{(M-1)!L!}, \tag{A.2}$$

thus the number of resources to describe the full information contained in a many-body state grow exponentially with the size of the system. The computation cost results limits the possibility to simulate many-body physics with a classical computer. Indeed, standard diagonalisation techniques, where all the matrix elements

[1] In general the number of states to be stored depends on the nature of the atoms and on the number of internal degrees of freedom considered.

are stored and no symmetries are exploited, cannot face problems over $M = L > 8$ in ordinary computers [12]. Several techniques make possible to overcome these limitations, namely

- Symmetries in the Hamiltonian allow reducing the Hilbert space to an effective subset of states that can be populated during the dynamics [84, 85].
- The Hamiltonian of the system has generally a sparse matrix structure, which can be stored efficiently on a classical computer via mapping methods (namely by storing only the non-zero matrix elements only) [256].
- Adaptive cutting techniques of the Hilbert space, based on an energy cut-off in the energy spectrum (NRG), on an entanglement threshold of the system state (MPS and DMRG) or limiting the maximum site occupation, can be employed to reduce the computational expense of the many-body state representation [257–260].

A.0.1 Symmetries

The physical description of a quantum system can be simplifies thanks to symmetry proprieties. A symmetry is mathematically described as operator that commutes with the Hamiltonian of the system [84, 85]. The Bose-Hubbard model, Eq. (1.64), has a number of symmetries [255], as

$$\left[H, \sum_{j=1}^{L} n_j \right] = 0, \tag{A.3}$$

that ensures the total number of particles to be preserved during the dynamics. Matrix elements of H between states with a different particle numbers are thus zero, and the Hamiltonian (1.64) can be reshaped to a block diagonal form, grouping the basis states with the same number of excitations. The block diagonal structure, means also that different subspaces are not mixed during the dynamics [85], and for time evolution purposes, the Hilbert space can be restricted to a subspace with the same particle number as the initial state. In the same fashion, in the XXZ chain model Eq. (1.104), the total magnetisation $\sum_{j=1}^{L} S_j^z$ is a constant of the motion and allows

block diagonalising the Hamiltonian of the system. The latter two examples are indeed a general propriety of commutating observables [85]. If one has a set of two commutating observable, A and B, and $|\psi\rangle$ is an eigenvector of A, then $B|A\rangle$ is still an eigenvector with the same eigenvalue. Furthermore the matrix elements of B between orthogonal eigenvectors of A are zero. Thus the matrix representation of B in the basis of eigenvectors of A is block diagonal. The key point is that, to describe the system dynamics, it is sufficient to take the projection of the Hamiltonian in the subspace $\mathscr{H}_m \subset \mathscr{H}$ generated by states with M excitations.

A.0.2 Efficient Computation and Storage

Once chosen the basis (A.1) to represent the Hilbert space of the system, the next step to simulate the evolution of the system, is to compute the matrix elements of the Hamiltonian (1.64), $H_{ab} = \langle a|H|b\rangle$, for all the basis vectors $|a\rangle, |b\rangle \in \mathscr{H}$. However, due to the sparse structure of the Hamiltonian, is not efficient to evaluate and store the full matrix in a computer (the memory cost would be of the order of D^2, where D is the size of the Hilbert space $\mathscr{H}$), but to figure out what are the non-zero elements, and store their positions (e.g. row and column index). Sparse arrays have efficient storage schemes depending on how much the pattern of non-zero elements is regular. The simplest format for a sparse matrix with an irregular pattern is the Coordinate Storage Scheme (COO) [261], that uses three 1D arrays: the first one contains the values of the non-zero matrix elements, while the other two are respectively two integer arrays that contain the corresponding row and column indices of these elements. The scheme is efficient when the number of non-zero elements is much smaller than the total number of elements of the matrix[2].

Once the basis, Eq. (A.1), is built and stored in the computer memory, to efficiently compute the matrix elements a hashing technique is exploited to tag each basis vector, namely to condense the information of the vector into a single number [3] [256]. Diagonal terms of the Hamiltonian (1.64), namely the onsite interaction and

[2]The main drawback of the COO is that the column and row index vectors often contains repetitions. An alternative storage scheme is the compressed form [261]. We do not further discuss this topic as it is out of the purposes of this section.

[3]The advantage is that, during the computation, one needs to compare two numbers instead of all the elements of arrays.

the local chemical potential, are easily computable for all the basis vector. For the hopping part, given an arbitrary basis vector $|v\rangle$, to evaluate the hopping from site j to $j+1$ we first calculate the action of $a_j a_{j+1}^\dagger |v\rangle$. This gives both the numerical value of the matrix element, but also a new vector $|v'\rangle$. Finally, from the tag of $|v\rangle$ and $|v'\rangle$ one builds the correspondent non-zero matrix element of the Hamiltonian [256].

A.0.3 Vectorisation and Matricisation

In this section we briefly discuss a technique to flattering an $n \times n$ matrix to a vector with n^2 elements (*vectorisation*) and an $n \times n \times n \times n$ superoperator[4] into an $n^2 \times n^2$ matrix (*matricisation*) [262, 263]. The vectorisation procedure consists in representing a matrix as a vector, using its representation in the canonical basis, with a column ordering. For instance for a 2×2 matrix,

$$A = \begin{pmatrix} A_{11} & A_{12} \\ A_{21} & A_{22} \end{pmatrix} = A_{11} \begin{pmatrix} 1 & 0 \\ 0 & 0 \end{pmatrix} + A_{21} \begin{pmatrix} 0 & 0 \\ 1 & 0 \end{pmatrix} + \ldots \rightarrow \mathrm{vec}(A) = \begin{pmatrix} A_{11} \\ A_{21} \\ A_{12} \\ A_{22} \end{pmatrix}, \tag{A.4}$$

namely the vectorisation $\mathrm{vec}(A)$ is a column vector whose elements are the components of A in the canonical basis. For a general square matrix $L \times L$ the vectorisation corresponds to a mapping $v_{(k-1)L+j} = A_{jk}$, where $j,k \in \{1,\ldots L\}$. Using the same procedure a superoperator with elements $S_{jk,lm}$ can be reduced to a matrix form with the mapping $S_{j+L(k-1),l+L(m-1)}$, where $j,k,l,m \in \{1,\ldots,L\}$.

A.1 Time Evolution for closed systems

The time evolution of a Quantum system, from time 0 to t is governed by the Shrödinger equation [84, 264],

$$\frac{d}{dt}U(t,0) = -iH(t)U(t,0), \tag{A.5}$$

[4] These are linear operators in the *Liouville space*, namely the vector space of linear operators. Superoperators act on the matrix representation of a linear operator and map it to a matrix [123].

whose formal solution can be given in terms of a time-ordered integral [231]

$$|\psi(t)\rangle = U(t,0)|\psi(0)\rangle = \hat{T}\exp\left(-i\int_0^t H(t')dt'\right)|\psi(0)\rangle\ , \tag{A.6}$$

where $\hat{T}$ is the time ordering operator. The numerical solution can be found by breaking up the total evolution operator (A.6), into small increments Δt, in which the variation of the Hamiltonian is small, as a product formula,

$$U(t,0) = \prod_{n=0}^{N-1} U((n+1)\Delta t, n\Delta t), \tag{A.7}$$

where $\Delta t = t/N$ and $U(t+\Delta t,t) = e^{-iH(t)\Delta t}$ [264,265]. To get the time evolution of a time independent Hamiltonian, one has to compute the dynamics for a small time step Δt as

$$|\psi(t+\Delta t)\rangle = e^{-iH\Delta t}|\psi(t)\rangle, \tag{A.8}$$

namely a matrix exponential operation applied to the vector $|\psi(t)\rangle$. The computational effort is reduced in a truncated Hilbert basis. Specifically, the action of the time-evolution operator acting to a generic vector v is formally

$$e^w v \equiv \sum_{j=0}^{\infty} \frac{W^j}{j!} v, \tag{A.9}$$

where $W \equiv -iHt$, which means that the vector $\exp(W)\,v$ belongs to the subspace spanned by the basis

$$\mathscr{K}_m(W;v) \equiv \{v, Wv, \ldots, W^m v, \ldots\}\,, \tag{A.10}$$

which takes the name of *Krylov subspace* [261]. The idea behind the Krylov approximation is to truncate the subspace (A.10), to get a polynomial approximation of a matrix exponential [255,266,267] as

$$U(t) = e^W v \simeq p_{m-1}(W)v \tag{A.11}$$

where $p_{m-1}(W)v$ is a polynomials of degree m and W and v are respectively a n-order matrix and vector. As a first step, to find the state propagated, Eq. (A.8), given the state $|\psi(t)\rangle$, one first build the Krylov vectors $v'_j = W^j|\psi(t)\rangle$, as $V' = [v'_1,\ldots,v'_m]$ and then orthogonalise the basis of the subspace of size m, finding $V = [v_1,\ldots,v_m]$. The first Krylov vector is $|v_1\rangle = |\psi(t)\rangle = V|e_1\rangle$, where $|e_1\rangle \equiv (1,0,\ldots,0)^T$. By approximating the matrix exponential one finds [266]

$$e^{-iH\Delta t}|v_1\rangle \simeq VV^\dagger e^{-iH\Delta t}|v_1\rangle = VV^\dagger e^{-iH\Delta t}V|e_1\rangle = Ve^{-iV^\dagger HV\Delta t}|e_1\rangle, \qquad (A.12)$$

and because $VHV^\dagger$ is a $m\times m$ matrix, with size less than the total Hilbert space $\mathscr{H}$, the computational effort for evaluating the (A.8) is reduced. Furthermore, the projected subspace representation of the Hamiltonian, has a tridiagonal form, whose diagonalisation can be computed efficiently [265]. Finally calling $M \equiv \exp\left(-iVHV^\dagger\Delta t\right)$ the matrix exponential is approximated by

$$e^{-iH\Delta t}|v_1\rangle \simeq VM|v_1\rangle = \sum_{j=1}^{m} M_{1,j}|v_j\rangle, \qquad (A.13)$$

which represents the approximation for the propagated state (A.8). We mention that an alternative method for computing the time evolution, Eq. (A.8), solving the matrix exponential, is the Chebyshev expansion [268].

A.2 Numerical Solution of the Master Equation

Spontaneous emission effects for particle dynamics in an optical lattice are described by Eq. (1.72). To simulate the particle dynamics numerically, we transform the Master equation, Eq. (1.72), using a vectorisation procedure. Once chosen the canonical column basis to vectorise the density operator ρ, as discussed in Sec. A.0.3, the action of an operator H on the left or the right of the density matrix ρ can be written as [261, 262, 269],

$$H\rho = (\mathbf{1}_L \otimes H)\,\mathrm{vec}(\rho)\,, \qquad (A.14)$$

$$\rho H = \left(H^t \otimes \mathbf{1}_L\right)\mathrm{vec}(\rho)\,, \qquad (A.15)$$

and for the dissipative part, by using the identities

$$\begin{aligned} \mathrm{vec}(ABC) &= \left(C^t \otimes A\right) \mathrm{vec}(B) = (\mathbf{1}_L \otimes AB)\,\mathrm{vec}(C) = \qquad (A.16)\\ &= \left(C^t B^t \otimes \mathbf{1}_L\right) \mathrm{vec}(A)\ , \\ \mathrm{vec}(AB) &= (\mathbf{1}_L \otimes A)\,\mathrm{vec}(B) = \left(B^t \otimes \mathbf{1}_L\right) \mathrm{vec}(A)\ , \qquad (A.17) \end{aligned}$$

we find that

$$\begin{aligned} n_i n_i \rho &= (\mathbf{1}_L \otimes n_i n_i)\,\mathrm{vec}(\rho)\ , \qquad (A.18)\\ \rho n_i n_i &= \left((n_i n_i)^t \otimes \mathbf{1}_L\right) \mathrm{vec}(\rho)\ , \qquad (A.19)\\ n_i \rho n_i &= \left((n_i)^t \otimes n_i\right) \mathrm{vec}(\rho)\ . \qquad (A.20) \end{aligned}$$

Hence if H and ρ describe a fixed particle number subspace, the vectorised form of the Master Equation (1.72) is

$$\partial_t \mathrm{vec}(\rho(t)) = \mathscr{L}_v \mathrm{vec}(\rho(t))\ , \qquad (A.21)$$

where the operator $\mathscr{L}_v$ is defined as

$$\begin{aligned} \mathscr{L}_v \equiv\ & -i\left\{(\mathbf{1}_L \otimes H) - \left(H^t \otimes \mathbf{1}_L\right)\right\} - \gamma \sum_j \left\{\left(n_j^t \otimes n_j\right) + \qquad (A.22)\right.\\ & \left. - \frac{1}{2}\left(\mathbf{1}_L \otimes n_j^2\right) - \frac{1}{2}\left((n_j^2)^t \otimes \mathbf{1}_L\right)\right\}. \end{aligned}$$

Finally, to simulate the dynamics we solve numerically Eq. (A.21), by computing the matrix exponential, using the techniques described in Sec. A.1.

A.3 Time Evolution for Two Walkers in a 1D Lattice Model

In the special case of two walkers, the dynamics of two particles can be evaluated in the subspace spanned by eigenstates of number operator [170]

$$\begin{aligned}\mathscr{H}_2^b &= \left\{ |\psi\rangle \in \mathscr{H}^b : |\psi(t)\rangle = \sum_{j\leq k} \left(1+\delta_{jk}\right)^{-1/2} A_{jk}(t)\ \hat{a}_j^\dagger \hat{a}_k^\dagger |0\rangle \right\}, \\ \mathscr{H}_2^{f/hcb} &= \left\{ |\psi\rangle \in \mathscr{H}^{f/hcb} : |\psi(t)\rangle = \sum_{j<k} A_{jk}(t)\ \hat{a}_j^\dagger \hat{a}_k^\dagger |0\rangle \right\}, \end{aligned} \tag{A.23}$$

where the indexes b, f and hcb represent respectively the boson, fermion and hard-core boson case. For two fermions the Shrödinger equation can be rearranged as

$$i\sum_{j<k} \dot{A}_{jk}(t)\ \hat{a}_j^\dagger \hat{a}_k^\dagger |0\rangle = \sum_{j<k} A_{jk}(t)\ \left[\hat{H}, \hat{a}_j^\dagger \hat{a}_k^\dagger\right] |0\rangle + E_0 |\psi\rangle, \tag{A.24}$$

where $A_{jk}(t)$ represents the amplitude probability to have one particle in site j and the other in site k. Same calculations hold for bosons and hard-core bosons. Hereafter we get rid of the constant energy shift E_0. By evaluating the commutator on the right hand side of the (A.24) for bosons, fermions and hard-core bosons, using the identities

$$[AB,CD] = A[B,C]D + AC[B,D] + [A,C]DB + C[A,D]B, \tag{A.25}$$

$$[AB,CD] = A\{B,C\}D - C\{A,D\}B - \{A,C\}BD + CA\{B,D\}, \tag{A.26}$$

$$[AB,C] = A\{B,C\} - \{A,C\}B, \tag{A.27}$$

$$[A,BC] = \{A,B\}C - B\{A,C\}, \tag{A.28}$$

$$\{AB,C\} = A[B,C] + \{A,C\}B = A\{B,C\} - [A,C]B, \tag{A.29}$$

$$\{A,BC\} = [A,B]C + B\{A,C\} = \{A,B\}C - B[A,C], \tag{A.30}$$

the time evolution for two particles is reduced to the differential coupled system

$$i\partial_t A_{jk}(t) = \sum_{j<k,l<m} K_{jk,lm} A_{lm}(t), \tag{A.31}$$

where the superoperator $K_{jk,lm}$ is determined via canonical commutation rules, as

$$\begin{aligned} K^{b}_{jk,lm} &= \frac{J_{j-1}}{2}\delta_{j-1,l}\delta_{k,m} + \frac{J_{k-1}}{2}\delta_{j,l}\delta_{k-1,m} + \frac{J_j}{2}\delta_{j+1,l}\delta_{k,m} + \\ &+ \frac{J_k}{2}\delta_{j,l}\delta_{k+1,m} - \left(\mu_k + \mu_j\right)\delta_{j,l}\delta_{k,m} + U_j\delta_{j,k}\delta_{j,l}\delta_{k,m} \\ K^{f/hcb}_{jk,lm} &= \frac{J_{j-1}}{2}\delta_{j-1,l}\delta_{k,m} + \frac{J_{k-1}}{2}\delta_{j,l}\delta_{k-1,m} + \frac{J_j}{2}\delta_{j+1,l}\delta_{k,m} + \\ &+ \frac{J_k}{2}\delta_{j,l}\delta_{k+1,m} - \left(\mu_k + \mu_j\right)\delta_{j,l}\delta_{k,m}. \end{aligned} \tag{A.32}$$

We note that Hard-Core bosons and fermions have exactly the same dynamics in real space, as mentioned in [170]. Similar calculation can be applied for two distinguishable particles (e.g. two internal states of an atom). The dynamics of the system (A.31) is found solving numerically[5] the formal solution

$$A_{jk}(t) = \sum_{l<m} \exp\left(-iK_{jk,lm}t\right) A_{lm}(0). \tag{A.33}$$

once the latter is transformed to a linear system via a vectorisation procedure, described in Sec. A.0.3.

[5] Although the procedure developed in this section can be easily generalised, the calculations for determining the (A.32) are usually cumbersome when more walkers are involved, and numerical methods, described in Sec. A.0.2, have been preferred for the simulations in this Thesis work.

Appendix B

Quasi-Uniform Tridiagonal Matrices

This section is rather technical and its purpose is merely to show how the effect of impurities in the model Eq. (1.64) can be evaluated analytically. We consider a symmetric $T \in \mathscr{M}_{l\times l}$ tridiagonal matrix, where $T_{\mu\mu} = a_\mu (\mu \in \{1,\dots,l\})$ and $T_{\mu,\mu+1} = T_{\mu+1,\mu} = b_\mu (\mu \in \{1,\dots,l-1\})$ [142, 150] as

$$T = \begin{pmatrix} a_1 & b_1 & & \\ b_1 & a_2 & & \\ & & \ddots & b_{l-1} \\ & & b_{l-1} & a_l \end{pmatrix} \tag{B.1}$$

The matrix is said *mirror-symmetric* if it is symmetric with respect to the skew diagonal, namely if $[M,T] = 0$, where M is the mirroring matrix (whose matrix elements are $M_{\mu,\nu} = \delta_{\mu,l+1-\nu}$). The spectral decomposition is $T = O^\dagger \Lambda O$ where O is a matrix whose entries $O_{k\mu}$ are the l eigenvectors of T arranged in rows, and $\Lambda = \mathrm{diag}\{\lambda_k\}$, where λ_k are the eigenvalues of T. A propriety of a mirror-symmetric matrix in Eq. (B.1), is that eigenvectors are symmetric or antisymmetric[1] [142, 150, 270],

$$O_{k,l+1-\mu} = (-1)^{k+1} O_{k\mu}. \tag{B.2}$$

For a general mirror-symmetric tridiagonal matrix, the eigenvectors can be expressed in terms of characteristic polynomials of submatrices of T, once known

[1] Here $b_\mu > 0$ and λ_k are sorted in decreasing order.

all the eigenvalues [150]. By defining the submatrices as

$$T_{\mu:\nu} = \begin{pmatrix} a_\mu & b_\mu & & \\ b_\mu & a_{\mu+1} & & \\ & & \ddots & b_{\nu-1} \\ & & b_{\nu-1} & a_\nu \end{pmatrix}, \tag{B.3}$$

the correspondent characteristic polynomial

$$\chi_{\mu:\nu} \equiv \det\left[\lambda \mathbf{1} - T_{\mu:\nu}\right], \tag{B.4}$$

where $\mu \leq \nu$, then $T_{1:l} \equiv T$ and $\chi_{1:l} \equiv \chi(\lambda)$ and the eigenvalues of T are the solutions of $\chi(\lambda) = 0$. The submatrix polynomials satisfy recurrence relations

$$\chi_{\mu:\nu} = (\lambda - a_\nu)\chi_{\mu:\nu-1}(\lambda) - b_{\nu-1}^2 \chi_{\mu:\nu-2}(\lambda), \tag{B.5}$$

$$\chi_{\mu:\nu} = (\lambda - a_\nu)\chi_{\mu+1:\nu}(\lambda) - b_\mu^2 \chi_{\mu+2:\nu}(\lambda), \tag{B.6}$$

and the following relation holds for the product of components of the same eigenvector

$$\chi'(\lambda_k) O_{k,\mu} O_{k,\nu} = \chi_{l:\mu-1}(\lambda_k) \left(\prod_{\sigma=\mu}^{\nu-1} b_\sigma \right) \chi_{\nu+1:l}(\lambda_k) \tag{B.7}$$

where $\chi'(\lambda_k)$ is the derivative of the characteristic polynomials evaluated in λ_k [150]. For instance

$$O_{k,1} O_{k,l}\ \chi'(\lambda_k) = b_1 \ldots b_{l-1}. \tag{B.8}$$

From Eq. (B.7), one finds an explicit formula for the first/last component of the eigenvectors:

$$O_{k,1}^2 = \frac{\chi_{2:l}(\lambda_k)}{\chi'(\lambda_k)}, \qquad O_{k,l}^2 = \frac{\chi_{1:l-1}(\lambda_k)}{\chi'(\lambda_k)}. \tag{B.9}$$

All the other components can be determined via the recurrence formula

$$O_{k,\nu+1} = \frac{\lambda_k - a_\nu}{b_\nu} O_{k,\nu} - \frac{b_{\nu-1}}{b_\nu} O_{k,\nu-1} \quad (\nu \in \{1, \ldots, l-1\}) \tag{B.10}$$

with the assumption $O_{k,0} = 0$.

B.0.1 Uniform Tridiagonal Matrices

Eigenvalues and eigenvectors of a uniform block of size l can be computed using Chebyshev polynomials. Indeed, it has been proved in [142], that for the matrix (B.1) holds

$$\chi_{1:1}(\lambda) \equiv 1, \qquad \chi_{1:2}(\lambda) \equiv \lambda - a_1, \tag{B.11}$$

$$\chi_{1:j}(\lambda) = (\lambda - a_j)\chi_{1:j-1}(\lambda) - b_{j-1}^2 \chi_{1:j-2}(\lambda), \tag{B.12}$$

and that the eigenvector $|k\rangle = \sum_{j=1}^{l} a_j^{(k)} |\mathbf{j}\rangle$, where $|\mathbf{j}\rangle \equiv |0\rangle^{\otimes j-1} |j\rangle |0\rangle^{\otimes l-j}$, are determined by

$$a_j^{(k)} = \frac{\chi_{1:j-1}(\lambda_k)}{b_1 \dots b_{j-1}} a_1^{(k)} \tag{B.13}$$

and the first component of the eigenvector is determined by the normalisation $\sum_{j=1}^{l} |a_j|^2 = 1$. Moreover, the Chebyshev polynomials of second kind satisfy the recurrence relation [90]

$$\mathscr{U}_0(\lambda) = 1, \qquad \mathscr{U}_1(\lambda) = 2\lambda, \tag{B.14}$$

$$\mathscr{U}_{j+2}(\lambda) = 2\lambda \mathscr{U}_{j+1}(\lambda) - \mathscr{U}_j(\lambda). \tag{B.15}$$

Therefore, the characteristic polynomial of the matrix (B.1), for $b_\mu = 1$ and $a_\mu = 0$, in terms of Chebyshev polynomials is $\chi_{1:l}(\lambda) = \mathscr{U}_l(\lambda/2)$ [150]. Chebyshev polynomials of first/second kind can be expressed in trigonometric form, via the change of variable $\lambda = 2\cos k$, [90, 207], as

$$\mathscr{T}_l(\cos k) = \cos lk, \tag{B.16}$$

$$\mathscr{U}_l(\cos k) = \frac{\sin(l+1)k}{\sin\, k}, \tag{B.17}$$

so that the eigenvalue equation, $\chi_{1:l}(\lambda) = \mathscr{U}_L(2\cos k) = 0$, can be defined as [150]

$$k \equiv k_j = \frac{\pi j}{L+1}, \qquad j \in \{1, \dots, l\}, \tag{B.18}$$

where the components of the eigenvectors are

$$O_{k,\mu} = \sqrt{\frac{2}{L+1}} \sin \mu k. \tag{B.19}$$

The density of modes, μ_k, (i.e the inverse of the spacing between two subsequent allowed eigenvalues) can be evaluated from Eq. (B.18) as

$$\mu_k^{-1} \equiv \partial_j k_j = \frac{\pi}{L+1}, \tag{B.20}$$

which means the mode spacing is constant, while the spectrum spacing goes as

$$\partial_j \lambda_{k_j} = 2\sin(k_j)\partial_j k_j = \frac{2\pi}{L+1} \sin\left(\frac{j\pi}{L+1}\right), \qquad j \in \{1,\ldots,L\}. \tag{B.21}$$

B.0.2 Quasi-Uniform Tridiagonal Matrices

A tridiagonal matrix is a QUTM, if constituted by a large uniform tridiagonal block, of size n, and of a number of elements l, whose number is much smaller than the size of the matrix, that make it non-uniform. An example is provided by the matrix (B.1), respectively with with one and two boundary local impurities

$$H_l^{\beta_1} = \begin{pmatrix} \beta_1 & 1 & & \\ 1 & 0 & & \\ & & \ddots & 1 \\ & & 1 & 0 \end{pmatrix}, \qquad H_l^{\beta_1\beta_L} = \begin{pmatrix} \beta_1 & 1 & & \\ 1 & 0 & & \\ & & \ddots & 1 \\ & & 1 & \beta_L \end{pmatrix}. \tag{B.22}$$

As for the uniform case, it has been proved that the characteristic polynomial for QUTM matrices can be expressed in terms of Chebyshev polynomials [150]. For instance, for the matrices, Eq. (B.22), we find

$$\chi_{1:l}^{(\beta_1)}(\lambda) = \mathscr{U}_l(\lambda/2) - \beta_1 \mathscr{U}_{l-1}(\lambda/2)\,, \tag{B.23}$$

$$\chi_{1:l}^{(\beta_1\beta_L)}(\lambda) = \mathscr{U}_l(\lambda/2) - (\beta_1+\beta_L)\mathscr{U}_{L-1}(\lambda/2) + \beta_1\beta_L \mathscr{U}_{L-2}(\lambda/2)\,. \tag{B.24}$$

In the general case, Eq. (B.1), the characteristic polynomial can be expressed in terms of Chebyshev polynomials, by starting from a uniform block $\chi_{u:v}$ and enlarging it, until the full matrix size is recovered, using the recurrence equations Eq. (B.6). This procedure leads to the decomposition [150]

$$\chi_{1:l}(2\xi) = u(\xi)\mathscr{U}_n(\xi) + t(\xi)\mathscr{T}_{n+1}, \tag{B.25}$$

where $u(\xi)$ and $t(\xi)$ are polynomials of degree not larger than $l-n$ and $l-n+1$. Finally, in terms of trigonometric functions, via Eq. (B.17), the eigenvalue problem is equivalent to find the values of k that solve the equation

$$\chi_{1:l}(2\cos k) = (\sin(l+1)k - 2\phi_k) = 0, \tag{B.26}$$

where

$$2\phi_k = (l-n)k - \tan^{-1}\left(\frac{t(\cos k)}{u(\cos k)}\sin k\right), \tag{B.27}$$

and with the parametrisation[2], $\lambda = 2\cos k$, where $k \in [0,\pi]$, the eigenvalues are obtained from

$$k \equiv k_j = \frac{\pi j + 2\phi_k}{l+1}, \qquad j \in \{1,\ldots,l\}. \tag{B.28}$$

By comparing the latter with Eq. (B.18), it is clear that the shifts ϕ_k represent the deviation from a uniform tridiagonal matrix. The eigenvectors can be computed using Eq. (B.9), and the characteristic polynomials, in terms of Chebyshev polynomials, Eq. (B.25) is [150]

$$O^2_{k,1} = \frac{2\sin^2 k}{l+1-2\phi'_k}\frac{u^{\ulcorner}(\xi_k)t(\xi_k) - t^{\ulcorner}(\xi_k)u(\xi_k)}{u^2(\xi_k) + t^2(\xi_k)\sin^2 k}, \tag{B.29}$$

$$O^2_{k,l} = \frac{2\sin^2 k}{l+1-2\phi'_k}\frac{u_{\llcorner}(\xi_k)t(\xi_k) - t_{\llcorner}(\xi_k)u(\xi_k)}{u^2(\xi_k) + t^2(\xi_k)\sin^2 k}, \tag{B.30}$$

[2]The parametrisation does not imply that all the eigenvalues are included in the band $[-2,2]$. Although this is generally true for the largest part of the spectrum, few eigenvalues can emerge, when the elements of the QUTM are large enough, above or below the band. When it happens Eq. (B.28) cannot be solved for few values of j, (i.e. it has less than l solutions for $k \in [0,\pi]$). On the other hand, out-of-band modes are still described by Eq. (B.28) but with complex value of $k = q + ip$, where $q \in \{0,\pi\}$ and $p \geq 0$ to have a real eigenvalue. Out-of-band modes can be found via using the parametrisation $\lambda = \pm 2\cosh p$ in the Chebyshev polynomials [150].

where $\xi_k \equiv \lambda_k/2$ are the solution of $\chi_{1:l}(\lambda_k) = 0$, and $u^{\ulcorner}(\xi_k)$, $v^{\ulcorner}(\xi_k)$ and $u_{\llcorner}(\xi_k)$, $v_{\llcorner}(\xi_k)$ are the coefficients of the decompositions in terms of Chebyshev polynomials of the submatrices, respectively

$$\chi_{2:l}(2\lambda) = u^{\ulcorner}(\lambda)\mathscr{U}_n(\lambda) + v^{\ulcorner}(\lambda)\mathscr{T}_{n+1}(\lambda), \tag{B.31}$$

$$\chi_{1:l-1}(2\lambda) = u_{\llcorner}(\lambda)\mathscr{U}_n(\lambda) + v_{\llcorner}(\lambda)\mathscr{T}_{n+1}(\lambda). \tag{B.32}$$

Compared to the case of a uniform QUTM, the spacing between subsequent allowed values for k is modified by the phase shifts. The density of modes, $\mu(k)$, is then

$$\mu_k^{-1} \equiv \partial_n k_n = \frac{\pi + 2\phi'_{k_n}\partial_n k_n}{L+1} = \frac{\pi}{L+1-2\phi'_{k_n}}. \tag{B.33}$$

Therefore, the inhomogeneities in a QUTM, directly influences the mode density via the phase shifts. This is important because it can be exploited to improve the transfer efficiency, by narrowing the relevant modes in the linear part of the spectrum, as discussed in Sec. 1.6.4. From Eq. (B.33) it is clear that for a very long chain the density of modes can be approximated by a continuous function, which makes possible to transform a sum over the eigenmodes in an integral [150]. Specifically,

$$\sum_n \to \int_0^\pi dk\, \mu(k) = \int_0^\pi dk\, \left(\frac{L+1-2\partial_k\phi(k)}{\pi}\right) = \int_{-\pi/2}^{\pi/2} dq\, \left(\frac{L+1-2\partial_q\phi(q)}{\pi}\right), \tag{B.34}$$

where in the last term the integration variable have been changed to $q \equiv k - \pi/2$. The continuous limit usually involve the *Jacobi-Anger expansion* [90],

$$\begin{aligned}
e^{iz\cos\theta} &= \sum_{n=-\infty}^{+\infty} i^n J_n(z) e^{in\theta} = J_0(z) + 2\sum_{n=1}^{+\infty} i^n J_n(z)\cos n\theta, \\
\cos(z) &= J_0(z) + 2\sum_{n=1}^{+\infty} (-1)^n J_{2n}(z), \\
\sin(z) &= 2\sum_{n=0}^{+\infty} (-1)^n J_{2n+1}(z), \\
e^{iz\sin\theta} &= \sum_{n=-\infty}^{+\infty} J_n(z) e^{in\theta},
\end{aligned} \tag{B.35}$$

where we have used the relation, $J_{-n}(z) = (-1)^n J_n(z)$, valid for any integer n [271]. The last expression has been found with the change of variable $\theta = \theta' - \pi/2$, and using $\exp(-i\pi n/2) = i^{-n}$. Expressions (B.34) and (B.35) can be used to find asymptotic expressions, for $L \gg 1$, for the transfer fidelity, by taking the time t of the order of the length, L, of the chain [62, 63, 146, 148, 272].

Appendix C

Effective Beam Splitter Transformation on a 1D Lattice

C.0.1 Analytical derivation of the beam splitter operation for an odd length chain

We consider the dynamics of a single particle in a chain, described by the Hamiltonian (1.64), with $L = 2N+1$ sites, with a local energy barrier in position $N+1$, modelled as an impurity in the chemical potential as

$$H = -\frac{J}{2}\left(\sum_{n=1}^{2N} |n\rangle\langle n+1| + \text{H.}c.\right) - \beta J|N\rangle\langle N| \,. \tag{C.1}$$

We define reflection and transmission coefficients, Eq. (2.7), as

$$R(t) = \langle 1|e^{-itH}|1\rangle = \sum_k O_{k1}^2 e^{-iE_k t} \,, \tag{C.2}$$

$$T(t) = \langle L|e^{-itH}|1\rangle = \sum_k O_{k1} O_{kL} e^{-iE_k t} \,, \tag{C.3}$$

where in the right member we have used the spectral decomposition $H = OEO^T$. Because the Hamiltonian (C.1) has QUTM form, the eigensystem can be computed using methods in Appendix B. Firstly, we find that the decomposition of the characteristic polynomial in terms of Chebyshev polynomials, $\mathscr{U}_n(x)$, for the rescaled

matrix $-H/(2J)$, is

$$\chi_{1:L}(\lambda) = (\beta-\lambda)\mathscr{U}_L^2\left(\frac{-\lambda}{2}\right) - 2\mathscr{U}_{L-1}\left(\frac{-\lambda}{2}\right)\mathscr{U}_L\left(\frac{-\lambda}{2}\right), \tag{C.4}$$

$$\begin{aligned}\chi_{2:L}(\lambda) = (\beta-\lambda)\,&\mathscr{U}_L\left(\frac{-\lambda}{2}\right)\mathscr{U}_{L-1}\left(\frac{-\lambda}{2}\right) - \mathscr{U}_{L-2}\left(\frac{-\lambda}{2}\right)\mathscr{U}_L\left(\frac{-\lambda}{2}\right)\\ &- \mathscr{U}_{L-1}^2\left(\frac{-\lambda}{2}\right),\end{aligned} \tag{C.5}$$

and $\chi_{2:L}(\lambda) = \chi_{1:L-1}(\lambda)$. We compute the eigenvalues E_k of H from the roots of $\chi(\lambda)$, using the methods in Appendix B. We find that

$$E_k = E(q_k)\,, \qquad\qquad E(q) = J\cos q\,, \tag{C.6}$$

and that there exist three types of modes[1]. In general there are N type-I modes, N type-II modes and one out-of-band mode which, as described in Sec. B, has complex[2] q_k. As the out-of-band mode is localised close to the impurity we consider only type-I and type-II modes in our discussion. We find

$$q_k^{\mathrm{I}} = \frac{k\pi}{N+1}\,, \qquad q_k^{II} = \frac{k\pi - \phi_\beta\left(q_k^{II}\right)}{N+1}\,, \qquad k = 1,\ldots,N\,, \tag{C.7}$$

where $\phi_\beta(q) = \arctan\left(\frac{\sin q}{\beta}\right)$. Moreover, as discussed in Appendix B, one can prove that for type-I modes $O_{k1}^{\mathrm{I}} = -O_{kL}^{\mathrm{I}}$ while for type-II modes $O_{k1}^{\mathrm{II}} = O_{kL}^{\mathrm{II}}$, so that

$$R(t) \simeq U^{\mathrm{I}}(t) + U^{\mathrm{II}}(t)\,, \qquad\qquad T(t) \simeq -U^{\mathrm{I}}(t) + U^{\mathrm{II}}(t)\,, \tag{C.8}$$

where the approximation is in neglecting the out-of-band mode, $U^{\mathrm{I,II}}(t) \equiv \sum_k \left(O_k^{\mathrm{I,II}}\right)^2 e^{-itE(q_k^{\mathrm{I,II}})}$, and

$$\left(O_{1k}^{\mathrm{I}}\right)^2 = \frac{\sin^2 q_k^{\mathrm{I}}}{N+1}\,, \qquad\qquad \left(O_{1k}^{\mathrm{II}}\right)^2 = \frac{\sin^2 q_k^{\mathrm{II}}}{N+1+\phi_\beta'\left(q_k^{\mathrm{II}}\right)}\,. \tag{C.9}$$

[1] We find that the characteristic polynomial can be factorised as $\chi(\lambda) = F(k)G(k,\beta)$, where $F(k)$ is independent from β, and corresponds to N type-I modes, in the interval $k \in (0,\pi)$. In the same fashion $G(k,\beta)$ allows us to find the phase shifts.

[2] In any case the eigenvalue $E(q_k)$ is real.

The effect of the energy barrier β is to split an incident wave packet into a reflected and transmitted component. For a initially localised wavefunction, in site 1, then the transmitted component travels towards the edge site L, while the reflected component travels back towards the initial site. The coefficients $|T(t)|^2$ and $|R(t)|^2$ then measures respectively the probability that the transmitted wave packet is reconstructed at site L and the reflected wave packet is reconstructed at site 1. A $50/50$ splitting is achieved under the condition $|T(t^*)| = |R(t^*)|$ at the transmission time $t^* \simeq L/J$. We observe numerically that $|U^{\mathrm{I}}(t^*)| \simeq |U^{\mathrm{II}}(t^*)|$, so that the $50/50$ splitting is obtained when $U^{\mathrm{I}}(t^*) \simeq \pm iU^{\mathrm{II}}(t^*)$. In the following we use the developed analytic solution to model quantitatively the wave function splitting process. One can show that $U^{\mathrm{I}}(t)$ is formally analogous to one half of reflection coefficient of a chain with N sites and without impurity [149]. Exploiting this analogy, using the expansion (B.35) and some proprieties of Bessel functions [271] one obtains[3]

$$U^{\mathrm{I}}(t) = 2(-1)^{N+1}\left[\left(\frac{2N+2}{Jt}\right)^2 \mathscr{J}_{2N+2}(Jt) - \frac{1}{Jt}\mathscr{J}'_{2N+2}(Jt)\right], \tag{C.10}$$

where the transmission is $Jt^* \approx 2N+2+\xi(N+1)^{1/3}$, where $\xi \approx 1.019$ [149]. Even though the term $U^{\mathrm{II}}(t)$ is more complicated, since we know the transfer time t^* from the analysis of U^{I}(t) we can find a simple expansion of $U^{\mathrm{II}}(t^*)$ in the limit $L \gg 1$. To simplify the notation, we set $q \equiv q^{\mathrm{II}}$. By multiplying and dividing the mode expansion $U^{\mathrm{II}}(t) = \sum_k \left(O_k^{\mathrm{II}}\right)^2 e^{-itE(q_k^{\mathrm{II}})}$ for $e^{i(2N+2)q}$, using (C.7) and going to the continuum limit one obtains

$$\begin{aligned} U^{\mathrm{II}}(t^*) &= \frac{1}{\pi}\int_0^{\pi} dq\, e^{-it\cos q - i(2N+2)q} e^{-i2\phi_\beta(q)}\, \sin^2 q \\ &= \frac{(-1)^{N+1}}{\pi}\int_{-\frac{\pi}{2}}^{\frac{\pi}{2}} dq\, e^{it\sin q - i(2N+2)q} e^{-i2\phi_\beta(q+\pi/2)}\, \cos^2 q. \end{aligned} \tag{C.11}$$

In the limit $N \gg 1$, the biggest contribution to the integral comes from the points such that $q \approx \sin q$, namely $q \approx 0$. Expanding the first phase around this point one obtains $t^*\sin q - (2N+2)q \approx \xi N^{1/3} q - \frac{t^*}{6}q^3$. Then, to properly take into account

[3]The approximation consists in neglecting Bessel functions of order $m(N+2)$, where $m \geq 2$ in the expansion, as it can be showed they contribute only after time of order $mN/2J$ [149].

the scaling with N we set $x{=}N^{1/3}\tan q$ and we perform the limit $N{\to}\infty$. The result is

$$U^{\mathrm{II}}(t) \simeq \frac{(-1)^{N+1}}{\pi N^{1/3}} \int_{-\infty}^{\infty} dx\, e^{i\xi x - ix^3/3} f(x,\beta)\ , \tag{C.12}$$

where $f(x,\beta)$ depends also on $1/N$. Keeping only the first order, one finds $U^{\mathrm{II}}(t^*) \simeq 2\frac{(-1)^{N+1}}{N^{1/3}}\mathrm{Ai}(-\xi)\frac{\beta-i}{\beta+i}$, $\mathrm{Ai}(x)$ being the Airy function [271]. $U^{\mathrm{I}}(t^*)$ can be obtained as well from this analysis since $U^{\mathrm{I}}(t^*) = \lim_{\beta\to\infty} U^{\mathrm{II}}(t^*)$. As discussed before, a 50/50 splitter is obtained when $U^{\mathrm{II}}(t^*) = -iU^{\mathrm{I}}(t^*)$, i.e., $\frac{\beta-i}{\beta+i} = -i$, and hence $\beta = 1$. To estimate the first-order corrections to this asymptotic value, we study the first subleading order in the $1/N$ expansion. The result can be written in terms of Airy functions and its derivatives and agrees with known asymptotic expansions of Bessel functions [149, 271]. We find that the first-order correction to $\beta = 1$ scales as $\beta = 1 - \eta N^{-2/3}$, and

$$\frac{R(t^*)}{T(t^*)} = -i + \frac{i}{2}(2\eta - \xi)N^{-2/3} + \mathscr{O}\left(N^{-4/3}\right)\ . \tag{C.13}$$

To have a balanced splitting then $\eta = \xi/2$. In summary, as $\xi \approx 1.019$ [149], the final result of this section is that for $L \gg 1$ a 50/50 splitting of the wave packet is obtained when the height of the barrier is

$$\beta^{50/50} \simeq 1 - \frac{0.510}{N^{2/3}} \simeq 1 - \frac{0.809}{L^{2/3}}\ . \tag{C.14}$$

C.0.2 Bessel function expansion of $U^{II}(t)$

An approximation for $U^{\mathrm{II}}(t)$ is obtained with the help of the Jacobi-Anger expansion (B.35),

$$U^{\mathrm{II}}(t) = \sum_k \rho_k^{\mathrm{II}} \sum_{m=0}^{\infty} \eta_m i^{-m} \mathscr{J}_m(t) \cos(m q_k^{\mathrm{II}})\ , \tag{C.15}$$

where $\eta_0 = 1$ and $\eta_m = 2$ for $m \neq 0$. As we are interested in the neighbourhood of $t = t^*$ and as the $\mathscr{J}_n(t) \simeq 0$ for $t \lesssim n$, we approximate the infinite sum by only

considering Bessel functions with an order $m \approx t^*$. By letting $m \to 2N+2+m$ one can write

$$U^{\mathrm{II}}(t) \simeq 2(-1)^{N+1} \sum_{m=-M}^{M} i^{-m} c_m \, \mathscr{J}_{L+1+m}(t) \, , \tag{C.16}$$

where M counts the number of Bessel functions considered in the approximation and

$$c_m = \sum_k \rho_k^{\mathrm{II}} \cos[(2N+2+m)q_k^{\mathrm{II}}] = \sum_k \rho_k^{\mathrm{II}} \cos\left[m q_k^{\mathrm{II}} - 2\phi_\beta\left(q_k^{\mathrm{II}}\right)\right] \, . \tag{C.17}$$

We note that c_m only slightly depends on the number of sites. Moreover, as the non-uniform spacing is already included in the dependence on β via the function ϕ_β, we consider q as a continuous variable and we substitute $\sum_k \to \frac{N}{\pi}\int_0^\pi dq$. After some algebra, we obtain

$$c_m \simeq \frac{4}{\pi}\int_{-\infty}^{\infty} \left(\frac{x-i}{x+i}\right)^m \frac{x^2}{(x^2+1)^3} \frac{x^2\beta - 2ix + \beta}{x^2\beta + 2ix + \beta} \, dx \, , \tag{C.18}$$

valid when $N \to \infty$. The dependence of c_m upon β is displayed in Fig. C.1 for some values of m. Negative values of m are omitted since $c_{-m} = (-1)^m c_m$. For $\beta \to \infty$

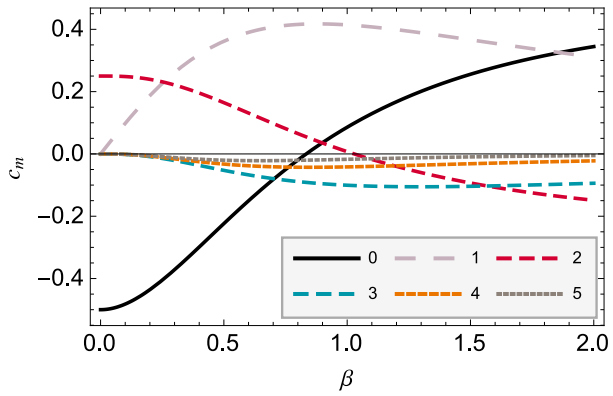

Figure C.1: Bessel expansion of $U^{\mathrm{II}}(t)$. Coefficients c_m vs the impurity strength β for different values of m. The values are obtained from the expression (C.18) valid when $N \to \infty$.

only two coefficients are different from zero $c_0 = \frac{1}{2}$ and $c_2 = \frac{1}{4}$. In that limit, with some algebra one can show that $U^{\mathrm{II}}(t) = U^{\mathrm{I}}(t)$: there is no transmission and the

dynamics mimic that of a chain with N sites. The dynamics of a single particle can be approximated by Eq. (C.16) with $M = 3$. Indeed, as shown in Fig. C.1, the coefficients c_m are negligible for $m > 3$. By solving Eq. (C.18) one obtains

$$c_0 = 2\beta^2 - \frac{2\beta^3}{\sqrt{\beta^2+1}} - \frac{1}{2} , \tag{C.19a}$$

$$c_1 = -2\beta^3 + \frac{2\beta^4}{\sqrt{\beta^2+1}} + \beta , \tag{C.19b}$$

$$c_2 = 4\beta^4 - \frac{4\beta^5+2\beta^3}{\sqrt{\beta^2+1}} + \frac{1}{4} , \tag{C.19c}$$

$$c_3 = -8\beta^5 - 2\beta^3 + \frac{8\beta^6+6\beta^4}{\sqrt{\beta^2+1}} . \tag{C.19d}$$

This approximation reproduces the dynamics around the transfer time t^* for chains as short as 11 sites and becomes more accurate for longer chains.

C.1 Analytical derivation of the beam splitter operation for an even chain

The beam splitter effect can be extended to even chains (where $L = 2N$), by introducing an impurity coupling J' in the middle of the chain. The Hamiltonian (1.64) in the single excitation subspace, and the characteristics polynomial of the rescaled matrix $-H/(2J)$ are

$$H = -\left(\frac{J}{2}\sum_{n=1}^{2N-1} |n\rangle\langle n+1| + \frac{J'-J}{2}|N\rangle\langle N+1|\right) + \text{H.c.} , \tag{C.20}$$

$$\chi_{1:L}(\lambda) = \mathscr{U}_{2N}(-\lambda/2) + \left(1-\eta^2\right)\mathscr{U}_{N-1}^2(-\lambda/2) , \tag{C.21}$$

where $\eta = J'/J$ and $\mathscr{U}_n(x)$ are Chebyshev polynomials of the second kind. Similarly to the previous case, we find that the eigenvalues of H are given by (C.6) with two different types of modes defined by

$$k_j^{\mathrm{I}} = \frac{j\pi - \phi^{\mathrm{I}}(k_j)}{N+1} , \qquad k_j^{\mathrm{II}} = \frac{j\pi - \phi^{\mathrm{II}}(k_j)}{N+1} , \tag{C.22}$$

where $j \in \{1,\ldots,N\}$ and

$$\phi^{\mathrm{I}}(k) = \arctan\left[\frac{\eta \sin k}{1-\eta\cos k}\right], \tag{C.23}$$

$$\phi^{\mathrm{II}}(k) = \arctan\left[\frac{\eta \sin k}{1+\eta\cos k}\right]. \tag{C.24}$$

We find that the type-I mode eigenvectors satisfy $O^{\mathrm{I}}_{1k}=-O^{\mathrm{I}}_{Lk}$ while type-II modes satisfy $O^{\mathrm{II}}_{1k}=O^{\mathrm{II}}_{Lk}$, similarly to the previous case, so Eqs.(C.8) are satisfied. The latter expressions can be evaluated in the limit $L \gg 1$. Indeed, similarly to Eq.(C.11) we find

$$U^{\mathrm{I,II}}(t) \simeq \frac{(-1)^{N+1}}{\pi N^{1/3}} \int_{-\infty}^{\infty} dx\, e^{i\xi x - ix^3/3} f^{\mathrm{I,II}}(x,\eta), \tag{C.25}$$

where $x=N^{1/3}\tan k$ and $f^{\mathrm{I,II}}(x,\eta)$ depend also on $1/N$. Keeping only the first order, we find

$$U^{\mathrm{I}}(t^*) \simeq 2\frac{(-1)^{N+1}}{N^{1/3}}\mathrm{Ai}(-\xi)\left[\frac{i-\eta}{i+\eta}\right], \tag{C.26}$$

$$U^{\mathrm{II}}(t^*) \simeq 2\frac{(-1)^{N+1}}{N^{1/3}}\mathrm{Ai}(-\xi)\left[\frac{i+\eta}{i-\eta}\right], \tag{C.27}$$

$\mathrm{Ai}(x)$ being the Airy function [271]. As discussed before, the balanced beam splitting condition is achieved for $U^{\mathrm{I}}(t^*) = iU^{\mathrm{II}}(t^*)$ that leads to the coupling value $\eta = \sqrt{2}-1$.

Appendix D

Effective Hamiltonian for Many-Body Systems

D.1 Quasi Degenerate Perturbation Theory

We consider a quantum system whose Hamiltonian can be written as the sum of two parts as $H = H_0 + \lambda T$, where λ is a perturbation parameter. The eigenvalues and the eigenvectors of H_0 are known, respectively E_n and $|\varphi_n\rangle$, while T is treated as a perturbation. We assume that the total Hilbert space of the system $\mathscr{H}$ can be separated into two weakly interacting subsets $\mathscr{H}_p$ and $\mathscr{H}_q$. The idea of the quasi degenerate perturbation theory [133, 134] is that the Hamiltonian can be transformed into a new Hamiltonian $\tilde{H}$, via a canonical transformation[1], so that in new Hamiltonian the states of the two subspaces $\mathscr{H}_p$ and $\mathscr{H}_q$ are separated at the desired order in λT, namely $\langle \psi_p | \tilde{H} | \psi_q \rangle = 0$, where $|\psi_p\rangle \in \mathscr{H}_p$ and $|\psi_q\rangle \in \mathscr{H}_q$. A procedure to derive an effective low-energy Hamiltonian, for strongly correlated many-body systems, is the SWT. This is a canonical transformation with general form

$$H_{\text{eff}} = e^{iS} H e^{-iS} = H + [iS, H] + \frac{1}{2!}[iS, [iS, H]] + \ldots \equiv \sum_{m=0}^{+\infty} \frac{1}{m!} [iS, H]_m \ , \qquad \text{(D.1)}$$

where S is a unitary operator and the right member comes out from the Baker-Campbell-Hausdorff formula [135]. The transformation is then equivalent to a rota-

[1] By definition, canonical transformations preserve the hermiticity (Hamiltonians are transformed in Hamiltonians under the transformation).

tion in the Hilbert space, and S is designed on the effective description of the system required. Specifically, the unitary transformation, generated by S, is built to find an effective Hamiltonian in a block diagonal form [273]

$$H_{\text{eff}} = \left(\begin{array}{c|c} H_{\text{eff},p} & 0 \\ \hline 0 & H_{\text{eff},q} \end{array}\right). \tag{D.2}$$

Generally the effective hamiltonian H_{eff} and the generator of the transformation, S, are computed perturbatively. Specifically, to build S one expands H_{eff} and S in power series as [134, 274]:

$$H_{\text{eff}} = \sum_{n=0}^{\infty} H_{\text{eff}}^{(n)}, \qquad S = \sum_{n=0}^{\infty} \lambda^n S^{(n)}. \tag{D.3}$$

where $H_{\text{eff}}^{(n)}$ contains all the terms in λ^n. In the specific case of the Bose-Hubbard model (1.93), in the strong coupling regime, the hopping term can be considered as a perturbation on the atom-atom interaction. Therefore, to find the second order effective Hamiltonian, one imposed that states with more particles in the same site are not connected via first order hopping terms. Explicitly, once written the Hamiltonian (1.93) as $H = H_0 + \lambda T$, using Eq. (D.3) in the (D.1), one finds (up to the second order)

$$H_{\text{eff}}^{(0)} = H_0, \tag{D.4}$$

$$H_{\text{eff}}^{(1)} = \lambda T + \left[i\lambda S^{(1)}, H_0\right], \tag{D.5}$$

$$H_{\text{eff}}^{(2)} = \left[i\lambda S^{(1)}, \lambda T\right] + \frac{1}{2}\left[i\lambda S^{(1)}, \left[i\lambda S^{(1)}, H_0\right]\right]. \tag{D.6}$$

The form of $S^{(1)}$ can be found explicitly by imposing that first order hoppings are zero, namely $H_{\text{eff}}^{(1)} = 0$. Finally one obtains the second order effective model $H_{\text{eff}}^{(2)}$ as, using the eigenvectors $H_0|\alpha\rangle = E_\alpha|\alpha\rangle$ and the hermiticity of H_0, the $S^{(1)}$ can be

found directly from Eq. (D.5) as

$$\sum_{\alpha\beta}\langle\alpha|H^{(1)}_{\text{eff}}|\beta\rangle|\alpha\rangle\langle\beta| = \sum_{\alpha\beta}\lambda\langle\alpha|T|\beta\rangle|\alpha\rangle\langle\beta| + \\ + i\lambda\sum_{\alpha\beta}\langle\alpha|\left(S^{(1)}H_0 - H_0S^{(1)}\right)|\beta\rangle|\alpha\rangle\langle\beta|, \tag{D.7}$$

which implies the matrix elements are

$$\langle\alpha|S^{(1)}|\beta\rangle = i\frac{\langle\alpha|T|\beta\rangle}{\varepsilon_\beta - \varepsilon_\alpha}. \tag{D.8}$$

The explicit formula for the second order effective Hamiltonian can be found in a similar fashion [274],

$$H^{(2)}_{\text{eff},nm} = \frac{1}{2}\sum_l T_{nl}T_{lm}\left(\frac{1}{E_n - E_l} + \frac{1}{E_m - E_l}\right), \tag{D.9}$$

where n,m indicates the states in $\mathscr{H}_p$ and the sum is over states belonging to $\mathscr{H}_q$. The degenerate perturbation theory method can be made more general for an Hamiltonian in the form $H = H^0 + H'$, where H' is a perturbation, and explicit formulas for the effective Hamiltonian, up to the forth order, can be found in [273]. Here we report the effective Hamiltonian expressions up to the third order, namely

$$H^{(0)}_{\text{eff},mm'} = H^0_{mm'}\ , \tag{D.10}$$

$$H^{(1)}_{\text{eff},mm'} = H^{'}_{mm'}\ , \tag{D.11}$$

$$H^{(2)}_{\text{eff},mm'} = \frac{1}{2}\sum_l H^{'}_{ml}H^{'}_{lm'}\left[\frac{1}{E_m - E_l} + \frac{1}{E'_m - E_l}\right]\ , \tag{D.12}$$

$$H^{(3)}_{\text{eff},mm'} = -\frac{1}{2}\sum_{l,m''}\left[\frac{H^{'}_{ml}H^{'}_{lm''}H^{'}_{m''m'}}{(E'_m - E_l)(E''_m - E_l)} + \frac{H^{'}_{mm''}H^{'}_{m''l}H^{'}_{lm'}}{(E_m - E_l)(E''_m - E_l)}\right] \\ + \frac{1}{2}\sum_{ll'}H^{'}_{ml}H^{'}_{ll'}H^{'}_{l'm}\left[\frac{1}{(E_m - E_l)\left(E_m - E'_l\right)} + \frac{1}{(E'_m - E_l)\left(E'_m - E'_l\right)}\right]. \tag{D.13}$$

D.2 Jordan-Wigner Transformation

A spin chain $1/2$ model can be mapped to an equivalent fermionic lattice model via the Jordan-Wigner transformation [275,276]. To illustrate how this mapping works, we consider the XX chain Hamiltonian

$$H = \sum_j S_j^x S_{j+1}^x + S_j^y S_{j+1}^y = \sum_j \frac{1}{2}\left(S_j^+ S_{j+1}^- + S_j^- S_{j+1}^+\right) , \tag{D.14}$$

where spin operators $S_j^\alpha = \sigma_j^\alpha/2$, obey to mixed commutation relations [59], as

$$\left[S_i^z, S_j^\pm\right] = \pm\delta_{ij} S_i^\pm, \qquad \left[S_i^+, S_j^-\right] = 2\delta_{ij} S_i^z . \tag{D.15}$$

Two possibilities are to map the system to a boson/fermion model[2] [59, 278, 279]. The Hamiltonian (D.14), can be transformed introducing raising and lowering operators as

$$a_j^\dagger = S_j^x + iS_j^y, \qquad a_j = S_j^x - iS_j^y, \tag{D.16}$$

so that

$$S_j^x = (a_j + a_j^\dagger)/2, \quad S_j^y = (a_j - a_j^\dagger)/2i, \tag{D.17}$$

$$S_j^z = a_j^\dagger a_j - 1/2, \tag{D.18}$$

and the Hamiltonian becomes

$$H = \frac{1}{2}\sum_j \left(a_j^\dagger a_{j+1} + H.c.\right). \tag{D.19}$$

The a_j operators anticommute in the same site and commute in different sites, as

$$\left\{a_j, a_j^\dagger\right\} = 1, \ \left\{a_j, a_j\right\} = \left\{a_j^\dagger, a_j^\dagger\right\} = 0, \tag{D.20}$$

$$\left[a_i, a_j\right] = \left[a_i, a_j^\dagger\right] = \left[a_i^\dagger, a_j^\dagger\right] = 0 \quad \text{for } i \neq j. \tag{D.21}$$

[2] The Hamiltonian (D.14) can be transformed in a system of bosons or fermions by using respectively the *Holstein-Primakoff* transformations (usually for spin $s \geq 1/2$) and the *Jordan-Wigner* transformations [59, 277–279].

The latter means that the a_j operators resemble Fermi operators in the same site, $\left(a_j^\dagger\right)^2 = a_j^2 = 0$, and boson operators in different sites. Therefore, as mixed commutation rules are satisfied, the Hamiltonian (D.19) cannot just be diagonalised by a linear transformation [278, 280]. Therefore, the mapping (D.16) must be modified to keep the local commutation relations, while to change commutation to anticommutation in different sites. In other words, if there is more than one spin in the system, independent spin operators commute but independent fermions anticommute. A solution to this problem, in a 1D setting, is called *Jordan-Wigner* transformation [278], which converts the Hamiltonian (D.19) in a system of spinless fermions [278, 279], as

$$c_i = \exp\left(i\pi \sum_{j=1}^{i-1} a_j^\dagger a_j\right) a_i, \qquad c_i^\dagger = a_i^\dagger \exp\left(-i\pi \sum_{j=1}^{i-1} a_j^\dagger a_j\right), \tag{D.22}$$

where the operators obey to fermion commutation rules,

$$\left\{c_i, c_j^\dagger\right\} = \delta_{ij}, \ \left\{c_i, c_j\right\} = \left\{c_i^\dagger, c_j^\dagger\right\} = 0. \tag{D.23}$$

The inverse transformations are

$$a_i = \exp\left(-i\pi \sum_{j=1}^{i-1} c_j^\dagger c_j\right) c_i \ , \qquad a_i^\dagger = c_i^\dagger \exp\left(i\pi \sum_{j=1}^{i-1} c_j^\dagger c_j\right) \ . \tag{D.24}$$

In other words, the spin operator is transformed as $S^+ = a_j^\dagger e^{i\phi_j}$, where $e^{i\phi_j}$, known as *string operator*, contains the sum over all fermion occupancies of sites to the left of j. The complete Jordan-Wigner transformation is

$$S_j^+ = c_j e^{i\pi \Sigma_{l<j} n_l}, \qquad S_j^- = c_j e^{-i\pi \Sigma_{l<j} n_l}, \tag{D.25}$$

$$S_j^z = c_j^\dagger c_j - 1/2. \tag{D.26}$$

As $e^{i\pi n_j}$ is hermitian, the overall sign of the phase factors can be reversed without changing the spin operator [281]. A propriety of the string operator is that it anticommutes with any fermion operator to the left of its free end and commutes, while

commutes with fermions at all other sites, namely

$$\left\{e^{i\phi_j}, c_l^\dagger\right\} = 0, \qquad \text{for } l < j \tag{D.27}$$

$$\left[e^{i\phi_j}, c_l^\dagger\right] = 0, \qquad \text{for } l \geq j \tag{D.28}$$

For the specific case of the Hamiltonian (D.14), the transformation (D.26) gives

$$\hat{H} = \sum_{j=1}^{N} \hat{c}_j^\dagger \hat{c}_{j+1} + \hat{c}_j \hat{c}_{j+1}^\dagger \tag{D.29}$$

that is a quadratic form in the operators $\hat{c}_j$ and can be reduced to a diagonal form by canonical transformations [275, 280, 281], as

$$\hat{H} = \sum_{\nu} \varepsilon_\nu a_\nu^\dagger a_\nu. \tag{D.30}$$

The latter corresponds to a system of free fermions. In the same fashion, the XXZ Hamiltonian, Eq. (1.104), in an external magnetic field, is transformed, under the Jordan-Wigner transformation, in a system of interacting fermions, [279], as

$$H = -t\sum_j \left(c_{j+1}^\dagger c_j + H.c.\right) + V\sum_j \left(c_{j+1}^\dagger c_{j+1} - \frac{1}{2}\right)\left(c_j^\dagger c_j - \frac{1}{2}\right) - h\sum_j \left(c_j^\dagger c_j - \frac{1}{2}\right), \tag{D.31}$$

where $t = -J/2$ and $V = J\Delta$.

D.3 Effective Hamiltonian for Bound States in the Bose-Hubbard Model

We briefly describe a projective technique, developed in [282], to derive an effective Hamiltonian description, when the Hilbert space of the system has two subspaces with a large spectral separation. In this appendix we apply this technique to the Bose-Hubbard model (1.64) to derive an effective Hamiltonian for a bound state with M particles. We assume that the Hilbert space of the system $\mathscr{H}$ can be divided respectively in a relevant, $\mathscr{H}_p$ and irrelevant, $\mathscr{H}_q$, subspaces and that the two subspaces are well separated in energy. We define a projection operator $\mathbb{P}$ which projects the states

to the relevant subspace and the complementary operator $\mathbb{Q}=\mathbf{1}-\mathbb{P}$. Because $\mathbb{P}$ and $\mathbb{Q}$ operate onto disconnected subspaces we have [82]

$$\begin{aligned} \mathbb{P}+\mathbb{Q} &= \mathbf{1}\,, \\ \mathbb{P}\mathbb{Q} &= \mathbb{Q}\mathbb{P}=0\,, \\ \mathbb{P}^2 &= \mathbb{P}\,, \\ \mathbb{Q}^2 &= \mathbb{Q}\,. \end{aligned} \tag{D.32}$$

Eq. (D.32) can be applied on the Schrödinger equation, to obtain a system of two coupled equations for the dynamics in the relevant/irrelevant subspaces, namely

$$i\partial_t \mathbb{P}|\psi\rangle = (\mathbb{P}H\mathbb{P}+\mathbb{P}H\mathbb{Q})\,|\psi\rangle\,, \tag{D.33}$$

$$i\partial_t \mathbb{Q}|\psi\rangle = (\mathbb{Q}H\mathbb{P}+\mathbb{Q}H\mathbb{Q})\,|\psi\rangle\,. \tag{D.34}$$

Finally, using the two last expression in (D.32) one obtains the system

$$i\partial_t \begin{pmatrix} |\psi_p\rangle \\ |\psi_q\rangle \end{pmatrix} = \begin{pmatrix} H_p & V \\ V^\dagger & H_q \end{pmatrix} \begin{pmatrix} |\psi_p\rangle \\ |\psi_q\rangle \end{pmatrix} \tag{D.35}$$

where

$$\begin{aligned} H_p =& \mathbb{P}H\mathbb{P}\,, \qquad H_q = \mathbb{Q}H\mathbb{Q}\,, \qquad V = \mathbb{P}H\mathbb{Q}\,, \\ |\psi_P\rangle =& \mathbb{P}\,|\psi\rangle\,, \qquad |\psi_Q\rangle = \mathbb{Q}\,|\psi\rangle\,. \end{aligned} \tag{D.36}$$

Here $|\psi_p\rangle$ and $|\psi_q\rangle$ are respectively the projection of the state $|\psi\rangle$ in the relevant/irrelevant subspaces. In the interaction picture [135]

$$|\psi_p\rangle = e^{-iH_p t}|\hat{\phi}_p\rangle\,, \tag{D.37}$$

$$|\psi_q\rangle = e^{-iH_q t}|\hat{\phi}_q\rangle\,, \tag{D.38}$$

the free evolution is eliminated,

$$i\partial_t|\hat{\phi}_p\rangle = e^{+iH_pt}Ve^{-iH_qt}|\hat{\phi}_q\rangle \equiv \hat{V}(t)|\hat{\phi}_q\rangle \,, \tag{D.39}$$

$$i\partial_t|\hat{\phi}_q\rangle = e^{+iH_qt}V^\dagger e^{-iH_pt}|\hat{\phi}_p\rangle \equiv \hat{V}^\dagger(t)|\hat{\phi}_p\rangle \,. \tag{D.40}$$

We introduce U_p and U_q, operators that diagonalise H_p and H_q,

$$H_p = U_p\lambda_pU_p^\dagger \,, \qquad H_q = U_q\lambda_qU_q^\dagger \,, \tag{D.41}$$

where λ_p=diag$\{\lambda_p^i\}$ and λ_q=diag$\{\lambda_q^i\}$, and defining $|\tilde{\phi}_p\rangle \equiv U_p^\dagger|\hat{\phi}_p\rangle$, and $|\tilde{\phi}_q\rangle \equiv U_q^\dagger|\hat{\phi}_q\rangle$, we have

$$i\partial_t|\tilde{\phi}_p\rangle = \tilde{V}(t)|\tilde{\phi}_q\rangle \,, \tag{D.42}$$

$$i\partial_t|\tilde{\phi}_q\rangle = \tilde{V}^\dagger(t)|\tilde{\phi}_p\rangle \,, \tag{D.43}$$

where

$$\tilde{V}(t) = U_p^\dagger\hat{V}(t)U_q = e^{i\lambda_pt}\hat{V}(t)e^{-i\lambda_qt} \,. \tag{D.44}$$

Assuming that the population of the irrelevant space is initially zero $|\hat{\phi}_q(0)\rangle = |0\rangle$, the formal solution of system (D.35) is, in components

$$\tilde{\phi}_{q,k}(t) = -i\sum_j\int_0^t dt'\; V_{jk}^*e^{i(\lambda_{q,k}-\lambda_{p,j})t'}\tilde{\phi}_{p,j}(t') \,, \tag{D.45}$$

and after partial integration one finds

$$\begin{aligned}\tilde{\phi}_{q,k}(t) = -i\sum_j\Bigg\{&\left.\frac{e^{i(\lambda_{q,k}-\lambda_{p.j})t'}}{i(\lambda_{q,k}-\lambda_{p.j})}V_{jk}^*\tilde{\phi}_{p,j}(t')\right|_0^t \\ &-\int_0^t dt'\;\frac{e^{i(\lambda_{q,k}-\lambda_{p.j})t'}}{i(\lambda_{q,k}-\lambda_{p.j})}\frac{d}{dt'}\tilde{\phi}_{p,j}(t')\Bigg\} \,.\end{aligned} \tag{D.46}$$

The second integral can be neglected, as carrying on the partial integration procedure the next term is of the order of $(\lambda_{q,k}-\lambda_{p.j})^{-2}$. Indeed because the subspaces $\mathscr{H}_p$ and $\mathscr{H}_q$ are energetically separated, $|\lambda_Q^k-\lambda_P^j|\gg 1$, and when the edge term is zero

one has

$$\tilde{\phi}_{q,k}(t) = -\sum_j \tilde{W}_{kj}(t)\tilde{\phi}_{p,j}(t) \ , \tag{D.47}$$

where

$$\tilde{W}_{kj}(t) = V^*_{jk} \frac{\exp\left[i\left(\lambda_Q^k - \lambda_P^j\right)t\right]}{\lambda_Q^k - \lambda_P^j} \ . \tag{D.48}$$

Finally one find that the effective Schrödinger equation for the relevant space dynamics is

$$i\partial_t|\psi_p\rangle \simeq H_{\text{eff}}|\psi_p\rangle \ , \tag{D.49}$$

where the effective Hamiltonian is

$$H_{\text{eff}} = H_p - VW \ , \tag{D.50}$$

and W satisfies

$$H_q W - W H_p = V^\dagger . \tag{D.51}$$

When H_p consists of a degenerate levels with energy E_0 the above effective theory corresponds to the usual degenerate perturbation theory [132],

$$\langle\phi|H_{\text{eff}}|\phi'\rangle \simeq \langle\phi|H|\phi'\rangle + \sum_{m\in\mathscr{H}_q} \frac{\langle\phi|V|m\rangle\langle m|V|\phi'\rangle}{E_0 - E_m} + \cdots \ , \tag{D.52}$$

where $\mathscr{H}_p$ and $\mathscr{H}_q$ are the relevant/irrelevant Hilbert subspaces and $|\phi\rangle, |\phi'\rangle \in \mathscr{H}_p$. We derive explicitly the effective Hamiltonian for a Bose-Hubbard model, Eq. (1.64). The Hilbert space $\mathscr{H}$ with fixed number of particle M in a chain with length L has size

$$\dim\mathscr{H} = \frac{(M+L-1)!}{M!(L-1)!} . \tag{D.53}$$

The relevant space $\mathscr{H}_p \equiv \mathscr{H}_M$ is defined as

$$\mathscr{H}_p = \left\{ |\psi_m^b\rangle \in \mathscr{H} : \ |\psi_m^b\rangle = |0,\ldots,0,M_m,0,\ldots,0\rangle \right\}, \tag{D.54}$$

where $M_m = M$. Clearly $\dim\mathscr{H}_p = L$. The irrelevant space $\mathscr{H}_q = \mathscr{H} \setminus \mathscr{H}_p$ is

$$\mathscr{H}_q = \left\{ |\psi_m^u\rangle \in \mathscr{H} : \ |\psi_m^u\rangle = |n_1,\ldots,n_L\rangle, \text{where } \sum_j n_j = M \text{ and } n_j \neq M \right\}. \tag{D.55}$$

Given the above definition we rename the basis of the Hilbert space as $|m\rangle$, with $m = 1,\ldots,\dim\mathscr{H}$ such that $|m\rangle = |\psi_m^b\rangle$ for $m = 1,\ldots,L$. The Hamiltonian then takes the following block form

$$H = \left(\begin{array}{c|c} H_p & V \\ \hline V^\dagger & H_q \end{array} \right), \tag{D.56}$$

where each block can be evaluated explicitly with the following projection operators

$$\mathbb{P} = \sum_{m=1}^{L} |m\rangle\langle\psi_m^b| \,, \qquad \mathbb{Q} = \sum_{m=1}^{\dim H_q} |L+m\rangle\langle\psi_m^u| \,. \tag{D.57}$$

Clearly $\dim\mathscr{H}_p = (L,L)$, $\dim\mathscr{H}_q = (\dim\mathscr{H} - L, \dim\mathscr{H} - L)$ and $\dim V = (L, \dim\mathscr{H} - L)$. The effective Hamiltonian (D.50) can be computed explicitly using a series expansion for large $U_j = U$. The relevant Hamiltonian for the Bose-Hubbard model (1.64) takes the simple form

$$H_p = \sum_{m=1}^{L} \frac{U}{2} M(M-1)|m\rangle\langle m| - \sum_{m=1}^{L} \mu_m M |m\rangle\langle m|. \tag{D.58}$$

Similarly H_q and V can be computed explicitly. The effective model can be obtained by solving Eq. (D.50) and (D.51). To find the W matrix we vectorise Eq. (D.51), as explained in Sec. A.0.3 and in [283], finding

$$G\text{vec}(W) = \text{vec}(V^\dagger), \tag{D.59}$$

where

$$G = \left(\mathbf{1}_{\dim H_p} \otimes H_q\right) - \left(H_p^t \otimes \mathbf{1}_{\dim H_q}\right). \tag{D.60}$$

It it is convenient to write $G = G^{\text{large}} + G^{\text{small}}$ where

$$G^{\text{large}} = \mathbf{1}_{\dim H_p} \otimes H_q^{\text{large}} - \left(H_p^{\text{large}}\right)^t \otimes \mathbf{1}_{\dim H_q}, \tag{D.61}$$

$$G^{\text{small}} = \mathbf{1}_{\dim H_p} \otimes H_q^{\text{small}} - \left(H_p^{\text{small}}\right)^t \otimes \mathbf{1}_{\dim H_p}. \tag{D.62}$$

and H^{large} is the part of the Hamiltonian (1.64) that contains the terms in U, namely $H^{\text{large}} = \sum_{j=1}^{L} \frac{U}{2} n_j(n_j - 1)$ and $H^{\text{small}} = H - H^{\text{large}}$. The system (D.59) can be formally solved by taking the inverse of the G matrix as

$$\text{vec}(W) = \frac{1}{G^{\text{large}} + G^{\text{small}}} \text{vec}(V^\dagger) \tag{D.63}$$

and using the following identity, valid for two operators A and B:

$$\frac{1}{A+B} = \frac{1}{A}\left(1 - B\frac{1}{A+B}\right). \tag{D.64}$$

Indeed one can easily find that

$$\begin{aligned} &\frac{1}{A}\left(1 - B\frac{1}{A+B}\right) = A^{-1}(1 - B(A+B)^{-1}) = \\ &= A^{-1}\left[(A+B)(A+B)^{-1} - B(A+B)^{-1}\right] = \\ &= A^{-1}\left[A(A+B)^{-1}\right] = \frac{1}{A+B}. \end{aligned} \tag{D.65}$$

Using recursively the Eq. (D.64) one finds the expansion

$$\frac{1}{G^{\text{large}} + G^{\text{small}}} = \left(G^{\text{large}}\right)^{-1} \sum_{n=0}^{+\infty} (-1)^n (G^{\text{small}} \left(G^{\text{large}}\right)^{-1})^n, \tag{D.66}$$

that corresponds to a series expansion in the onsite interaction parameter U (which is contained in G^{large}). Moreover,

$$G^{\text{large}} = -\frac{U}{2} \sum_{m=1}^{L} \sum_{n=1}^{\dim H_q} g(n,m)\ |L+n,m\rangle\langle L+n,m|, \tag{D.67}$$

where

$$g(n,m) = \sum_j M(M-1)\delta_{jm} - n_j(n_j-1) > 0,$$

since in $\mathscr{H}_q$ it is $n_j < M$ and $\sum_j n_j = M$. Therefore, G^{large} is diagonal and non-singular for each value of M. By truncating the expansion (D.66) at the relevant order n in U one obtains the matrix W from Eq. (D.63) and then the effective Hamiltonian from Eq. (D.50), valid to the n-th order.

As an example of the general procedure outlined above we consider explicitly the first order solution where $M = 2$ and (D.66) reduces to

$$(G^{\text{large}} + G^{\text{small}})^{-1} \approx (G^{\text{large}})^{-1} \tag{D.68}$$

$$= -U^{-1} \sum_{m=1}^{L} \sum_{n=1}^{\dim H_q} |L{+}n, m\rangle\langle L{+}n, m| \tag{D.69}$$

$$= -\frac{\mathbf{1}_q \otimes \mathbf{1}_p}{U}\,. \tag{D.70}$$

Therefore, according to (D.59), $W = -V^\dagger/U$, so

$$H_{\text{eff}} \simeq -\sum_{m=1}^{L} \mu_m M |m\rangle\langle m| + \sum_{m,m'=1}^{L} |m\rangle \frac{\langle \psi_m^b | V \mathbb{Q} V^\dagger | \psi_{m'}^b \rangle}{U} \langle m'|, \tag{D.71}$$

where we have explicitly omitted the terms proportional to the identity. For the interaction term V between $\mathscr{H}_p$ and $\mathscr{H}_q$ we observe that the only non-zero matrix elements are $\langle \psi_m^b | a_j a_{j+1}^\dagger | \psi_n^u \rangle$ (as well as their Hermitian conjugate) when

$$|\psi_m^b\rangle = |0, \ldots, M_j, \ldots, 0\rangle \tag{D.72}$$

$$|\psi_n^u\rangle = |0, \ldots, 1_j, (M-1)_{j+1}, \ldots, 0\rangle. \tag{D.73}$$

These can give rise to a hopping from $|m\rangle$ to $|m+1\rangle$ only for $M = 2$. Indeed, this is done with the following steps. Starting from $|m\rangle = |0, \ldots, 2_m, 0\ldots\rangle$ the operator $a_m a_{m+1}^\dagger$ in V maps this state to $|0, \ldots, 1_m, 1_{m+1}, 0\ldots\rangle$ which is in $\mathscr{H}_q$. Then the operator $a_m a_{m+1}^\dagger$ in $V^\dagger$ maps that state to $|m+1\rangle = |0, \ldots, 2_{m+1}, 0\ldots\rangle$. By generalising

the above argument, with simple calculations one finds then

$$H_{\rm eff}^{M=2} \simeq -\sum_{m=1}^{L} \mu_m M |m\rangle\langle m| + \sum_{m}^{L-1} \frac{J_m^2}{2U} \left(|m\rangle\langle m+1| + \text{h.}c.\right). \tag{D.74}$$

The generalisation to higher values of M proceeds along the same lines. For instance for $M = 3$ one has to consider the second order expansion in (D.66) which depends also on $G^{\rm small}$. Indeed, an effective hopping can happen only via a three step procedure

$$|m\rangle = |0,\ldots,3_m,0\ldots\rangle \to |0,\ldots,2_m,1_{m+1}0\ldots\rangle \tag{D.75}$$

$$\to |0,\ldots,1_m,2_{m+1}0\ldots\rangle \tag{D.76}$$

$$\to |0,\ldots,3_{m+1}0\ldots\rangle \equiv |m+1\rangle. \tag{D.77}$$

By doing explicit calculations we find the effective Hamiltonians mentioned in the main text.

D.4 Minimal engineering of the Three Particle Bound state propagation

The state transfer fidelity of the three particle bound state can be improved by introducing an optimal coupling scheme, namely tuning the first and the last tunnelling coupling to $J_1 = J_{L-1} = J_0$ and the rest of the chain to $J_j = J$. We find that, in order to delocalise the bound state, two pairs of localised fields in the endpoints are necessary, respectively $\mu_j = -\beta_1(\delta_{j,1} + \delta_{j,L})$ and $\mu_j = -\beta_2(\delta_{j,2} + \delta_{j,L-1})$ where $\beta_1 = (2J^2 - J_0^2)/8U$ and $\beta_2 = (J^2 - J_0^2)/8U$. In this case the beam splitting condition for $L \gg 1$ is realised when a local field $\mu_j = -\beta\,\delta_{j,L/2+1}$ with strength $\beta = \tilde{\beta}J^3/8U^2$

is added in the middle of the chain. The effective Hamiltonian is it in this case

$$H^{III}_{\rm opt}/2J^{III}_{\rm eff} = \begin{pmatrix} U^{III}_{\rm opt} & \frac{J_0^3}{2J^3} & & & & & \\ \frac{J_0^3}{2J^3} & \ddots & 1/2 & & & & \\ & 1/2 & U^{III}_{\rm opt} & \ddots & & & \\ & & \ddots & U^{III}_{\rm opt}+\tilde{\beta} & \ddots & & \\ & & & \ddots & U^{III}_{\rm opt} & 1/2 & \\ & & & & 1/2 & \ddots & \frac{J_0^3}{2J^3} \\ & & & & & \frac{J_0^3}{2J^3} & U^{III}_{\rm opt} \end{pmatrix} \tag{D.78}$$

where $J^{III}_{\rm eff} = 3J^3/16U^2$, $U^{III}_{\rm opt} = 8(U/J)^3 + 2U/J + 16(J/U)^2$. In order to have a perfectly balanced beam splitter in this single-particle Hamiltonian, as shown in Chap. 2, one needs $\tilde{\beta} = 1$. Therefore, $\beta^{50/50}{=}J^3/8U^2$. Our method is straightforwardly generalisable to bound states with a higher number of particles.

Appendix E

Numerical Data

Constant	Symbol	Value
Planck Constant	h	$6.626\,068\,96 \times 10^{-34}\ J\ s$
Reduced Planck Constant	$\hbar$	$1.054\,571\,628 \times 10^{-34}\ J\ s$
Bohr Radius	a_0	$0.529\,177\,208\,59 \times 10^{-10}\ m$
Atomic Mass Unit	u	$1.660\,538\,782 \times 10^{-27}\ kg$
Elementary Charge	e	$1.602\,176\,487 \times 10^{-19}\ C$
Boltzmann's Constant	k_B	$1.380\,6504 \times 10^{-23}\ J/K$

Table E.1: Physical constants [79].

	Atomic Mass
^{23}Na	$0.381\,754\,035 \times 10^{-25}\ kg$ [284]
^{39}K	$0.6470\,07 \times 10^{-25}\ kg$ [285]
^{41}K	$0.6801\,87 \times 10^{-25}\ kg$ [285]
^{87}Rb	$1.443\,160\,648 \times 10^{-25}\ kg$ [79]
^{133}Cs	$2.206\,946\,50 \times 10^{-25}\ kg$ [286]

Table E.2: Atomic masses of some alkali atoms.

Scattering length	Value
a_{AA}	$100.4\ a_0$ [287]
a_{BB}	$95.44\ a_0$ [288]
a_{AB}	$98.006\ a_0$ [288]

Table E.3: s-wave scattering length for ^{87}Rb in the states $|A\rangle \equiv |F=1, m_F=-1\rangle$ and $|B\rangle \equiv |F=2, m_F=1\rangle$, where a_0 is the Bohr radius.

Bibliography

[1] A. Celi, A. Sanpera, V. Ahufinger and M. Lewenstein: *Quantum optics and frontiers of physics: the third quantum revolution*. Phys. Scr. **92**, 013003 (2017).

[2] A. Trabesinger: *Quantum simulation*. Nat Phys **8**, 263 (2012).

[3] L. Amico, G. Birkl, M. Boshier and L.-C. Kwek: *Focus on atomtronics-enabled quantum technologies*. New J. Phys. **19**, 020201 (2017).

[4] H. Bernien, S. Schwartz, A. Keesling, H. Levine, A. Omran, H. Pichler, S. Choi, A. S. Zibrov, M. Endres, M. Greiner, V. Vuletić and M. D. Lukin: *Probing many-body dynamics on a 51-atom quantum simulator*. arXiv:1707.04344 (2017).

[5] T. D. Ladd, F. Jelezko, R. Laflamme, Y. Nakamura, C. Monroe and J. L. O'Brien: *Quantum computers*. Nature **464**, 45 (2010).

[6] J. L. O'Brien, A. Furusawa and J. Vučković: *Photonic quantum technologies*. Nat Photon **3**, 687 (2009).

[7] V. Vedral: *Introduction to Quantum Information Science* (Oxford University Press, Oxford), 1st ed. (2007).

[8] S. Haroche and J.-M. Raimond: *Exploring the Quantum: Atoms, Cavities, and Photons*. Oxford Graduate Texts (Oxford University Press, Oxford, New York) (2013).

[9] K. Bongs, M. Holynski and Y. Singh: *Ψ in the sky*. Nat Phys **11**, 615 (2015).

[10] Y. Tokura, M. Kawasaki and N. Nagaosa: *Emergent functions of quantum materials*. Nat Phys **advance online publication** (2017).

[11] J. P. Dowling and G. J. Milburn: *Quantum Technology: The Second Quantum Revolution*. arXiv:quant-ph/0206091 (2002).

[12] M. Lewenstein, A. Sanpera and V. Ahufinger: *Ultracold Atoms in Optical Lattices: Simulating quantum many-body systems* (Oxford University Press, Oxford, U.K), 1st ed. (2012).

[13] I. Bloch, J. Dalibard and W. Zwerger: *Many-body physics with ultracold gases*. Rev. Mod. Phys. **80**, 885 (2008).

[14] I. Bloch, J. Dalibard and S. Nascimbène: *Quantum simulations with ultracold quantum gases*. Nat Phys **8**, 267 (2012).

[15] C. Weitenberg, M. Endres, J. F. Sherson, M. Cheneau, P. Schauß, T. Fukuhara, I. Bloch and S. Kuhr: *Single-spin addressing in an atomic Mott insulator*. Nature **471**, 319 (2011).

[16] J. F. Sherson, C. Weitenberg, M. Endres, M. Cheneau, I. Bloch and S. Kuhr: *Single-atom-resolved fluorescence imaging of an atomic Mott insulator*. Nature **467**, 68 (2010).

[17] W. S. Bakr, J. I. Gillen, A. Peng, S. Fölling and M. Greiner: *A quantum gas microscope for detecting single atoms in a Hubbard-regime optical lattice*. Nature **462**, 74 (2009).

[18] H. Ott: *Single atom detection in ultracold quantum gases: a review of current progress*. Rep. Prog. Phys. **79**, 054401 (2016).

[19] C. Gross and I. Bloch: *Microscopy of many-body states in optical lattices*. In *Annual Review of Cold Atoms and Molecules*, vol. 3 of *Annual Review of Cold Atoms and Molecules*, pp. 181–199 (World Scientific) (2015).

[20] A. Alberti, C. Robens, W. Alt, S. Brakhane, M. Karski, R. Reimann, A. Widera and D. Meschede: *Super-resolution microscopy of single atoms in optical lattices*. New Journal of Physics **18**, 053010 (2016).

[21] T. Gericke, P. Würtz, D. Reitz, T. Langen and H. Ott: *High-resolution scanning electron microscopy of an ultracold quantum gas*. Nat Phys **4**, 949 (2008).

[22] P. M. Preiss, R. Ma, M. E. Tai, A. Lukin, M. Rispoli, P. Zupancic, Y. Lahini, R. Islam and M. Greiner: *Strongly correlated quantum walks in optical lattices*. Science **347**, 1229 (2015).

[23] R. Yamamoto, J. Kobayashi, T. Kuno, K. Kato and Y. Takahashi: *An ytterbium quantum gas microscope with narrow-line laser cooling*. New J. Phys. **18**, 023016 (2016).

[24] M. Miranda, R. Inoue, Y. Okuyama, A. Nakamoto and M. Kozuma: *Site-resolved imaging of ytterbium atoms in a two-dimensional optical lattice*. Phys. Rev. A **91**, 063414 (2015).

[25] C. Gross and I. Bloch: *Quantum simulations with ultracold atoms in optical lattices*. Science **357**, 995 (2017).

[26] P. Zupancic, P. M. Preiss, R. Ma, A. Lukin, M. E. Tai, M. Rispoli, R. Islam and M. Greiner: *Ultra-precise holographic beam shaping for microscopic quantum control*. Opt. Express **24**, 13881 (2016).

[27] M. R. Sturm, M. Schlosser, R. Walser and G. Birkl: *Quantum simulators by design: Many-body physics in reconfigurable arrays of tunnel-coupled traps*. Phys. Rev. A **95**, 063625 (2017).

[28] I. B. Spielman: *Atomic physics: A route to quantum magnetism*. Nature **472**, 301 (2011).

[29] M. Anderlini, P. J. Lee, B. L. Brown, J. Sebby-Strabley, W. D. Phillips and J. V. Porto: *Controlled exchange interaction between pairs of neutral atoms in an optical lattice*. Nature **448**, 452 (2007).

[30] J. Simon, W. S. Bakr, R. Ma, M. E. Tai, P. M. Preiss and M. Greiner: *Quantum simulation of antiferromagnetic spin chains in an optical lattice*. Nature **472**, 307 (2011).

[31] L.-M. Duan, E. Demler and M. D. Lukin: *Controlling Spin Exchange Interactions of Ultracold Atoms in Optical Lattices*. Phys. Rev. Lett. **91**, 090402 (2003).

[32] T. Fukuhara, P. Schauß, M. Endres, S. Hild, M. Cheneau, I. Bloch and C. Gross: *Microscopic observation of magnon bound states and their dynamics*. Nature **502**, 76 (2013).

[33] T. Fukuhara, A. Kantian, M. Endres, M. Cheneau, P. Schauß, S. Hild, D. Bellem, U. Schollwöck, T. Giamarchi, C. Gross, I. Bloch and S. Kuhr: *Quantum dynamics of a mobile spin impurity*. Nat Phys **9**, 235 (2013).

[34] M. Boll, T. A. Hilker, G. Salomon, A. Omran, J. Nespolo, L. Pollet, I. Bloch and C. Gross: *Spin- and density-resolved microscopy of antiferromagnetic correlations in Fermi-Hubbard chains*. Science **353**, 1257 (2016).

[35] M. Bruderer, A. Klein, S. R. Clark and D. Jaksch: *Polaron physics in optical lattices*. Phys. Rev. A **76**, 011605 (2007).

[36] I. Bloch: *Ultracold quantum gases in optical lattices*. Nat Phys **1**, 23 (2005).

[37] D. Jaksch, C. Bruder, J. I. Cirac, C. W. Gardiner and P. Zoller: *Cold Bosonic Atoms in Optical Lattices*. Phys. Rev. Lett. **81**, 3108 (1998).

[38] J. H. Lee, E. Montano, I. H. Deutsch and P. S. Jessen: *Robust site-resolvable quantum gates in an optical lattice via inhomogeneous control*. Nature Communications **4**, 2027 (2013).

[39] T. Calarco: *Quantum computations with atoms in optical lattices: Marker qubits and molecular interactions*. Phys. Rev. A **70**, 012306 (2004).

[40] K.-A. B. Soderberg, N. Gemelke and C. Chin: *Ultracold molecules: vehicles to scalable quantum information processing*. New J. Phys. **11**, 055022 (2009).

[41] N. B. Jørgensen, M. G. Bason and J. F. Sherson: *One- and two-qubit quantum gates using superimposed optical-lattice potentials*. Phys. Rev. A **89**, 032306 (2014).

[42] G. De Chiara, T. Calarco, M. Anderlini, S. Montangero, P. J. Lee, B. L. Brown, W. D. Phillips and J. V. Porto: *Optimal control of atom transport for quantum gates in optical lattices*. Phys. Rev. A **77**, 052333 (2008).

[43] D. Meschede: *Quantum information processing: Move around the clock*. Nat Phys **3**, 684 (2007).

[44] D. Stuart and A. Kuhn: *Single-atom trapping and transport in DMD-controlled optical tweezers*. arXiv:1708.06672 (2017).

[45] C. Weitenberg: *Quantum computation architecture using optical tweezers*. Phys. Rev. A **84**, 032322 (2011).

[46] A. M. Kaufman, B. J. Lester, C. M. Reynolds, M. L. Wall, M. Foss-Feig, K. R. A. Hazzard, A. M. Rey and C. A. Regal: *Two-particle quantum interference in tunnel-coupled optical tweezers*. Science **345**, 306 (2014).

[47] T. Wilk, A. Gaëtan, C. Evellin, J. Wolters, Y. Miroshnychenko, P. Grangier and A. Browaeys: *Entanglement of Two Individual Neutral Atoms Using Rydberg Blockade*. Phys. Rev. Lett. **104**, 010502 (2010).

[48] L. Isenhower, E. Urban, X. L. Zhang, A. T. Gill, T. Henage, T. A. Johnson, T. G. Walker and M. Saffman: *Demonstration of a Neutral Atom Controlled-NOT Quantum Gate*. Phys. Rev. Lett. **104**, 010503 (2010).

[49] A. Cesa and J. Martin: *Two-qubit entangling gates between distant atomic qubits in a lattice*. Phys. Rev. A **95**, 052330 (2017).

[50] G. K. Brennen, C. M. Caves, P. S. Jessen and I. H. Deutsch: *Quantum Logic Gates in Optical Lattices*. Phys. Rev. Lett. **82**, 1060 (1999).

[51] C. Robens, S. Brakhane, D. Meschede and A. Alberti: *Quantum Walks with Neutral Atoms: Quantum Interference Effects of One and Two Particles*. In *Laser Spectroscopy*, pp. 1–15 (World Scientific) (2016).

[52] D. Jaksch and P. Zoller: *The cold atom Hubbard toolbox*. Annals of Physics **315**, 52 (2005).

[53] D. Jaksch, H.-J. Briegel, J. I. Cirac, C. W. Gardiner and P. Zoller: *Entanglement of Atoms via Cold Controlled Collisions*. Phys. Rev. Lett. **82**, 1975 (1999).

[54] O. Mandel, M. Greiner, A. Widera, T. Rom, T. W. Hänsch and I. Bloch: *Controlled collisions for multi-particle entanglement of optically trapped atoms*. Nature **425**, 937 (2003).

[55] A. J. Daley, J. Ye and P. Zoller: *State-dependent lattices for quantum computing with alkaline-earth-metal atoms*. Eur. Phys. J. D **65**, 207 (2011).

[56] T. Calarco, E. A. Hinds, D. Jaksch, J. Schmiedmayer, J. I. Cirac and P. Zoller: *Quantum gates with neutral atoms: Controlling collisional interactions in time-dependent traps*. Phys. Rev. A **61**, 022304 (2000).

[57] Y. Lahini, G. R. Steinbrecher, A. D. Bookatz and D. Englund: *Quantum Logic with Interacting Bosons in 1D*. arXiv:1501.04349 (2015).

[58] M. I. Makin, J. H. Cole, C. D. Hill and A. D. Greentree: *Spin Guides and Spin Splitters: Waveguide Analogies in One-Dimensional Spin Chains*. Phys. Rev. Lett. **108**, 017207 (2012).

[59] P. Longo, A. D. Greentree, K. Busch and J. H. Cole: *Quantum Bocce: Magnon–magnon collisions between propagating and bound states in 1D spin chains*. Physics Letters A **377**, 1242 (2013).

[60] Y. Lahini, M. Verbin, S. D. Huber, Y. Bromberg, R. Pugatch and Y. Silberberg: *Quantum walk of two interacting bosons*. Phys. Rev. A **86**, 011603 (2012).

[61] P. M. Preiss, R. Ma, M. E. Tai, J. Simon and M. Greiner: *Quantum gas microscopy with spin, atom-number, and multilayer readout*. Phys. Rev. A **91**, 041602 (2015).

[62] S. Bose: *Quantum Communication through an Unmodulated Spin Chain*. Phys. Rev. Lett. **91**, 207901 (2003).

[63] S. Bose: *Quantum communication through spin chain dynamics: an introductory overview*. Contemporary Physics **48**, 13 (2007).

[64] R. Grimm, M. Weidemüller and Y. B. Ovchinnikov: *Optical Dipole Traps for Neutral Atoms*. Advances In Atomic, Molecular, and Optical Physics **42**, 95 (2000).

[65] P. Meystre: *Atom Optics* (Springer, New York) (2001).

[66] H. Pichler, A. J. Daley and P. Zoller: *Nonequilibrium dynamics of bosonic atoms in optical lattices: Decoherence of many-body states due to spontaneous emission*. Phys. Rev. A **82**, 063605 (2010).

[67] H. Pichler, J. Schachenmayer, A. J. Daley and P. Zoller: *Heating dynamics of bosonic atoms in a noisy optical lattice*. Phys. Rev. A **87**, 033606 (2013).

[68] K. Pawlowski and K. Rzazewski: *Background atoms and decoherence in optical lattices*. Physical Review A **81**, 013620 (2010).

[69] M. Schreiber, S. S. Hodgman, P. Bordia, H. P. Lüschen, M. H. Fischer, R. Vosk, E. Altman, U. Schneider and I. Bloch: *Observation of many-body*

localization of interacting fermions in a quasirandom optical lattice. Science **349**, 842 (2015).

[70] J. C. Sanders, O. Odong, J. Javanainen and M. Mackie: *Bound states of two bosons in an optical lattice near an association resonance*. Phys. Rev. A **83**, 031607 (2011).

[71] F. Meinert, M. Mark, E. Kirilov, K. Lauber, P. Weinmann, M. Gröbner and H.-C. Nägerl: *Interaction-Induced Quantum Phase Revivals and Evidence for the Transition to the Quantum Chaotic Regime in 1D Atomic Bloch Oscillations*. Phys. Rev. Lett. **112**, 193003 (2014).

[72] R. J. Glauber: *Coherent and Incoherent States of the Radiation Field*. Phys. Rev. **131**, 2766 (1963).

[73] D. F. Walls and G. J. Milburn: *Quantum Optics* (Springer, Berlin), 2nd ed. (2008).

[74] C. Cohen-Tannoudji, J. Dupont-Roc and G. Grynberg: *Atom-Photon Interactions: Basic Processes and Applications* (Wiley-VCH, New York) (1998).

[75] J.-M. Raimond and J. Zinn-Justin, eds.: *Fundamental Systems in Quantum Optics* (North Holland, Amsterdam ; New York) (1993).

[76] R. Loudon: *The Quantum Theory of Light* (Oxford University Press, Oxford, New York), 3rd ed. (2000).

[77] C. J. Pethick and H. Smith: *Bose–Einstein Condensation in Dilute Gases* (Cambridge University Press, Cambridge ; New York), 2nd ed. (2008).

[78] C. Cohen-Tannoudji, B. Diu and F. Laloe: *Quantum Mechanics, Vol. 1* (Wiley, New York), 1st ed. (1991).

[79] D. A. Steck: *Rubidium 87 D Line Data*. Version 2.1.5, URL: http://steck.us/alkalidata/ (2015).

[80] E. Duchon, Y. L. Loh and N. Trivedi: *Optical Lattice Emulators: Bose and Fermi Hubbard Models*. arXiv:1311.0543 (2013).

[81] H. Carmichael: *An Open Systems Approach to Quantum Optics: Lectures Presented at the Université Libre de Bruxelles, October 28 to November 4, 1991* (Springer, Berlin) (2013).

[82] H.-P. Breuer and F. Petruccione: *The Theory of Open Quantum Systems* (OUP Oxford, Oxford) (2007).

[83] A. J. Leggett: *Bose-Einstein condensation in the alkali gases: Some fundamental concepts*. Rev. Mod. Phys. **73**, 307 (2001).

[84] J. J. Sakurai and J. J. Napolitano: *Modern Quantum Mechanics* (Pearson, Boston), 2nd ed. (2010).

[85] C. Cohen-Tannoudji, B. Diu and F. Laloe: *Quantum Mechanics, Volume 2* (Wiley-VCH, New York, NY), 1st ed. (1991).

[86] X.-G. Wen: *Quantum Field Theory of Many-Body Systems: From the Origin of Sound to an Origin of Light and Electrons* (OUP Oxford, Oxford) (2007).

[87] F. Dalfovo, S. Giorgini, L. P. Pitaevskii and S. Stringari: *Theory of Bose-Einstein condensation in trapped gases*. Rev. Mod. Phys. **71**, 463 (1999).

[88] L. P. Pitaevskii and S. Stringari: *Bose-Einstein Condensation*. International Series of Monographs on Physics (Oxford University Press, Oxford, New York) (2003).

[89] B. H. Bransden and C. J. Joachain: *Physics of Atoms and Molecules* (Addison-Wesley, Harlow, England ; New York), 2nd ed. (2003).

[90] G. B. Arfken, H. J. Weber and F. E. Harris: *Mathematical Methods for Physicists, Seventh Edition: A Comprehensive Guide* (Academic Press, Amsterdam, Boston), 7th ed. (2012).

[91] L. D. Landau and E. M. Lifshitz: *Quantum Mechanics Non-Relativistic Theory, Third Edition: Volume 3* (Butterworth-Heinemann, Oxford), 3rd ed. (1981).

[92] R. A. Duine and H. T. C. Stoof: *Atom–molecule coherence in Bose gases*. Physics Reports **396**, 115 (2004).

[93] Y. Castin: *Bose-Einstein Condensates in Atomic Gases: Simple Theoretical Results*. In *Coherent atomic matter waves*, pp. 1–136 (Springer, Berlin, Heidelberg) (2001).

[94] I. E. Mazets and J. Schmiedmayer: *Thermalization in a quasi-one-dimensional ultracold bosonic gas*. New J. Phys. **12**, 055023 (2010).

[95] J. Catani, G. Lamporesi, D. Naik, M. Gring, M. Inguscio, F. Minardi, A. Kantian and T. Giamarchi: *Quantum dynamics of impurities in a one-dimensional Bose gas*. Phys. Rev. A **85**, 023623 (2012).

[96] M. Olshanii: *Atomic Scattering in the Presence of an External Confinement and a Gas of Impenetrable Bosons*. Phys. Rev. Lett. **81**, 938 (1998).

[97] C. Chin, R. Grimm, P. Julienne and E. Tiesinga: *Feshbach resonances in ultracold gases*. Rev. Mod. Phys. **82**, 1225 (2010).

[98] T. Volz, S. Dürr, S. Ernst, A. Marte and G. Rempe: *Characterization of elastic scattering near a Feshbach resonance in ^{87}Rb*. Phys. Rev. A **68**, 010702 (2003).

[99] A. Marte, T. Volz, J. Schuster, S. Dürr, G. Rempe, E. G. M. van Kempen and B. J. Verhaar: *Feshbach Resonances in Rubidium 87: Precision Measurement and Analysis*. Phys. Rev. Lett. **89**, 283202 (2002).

[100] A. Widera, O. Mandel, M. Greiner, S. Kreim, T. W. Hänsch and I. Bloch: *Entanglement Interferometry for Precision Measurement of Atomic Scattering Properties*. Phys. Rev. Lett. **92**, 160406 (2004).

[101] W. Hofstetter: *Ultracold atoms in optical lattices: tunable quantum many-body systems*. Philosophical Magazine **86**, 1891 (2006).

[102] A. J. Leggett: *Quantum Liquids: Bose condensation and Cooper pairing in condensed-matter systems* (OUP Oxford, Oxford , New York) (2006).

[103] N. Marzari, A. A. Mostofi, J. R. Yates, I. Souza and D. Vanderbilt: *Maximally localized Wannier functions: Theory and applications*. Rev. Mod. Phys. **84**, 1419 (2012).

[104] W. Kohn: *Analytic Properties of Bloch Waves and Wannier Functions*. Phys. Rev. **115**, 809 (1959).

[105] A. Daley: *Manipulation and Simulation of Cold Atoms in Optical Lattices*. Ph.D. thesis, Leopold-Franzens-Universitat Innsbruck, Innsbruck (2005).

[106] M. Bruderer, A. Klein, S. R. Clark and D. Jaksch: *Transport of strong-coupling polarons in optical lattices*. New J. Phys. **10**, 033015 (2008).

[107] F. Gerbier, A. Widera, S. Fölling, O. Mandel, T. Gericke and I. Bloch: *Interference pattern and visibility of a Mott insulator*. Phys. Rev. A **72**, 053606 (2005).

[108] S. Krinner, T. Esslinger and J.-P. Brantut: *Two-terminal transport measurements with cold atoms*. arXiv:1706.01085 (2017).

[109] P. Würtz, T. Langen, T. Gericke, A. Koglbauer and H. Ott: *Experimental Demonstration of Single-Site Addressability in a Two-Dimensional Optical Lattice*. Phys. Rev. Lett. **103**, 080404 (2009).

[110] S. Kuhr, W. Alt, D. Schrader, M. Müller, V. Gomer and D. Meschede: *Deterministic Delivery of a Single Atom*. Science **293**, 278 (2001).

[111] C. Kittel: *Introduction to Solid State Physics* (John Wiley & Sons, Hoboken, NJ), 8th ed. (2004).

[112] M. Greiner, O. Mandel, T. Esslinger, T. W. Hänsch and I. Bloch: *Quantum phase transition from a superfluid to a Mott insulator in a gas of ultracold atoms*. Nature **415**, 39 (2002).

[113] C. Salomon, G. V. Shlyapnikov and L. F. Cugliandolo: *Many-Body Physics with Ultracold Gases: Lecture Notes of the Les Houches Summer School: Volume 94, July 2010* (Oxford University Press, Oxford) (2013).

[114] S. Kuhr: *Quantum-gas microscopes: a new tool for cold-atom quantum simulators*. Natl Sci Rev **3**, 170 (2016).

[115] N. P. Proukakis, D. W. Snoke and P. B. Littlewood, eds.: *Universal Themes of Bose-Einstein Condensation* (Cambridge University Press, Cambridge, United Kingdom ; New York, NY), 1st ed. (2017).

[116] N. Gemelke, X. Zhang, C.-L. Hung and C. Chin: *In situ observation of incompressible Mott-insulating domains in ultracold atomic gases*. Nature **460**, 995 (2009).

[117] C. Weitenberg: *Fluorescence Imaging of Quantum Gases*. In *Quantum Gas Experiments*, vol. Volume 3 of *Cold Atoms*, pp. 121–143 (Imperial College Press) (2014).

[118] E. Haller, J. Hudson, A. Kelly, D. A. Cotta, B. Peaudecerf, G. D. Bruce and S. Kuhr: *Single-atom imaging of fermions in a quantum-gas microscope*. Nat Phys **11**, 738 (2015).

[119] M. F. Parsons, F. Huber, A. Mazurenko, C. S. Chiu, W. Setiawan, K. Wooley-Brown, S. Blatt and M. Greiner: *Site-Resolved Imaging of Fermionic ^{6}Li in an Optical Lattice*. Phys. Rev. Lett. **114**, 213002 (2015).

[120] H. Karttunen, P. Kröger and H. Oja, eds.: *Fundamental Astronomy* (Springer, Berlin ; New York), 5th ed. (2007).

[121] H. S. Han, H. G. Lee, S. Yoon and D. Cho: *Fluorescence detection of single lithium atoms in an optical lattice using Doppler-cooling beams*. arXiv:1703.07084 (2017).

[122] P. Sompet, A. V. Carpentier, Y. H. Fung, M. McGovern and M. F. Andersen: *Dynamics of two atoms undergoing light-assisted collisions in an optical microtrap*. Phys. Rev. A **88**, 051401 (2013).

[123] J. Audretsch: *Entangled Systems: New Directions in Quantum Physics* (Wiley-VCH, Weinheim), 1st ed. (2007).

[124] G. Barontini, R. Labouvie, F. Stubenrauch, A. Vogler, V. Guarrera and H. Ott: *Controlling the Dynamics of an Open Many-Body Quantum System with Localized Dissipation*. Phys. Rev. Lett. **110**, 035302 (2013).

[125] J. I. Cirac: *Entanglement in many-body quantum systems*. arXiv:1205.3742 (2012).

[126] E. Brion, L. H. Pedersen and K. Mølmer: *Adiabatic elimination in a lambda system*. J. Phys. A: Math. Theor. **40**, 1033 (2007).

[127] M. P. A. Jones, J. Beugnon, A. Gaëtan, J. Zhang, G. Messin, A. Browaeys and P. Grangier: *Fast quantum state control of a single trapped neutral atom*. Phys. Rev. A **75**, 040301 (2007).

[128] S. Olmschenk, R. Chicireanu, K. D. Nelson and J. V. Porto: *Randomized benchmarking of atomic qubits in an optical lattice*. New J. Phys. **12**, 113007 (2010).

[129] D. Greif, T. Uehlinger, G. Jotzu, L. Tarruell and T. Esslinger: *Short-Range Quantum Magnetism of Ultracold Fermions in an Optical Lattice*. Science **340**, 1307 (2013).

[130] T. Barthel, C. Kasztelan, I. P. McCulloch and U. Schollwöck: *Magnetism, coherent many-particle dynamics, and relaxation with ultracold bosons in optical superlattices*. Phys. Rev. A **79**, 053627 (2009).

[131] S. Trotzky, P. Cheinet, S. Fölling, M. Feld, U. Schnorrberger, A. M. Rey, A. Polkovnikov, E. A. Demler, M. D. Lukin and I. Bloch: *Time-Resolved Observation and Control of Superexchange Interactions with Ultracold Atoms in Optical Lattices*. Science **319**, 295 (2008).

[132] F. Mila and K. P. Schmidt: *Strong-Coupling Expansion and Effective Hamiltonians*. In C. Lacroix, P. Mendels and F. Mila, eds., *Introduction to Frustrated Magnetism*, no. 164 in Springer Series in Solid-State Sciences, pp. 537–559 (Springer Berlin Heidelberg) (2011).

[133] S. Bravyi, D. P. DiVincenzo and D. Loss: *Schrieffer–Wolff transformation for quantum many-body systems*. Annals of Physics **326**, 2793 (2011).

[134] J. Tangpanitanon, V. M. Bastidas, S. Al-Assam, P. Roushan, D. Jaksch and D. G. Angelakis: *Topological Pumping of Photons in Nonlinear Resonator Arrays*. Phys. Rev. Lett. **117**, 213603 (2016).

[135] S. M. Barnett and P. M. Radmore: *Methods in Theoretical Quantum Optics* (Clarendon Press, Oxford : New York), 1st ed. (1997).

[136] J. C. Halimeh, A. Wöllert, I. McCulloch, U. Schollwöck and T. Barthel: *Domain-wall melting in ultracold-boson systems with hole and spin-flip defects*. Phys. Rev. A **89**, 063603 (2014).

[137] J. J. García-Ripoll and J. I. Cirac: *Spin dynamics for bosons in an optical lattice*. New J. Phys. **5**, 76 (2003).

[138] G. M. Nikolopoulos and I. Jex, eds.: *Quantum State Transfer and Network Engineering* (Springer, New York), 2014th ed. (2013).

[139] L. Banchi: *Ballistic quantum state transfer in spin chains: General theory for quasi-free models and arbitrary initial states*. Eur. Phys. J. Plus **128**, 1 (2013).

[140] Z.-M. Wang, L.-A. Wu, M. Modugno, W. Yao and B. Shao: *Fault-tolerant almost exact state transmission*. Sci. Rep. **3**, 3128 (2013).

[141] A. Kay: *Perfect, efficient, state transfer and its application as a constructive tool*. Int. J. Quantum Inform. **08**, 641 (2010).

[142] M.-H. Yung and S. Bose: *Perfect state transfer, effective gates, and entanglement generation in engineered bosonic and fermionic networks*. Phys. Rev. A **71**, 032310 (2005).

[143] M. Christandl, N. Datta, A. Ekert and A. Landahl: *Perfect State Transfer in Quantum Spin Networks*. Phys. Rev. Lett. **92** (2004).

[144] A. Zwick, G. A. Álvarez, J. Stolze and O. Osenda: *Robustness of spin-coupling distributions for perfect quantum state transfer*. Phys. Rev. A **84**, 022311 (2011).

[145] A. Zwick, G. A. Álvarez, J. Stolze and O. Osenda: *Quantum state transfer in disordered spin chains: How much engineering is reasonable?* arXiv:1306.1695 (2013).

[146] L. Banchi, T. J. G. Apollaro, A. Cuccoli, R. Vaia and P. Verrucchi: *Long quantum channels for high-quality entanglement transfer*. New J. Phys. **13**, 123006 (2011).

[147] L. Banchi, T. J. G. Apollaro, A. Cuccoli, R. Vaia and P. Verrucchi: *Efficient Quantum Information Transfer Through a Uniform Channel*. Nanomaterials and Nanotechnology **1**, 24 (2011).

[148] T. J. G. Apollaro, L. Banchi, A. Cuccoli, R. Vaia and P. Verrucchi: *99%-fidelity ballistic quantum-state transfer through long uniform channels*. Phys. Rev. A **85**, 052319 (2012).

[149] A. Bayat, L. Banchi, S. Bose and P. Verrucchi: *Initializing an unmodulated spin chain to operate as a high-quality quantum data bus*. Phys. Rev. A **83**, 062328 (2011).

[150] L. Banchi and R. Vaia: *Spectral problem for quasi-uniform nearest-neighbor chains*. Journal of Mathematical Physics **54**, 043501 (2013).

[151] M. Bello, C. E. Creffield and G. Platero: *Long-range doublon transfer in a dimer chain induced by topology and ac fields*. Sci. Rep. **6**, 22562 (2016).

[152] M. Bello, C. E. Creffield and G. Platero: *Sublattice dynamics and quantum state transfer of doublons in two-dimensional lattices*. Phys. Rev. B **95**, 094303 (2017).

[153] S. Lorenzo, T. J. G. Apollaro, A. Sindona and F. Plastina: *Quantum-state transfer via resonant tunneling through local-field-induced barriers*. Phys. Rev. A **87**, 042313 (2013).

[154] K. Winkler, G. Thalhammer, F. Lang, R. Grimm, J. Hecker Denschlag, A. J. Daley, A. Kantian, H. P. Büchler and P. Zoller: *Repulsively bound atom pairs in an optical lattice*. Nature **441**, 853 (2006).

[155] A. R. Kolovsky, J. Link and S. Wimberger: *Energetically constrained co-tunneling of cold atoms*. New J. Phys. **14**, 075002 (2012).

[156] D. N. Maksimov and A. R. Kolovsky: *Escape dynamics of a Bose-Hubbard dimer out of a trap*. Phys. Rev. A **89**, 063612 (2014).

[157] D. Petrosyan, B. Schmidt, J. R. Anglin and M. Fleischhauer: *Quantum liquid of repulsively bound pairs of particles in a lattice*. Phys. Rev. A **76**, 033606 (2007).

[158] M. Valiente, D. Petrosyan and A. Saenz: *Three-body bound states in a lattice*. Phys. Rev. A **81**, 011601 (2010).

[159] M. Valiente and D. Petrosyan: *Two-particle states in the Hubbard model*. J. Phys. B: At. Mol. Opt. Phys. **41**, 161002 (2008).

[160] L. D. Landau and E. M. Lifshitz: *Mechanics, Third Edition: Volume 1* (Butterworth-Heinemann, Amsterdam), 3rd ed. (1976).

[161] V. Alba, K. Saha and M. Haque: *Bethe ansatz description of edge-localization in the open-boundary XXZ spin chain*. J. Stat. Mech. **2013**, P10018 (2013).

[162] M. Haque: *Self-similar spectral structures and edge-locking hierarchy in open-boundary spin chains*. Phys. Rev. A **82**, 012108 (2010).

[163] R. A. Pinto, M. Haque and S. Flach: *Edge-localized states in quantum one-dimensional lattices*. Phys. Rev. A **79**, 052118 (2009).

[164] M. Fox: *Quantum Optics: An Introduction*. Oxford Master Series in Physics (Oxford University Press, Oxford, New York) (2006).

[165] E. Knill, R. Laflamme and G. J. Milburn: *A scheme for efficient quantum computation with linear optics*. Nature **409**, 46 (2001).

[166] B. T. Gard, K. R. Motes, J. P. Olson, P. P. Rohde and J. P. Dowling: *An Introduction to Boson-Sampling*. In *From Atomic to Mesoscale*, pp. 167–192 (World Scientific) (2015).

[167] F. Laloë and W. J. Mullin: *Quantum Properties of a Single Beam Splitter*. Found Phys **42**, 53 (2012).

[168] C. K. Hong, Z. Y. Ou and L. Mandel: *Measurement of subpicosecond time intervals between two photons by interference*. Phys. Rev. Lett. **59**, 2044 (1987).

[169] Y. Bromberg, Y. Lahini, R. Morandotti and Y. Silberberg: *Quantum and Classical Correlations in Waveguide Lattices*. Phys. Rev. Lett. **102**, 253904 (2009).

[170] X. Qin, Y. Ke, X. Guan, Z. Li, N. Andrei and C. Lee: *Quantum Walks of Two Interacting Particles in One Dimension*. arXiv:1402.3349 (2014).

[171] X. Qin, Y. Ke, X. Guan, Z. Li, N. Andrei and C. Lee: *Statistics-dependent quantum co-walking of two particles in one-dimensional lattices with nearest-neighbor interactions*. Phys. Rev. A **90**, 062301 (2014).

[172] J. Dunningham and T. Kim: *Using quantum interferometers to make measurements at the Heisenberg limit*. Journal of Modern Optics **53**, 557 (2006).

[173] R. Demkowicz-Dobrzański, M. Jarzyna and J. Kołodyński: *Quantum Limits in Optical Interferometry*. Progress in Optics **60**, 345 (2015).

[174] H. Lee, P. Kok and J. P. Dowling: *A quantum Rosetta stone for interferometry*. Journal of Modern Optics **49**, 2325 (2002).

[175] W. J. Mullin and F. Laloë: *Creation of NOON States from Double Fock-State/Bose-Einstein Condensates*. J Low Temp Phys **162**, 250 (2011).

[176] H. Cable, F. Laloë and W. J. Mullin: *Formation of NOON states from Fock-state Bose-Einstein condensates*. Phys. Rev. A **83**, 053626 (2011).

[177] J. P. Dowling: *Quantum optical metrology – the lowdown on high-N00N states*. Contemporary Physics **49**, 125 (2008).

[178] J. Xiao-Xing, L. Jing, Z. Wei and W. Xiao-Guang: *Quantum Fisher Information of Entangled Coherent States in a Lossy Mach—Zehnder Interferometer*. Commun. Theor. Phys. **61**, 115 (2014).

[179] R. Yamamoto, J. Kobayashi, K. Kato, T. Kuno, Y. Sakura and Y. Takahashi: *Site-resolved imaging of single atoms with a Faraday quantum gas microscope*. Phys. Rev. A **96**, 033610 (2017).

[180] S. Bose: *Condensed-matter physics: Quantum togetherness*. Nature **502**, 40 (2013).

[181] A. P. Lund, M. J. Bremner and T. C. Ralph: *Quantum sampling problems, BosonSampling and quantum supremacy*. NPJ Quantum Information **3**, 15 (2017).

[182] A. Crespi, R. Osellame, R. Ramponi, D. J. Brod, E. F. Galvão, N. Spagnolo, C. Vitelli, E. Maiorino, P. Mataloni and F. Sciarrino: *Integrated multimode interferometers with arbitrary designs for photonic boson sampling*. Nature Photonics **7**, 545 (2013).

[183] H. Wang, Y. He, Y.-H. Li, Z.-E. Su, B. Li, H.-L. Huang, X. Ding, M.-C. Chen, C. Liu, J. Qin, J.-P. Li, Y.-M. He, C. Schneider, M. Kamp, C.-Z. Peng, S. Höfling, C.-Y. Lu and J.-W. Pan: *High-efficiency multiphoton boson sampling*. Nature Photonics **11**, 361 (2017).

[184] T. Fogarty, A. Kiely, S. Campbell and T. Busch: *Effect of interparticle interaction in a free-oscillation atomic interferometer*. Phys. Rev. A **87**, 043630 (2013).

[185] B. Gertjerenken: *Bright-soliton quantum superpositions: Signatures of high- and low-fidelity states*. Phys. Rev. A **88**, 053623 (2013).

[186] M. Leder, C. Grossert and M. Weitz: *Veselago lensing with ultracold atoms in an optical lattice*. Nature Communications **5**, 3327 (2014).

[187] T. Kovachy, J. M. Hogan, D. M. S. Johnson and M. A. Kasevich: *Optical lattices as waveguides and beam splitters for atom interferometry: An analytical treatment and proposal of applications*. Phys. Rev. A **82**, 013638 (2010).

[188] R. Islam, R. Ma, P. M. Preiss, M. Eric Tai, A. Lukin, M. Rispoli and M. Greiner: *Measuring entanglement entropy in a quantum many-body system*. Nature **528**, 77 (2015).

[189] W. J. Mullin and F. Laloë: *Interference Effects in Potential-Wells*. arXiv:1503.04183 (2015).

[190] I. Danshita and A. Polkovnikov: *Superfluid-to-Mott-insulator transition in the one-dimensional Bose-Hubbard model for arbitrary integer filling factors*. Phys. Rev. A **84**, 063637 (2011).

[191] S. Sarkar, S. Langer, J. Schachenmayer and A. J. Daley: *Light scattering and dissipative dynamics of many fermionic atoms in an optical lattice*. Phys. Rev. A **90**, 023618 (2014).

[192] S. Popescu: *Knill-Laflamme-Milburn Linear Optics Quantum Computation as a Measurement-Based Computation*. Phys. Rev. Lett. **99**, 250501 (2007).

[193] L. Sansoni, F. Sciarrino, G. Vallone, P. Mataloni, A. Crespi, R. Ramponi and R. Osellame: *Two-Particle Bosonic-Fermionic Quantum Walk via Integrated Photonics*. Phys. Rev. Lett. **108**, 010502 (2012).

[194] J. I. Cirac, P. Zoller, H. J. Kimble and H. Mabuchi: *Quantum State Transfer and Entanglement Distribution among Distant Nodes in a Quantum Network*. Phys. Rev. Lett. **78**, 3221 (1997).

[195] S. Ritter, C. Nölleke, C. Hahn, A. Reiserer, A. Neuzner, M. Uphoff, M. Mücke, E. Figueroa, J. Bochmann and G. Rempe: *An elementary quantum network of single atoms in optical cavities*. Nature **484**, 195 (2012).

[196] A. E. Kaplan, I. Marzoli, W. E. Lamb and W. P. Schleich: *Multimode interference: Highly regular pattern formation in quantum wave-packet evolution*. Phys. Rev. A **61**, 032101 (2000).

[197] R. W. Robinett: *Quantum wave packet revivals*. Physics Reports **392**, 1 (2004).

[198] M. Berry, I. Marzoli and W. Schleich: *Quantum carpets, carpets of light*. Phys. World **14**, 39 (2001).

[199] X.-B. Song, H.-B. Wang, J. Xiong, K. Wang, X. Zhang, K.-H. Luo and L.-A. Wu: *Experimental Observation of Quantum Talbot Effects*. Phys. Rev. Lett. **107**, 033902 (2011).

[200] J. Kempe: *Quantum random walks: An introductory overview*. Contemporary Physics **44**, 307 (2003).

[201] A. M. Childs: *Universal Computation by Quantum Walk*. Phys. Rev. Lett. **102**, 180501 (2009).

[202] A. M. Childs, R. Cleve, E. Deotto, E. Farhi, S. Gutmann and D. A. Spielman: *Exponential Algorithmic Speedup by a Quantum Walk*. In *Proceedings of the Thirty-fifth Annual ACM Symposium on Theory of Computing*, STOC '03, pp. 59–68 (ACM, New York, NY, USA) (2003).

[203] S. Longhi: *Periodic wave packet reconstruction in truncated tight-binding lattices*. Phys. Rev. B **82**, 041106 (2010).

[204] B. Alkurtass, L. Banchi and S. Bose: *Optimal quench for distance-independent entanglement and maximal block entropy*. Phys. Rev. A **90**, 042304 (2014).

[205] C. Di Franco, M. Paternostro and M. S. Kim: *Nested entangled states for distributed quantum channels*. Phys. Rev. A **77**, 020303 (2008).

[206] S. Friedland, J. Nocedal and M. Overton: *The Formulation and Analysis of Numerical Methods for Inverse Eigenvalue Problems*. SIAM J. Numer. Anal. **24**, 634 (1987).

[207] K. F. Riley, M. P. Hobson and S. J. Bence: *Mathematical Methods for Physics and Engineering: A Comprehensive Guide* (Cambridge University Press, Cambridge ; New York), 3rd ed. (2006).

[208] J. P. Keating, N. Linden, J. C. F. Matthews and A. Winter: *Localization and its consequences for quantum walk algorithms and quantum communication*. Phys. Rev. A **76**, 012315 (2007).

[209] J. Stasińska, M. Łącki, O. Dutta, J. Zakrzewski and M. Lewenstein: *Bose-Hubbard model with random impurities: Multiband and nonlinear hopping effects*. Phys. Rev. A **90**, 063634 (2014).

[210] S. Ospelkaus, C. Ospelkaus, O. Wille, M. Succo, P. Ernst, K. Sengstock and K. Bongs: *Localization of Bosonic Atoms by Fermionic Impurities in a Three-Dimensional Optical Lattice*. Phys. Rev. Lett. **96**, 180403 (2006).

[211] I. Afek, O. Ambar and Y. Silberberg: *High-NOON States by Mixing Quantum and Classical Light*. Science **328**, 879 (2010).

[212] Y. Israel, I. Afek, S. Rosen, O. Ambar and Y. Silberberg: *Experimental tomography of NOON states with large photon numbers*. Phys. Rev. A **85**, 022115 (2012).

[213] H. F. Hofmann and T. Ono: *High-photon-number path entanglement in the interference of spontaneously down-converted photon pairs with coherent laser light*. Phys. Rev. A **76**, 031806 (2007).

[214] P. Kok, W. J. Munro, K. Nemoto, T. C. Ralph, J. P. Dowling and G. J. Milburn: *Linear optical quantum computing with photonic qubits*. Rev. Mod. Phys. **79**, 135 (2007).

[215] K. Stiebler, B. Gertjerenken, N. Teichmann and C. Weiss: *Spatial two-particle NOON-states in periodically shaken three-well potentials*. J. Phys. B: At. Mol. Opt. Phys. **44**, 055301 (2011).

[216] G. Kordas, S. Wimberger and D. Witthaut: *Dissipation-induced macroscopic entanglement in an open optical lattice*. EPL **100**, 30007 (2012).

[217] M. A. Leung, K. W. Mahmud and W. P. Reinhardt: *Dynamical studies of macroscopic superposition states: phase engineering of controlled entangled number states of Bose–Einstein condensates in multiple wells*. Molecular Physics **110**, 801 (2012).

[218] L. Dell'Anna, G. Mazzarella, V. Penna and L. Salasnich: *Entanglement entropy and macroscopic quantum states with dipolar bosons in a triple-well potential*. Phys. Rev. A **87**, 053620 (2013).

[219] E. Rocco, R. N. Palmer, T. Valenzuela, V. Boyer, A. Freise and K. Bongs: *Fluorescence detection at the atom shot noise limit for atom interferometry*. New J. Phys. **16**, 093046 (2014).

[220] C. Gross, T. Zibold, E. Nicklas, J. Estève and M. K. Oberthaler: *Nonlinear atom interferometer surpasses classical precision limit*. Nature **464**, 1165 (2012).

[221] M. J. Bremner, C. M. Dawson, J. L. Dodd, A. Gilchrist, A. W. Harrow, D. Mortimer, M. A. Nielsen and T. J. Osborne: *Practical scheme for quantum*

computation with any two-qubit entangling gate. Phys. Rev. Lett. **89**, 247902 (2002).

[222] J. I. Cirac and P. Zoller: *Quantum Computations with Cold Trapped Ions*. Phys. Rev. Lett. **74**, 4091 (1995).

[223] T. P. Spiller, K. Nemoto, S. L. Braunstein, W. J. Munro, P. v. Loock and G. J. Milburn: *Quantum computation by communication*. New J. Phys. **8**, 30 (2006).

[224] L. Banchi, A. Bayat, P. Verrucchi and S. Bose: *Nonperturbative Entangling Gates between Distant Qubits Using Uniform Cold Atom Chains*. Phys. Rev. Lett. **106**, 140501 (2011).

[225] F. Ciccarello, G. M. Palma, M. Zarcone, Y. Omar and V. R. Vieira: *Entanglement controlled single-electron transmittivity*. New J. Phys. **8**, 214 (2006).

[226] F. Ciccarello, M. Paternostro, M. S. Kim and G. M. Palma: *Extraction of Singlet States from Noninteracting High-Dimensional Spins*. Phys. Rev. Lett. **100**, 150501 (2008).

[227] L. Lamata and J. León: *Generation of bipartite spin entanglement via spin-independent scattering*. Phys. Rev. A **73**, 052322 (2006).

[228] D. S. Saraga, B. L. Altshuler, D. Loss and R. M. Westervelt: *Coulomb scattering cross section in a two-dimensional electron gas and production of entangled electrons*. Phys. Rev. B **71**, 045338 (2005).

[229] G. Cordourier-Maruri, F. Ciccarello, Y. Omar, M. Zarcone, R. de Coss and S. Bose: *Implementing quantum gates through scattering between a static and a flying qubit*. Phys. Rev. A **82**, 052313 (2010).

[230] X. Z. Zhang and Z. Song: *EPR pairing dynamics in Hubbard model with resonant U*. Sci. Rep. **6**, 18323 (2016).

[231] J. J. Sakurai: *Advanced Quantum Mechanics* (Addison-Wesley, Reading, Mass.), 01st ed. (1967).

[232] M. Gaudin: *The Bethe Wavefunction* (Cambridge University Press, Cambridge, United Kingdom ; New York), third edition ed. (2014).

[233] D. Bombardelli: *S-matrices and integrability*. J. Phys. A: Math. Theor. **49**, 323003 (2016).

[234] M. Karbach and G. Muller: *Introduction to the Bethe ansatz I*. arXiv:cond-mat/9809162 (1998).

[235] F. Levkovich-Maslyuk: *The Bethe ansatz*. J. Phys. A: Math. Theor. **49**, 323004 (2016).

[236] V. E. Korepin, N. M. Bogoliubov and A. G. Izergin: *Quantum Inverse Scattering Method and Correlation Functions* (Cambridge University Press, Cambridge) (1997).

[237] C. N. Yang: *Some Exact Results for the Many-Body Problem in one Dimension with Repulsive Delta-Function Interaction*. Phys. Rev. Lett. **19**, 1312 (1967).

[238] S. Bose and D. Home: *Generic Entanglement Generation, Quantum Statistics, and Complementarity*. Phys. Rev. Lett. **88**, 050401 (2002).

[239] W. Krauth: *Bethe ansatz for the one-dimensional boson Hubbard model*. Phys. Rev. B **44**, 9772 (1991).

[240] F. Göhmann and V. E. Korepin: *The Hubbard chain: Lieb–Wu equations and norm of the eigenfunctions*. Phys. Lett. A **263**, 293 (1999).

[241] L. Amico, A. Osterloh, F. Plastina, R. Fazio and G. Massimo Palma: *Dynamics of entanglement in one-dimensional spin systems*. Phys. Rev. A **69**, 022304 (2004).

[242] L. Amico, R. Fazio, A. Osterloh and V. Vedral: *Entanglement in many-body systems*. Rev. Mod. Phys. **80**, 517 (2008).

[243] W. K. Wootters: *Entanglement of Formation of an Arbitrary State of Two Qubits*. Phys. Rev. Lett. **80**, 2245 (1998).

[244] A. Ramšak, I. Sega and J. H. Jefferson: *Entanglement of two delocalized electrons*. Phys. Rev. A **74**, 010304 (2006).

[245] A. Ramsak, J. Mravlje, T. Rejec and A. Lautar: *Entanglement of electron pairs extracted from a many-body system*. EPL **86**, 40003 (2009).

[246] O. F. Syljuåsen: *Entanglement and spontaneous symmetry breaking in quantum spin models*. Phys. Rev. A **68**, 060301 (2003).

[247] V. X. Genest, L. Vinet and A. Zhedanov: *Quantum spin chains with fractional revival*. Annals of Physics **371**, 348 (2016).

[248] M. Christandl, L. Vinet and A. Zhedanov: *Exact State Revival in a Spin Chain with Next-To-Nearest Neighbour Interactions*. arXiv:1610.04796 (2016).

[249] G. Watanabe and H. Mäkelä: *Floquet analysis of the modulated two-mode Bose-Hubbard model*. Phys. Rev. A **85**, 053624 (2012).

[250] A. Eckardt and E. Anisimovas: *High-frequency approximation for periodically driven quantum systems from a Floquet-space perspective*. New J. Phys. **17**, 093039 (2015).

[251] S. Popescu: *Knill-Laflamme-Milburn Quantum Computation with Bosonic Atoms*. Phys. Rev. Lett. **99**, 130503 (2007).

[252] M. A. Kristensen, M. Gajdacz, P. L. Pedersen, C. Klempt, J. F. Sherson, J. J. Arlt and A. J. Hilliard: *Sub-atom shot noise Faraday imaging of ultracold atom clouds*. J. Phys. B: At. Mol. Opt. Phys. **50**, 034004 (2017).

[253] M. Gajdacz, P. L. Pedersen, T. Mørch, A. J. Hilliard, J. Arlt and J. F. Sherson: *Non-destructive Faraday imaging of dynamically controlled ultracold atoms*. Review of Scientific Instruments **84**, 083105 (2013).

[254] D. Raventós, T. Graß, M. Lewenstein and B. Juliá-Díaz: *Cold bosons in optical lattices: a tutorial for exact diagonalization*. J. Phys. B: At. Mol. Opt. Phys. **50**, 113001 (2017).

[255] H. Fehske, R. Schneider and A. Weiße, eds.: *Computational Many-Particle Physics* (Springer, Berlin ; New York), 2008th ed. (2007).

[256] J. M. Zhang and R. X. Dong: *Exact diagonalization: the Bose–Hubbard model as an example*. Eur. J. Phys. **31**, 591 (2010).

[257] U. Schollwöck: *The density-matrix renormalization group in the age of matrix product states*. Annals of Physics **326**, 96 (2011).

[258] G. De Chiara, M. Rizzi, D. Rossini and S. Montangero: *Density Matrix Renormalization Group for Dummies*. Journal of Computational and Theoretical Nanoscience **5**, 1277 (2008).

[259] G. Vidal: *Efficient Simulation of One-Dimensional Quantum Many-Body Systems*. Phys. Rev. Lett. **93**, 040502 (2004).

[260] F. Verstraete, V. Murg and J. I. Cirac: *Matrix product states, projected entangled pair states, and variational renormalization group methods for quantum spin systems*. Advances in Physics **57**, 143 (2008).

[261] A. Björck: *Numerical Methods in Matrix Computations* (Springer, New York), 2015th ed. (2014).

[262] M. Am-Shallem, A. Levy, I. Schaefer and R. Kosloff: *Three approaches for representing Lindblad dynamics by a matrix-vector notation*. arXiv:1510.08634 (2015).

[263] X.-D. Zhang: *Matrix Analysis and Applications* (Cambridge University Press, Cambridge) (2017).

[264] D. Poulin, A. Qarry, R. Somma and F. Verstraete: *Quantum Simulation of Time-Dependent Hamiltonians and the Convenient Illusion of Hilbert Space*. Phys. Rev. Lett. **106**, 170501 (2011).

[265] C. Leforestier, R. H. Bisseling, C. Cerjan, M. D. Feit, R. Friesner, A. Guldberg, A. Hammerich, G. Jolicard, W. Karrlein, H. D. Meyer, N. Lipkin, O. Roncero and R. Kosloff: *A comparison of different propagation schemes for the time dependent Schrödinger equation*. Journal of Computational Physics **94**, 59 (1991).

[266] D. Jaschke, M. L. Wall and L. D. Carr: *Open source Matrix Product States: Opening ways to simulate entangled many-body quantum systems in one dimension*. arXiv:1703.00387 (2017).

[267] E. Gallopoulos and Y. Saad: *Efficient Solution of Parabolic Equations by Krylov Approximation Methods*. SIAM J. Sci. and Stat. Comput. **13**, 1236 (1992).

[268] T. V. Laptyeva, E. A. Kozinov, I. B. Meyerov, M. V. Ivanchenko, S. V. Denisov and P. Hänggi: *Calculating Floquet states of large quantum systems: A parallelization strategy and its cluster implementation*. Computer Physics Communications **201**, 85 (2016).

[269] C. Navarrete-Benlloch: *Open systems dynamics: Simulating master equations in the computer*. arXiv:1504.05266 (2015).

[270] A. Cantoni and P. Butler: *Eigenvalues and eigenvectors of symmetric centrosymmetric matrices*. Linear Algebra and its Applications **13**, 275 (1976).

[271] M. Abramowitz and I. A. Stegun, eds.: *Handbook of Mathematical Functions: with Formulas, Graphs, and Mathematical Tables* (Dover Publications, New York, NY), 9th ed. (1965).

[272] M.-H. Yung, D. W. Leung and S. Bose: *An exact effective two-qubit gate in a chain of three spins*. arXiv:quant-ph/0312105 (2003).

[273] R. Winkler: *Quasi-Degenerate Perturbation Theory*. In *Spin–Orbit Coupling Effects in Two-Dimensional Electron and Hole Systems*, Springer Tracts in Modern Physics, pp. 201–206 (Springer, Berlin, Heidelberg).

[274] A. Farrell and T. Pereg-Barnea: *Strong coupling expansion of the extended Hubbard model with spin-orbit coupling*. Phys. Rev. B **89**, 035112 (2014).

[275] J. I. Latorre and A. Riera: *A short review on entanglement in quantum spin systems*. J. Phys. A: Math. Theor. **42**, 504002 (2009).

[276] L. Campos Venuti, S. M. Giampaolo, F. Illuminati and P. Zanardi: *Long-distance entanglement and quantum teleportation in XX spin chains*. Phys. Rev. A **76**, 052328 (2007).

[277] W. Nolting and A. Ramakanth: *Quantum Theory of Magnetism* (Springer, Heidelberg ; New York), 2010th ed. (2009).

[278] E. Lieb, T. Schultz and D. Mattis: *Two soluble models of an antiferromagnetic chain*. Annals of Physics **16**, 407 (1961).

[279] T. Giamarchi: *Quantum Physics in One Dimension* (Clarendon Press, Oxford, New York), 1st ed. (2004).

[280] A. S. Davydov: *Quantum Mechanics: International Series in Natural Philosophy* (Pergamon) (2013).

[281] P. Coleman: *Introduction to Many-Body Physics* (Cambridge University Press, New York, NY), 1st ed. (2016).

[282] N. Jia, L. Banchi, A. Bayat, G. Dong and S. Bose: *Integrated information storage and transfer with a coherent magnetic device*. Sci. Rep. **5**, 13665 (2015).

[283] R. A. Horn and C. R. Johnson: *Topics in Matrix Analysis* (Cambridge University Press, Cambridge) (1994).

[284] D. A. Steck: *Sodium D Line Data*. Version 2.1.5, URL: http://steck.us/alkalidata/ (2010).

[285] T. G. Tiecke: *Properties of Potassium*. Ph.D. thesis, University of Amsterdam, The Netherlands (2010).

[286] D. A. Steck: *Cesium D Line Data*. Version 2.1.4, URL: http://steck.us/alkalidata/ (2010).

[287] A. D. Lercher, T. Takekoshi, M. Debatin, B. Schuster, R. Rameshan, F. Ferlaino, R. Grimm and H.-C. Nägerl: *Production of a dual-species Bose-Einstein condensate of Rb and Cs atoms*. Eur. Phys. J. D **65**, 3 (2011).

[288] M. Egorov, B. Opanchuk, P. Drummond, B. V. Hall, P. Hannaford and A. I. Sidorov: *Measurement of s-wave scattering lengths in a two-component Bose-Einstein condensate*. Phys. Rev. A **87**, 053614 (2013).